Optimized Permanent Magnet Generator Topologies for Direct-Drive Wind Turbines

Optimized Permanent Magnet Generator Topologies for Direct-Drive Wind Turbines

PROEFSCHRIFT

ter verkrijging van de graad van doctor
aan de Technische Universiteit Delft,
opgezag van de Rector Magnificus prof. dr. ir. J. T. Fokkema,
voorzitter van het College voor Promoties,
in het openbaar te verdedigen op maandag 26 januari 2004 om 10.30 uur
door

Maxime Roger Joseph DUBOIS

Bachelier ès sciences appliquées
Maître ès sciences

geboren te Alma (Canada)

Dit proefschrift is goedgekeurd door de promotors:

Prof. dr. J.A. Ferreira
Dr. ir. H. Polinder

Samenstelling promotiecommissie:

Rector Magnificus, voorzitter
Prof. dr. J.A. Ferreira, Technische Universiteit Delft, promotor
Dr. ir. H. Polinder, Technische Universiteit Delft, toegevoegd promotor
Prof. dr. B. C. Mecrow, University of Newcastle upon Tyne, UK
Prof. dr. ir. J. van Eijk, Technische Universiteit Delft
Prof. dr. ir. A. J. A. Vandenput, Technische Universiteit Eindhoven
Prof. ir. L. van der Sluis, Technische Universiteit Delft
Prof. dr. P. Viarouge, Université Laval, Canada

This research was funded by Delft University WIND research program (DU-WIND) in the Netherlands, by the Fond pour Chercheurs et Aide à la Recherche (FCAR) in Canada and by Éocycle Technologies Inc. in Canada.

Printed by Les Imprimeries ABC Inc.
Lévis, Canada

ISBN 0-9734585-0-X

to prof. Jean-Marc Martel
for his inspiring love of research

Table of contents

List of symbols

Latin symbols

A	current loading (*A/m*);
$\vec{A}$	magnetic vector potential (*Wb/m*);
A_{Cur}	cross-section of copper conductor in the rotor of wound-rotor synchronous machines (m^2);
A_{Cus}	cross-section of a copper conductor in the stator (m^2);
A_p	area of one pole (m^2);
A_{pi}	area covered by one pole where saturation occurs in the slotted axial-flux PM machine (m^2);
A_{po}	area covered by one pole where no saturation occurs in the slotted axial-flux PM machine (m^2);
b_{perp}	penetration depth of eddy currents related to perpendicular fields (*m*);
b_s	slot width of a conventional machine stator (*m*);
b_t	tooth width of a conventional machine stator (*m*);
b_{ti}	tooth width of the slotted axial-flux PM machine at the inner laminations radius (*m*);
b_{to}	outer tooth width in the slotted axial-flux PM machine (*m*);
$\vec{B}$	magnetic flux-density vector (*T*);
$\vec{B}_a$	stator-created magnetic flux density in the machine (*T*);
B_{Fesat}	iron saturation flux density; (*T*)
B_g	air gap flux density (*T*);
B_m	magnetic flux density in permanent magnets (*T*);
B_{perpnl}	flux density of the perpendicular field in the stator of the TFPM machine with toothed rotor (*T*);
$\vec{B}_{PM}$	magnetic flux density created by the PM in the machine (*T*);
B_r	remanent flux density of permanent magnets (*T*);
B_{rbi}	maximum flux density in the rotor back iron (*T*);

$\hat{B}_{st(rad)}$ peak flux density in the stator tooth of a longitudinal radial-flux machine (T);

$\hat{B}_{st1(rad)}$ amplitude of the fundamental frequency component of the flux density in the stator teeth for the conventional PM synchronous machine(T);

$\overline{B}_{st1(ax)}$ average of the fundamental frequency component of the flux density in the stator teeth for the slotted axial-flux PM machine(T);

$\hat{B}_{sti(ax)}$ amplitude of flux density in the stator tooth of the slotted axial-flux PM machine at inner radius (T);

B_{st1} fundamental frequency component of the tooth flux density (T);

B_{sy} maximum flux density in the stator yoke (T);

$\hat{B}_{sy1}$ amplitude of the fundamental frequency component of the flux density in the stator yoke (T);

$\hat{B}_1$ amplitude of air gap flux density sinusoidally varying in time and sinusoidally distributed in space (T);

c_{Cu} specific cost of copper (*Euro/kg*);

c_{Fe} specific cost of laminated steel (*Euro/kg*);

c_{pm} specific cost of permanent magnets (*Euro/kg*);

C_{act} cost of active material (*Euro*);

d_{out} machine outside diameter (m);

d_r diameter of the area swept by the blades of a wind turbine (m);

d_{side} distance between the stator core and the rotor flux concentrator in the TFPM machine with toothed rotor (m);

$d\vec{n}$ vector perpendicular to an infinitely small surface element;

$\mathrm{d}\vec{u}$ infinitesimal vector (parallel to $d\vec{\sigma}$ and also parallel to $\vec{j}$ and $\delta\vec{j}$);

$d\vec{\sigma}$ infinitesimal vector (parallel to $\mathrm{d}\vec{u}$ and also parallel to $\vec{j}$ and $\delta\vec{j}$);

e no-load voltage (V);

$\hat{e}$ amplitude of the no-load phase voltage (V);

E rms no-load voltage (V);

$\overline{E}$ average no-load voltage during one half-cycle (V);

f electrical frequency (Hz);

$\vec{F}_{mc}$ force exerted by the field on equivalent magnetic charges (N);

$\vec{F}_p$ force vector per pole pair (N);

F_{pa} attractive force per pole pair (N);

F_{pt} tangential force per pole pair (N);

F_t total tangential force (N);

$\overline{F}_t$ average tangential force (N);

F_x total instantaneous force exerted in the x direction in a linear machine (N);

$\overline{F}_x$ total average force exerted in the x direction in a linear machine (N);

$\Im_m$ MMF of a single permanent magnet (*A-turns*);
$\ddot{\Im}_s$ stator magnetomotive force (*A-turns*);
$\hat{\Im}_s$ amplitude of the stator magnetomotive force (*A-turns*);
g thickness of the air gap (*m*);
g_{eff} effective air gap thickness (*m*);
g_{tot} total air gap thickness (*m*);
h_{bi} thickness of rotor back iron (*m*);
h_{Cur} thickness of coil material in wound-motor electromagnets (*m*);
h_m magnet thickness (*m*);
h_{PM} thickness of PM material in conventional PM synchronous machines (*m*);
h_{ri} thickness of the insulation layer between the flux concentrator and the slot bottom in the rotor of the TFPM machine with toothed rotor (*m*);
h_{rt1} rotor slot height in the TFPM machine with toothed rotor (*m*);
h_{ru} distance between the tooth tip and the top of flux concentrator in the rotor of the TFPM machine with toothed rotor (*m*);
h_s slot depth in longitudinal machines (*m*);
h_{sy} stator yoke thickness (*m*);
h_w thickness of non-magnetic wedge in slotted longitudinal machines (*m*);
h_w height of the stator winding window in TFPM machines (*m*);
$\vec{H}$ magnetic field vector (*A/m*);
$\vec{H}_a$ externally applied magnetic field (*A/m*);
H_m magnetic field intensity in permanent magnets (*A/m*);
$\vec{H}_{PM}$ magnetic field intensity created by the PM in the machine (*A/m*);
i instantaneous phase current (*A*);
$\hat{i}_s$ peak value of the stator current (*A*);
$\hat{i}_{sc}$ short-circuit current (*A*);
I rms value of the phase current (*A*);
I_{max} maximum rms stator current (*A*);
I_s stator rms current (*A*);
$\vec{J}'$ equivalent volume current distribution (A/m^2);
$\vec{j}$ instantaneous current density vector (A/m^2);
J_r RMS current density in wound-motor electromagnets (A/m^2);
$k_{addloss}$ additional iron losses factor;
k_{Carter} Carter factor;
$k_{Carterave}$ average value of the Carter factor;
k_{conc} ratio of concentrator width over pole pitch in flux-concentrating conventional PM synchronous machines;

k_d	winding distribution factor;
$k_{eddysteel}$	specific eddy current losses in steel laminations (*W/kg*);
k_{exc}	excitation constant;
$k_{hysteel}$	specific hysteresis losses in steel laminations (*W/kg*);
k_{mag}	ratio of magnet width over pole pitch;
k_p	winding pitching factor;
$k_{powiron}$	specific losses of powdered iron at 1.5T/50 Hz (*W/kg*);
k_{rfill}	filling factor of rotor conductors;
k_{sfill}	filling factor of stator conductors;
k_{topo}	machine topology constant;
k_{sw}	skewing factor, which takes into account the reduction of emf due to slot skewing;
K	constant relating the machine torque to the machine current;
$\vec{K}'$	equivalent surface current distribution (*A/m*);
K_{ax}	ratio of inner lamination radius over outer lamination radius in axial-flux PM machine;
K_{axsat}	ratio of the radius from which saturation occurs over the outer lamination radius r_{lo};
K_{rad}	ratio of stator axial length over outer radius in a conventional PM synchronous machine;
l_{Cuew}	additional conductor length due to end windings in longitudinal machines (*m*);
l_{ew}	length of the end-windings in the longitudinal radial-flux machines (*m*);
l_{ewi}	length of the inner end-windings in the slotted axial-flux PM machine (*m*);
l_{ewo}	length of the outer end-windings in the slotted axial-flux PM machine (*m*);
l_f	stator foot axial length in TFPM machines (*m*);
l_{leg}	width of the stator leg in a TFPM machine (*m*);
l_{rt1}	length of flux concentrator in TFPM machines (*m*);
l_s	axial length of stator laminations in a conventional PM synch. machine (*m*);
l_w	width of the stator winding window in TFPM machines (*m*);
L_a	inductance of the stator core in the aligned position (*H*);
L_{mq}	magnetizing inductance in the quadrature axis of longitudinal PM synchronous machines (*H*);
L_s	stator inductance per phase (*H*);
L_u	inductance of the stator core in the unaligned position (*H*);
$L_{\sigma ew}$	leakage inductance in the end windings of longitudinal PM synchronous machines (*H*);
$L_{\sigma g}$	intertooth leakage inductance (*H*);

$L_{\sigma s}$ slot leakage inductance of longitudinal PM synchronous machines (*H*);
m number of phases in the machine;
m_{act} mass of active material (*kg*);
m_{bi} mass of back iron in surface-mounted longitudinal PM machines (*kg*);
m_c mass of flux concentrator in flux-concentrating longitudinal PM mach. (*kg*);
m_{Cu} mass of copper (*kg*);
m_{Fe} mass of laminated steel (*kg*);
$m_{fluxconc}$ mass of the flux concentrators in the TFPM machine with toothed rotor (*kg*);
m_{pm} mass of permanent magnets (*kg*);
m_{st} mass of stator teeth (*kg*);
m_{sy} mass of stator yoke (*kg*);
m_{top} mass of nacelle, blades and content of the nacelle in a wind turbine (*kg*);
$\vec{M}$ magnetization vector of a given material (*A/m*);
n rotational speed (rpm);
$\vec{n}$ unity vector normal to a surface;
$n_r I_r$ magnetomotive force of rotor electromagnets (*A-turns*);
N_s number of turns in the stator winding per phase (*turns*);
N_{slot} number of conductors inserted in one slot;
p number of pole pairs in a machine;
p_{Cu} instantaneous conduction loss in copper inside volume *V (W);*
$p_{eddyloss}$ eddy current losses per volume (W/m^3);
P_{Cu} average conduction losses in copper inside volume *V* (*W*)*;*
$P_{eddyperp}$ average eddy current losses in the stator due to perpendicular fields (*W*);
P_{elec} average electrical power extracted from the volume *V* (*W*)*;*
P_{Fe} average losses in iron inside volume *V* (*W*);
P_{Fes} average stator iron losses (*W*);
P_{mech} average mechanical power created by the machine (*W*);
$P_{powiron}$ average losses in the flux concentrators of the TFPM machine with toothed rotor (*W*);
q number of slots per pole per phase;
q^* equivalent magnetic charge *(Wb)*;
r multiple correlation coefficient;
r_g air gap radius of a machine (*m*);
r_{li} inner lamination radius in a slotted axial-flux PM machine (*m*);
r_{lo} outer lamination radius in a slotted axial-flux PM machine (*m*);
r_{out} machine outer radius (*m*);
R_s stator resistance per phase (Ω);

$\mathcal{U}_{ap}$ reluctance per pole pair seen by the stator core in the aligned position (*A/Wb*);
$\mathcal{U}_{bi}$ reluctance of rotor back iron in conventional PM synch. machines (*A/Wb*);
$\mathcal{U}_{c}$ reluctance of flux concentrators in flux-concentrating conventional PM synchronous machines (*A/Wb*);
$\mathcal{U}_{Ccore}$ reluctance of the stator horseshoe in a TFPM machine (*A/Wb*);
$\mathcal{U}_{ctc}$ lumped reluctance of the leakage path between the stator horseshoe or trapezium and the rotor flux concentrator of the neighbouring pole (*A/Wb*);
$\mathcal{U}_{ctcN}$ normalized reluctance for $\mathcal{U}_{ctc}$ (*A/Wb*);
$\mathcal{U}_{g}$ lumped reluctance of the air gap (*A/Wb*);
$\mathcal{U}_{gN}$ air gap normalized reluctance (*A/Wb*);
$\mathcal{U}_{hi}$ lumped reluctance of the leakage between the flux concentrator and the rotor core through the rotor slot (*A/Wb*);
$\mathcal{U}_{hiN}$ normalized reluctance for $\mathcal{U}_{hi}$ (*A/Wb*);
$\mathcal{U}_{icore}$ lumped reluctance of the leakage between one stator horseshoe and one trapezoidal stator core in the TFPM machine with toothed rotor (*A/Wb*);
$\mathcal{U}_{icoreN}$ normalized reluctance for $\mathcal{U}_{icore}$ (*A/Wb*);
$\mathcal{U}_{LEC}$ total reluctance of the leakage between two adjacent flux concentrators through their ends on one side (*A/Wb*);
$\mathcal{U}_{LEC1}$ reluctance of leakage between the ends of adjacent flux concentrators (*A/Wb*);
$\mathcal{U}_{LEC1N}$ normalized reluctance for $\mathcal{U}_{LEC1}$ (*A/Wb*);
$\mathcal{U}_{LEC2}$ reluctance of the leakage between the end of a flux concentrator and a rotor tooth (*A/Wb*);
$\mathcal{U}_{LEC2N}$ normalized reluctance for $\mathcal{U}_{LEC2}$ (*A/Wb*);
$\mathcal{U}_{m}$ reluctance of a single permanent magnet (*A/Wb*);
$\mathcal{U}_{side}$ reluctance between the stator core and the rotor flux concentrator in the unaligned position (*A/Wb*);
$\mathcal{U}_{sideN}$ normalized reluctance for $\mathcal{U}_{side}$ (*A/Wb*);
$\mathcal{U}_{SScore}$ reluctance of stator trapezium in TFPM machine with toothed rotor (*A/Wb*);
$\mathcal{U}_{stat}$ reluctance of both stator cores of TFPM machine with toothed rotor (*A/Wb*);
$\mathcal{U}_{statteeth}$ stator teeth reluctance in longitudinal machines (*A/Wb*);
$\mathcal{U}_{statyoke}$ stator yoke reluctance in longitudinal machines (*A/Wb*);
$\mathcal{U}_{t}$ reluctance of the gap between the stator core and a rotor tooth in the TFPM machine with toothed rotor (*A/Wb*);
$\mathcal{U}_{up}$ reluctance per pole pair seen by the stator coil in unaligned position (*A/Wb*);
$\vec{S}$ Poynting vector (W/m^2);
S_g air-gap area (m^2);
S_{coil} surface bounded by the machine coil (m^2);

S_{cond} cross-section of the conductor (m^2);
S_{pm} magnet cross-section per pole pair (m^2);
$\grave{t}$ magnetic tensile stress vector (N/m^2);
T instantaneous torque of a machine (Nm);
$\overline{T}$ average torque of a machine (Nm);
$\bar{T}_t$ average tangential torque (Nm);
v instantaneous terminal voltage (V);
v_s stator terminal voltage (V);
V volume enclosing the machine and all its magnetic field (m^3);
V_{air} volume of the remaining space within the machine boundary (m^3);
V_{Cu} copper volume (m^3);
$V_{cu(rad)}$ copper volume in longitudinal radial-flux PM machines (m^3);
V_{Feperp} volume of stator laminations involved in the calculations of eddy current losses caused by perpendicular fields (m^3);
V_g air-gap volume (m^3);
V_{iron} volume of steel contained in the machine (m^3);
V_{pm} volume of PM material in the machine (m^3);
V_{remain} volume of all universe outside the machine boundary (m^3);
w_{Cur} coil width in rotor electromagnets (m);
w_m magnet width (m);
w_{rc1} width of the stator tooth in the TFPM machine with toothed rotor (m);
w_{rc2} width of the flux concentrator in TFPM machines (m);
w_{sc} width of the horseshoe and trapezium stator cores in TFPM machines (m);
W_m stored magnetic energy inside volume V (J);
W'_m stored magnetic coenergy inside volume V (J);
W_{mag} magnetic energy in a system (including magnetic losses and stored magnetic energy) (J);
W'_{mag} magnetic coenergy inside volume V (including magnetic losses and stored coenergy) (J);
W_{mloss} magnetic losses (like hysteresis losses) inside volume V (J);
$X_{s\ p.u.}$ stator reactance (*per unit*);

Greek symbols

α electrical angle of the rotor with respect to the unaligned position (*rad*);

β_{ctc} normalization factor of U_{ctc};
β_g air gap normalization factor;
β_{hi} normalization factor of U_{hi};
β_{icore} normalization factor of U_{icore}
β_{LEC} normalization factor of U_{LEC};
β_{LEC1} normalization factor of U_{LEC1};
β_{LEC2} normalization factor of U_{LEC2};
β_{side} normalization factor of U_{side};
δ cosine of the angle between $\vec{H}_a$ and $\vec{B}_r$ at any given point inside the PM (*rad*);
η efficiency at full load;
θ electrical phase angle (*rad*);
λ flux linkage (*Wb-turns*);
λ_a stator-created flux linkage in the stator coil (*Wb-turns*);
λ_{PM} flux linkage created by the PM in the coil (*Wb-turns*);
λ_s flux linkage created by the armature reaction (*Wb-turns*);
μ_o magnetic permeability of empty space (*H/m*);
μ_r relative magnetic permeability;
μ_{rec} relative recoil permeability of permanent magnets;
μ_{rFe} magnetic permeability of steel laminations (*H/m*);
ρ electrical resistivity (*W-m*);
ρ^* volume distribution of equivalent magnetic charges *(Wb/m^3)*;
ρ_{Cu} copper specific mass (*kg/m^3*);
ρ_{Fe} steel specific mass (*kg/m^3*);
ρ_m magnet specific mass (*kg/m^3*);
$\rho_{powiron}$ powdered iron specific mass (*kg/m^3*);
ψ phase angle between the no-load voltage *e* and the phase current *i* (*rad*);
σ^* surface distribution of equivalent magnetic charges *(Wb/m^2)*;
σ_{Cu} conductivity of copper (*S/m*);
τ_p pole pitch (*m*);
τ_{pi} inner pole pitch in the axial-flux PM machines (*m*);
τ_{po} outer pole pitch in the axial-flux PM machine (*m*);
Φ_m no-load flux in permanent magnets (*Wb*);
Φ_{manl} flux flowing in the magnet at no-load (*Wb*);
Φ_{perpnl} magnetic flux perpendicular to the stator foot and the base of the trapezium in the unaligned position (*Wb*);
Φ_{pnl} no-load flux per pole pair (*Wb*);
$\hat{\Phi}_{pnl}$ amplitude of the no-load flux per pole pair (*Wb*);

Φ_{ps}	flux per pole pair created by the stator winding in the stator core (*Wb*);
Φ_{psat}	saturation flux per pole pair in TFPM machines (*Wb*);
Φ_{ptot}	total flux per pole pair in TFPM machines (*Wb*);
ω	electrical frequency (*rad/s*);
ω_m	angular rotational speed (*rad/s*);

Preface

"A scientist is never certain. We all know that. We know that all our statements are approximate statements with different degrees of certainty; that when a statement is made, the question is not whether it is true or false but rather how likely it is to be true or false."
- Richard Feynman, 1964, in The Pleasure of Finding Things Out.

Digging further into the field of electromagnetism and electrical machines reminded me of how complicated nature is and how deep and brilliant were the scientists who created the science of today. The Ph.D thesis presented in the following pages is only some dust falling down over the hard surface of science. With the uncertainties, mistakes, imperfections and wrong choices that appeared along this four-year journey, writing a thesis felt as a presumptuous and arrogant thing to do. But then I came across Richard Feynman's book (see quote above), to realize that even the best of scientists are still uncertain. This comforted me and gave me the strength I needed to write these pages.

In addition to Feynman's wisdom, many people have helped me throughout these years. I am especially grateful to Dr. Henk Polinder, my adjunct supervisor and friend. The number of hours I have spent in his office discussing machine concepts is countless. Dr. Polinder's door was always open to me and he has always showed the greatest concern on whatever small or big technical or personal difficulty I could come across.

I am grateful to Professor Jan Abraham Ferreira, who was my main supervisor and promoter during these four years. My stay in The Netherlands could not have lasted all these years without his kindness and understanding. Among many things, I am thankful to Prof. Ferreira for his openness of mind regarding my involvement in Eocycle Technologies.

I would like to thank Professor Gijs van Kuik and DUWIND for their financial and technical contribution to my work. The Fond de Chercheurs et d'Aide à la Recherche (FCAR) of Québec is gratefully acknowledged for their financial participation. I would also like to thank Mario Basque and Eocycle Technologies for their financial and technical involvement to my research.

A few other people have participated to this thesis. Their contributions are here acknowledged. Professor Jean-Marc Martel, Laval University (Canada) has reviewed the part on linear regression; Patrick Lemieux, Industrial Materials Institute (Canada) has reviewed the part on powdered iron; Isabelle Martel and Henk Paling have drawn many of the figures; Claude Gélinas and Quebec Metal Powders (Canada) have supplied the powdered iron material ATOMET-EM1 and shared their knowledge with me. Ruud van Schie, ECN (The Netherlands) has participated to the part on the slotted axial-flux PM machine.

I would like to express my gratitude to the members of my thesis committee, Professors Barrie Mecrow, Philippe Viarouge, André Vandenput, Lou van der Sluis and Jan van Eijk for reading the draft thesis and giving valuable suggestions.

I would like to thank the people of Electrical Power Processing for their support and friendship, especially Mark Gerber, Jelena Popovic, Martin Pavlovsky and my dear friend and coffee buddy Robert Holm. I would like to thank Sjoerd de Haan and Kees Weijermaans for their continuous struggle and patience in teaching me *de Nederlandse taal*.

Finally, I would like to express my gratitude to my wife Isabelle and daughter Gabrielle to whom I am indebted forever, for they left everything: friends, house, job, car, comfort to follow me into this Dutch adventure.

Chapter 1

Introduction

1.1. Electromechanical conversion in wind turbines

Wind energy is an increasing percentage of the energy supplied to the public electricity network. An average annual growth rate of 31% in the installed wind power capacity has been observed between 1997 and 2001 [BTM 2001]. To a certain extent, this strong growth rate is helped by the environmental policies and tax incentives of the various national governments. However, another determining factor has been the decreasing production cost of wind energy [EWE 1999]. Wind energy is now almost competitive with other more traditional sources of electrical energy like coal, gas and nuclear generation [Mil 2001]. Technology development is certainly one of the key factors in making wind energy more cost effective and reliable.

Wind turbines can be made with either constant-speed or variable-speed mechanical input. One of the areas where technological advances have played a major role in the last years is the development of innovative variable-speed wind turbines. The variable-speed wind turbine has several advantages, like higher energy extraction from the wind [Zin 1997], lower noise at low wind speed and cleaner power transfer to the grid [Car 1996]. For these reasons, the variable-speed wind turbine is taking an increasing share of the market nowadays. Variable-speed can be achieved in several ways. However, two configurations of variable-speed electromechanical converters are nowadays retaining attention: the direct-drive synchronous generator with power electronic converter and the doubly-fed induction generator with gearbox.

Figure 1-1 illustrates the direct-drive configuration. In that case, the electrical machine is a synchronous generator directly connected to the mechanical shaft. The generator electrical output is connected to a power electronic converter, which is connected to the electrical network (the grid). This configuration is discussed extensively in [Weh 1988a], [Gra 1996a], [Che 1996], [Pol 2001].

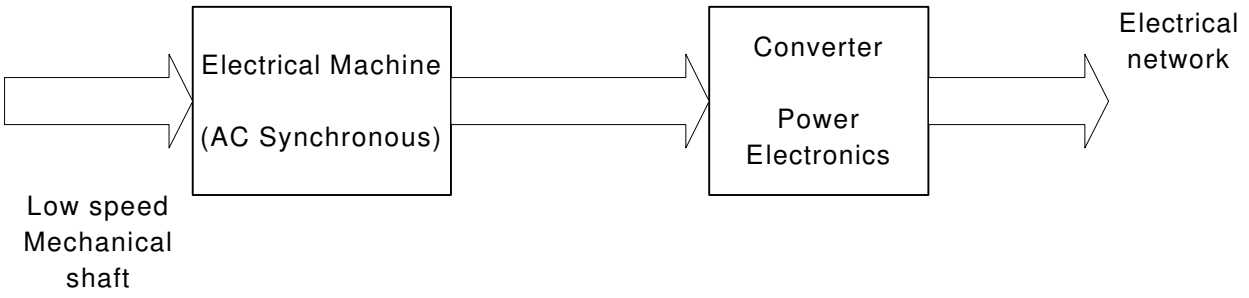

Figure 1-1: Basic components of a direct-drive electromechanical converter, using a synchronous machine and power electronics.

There are examples of wind turbine manufacturers who are developing around this configuration for high power wind turbines, like Enercon in Germany, Lagerwey in The Netherlands and Jeumont [Let 1997] in France.

The second popular configuration for electromechanical conversion in variable-speed wind turbines is the doubly-fed induction generator with gearbox [Smi 1981], [Pen 1996], illustrated in figure 1-2.

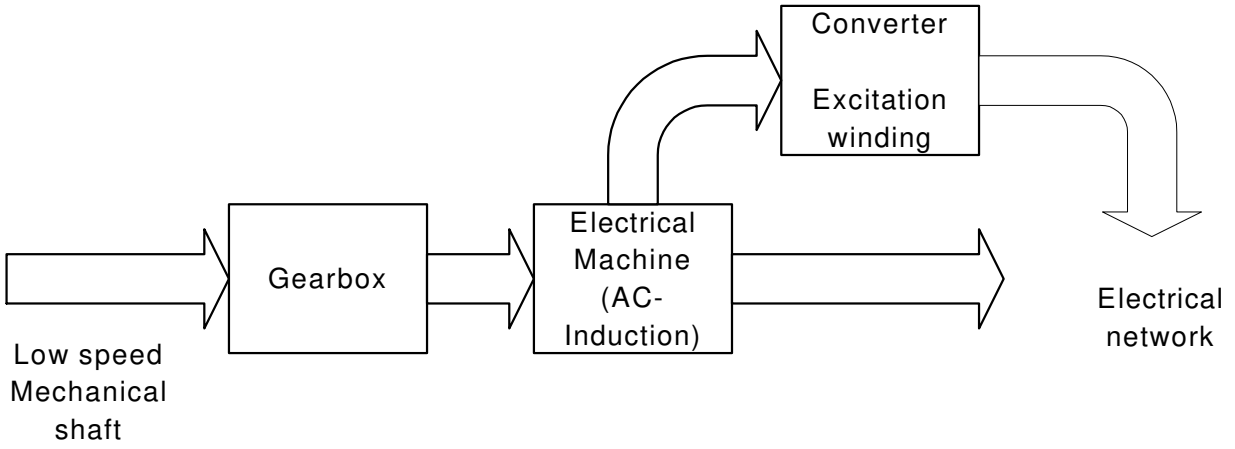

Figure 1-2: Basic components of a doubly-fed electromechanical converter, using an induction machine with slip rings.

The configuration of figure 1-2 uses an induction generator with a wound rotor and slip rings. The rotor circuit (excitation winding) is connected to an AC/AC power converter, which exchanges electrical energy between the rotor and the AC network. The induction generator is rotating at a conventional speed (1500 rpm for example) and a gearbox is needed to adapt the low-speed rotating shaft (25 rpm for example) to the generator.

The interest of the doubly-fed induction generator is the use of a low torque induction machine and the use of a power converter rated only a fraction of the nominal power extracted from the wind. In [Smi 1981], it is shown that a bidirectional converter rated only 30% of the wind turbine nominal power allows sufficient speed range for the wind turbine.

Examples of companies developing around the doubly-fed principle are Vestas and Neg-Micon in Denmark, General Electric in the United-States, and Nordex in Germany.

1.2. Advantages and disadvantages of direct-drive electromechanical conversion

Referring to figure 1-1, the direct-drive configuration eliminates the mechanical converter (the gearbox) and uses an electrical machine with low rotational speed. The choice between direct-drive and doubly-fed systems depends on many factors and it is not the intention of this thesis to state whether one is better than the other. However, we can give a few drawbacks of the doubly-fed configuration, as discussed in [Dub 2001b], [Slo 2003] and [Dit 2003]:

- heat dissipation caused by friction between gears;
- long-term wear due to friction between gears;
- oil is required, which must be replaced at regular intervals;
- audible noise from the gears rotational motion;
- limited capability of supplying reactive power to compensate the grid power factor;
- high torque peaks in the machine and large stator peak currents under grid fault conditions;
- external synchronization circuit required between the stator and the grid to limit the start-up current.

All the above-listed disadvantages favor the direct-drive configuration. However, one important drawback of direct-drive is the machine high torque rating. It is well-known [Har 1997], that the mass of electrical machines depends on their torque rating. For example, a 750-kW generator rotating at 25 rpm will be many times heavier and many times more expensive than a 750-kW generator rotating at 1500 rpm.

It is natural to electrical engineers to see the gearless, all-electric solution as the most elegant one. But the decision between a geared-drive and a direct-drive alternative is usually based on economical factors, space requirements, reliability, efficiency requirements and noise requirements. In many cases, the economical factors will prevail and the high cost of its electrical machine will make the direct-drive configuration a less interesting option. It is worth mentioning the study of Böhmeke *et al* [Böh 1997] (see table 1-1) which concludes that the electromechanical converter of a 1.5 MW wind turbine rotating at 19 rpm with a direct-driven wound-rotor synchronous generator would be about 25% more expensive than the geared-drive doubly-fed induction generator solution.

Table 1-1. Cost comparison between 1.5 MW gearbox/induction drive train and 1.5 MW direct-driven synchronous generators (source [Böh 1997]).

Parts considered	Cost of Geared technology	Cost of Direct-Drive technology
Gearbox, Shaft, Bearing, Hydraulics	25% of total turbine cost	1% of total turbine cost
Generator	8% of total turbine cost	36% of the total turbine cost
Electrics (including converters)	11% of total turbine cost	19% of total turbine cost
Total	44% of the total turbine cost	56% of the total turbine cost

In [Böh 2003], Böhmeke provides another comparison between the direct-drive and the doubly-fed configurations involving the masses of commercially-available wind turbines. The study is summarized in table 1-2, where m_{top} is the top mass of a wind turbine, including the blades, the nacelle and all the components inside the nacelle; d_r is the outside diameter of the turbine rotor. Table 1-2 indicates that direct-drive wind turbines found on the market have a top mass about 60% higher than for doubly-fed wind turbines for a given rotor swept area. However, the direct-drive wind turbines of [Böh 2003] are conventional wound-rotor synchronous generators. Thus, we could argue that the use of permanent magnets may reduce the turbine top mass. However, looking at the *J48* direct-drive wind turbine of Jeumont, which has the following characteristics:

- output power 750 kW;
- permanent magnet, slotted axial-flux generator;
- top mass $m_{top} = 47\ tons$;
- rotor diameter $d_r = 48\ m$,

it appears that the *J48* obeys the same rule as the one described in table 1-2 for wound-rotor direct-drive wind turbines. Whether or not the generator used by Jeumont is optimal in terms of topology and design is not clear at this point. However, it appears clearly that direct-drive

Table 1-2. Top mass relationship of commercially-available direct-drive and doubly-fed wind turbines (source [Böh 2003]).

Technology	Top mass relationship
Doubly-fed wind turbines	$m_{top} \approx 0,7 d_r^{2,75}$
Direct-drive wind turbines (with conventional wound-rotor synchronous machine)	$m_{top} \approx 1,1 d_r^{2,75}$

wind turbines are heavier and have more costly generators than the doubly-fed configuration.

Regarding the effect of the top mass increase on the wind turbine structure, a survey of wind turbine towers presented in [Hei 1998] shows a very large variation in the tower mass for a given turbine power rating. The study indicates large differences in the tower mass, according to the type of tower construction. Lately, three *J48* turbines were installed in Canada, with a tower height of 43 m and a tower mass of 45 tons, while the *N50* turbine of Nordex (which has a doubly-fed configuration) is sold with a tower height of 46 m and a tower mass of 51 tons. Therefore, no obvious correlation can be made at this point which indicates additional costs on the wind turbine structure linked to the presence of a direct-drive generator.

1.3. Problem definition

In a high-power wind turbine, the rotational speed is much lower than for conventional rotating machines (for example, 1500 rpm and 1800 rpm are conventional). Since the mass of an electrical machine increases with its nominal torque, the mass and the cost of a direct-drive generator will be much higher than that of a 1500 rpm-generator of the same power rating.

The use of a 1500 rpm-generator will be possible if a gearbox is inserted between the shaft of the wind turbine and the shaft of the electrical machine, leading to a generator with a higher rotational speed but lower torque rating. According to the manufacturers, the cost increase due to the addition of a gearbox is more than compensated by the cost reduction obtained with an electrical machine of reduced torque rating. In other words, the manufacturers will prefer the combination of a gearbox and a 1500 rpm machine, due to the higher cost of a gearless machine with high torque rating.

Although the doubly-fed configuration appears as a cost effective solution, the use of a gearbox will bring a few drawbacks. Gearboxes need oil, need regular maintenance for oil replacement, create additional heat losses due to friction, decrease the overall system reliability and create additional noise. These drawbacks are tolerated, provided that the economics still prove the doubly-fed configuration to be the most interesting option. The direct-drive configuration will avoid the above-mentioned drawbacks and is therefore desirable. However, to make the direct-drive solution really attractive, research is needed in order to reduce the cost of low-speed, high-torque machines. This is what underlines the main target of this thesis.

One of the first questions which should be addressed is: by how much must we reduce the cost of the direct-drive generator in order to make the gearless system competitive with the doubly-fed system? Unfortunately, this question will not be answered in this thesis. The cost of a direct-drive generator is dependent not only on the cost of its components, but also on the production facilities used, the number of machines sold, the profits made by the manufacturer and other variables which are beyond the scope of our research in electrical engineering. A complete picture would require market models and production models, which we will leave to researchers in industrial engineering and marketing.

Among several variables, the cost breakdown of an electrical machine includes the “active material”. The active material comprises all material inside the machine carrying either electric currents or magnetic fields, that is copper, laminated steel, permanent magnets and in some cases powdered iron material. At this point, we believe that further analysis of costs of active material for low-speed machines is relevant.

Following the statements and ideas described in the last paragraphs, this thesis is concerned with the minimization of mass and cost of active material in direct-drive generators for wind turbines. We have chosen to concentrate our research activity to the case of PM (permanent magnet) synchronous machines. As a matter of fact, several authors [Mit 1995], [Had 1999], [Lan 2000] have compared the PM synchronous machine with the induction machine and the switched reluctance machine in direct-drive configurations. All of the authors concluded that the use of PM synchronous machines lead to a lower mass of active material for a given torque rating.

Since the PM synchronous machine appears to be a good starting point for minimal mass and cost in low-speed machines, this thesis will focus on the minimization of active material in PM machines. In this thesis, the terminology “permanent magnet synchronous machine” does not refer to a specific PM machine geometry. It refers to the general concept of electrical machines carrying PM on their rotors and running in a synchronous manner. In this context, the thesis will investigate a wide range of PM topologies.

Even though it is not the intention of this thesis to calculate the production costs of any of the PM machine geometries, attention must be paid to the “ease of manufacturing” of a given machine geometry. Some of the machine topologies described in the thesis will exhibit very difficult manufacturing. Remembering that a low-speed machine must be economically competitive, the thesis will investigate PM machines with low mass of active material, but also easy construction.

1.4. Outline of the thesis

The thesis looks at a broad range of machine topologies for the application described in this introduction. Chapter 2 gives a wide overview of PM machine topologies. A classification is proposed based on four machine characteristics. At the end of chapter 2, two design targets are determined (cost/torque, torque/mass). In chapter 3, various methods of torque computation are briefly reviewed and a selection is made for the optimization and the calculation of torques.

In chapter 4, most of PM machine topologies described in chapter 2 are investigated on the basis of cost/torque and torque/mass. The investigation will indicate that the convention PM synchronous machine and the transverse-flux PM machine may be retained as the most suitable for the application. However, chapter 4 will point out that no comprehensive comparison actually exist between these two machine types.

In chapter 5, a digression is made on the subject of PM shapes. A method is presented, allowing to increase the contribution of the PM to the magnetic flux flowing in the stator coil at no-load. With the same method, we investigate the contribution of permanent magnets in

transverse-flux machines in the two cases of surface-mounted magnets and flux-concentrating magnets.

Chapter 6 describes the known topologies of flux-concentrating transverse-flux PM machines. They are compared together based on their cost/torque and torque/mass performances, but also based on their ease of construction. The subject of powdered iron is addressed and finally a new machine topology is derived, which is named “transverse-flux PM machine with toothed rotor”.

The modeling of the transverse-flux PM machine with toothed rotor is discussed in chapter 7. The aim of chapter 7 is to derive expressions for the complex 3-D structure discussed in chapter 6 to obtain the torque in analytical terms. A method based on finite element analysis and linear regression is employed.

In chapter 8, the analytical expressions developed are used to optimize the machine design. The performances obtained with the transverse-flux PM machine with toothed rotor are compared to those of the conventional PM synchronous machine for equal efficiencies.

In chapter 9, a prototype of the transverse-flux PM machine is built and the results are described.

Chapter 2

Overview of PM machine types

2.1. Introduction

The investigation of PM synchronous machines with minimal mass and cost of active material requires an overview of the various PM machine concepts. In chapter 1, we defined the "permanent magnet synchronous machine" as a machine with PM mounted on its rotor and running in a synchronous manner. A quick literature overview readily indicates the wide possibilities in the way PM can be mounted on a rotor. Among those possibilities, what will be the best PM machine topology for lowest mass, lowest cost and best manufacturing? This question is investigated in the thesis.

Section 2.2 will provide the main advantages of PM excitation versus synchronous machines excited with current-carrying coils. In section 2.3, the diverse families and geometries of PM machines found in the current scientific literature will shortly be described. As will be apparent from section 2.3, the sole understanding of their principle of operation is not sufficient to indicate what PM machine topology should be chosen. This will emphasize the need for optimization tools for each machine type for the purpose of comparing them together. The development of optimization tools for the various PM machine geometries will be the subject of chapters 4 and 8. The selection of optimization criteria will be treated in section 2.5. Those criteria will be used extensively in the remainder of the thesis for the comparison between PM machine geometries and for the detailed design optimization of given PM machine topologies.

2.2. Advantages of PM machines versus wound rotors and switched-reluctance machines.

The direct-drive configuration discussed in the thesis was illustrated in figure 1-1. Such a direct-drive system configuration is again illustrated in figure 2-1.

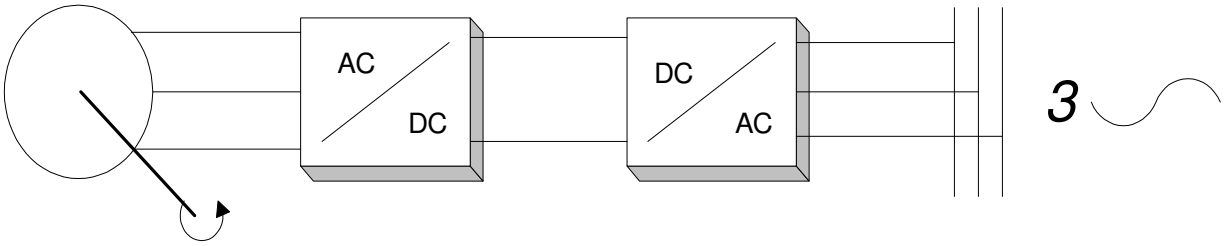

Figure 2-1: Direct-drive configuration

Synchronous machine vs induction machine

Several machine types may serve the function of direct-driven generator. As discussed previously, several authors [Mit 1995], [Had 1999], [Lan 2000a] have confirmed the advantage of the PM synchronous machine over the induction machine. The induction machine requires more active material and is more bulky than the PM synchronous machine. Induction machines supply the excitation field to their rotor via the stator winding. Consequently, the stator winding must carry both the active power obtained in the conversion and the reactive power required by the rotor for its excitation. This makes the stator losses higher and requires larger copper cross-section and slot space in the stator. Based on these ideas, the induction machine was discarded by those authors as a possible solution for reducing active material in direct-drive electrical machines and the same choice is made here.

Synchronous machine vs switched reluctance machine

Like the induction machine, the switched reluctance machine (SRM) also does not include excitation in the rotor. The principle of the SRM has been discussed in a number of publications, like in [Law 1980]. In [Har 1989], the SRM is compared to the induction machine and designs are obtained for both machine types. For equal efficiencies, the SRM appears as more compact and slightly lighter than the induction machine. This study also highlights the fact that the converter rating of the SRM is higher than that of the induction machine. In [Mil 1985] and [Mil 1993], it is discussed that the excitation current of the SRM leads to an "excitation penalty" in the order of 35-60%, making the volt-ampere rating of the converter switches higher than for other machine types. In [deH 1995], a study of a SRM in a wind turbine application also indicates that the converter rating of the SRM is higher than for the other machine topologies analyzed.

The specific application of SRM as direct-drive generators for wind turbines has been discussed in [Tor 1993], [deH 1994], [deH 1995], [Car 1995], [Hao 1997], [Liu 1998], and [Mue 1999]. In [Dub 2000], a comprehensive comparison is made between the various SRM prototypes built or designed by these authors to the conventional PM synchronous machine (radial type). According to the performance reported by the authors, the cost of the SRM machine are more or less comparable to the conventional PM synchronous machines for

diameters below 1 meter. For larger diameters, the SRM machine designed in [deH 1995], which is also compared in [Dub 2000] to the conventional PM synchronous machine gives much higher costs for the SRM. Based on the literature available, we choose to discard the SRM from our study. The SRM seems to have equivalent or higher cost compared to the conventional PM synchronous machine and the converter rating appears as significantly higher than that of the conventional PM synchronous machine. Thus, the induction and the SRM machines will not be analyzed further in the thesis.

Synchronous machine: PM excitation vs electrical excitation

The synchronous machine has the ability to provide its own excitation on the rotor. Such a rotor excitation may be obtained either by means of a current-carrying coil, or by the means of permanent magnets. In this thesis, the PM type will be analyzed in more detail, but it is necessary at this point to substantiate why the wound-rotor synchronous generator is less interesting for mass and cost reduction in the system of figure 2-1.

The wound-rotor synchronous machine has a very interesting feature compared to its PM counterpart: adjustable excitation current and, consequently, adjustable no-load voltage. This feature explains why most constant-speed grid-connected hydro and turbogenerators use wound-rotor instead of PM-excited rotors. In the wind turbine industry, the synchronous generator is in most cases connected to the grid via an electronic converter, as it is the case in the direct-drive wind turbines of the German manufacturer Enercon and the Dutch manufacturer Lagerwey. Therefore, the advantage of controllable no-load voltage is not as critical. Until now, these two wind turbine manufacturers have used a synchronous generator with electrically-excited rotor. But the trend is slowly moving towards the use of PM synchronous generators.

This trend is explained by the fact that, for a given torque rating, a synchronous machine with a higher number of pole pairs enables a mass reduction in the stator yoke and rotor back-iron [Gra 1996b]. In view of our present study, a high number of pole pairs is therefore attractive and synchronous machines with short pole pitches should be considered for cost and mass reduction. As discussed in [Jöc 1996][Lam 2000], synchronous machines with electrically-excited rotors are not adapted to short pole pitch configurations. Wound-rotors are heavier than PM rotors and have are bulky in short pole-pitch synchronous machines, as illustrated in figure 2-2. Figure 2-3 illustrates the pole thickness required in a PM rotor to create equivalent flux density in the air gap.

Appendix I derives expressions linking the thickness h_{Cur} of coil material to the thickness h_{PM} of PM material required to create the same flux density in the air gap.

In the derivation, the following assumptions are made:

- 1) PM have rigid magnetization (B_r constant) and relative recoil permeability equal to unity;
- 2) PM width is equal to pole pitch;
- 3) rotor shoe width is equal to pole pitch in the wound-rotor configuration;
- 4) stator and rotor steel has infinite permeability up to saturation;

- 5) PM demagnetization is not considered;
- 6) no saliency in the wound-rotor configuration.

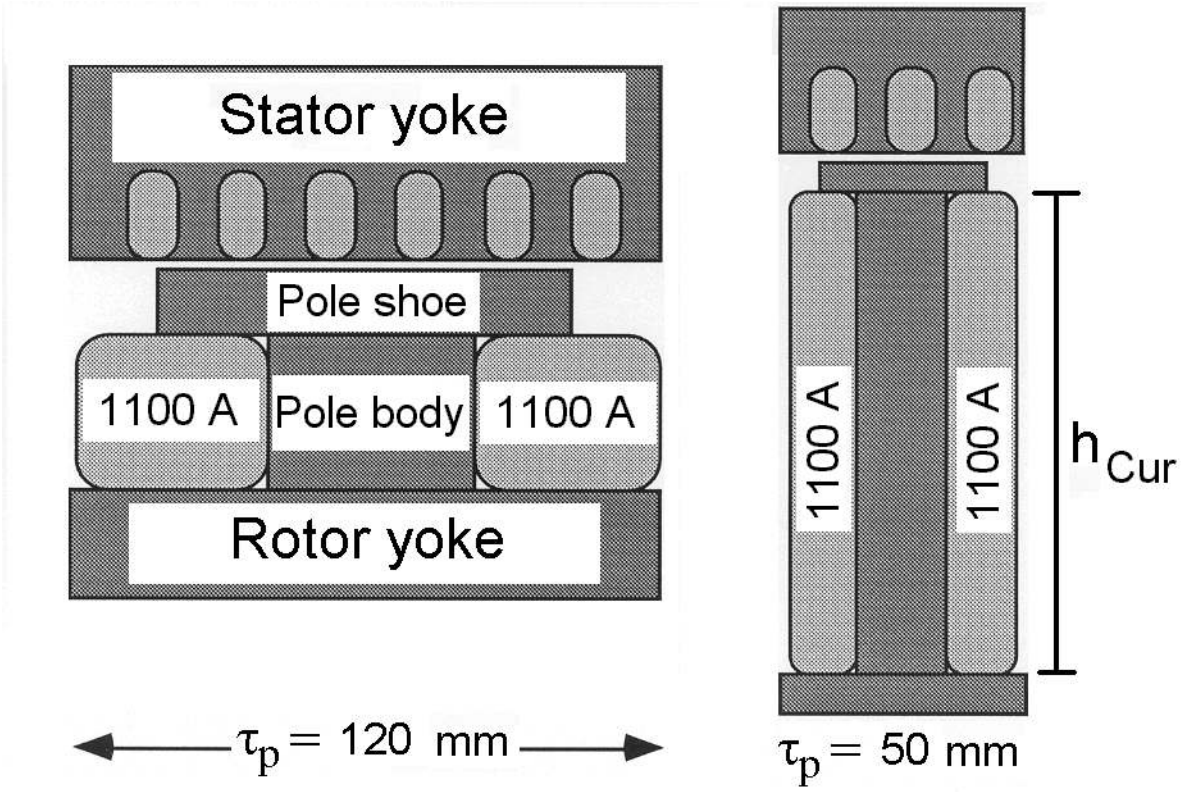

Figure 2-2: Increase of pole thickness in electrically-excited coils with short pole pitches.

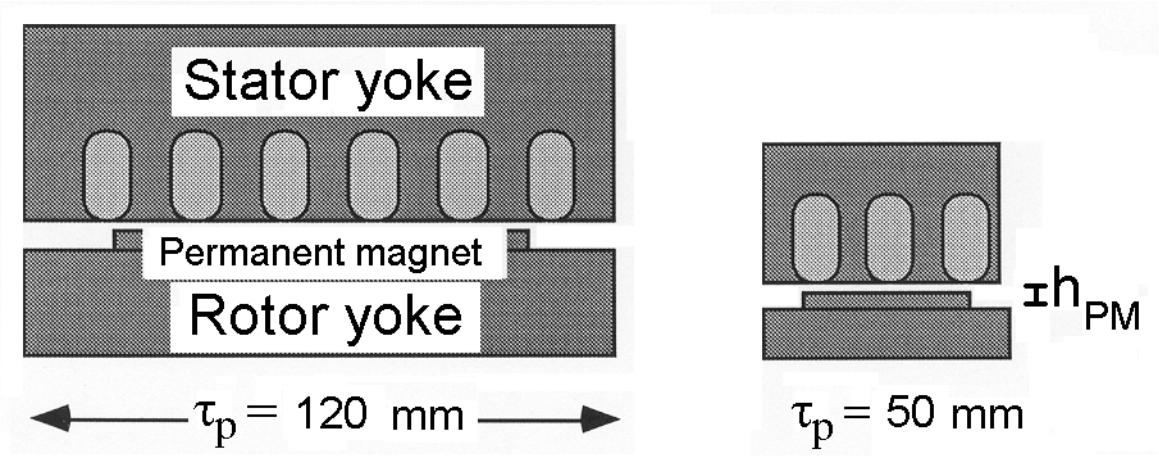

Figure 2-3: Constant thickness in PM-excited rotor poles with varying pole pitches.

$$\frac{h_{Cur}}{h_{PM}} = \frac{2B_{Fesat}(B_r - B_g)}{\mu_0 J_r k_{rfill} \tau_p (B_{Fesat} - B_g)} \qquad (2\text{-}1)$$

Equation (2-1) confirms that a decreasing pole pitch τ_p (and thus an increasing number of pole pairs) will be detrimental to the electrically-excited synchronous machine in terms of rotor thickness compared to PM excitation. If we assume the following values: iron saturation flux density $B_{Fesat} = 1.8\ T$, copper filling factor $k_{rfill} = 0.7$, remanent flux density $B_r = 1.2\ T$, a ratio of h_{Cur}/h_{PM} as illustrated in figure 2-4 is obtained. It must be noted that a low value of current density $J_r = 2\ A/mm^2$ is chosen, to provide acceptable machine efficiency.

In such conditions, the volume and mass of the rotor coils (and their cores) in wound-rotor synchronous machines will be significantly higher than the volume and mass of PM required to create a given air gap flux density at no-load. According to figure 2-4, this situation worsens as the pole pitch decreases.

Regarding costs, the specific costs of Nd-Fe-B PM material is about 5 to 15 times higher than the specific cost of copper and laminated steel. According to figure 2-4, a pole pitch of 10 cms gives a ratio of h_{Cur}/h_{PM} of about 10. If costs are considered, the PM rotor are likely to become a cheaper solution when pole pitches get shorter than 10 cms.

It is worth mentioning that equation (2-1) uses the assumption of a 180 degrees pole arc for the PM, while a shorter pole arc is normally used with PM excitation. Also, equation (2-1) assumes a constant air gap thickness in the electrically-excited rotor, while the pole shoe often has a round shape in order to obtain a more sinusoidal flux wave. These variants are not included in appendix I or equation (2-1).

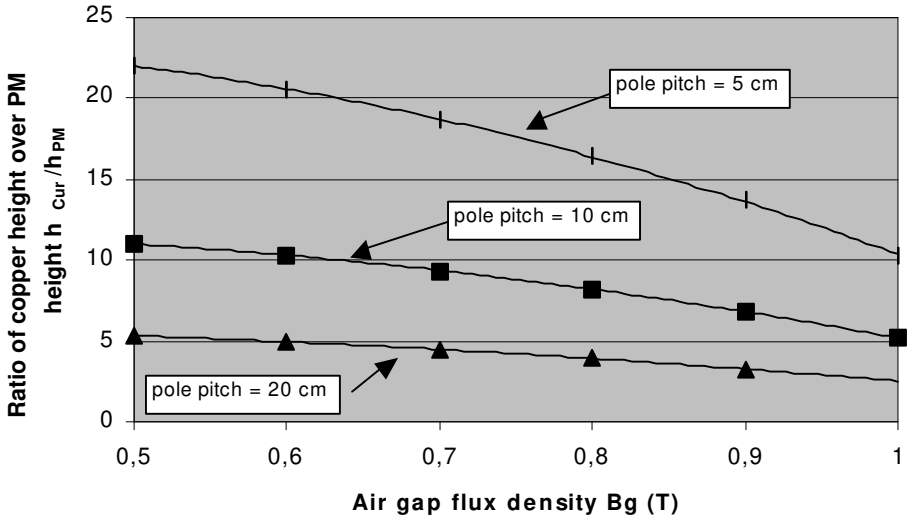

Figure 2-4: Ratio of coil thickness over PM thickness for an equivalent flux density in the air gap.

Another important disadvantage of the electrically-excited synchronous machine is the higher losses in the rotor windings. Although there will be some losses in the magnets caused by the circulation of eddy currents in the PM volume, they will usually be much lower than the copper losses of electrically-excited rotors. This increase in copper losses will also increase when increasing the number of poles.

To illustrate the limitations in pole pitch reduction for electrically-excited rotors, we refer to publications like [Bir 1991], [Pol 2001], which present optimized designs of direct-drive electrically-excited synchronous generators for wind turbines. Pole pitches between 20 and 45 cms were proposed in those cases. On the other hand, publications like [Gra 1996b], [Lam 1997], [Pol 2000] have presented optimized designs of PM synchronous generator for comparable applications and the pole pitches ranged between 6.8 and 10 cms.

In [Jöc 1996], a formal cost and mass comparison is carried out between large electrically-excited and PM-excited synchronous generators, which includes rotor and stator components. The comparison includes the cost of active material, but also the long-term cost of electrical losses. It is found that the PM synchronous machine has a total cost and a total mass lower than that of the wound-rotor synchronous machine, which as a matter of fact is explained by [Jöc 1996] by the ability of PM machines to reach lower pole pitch values.

2.3. Description of existing PM machine topologies

Chapter 1 has highlighted the need for cost and mass reduction in direct-drive machines. As mentioned in section 2.2, permanent magnets can generate magnetic flux in a compact manner, allowing machines with short pole pitches.

A very important aspect of PM rotors, which has not been discussed in the last section is the great flexibility of permanent magnets. PM may be spatially laid out with various shapes, positions, sizes and orientations, giving rise to almost endless possibilities in the number of machine topologies and variants. Giving a complete description of all the existing PM machine geometries discussed in scientific literature would require more than just a chapter of this thesis. This is why, we will limit ourselves to the description of what we believe are the prominent geometries.

To examine the various topological variants of PM machines, four main characteristics of PM machines can be given:

- air gap orientation with respect to rotational axis: radial (R) or axial (A);
- stator core orientation with respect to direction of movement: longitudinal (L) or transverse (T);
- PM orientation with respect to air gap: surface-mounted (SM) or flux-concentrating (FC);
- copper housing: slotted (S) or slotless (SL).

These characteristics are discussed below.

2.3.1. Air gap orientation: Radial (R) or axial (A)

The air gap is necessary as a means for mechanically separating the rotor from the stator. It forms a surface between the rotor and the stator. The vector normal to the air gap surface can either be radially oriented or axially oriented. In the first case, the vector is perpendicular to the axis of rotation, where in the second case, the vector is parallel to the axis of rotation. This is illustrated in figure 2-5.

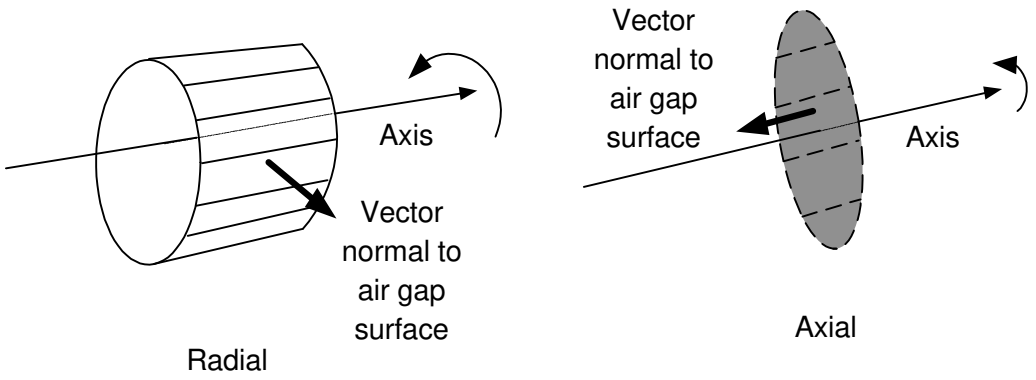

Figure 2-5: Air gap orientation: radial and axial.

2.3.2. Stator core orientation: longitudinal (L) or transverse (T)

The stator core carries flux around the stator winding in order to create an electromotive force in that winding. The flux can be transported in a direction parallel to the direction of motion or mainly perpendicular to the direction of motion. In the first case, the machine is said to be longitudinal and in the second case, the machine is said to be transverse.

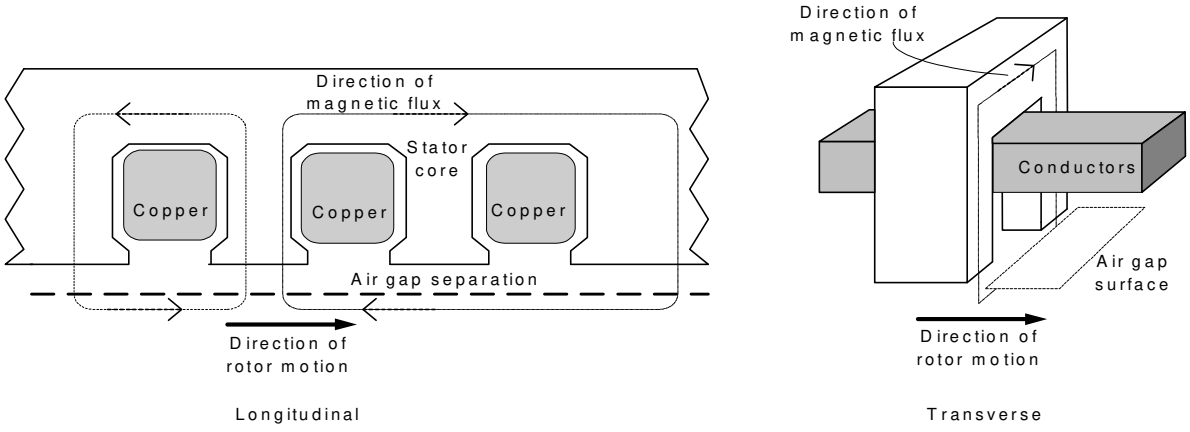

Figure 2-6: Stator core orientation: longitudinal and transverse.

Laithwaite [Lai 1971] was among the first authors to distinguish between longitudinal stators and transverse stators. Longitudinal stators see the space available for conductors decrease when the pole pitch decreases. The current loading, which is also known as the linear current density, is defined as:

$$A = \frac{N_{slot} I_s q m}{\tau_p} \tag{2-2}$$

where I_s is the stator rms current.

For a given tooth width and current density, if the pole pitch τ_p of a longitudinal machine is reduced, there will be less space available for copper and the value of $N_{slot}I_s$ will decrease. Thus, the current loading A of a longitudinal machine does not vary much with decreasing pole pitches.

In a transverse machine (q = 1 and m = 1), the space available for conductors is not dependent on the pole pitch value. If τ_p is reduced, the value of $N_{slot}I_s$ may remain the same or even increase if necessary. Thus, the current loading A of a transverse machine will increase as the pole pitch τ_p decreases.

2.3.3. PM orientation with respect to air gap: surface-mounted (SM) or flux-concentrating (FC)

The PMs are mounted onto the rotor iron. The PM magnetization has a direction, which can either be parallel or perpendicular to a vector normal to the surface of the air gap, as illustrated in figure 2-7. In the first case, the PMs are surface-mounted, while in the second case, PMs are mounted in a flux-concentrating manner.

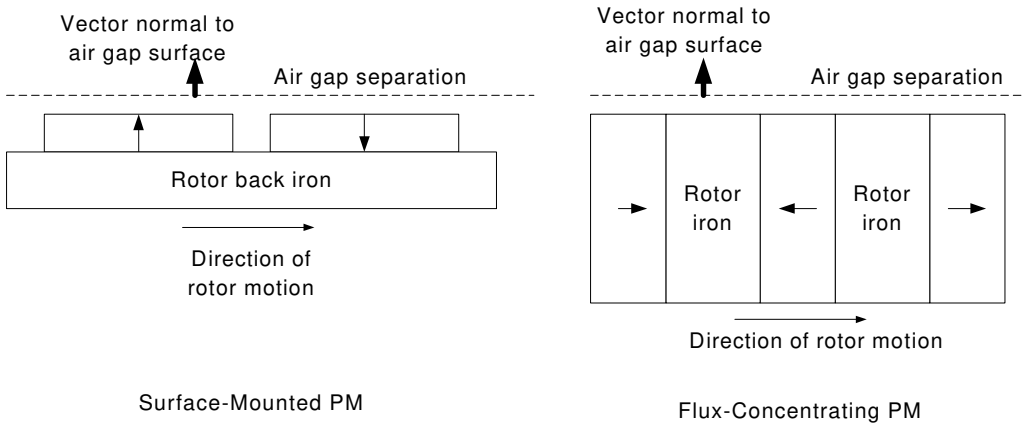

Figure 2-7: PM orientation with respect to air gap: surface-Mounted or flux-concentrating.

This classification only considers two possible layouts for the PMs on the rotor. However, [Sen 1997] has described other possible PM configurations, like the inset PM and the buried PM with radial magnetization. [Spo 1992a] has even proposed a combination of the surface-mounted and flux-concentrating arrangement. Also, [Hal 1980][Dub 2002a] describe the

advantages of using PM with variable magnetization angles. But in our case, we will limit the analysis to the two general cases shown in figure 2-7.

2.3.4. Copper housing: slotted (S) or slotless (SL)

The stator laminations can be made either with or without teeth. In the toothed stator, the teeth are used to carry the magnetic flux and to maintain the stator conductors in place. In the toothless stator, the stator conductors are placed in the air gap and the magnetic flux must then cross a much thicker space of non-magnetic medium, which will lead to thicker magnets or/and lower no-load flux density. For example, the slotless machine designs proposed in [Car 1999b] and [Fic 2001] have a peak air-gap flux density of *0.52 T* and *0.60 T*.

As will be described further, the slotless stator brings some advantages in machines with axially-oriented air gaps, because of the difficulty related to the production of slotted laminations for such machine types. However, the absence of slots lead to winding retention problems.

A second advantage of the slotless machines is the lower iron losses. In the slotted stator, most of the flux goes through the steel teeth, which behave like flux concentrators. The flux density and the specific iron losses are then higher in the teeth than in the yoke. In that respect, slotless machines can be interesting for high frequency applications, like flywheels [Ark 1992][Hol 2002]. However, in our low-speed application, the problem of no-load iron losses in the teeth is not seen as a significant drawback.

A disadvantage of the slotless machines in some cases, is the increase in copper losses due to the magnetic flux passing through the stator winding, even at no-load. This proximity effect is discussed in [Aca 1997] and leads to additional eddy current losses in the winding.

2.3.5. Main PM machine combinations

The four characteristics described above are more or less independent from one another. They can be combined, giving sixteen possibilities of PM machine concepts. Table 2-1 lists the different combinations.

The first six combinations listed in table 2-1 are regarded as interesting machine concepts, which can possibly be used as direct-drive PM machines. These machine concepts have been described in the scientific literature and we choose to investigate their performance in more details.

The remaining ten machine combinations are listed in the bottom part of table 2-1. For the reasons described in that table, we choose not to investigate these machine concepts. At this point, we are convinced that no additional benefits can be obtained from these ten combinations. The reasons will become more obvious in the course of the thesis. For the moment, we choose to concentrate only on the six machine types listed in the first part of table 2-1.

Table 2-1. Possible machine concepts from the 4 characteristics.

Name used in the thesis	Radial/ axial	Longitudinal/ transverse	Surface PM/ flux-concentrating PM	Slotted(S)/ slotless(SL)	Comments
Conventional PM synchronous machine	R	L	SM	S	Will be analyzed further in the thesis.
Conventional PM synchronous machine with flux concentration	R	L	FC	S	Will be analyzed further in the thesis.
Slotted axial-flux PM machine	A	L	SM	S	Will be analyzed further in the thesis.
TORUS	A	L	SM	SL	Will be analyzed further in the thesis.
Surface-mounted transverse-flux PM machine	R	T	SM	S	Will be analyzed further in the thesis.
Flux-concentrating transverse-flux PM machine	R	T	FC	S	Will be analyzed further in the thesis.
NOT ANALYZED IN THESIS NO NAME	R	L	SM/ FC	SL	No advantage is expected in terms of material reduction. The large air gap will lead to thicker magnets. The conventional synchronous PM machine will be preferred.
NOT ANALYZED IN THESIS NO NAME	R	T	SM/ FC	SL	Never discussed in literature. Not applicable.
NOT ANALYZED IN THESIS NO NAME	A	L	FC	S/SL	Never seen in literature. Amount of material expected is either higher or equal to the radial version.
NOT ANALYZED IN THESIS NO NAME	A	T	SM/ FC	SL	Never discussed in literature. Not applicable.
NOT ANALYZED IN THESIS NO NAME	A	T	SM/ FC	S	Never discussed in literature. Amount of material expected is either higher or equal to the radial version.

2.4. PM machines considered for further investigation

In this section, the six PM machines identified in the upper section of table 2-1 will be described in more detail.

2.4.1. Conventional PM synchronous machine

This machine is illustrated in figure 2-8. This type of machine has been described in scientific literature under different names. [Lam 2000] and [Gra 1996b] have talked about the "radial-flux PM machine with surface-mounted magnets", [Pol 1998] has discussed the "PM machine with surface-mounted magnets", [Sle 1992] has described the "PM machine", [Had 1999] has talked about the "PM synchronous machine". From the four characteristics that may be given to a machine and the resulting sixteen combinations, it appears that none of these names accurately describe the machine illustrated in figure 2-8. We choose to use the name "conventional PM synchronous machine" throughout the thesis, since this machine is more or less the most common type of PM machine.

The attribute "conventional" should be sufficient to refer to the PM geometry shown in figure 2-8, that is a machine with radial (R) air gap, longitudinal (L) stator with slots (S), and surface-mounted (SM) permanent magnets. It must be noted that our previous publications [Dub 2000][Dub 2001a][Dub 2001b][Dub 2002a] have often referred to this machine type by the name "Radial-flux PM machine", but in the scope of the thesis, we prefer using the name "conventional PM synchronous machine".

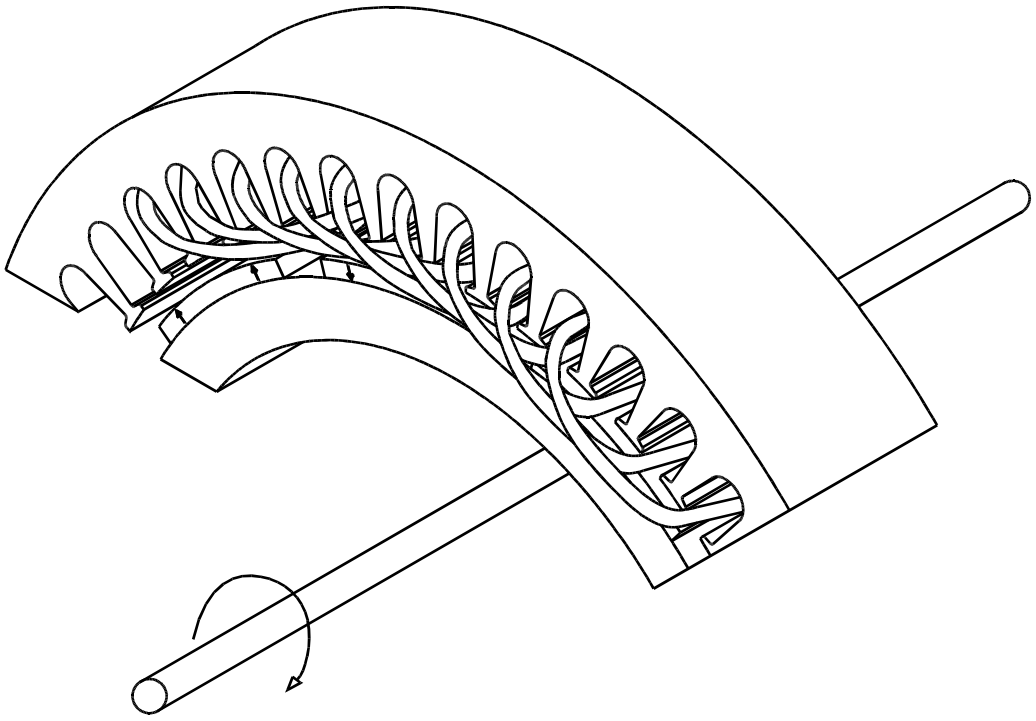

Figure 2-8: conventional PM synchronous machine.

In figure 2-8, an example shows a three-phase stator, with one slot per phase per pole. The winding is a two-layer winding, with two conductors per slot. This is the same winding arrangement discussed in [Gra 1996b].

2.4.2. Conventional PM synchronous machine with flux concentration

Figure 2-9 shows a PM machine with radial (R) air gap orientation, longitudinal (L) slotted (S) stator, and PMs in flux-concentration (FC). This machine is described by [Spo 1996][Sen 1997], who use different names for it. Because the stator is similar to the conventional PM synchronous machine, we choose the name "conventional PM synchronous machine with flux concentration". As pointed out by [Spo 1996], the conventional PM synchronous machine with flux concentration allows an air gap flux-density higher than the remanent flux-density of the PM. This leaves interesting possibilities for ferrite magnets to be used instead of the more expensive rare-earth magnets.

Another advantage of this machine geometry is the presence of saliency, which can be used to produce an additional reluctance torque and to increase the speed range in motor applications by extending its field-weakening range [Sen 1997]. However, it is arguable whether or not the concept of flux-weakening is suitable for wind-turbine generators.

Although cheap ferrite magnets may be used and although other advantages arise from the use of this machine geometry, no literature has been found which provides a comprehensive cost or mass comparison with the conventional PM synchronous machine. If ferrite magnets are used, we can expect a higher mass for a given torque due to the increase in the amount of PM material. Thus no mass saving is expected with this geometry. Regarding costs, it is not clear whether this geometry can bring an advantage. A cost comparison will be made in chapter 4.

In chapter 1, it was mentioned that easy manufacturing was an important issue. In this respect, the conventional synchronous PM machine with flux concentration is not superior to the conventional PM synchronous machine. The flux-concentrating rotor of figure 2-9 will probably increase the machine complexity.

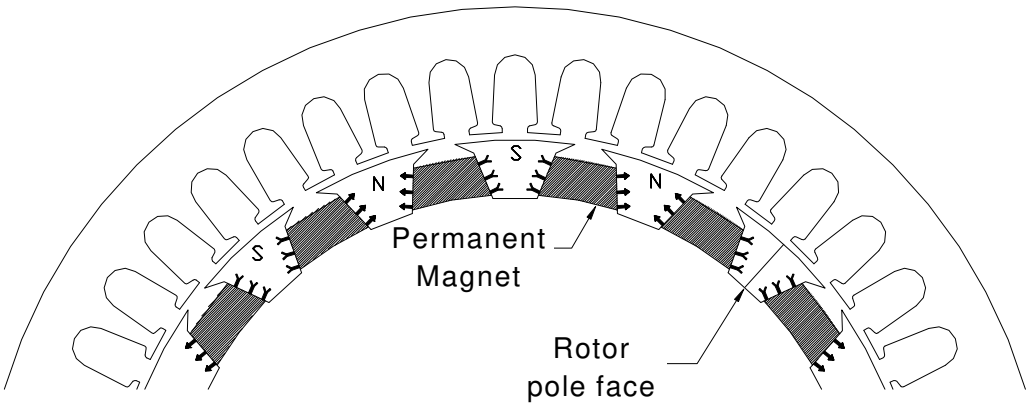

Figure 2-9: conventional synchronous PM machine with flux concentration.

In high-speed applications, this topology may allow better magnet retainment compared to the conventional PM synchronous machine. In the case of a direct-drive generator for wind turbine application, the rotational speed is low and magnet retainment is not a big concern.

2.4.3. Slotted axial-flux PM machine

The slotted axial-flux PM machine is shown in figure 2-10. The name “slotted axial-flux PM machine” is again not sufficient in itself to entirely describe the machine geometry. But it will be used in the thesis and will refer to the PM geometry with axial (A) air gap orientation, slotted stator (S) with longitudinal (L) orientation and surface-mounted (SM) permanent magnets. This machine has been described by [Let 1997][Pro 2000][Sah 2001]. The third publication describes a machine similar to the one shown in figure 2-10, where the two first publications describe a machine with a double-sided stator.

Many authors like [Zha 1996], [Sit 2000] have highlighted the compactness of slotted axial-flux PM machines. For a given outside diameter and a given torque rating, the machine can be many times shorter than a conventional PM synchronous machine [Dub 2001a]. In some applications where compactness is required, the slotted axial-flux PM machine should be considered. However, for mass and cost reduction, no literature was found which investigates the cost or weight advantage or disadvantage of the axial-flux PM machine compared to other PM machine types. This aspect will be further investigated in chapter 4.

A proper analysis of the slotted axial-flux PM machine must also highlight the difficulties in manufacturing the machine. The production of the stator core is here an important difficulty. The stator core must be laminated in a plane parallel to the direction of motion, and also parallel to the rotational axis, as shown in figure 2-10. In a slotless machine, this can be easily done by winding a steel tape on itself. However, in the slotted machine, the tooth width must be on the stator outer radius wider than on its inner radius. This issue must be carefully considered when constructing the slotted axial-flux PM machine.

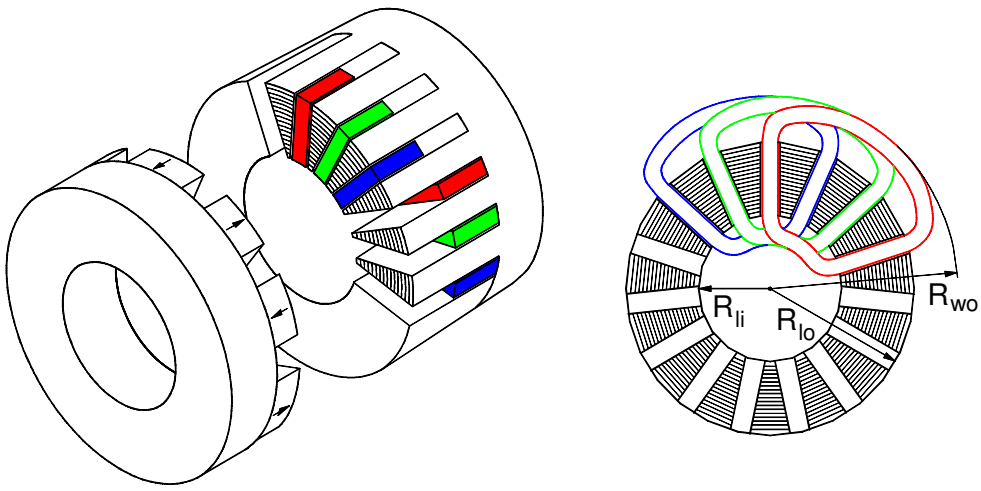

Figure 2-10: Slotted axial-flux PM machine.

2.4.4. TORUS

The TORUS machine is shown in figure 2-11. This PM machine, with axially-oriented (A) air gap, longitudinal (L) slotless (SL) stator, has two rotor discs and one toroidally-wound stator. This PM machine was discussed by [DiN 1991][Sti 1992][Söd 1997][Hua 1999].

Different names have been given to this machine geometry, but in the thesis, we will adopt the term "TORUS", which was proposed by [Spo 1992b]. In the TORUS machine, magnets are surface-mounted (SM) on the rotor discs, in a S-N-S-N-etc. arrangement. South poles face one another and so do north poles.

The stator offers a very simple construction. It is formed by an insulated steel tape, which is radially wound. However, this topology has the following drawbacks:

- large air gap width due to the absence of teeth, leading to large magnet height and high magnet costs as pointed out in [Spo 1996];
- copper density is limited because of inner torus diameter being lower than average torus diameter;
- conductors near the inner torus diameter contribute less to emf generation, due to lower tangential speed, although contributing equally to copper losses, as pointed out in [DiN 1991].

The last two points are also applicable to the slotted axial-flux PM machine. Again, very little literature provides a comprehensive comparison of costs and mass savings compared to other machine types. This will be the subject of chapter 4.

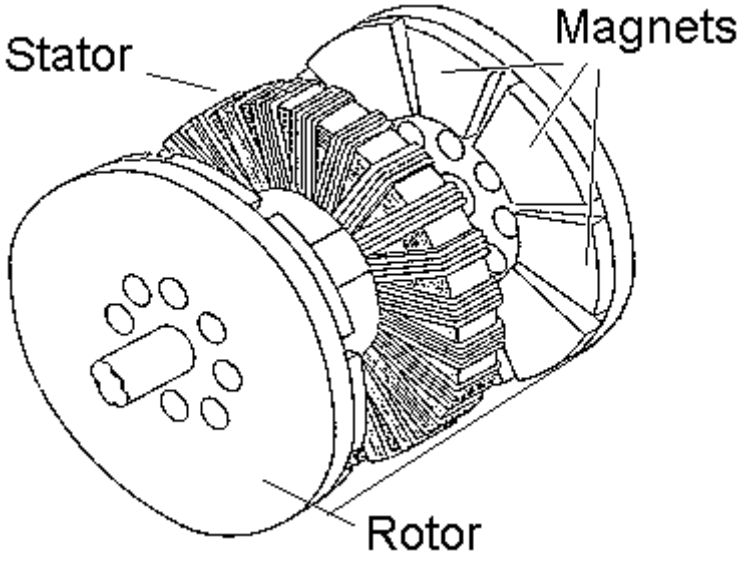

Figure 2-11: TORUS machine.

2.4.5. Surface-mounted transverse-flux PM machine

The surface-mounted transverse-flux PM machine is shown in figure 2-12. Authors like [Weh 1988b], [Har 1993] have discussed this machine geometry. Although the axial version is theoretically possible, it is assumed in the thesis that the surface-mounted transverse-flux PM machine has a radial (R) orientation of its air gap and has a slotted (S) stator with a transverse (T) orientation.

It was mentioned in section 2.3.2 that a transverse orientation of the stator core allows the winding window area to be independently chosen from the pole pitch value. This is indeed the case in the surface-mounted transverse-flux PM machine. The pole pitch can be reduced to values around 1 - 2 cm, and consequently the current loading may be increased to very high values.

From figure 2-12, it is noted that only half of the rotor poles contribute to the generation of electromotive force in the stator winding. The PM directly facing the stator cores create a useful flux around the stator coil, but the PM not facing the stator core exchange flux through air. This was not the case in any of the longitudinal machine geometries seen previously. However, if the pole pitch of the surface-mounted transverse-flux PM machine is made sufficiently small, the increase in current loading may possibly counterbalance this problem.

The presence of a short pole pitch and surface-mounted (SM) PM increases the effective air gap thickness and consequently increases fringing effect of the armature reaction. As discussed by [Har 1996], a large part of the armature flux leaks outside the pole area and a large part of the flux created by the PM does not enter the stator core, but leaks towards the neighboring magnet. This will reduce the amount of no-load flux density in the stator core and consequently reduce the available no-load voltage.

Other variants of surface-mounted transverse-flux machines have been discussed by [Weh 1986][Bor 1996].

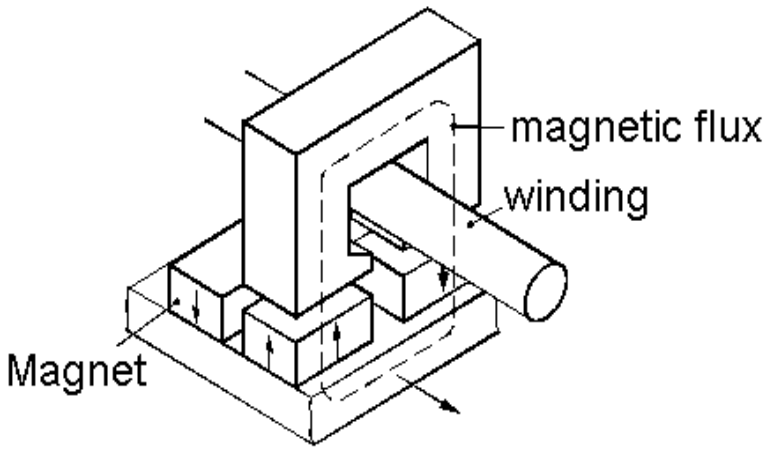

Figure 2-12: Surface-mounted transverse-flux PM machine.

2.4.6. Flux-concentrating transverse-flux PM machine

The flux-concentrating transverse-flux PM machine is illustrated in figure 2-13. As for the surface-mounted transverse-flux PM machine, the axial air gap is possible. However, in the thesis, the flux-concentrating transverse-flux PM machine will only refer to the radial (R) air gap configuration.

The flux-concentrating transverse-flux PM machine shown in figure 2-13 has been discussed by [Weh 1995], but we find a number of variants based on the same principles. The variants of this machine geometry will be described in detail in chapter 6.

The flux-concentrating transverse-flux PM machine mainly differs from the surface-mounted version by the directions of magnetization of its PMs, which are in the first case used in flux-concentration (FC). As will be detailed in chapter 5, this strongly reduces the leakage between adjacent rotor poles compared to the surface-mounted transverse-flux PM machine. The use of flux-concentrating PMs also allows additional degrees of freedom in the dimensions of the PM. The PM width can be increased without increasing the pole pitch, which was not the case with the surface-mounted machine.

2.5. Criteria for the comparison between PM machines

As described in section 2.4, PM machine characteristics can be combined in several ways to form sixteen different topologies. However, in section 2.3.5, we have selected six of these machine geometries for further investigations. Considering the goal of this thesis, which is the investigation of mass and cost reduction in PM machines, we must define criteria for the comparison of these six machine geometries.

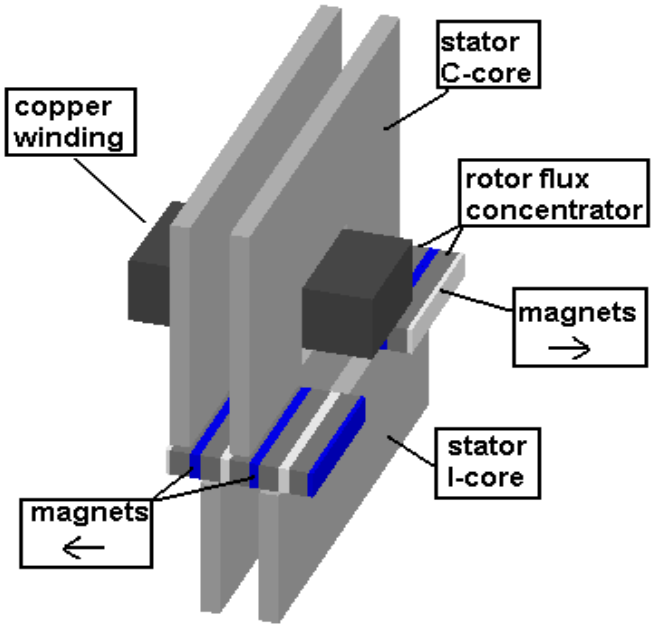

Figure 2-13: Flux-concentrating transverse-flux PM machine.

As mentioned in chapter 1, only active material is considered in this comparison. The ultimate target here is the reduction of mass and cost of active material, which is composed of:

- current-carrying conductors;
- PM material;
- magnetic flux-carrying steel;
- powdered iron (where used).

As mentioned earlier, active material is only one part of the machine construction and only one constituent of the total machine cost. In [Gra 1996b], the influence of the machine dimensions (diameter and length) on the costs of the machine mechanical structure are discussed. According to the author himself, the analysis is not thorough. However, it is stressed that the machine dimensions will have an impact on the total machine costs. Nevertheless, the choice was made in our thesis only to take into account the cost of active material. In the concluding chapter of the thesis, we will see how relevant it is to pay attention to other parts of the machine cost and mass.

Why is active material needed in an electrical machine? What is its purpose? Intuitively, we know that conductors are required to carry the electrical current and that steel and magnets are needed to carry and generate the magnetic flux required in the electromechanical conversion. As a consequence, active material is necessary for the conversion of mechanical power into electrical power. Since active material and electrical power are related, we can ask ourselves whether the ratio of electrical power over mass of active material could be an interesting basis for comparing machines together.

Let us write the electrical power of a single phase PM machine with no saliency,and where copper and iron losses are neglected. All electrical quantities are assumed as sinusoidal. We write:

$$P_{elec} = EI_{max}\cos\psi \tag{2-3}$$

where ψ is the phase angle between the no-load voltage *e(t)* and the phase current *i(t);*

I_{max} is the maximum rms stator current.

From Faraday's law, the no-load voltage is proportional to the angular rotational speed ω_m, therefore we may write equation (2-3) as:

$$P_{elec} = K\omega_m I_{max}\cos\psi \tag{2-4}$$

where *K* is a constant relating the machine torque to the machine current.

From equation (2-4), it appears that the use of P_{elec}/m_{act} as a criterion is uninteresting, because this ratio will vary with the machine rotational speed. By dividing equation (2-4) by ω_m, the resulting quantity will depend on the machine geometry and phase angle ψ.

$$\frac{P_{elec}}{\omega_m} = KI_{max}\cos\psi \tag{2-5}$$

If losses are neglected, the electrical power P_{elec} is equal to the mechanical power P_{mech}. The left-hand term of equation (2-5) is the nominal average torque.

Based on our statement that active material only is considered in this work, torque over mass of active material ($\overline{T}/m_{act}$) is chosen as the first criterion, which will be used throughout the thesis for determining the most interesting PM machine topologies for mass reduction.

Reducing the mass of active material may lead to cost reduction. However, it may not always be the case. For example, a given machine with large amounts of PM material can be lighter but more expensive than a machine with thin magnets but bulky stator. The high specific cost of PM material compared to the low cost of copper and steel makes the use of $\overline{T}/m_{act}$ insufficient to judge the cost performance of a PM machine.

This is circumvented by weighing each material type with a specific cost:

- specific cost of copper c_{Cu} = 6 Euros/kg;
- specific cost of laminated steel c_{Fe} = 6 Euros/kg;
- specific cost of powdered iron c_{Fe} = 6 Euros/kg;
- specific cost of Nd-Fe-B magnets c_{pm} = 40 Euros/kg;
- specific cost of ferrite magnets c_{pm} = 6 Euros/kg.

In the specific costs detailed above, the cost of laminated steel includes the inherent material loss obtained in the stamping process. In the same way, the specific cost of powdered iron includes the cost of pressing. The specific costs of steel, copper and magnets can not be given accurate numbers, since they depend to a large extent on the market. Orders of magnitude will have more values in such a cost analysis, and in this sense, it is relevant to give steel laminations, copper, powdered iron and ferrite magnets the same specific cost of 6 Euros/kg.

The criterion used for cost comparison is the ratio of cost of active material C_{act} over nominal average torque $\overline{T}$.

$$\frac{C_{act}}{\overline{T}} = \frac{[c_{Cu}m_{Cu} + c_{Fe}m_{Fe} + c_{pm}m_{pm}]}{\overline{T}} \tag{2-6}$$

where

m_{Cu} is the mass of copper;

m_{Fe} is the mass of laminated steel and powdered iron;

m_{pm} is the mass of permanent magnets.

The PM machine design that will obtain the best performance will have a high torque/mass and a low cost/torque.

2.6. Summary

In this chapter, the advantages of PM excitation over wound-rotor excitation have been emphasized. PM excitation gives cheaper rotors for pole pitches shorter than about 10 cms and lighter rotors for pole pitches shorter than about 20 cms. Also, PM rotors will give machine losses lower than those of a synchronous machine with wound rotor.

The great geometrical flexibility of PM allows many topological variants of the PM synchronous machine. Four main characteristics were highlighted, which can be combined into sixteen PM machine geometries. Among these sixteen geometries, six have been kept for further analysis:

- conventional PM synchronous machine;
- conventional PM synchronous machine with flux concentration;
- slotted axial-flux PM machine;
- TORUS;
- surface-mounted transverse-flux PM machine;
- flux-concentrating transverse-flux PM machine.

These six PM machine geometries have been described in this chapter and two criteria were proposed for the purpose of comparing them together: torque over mass and cost over torque.

Chapter 3

Torque calculation in machines

3.1. Introduction

Several PM machine geometries have been presented in chapter 2. The six PM machine topologies retained in section 2.4 will be evaluated on the basis of their torque/mass and cost/torque performance. To evaluate the cost/torque and torque/mass ratios, it becomes necessary predicting the cost, mass and torque of those machine types. The computation of mass and cost of active material is straightforward: once the geometrical parameters are known, the volume, masses and costs can easily be deduced.

Torque computation is a more difficult task. This chapter discussed the methods of torque computation, like the virtual work method and the average power balance method. Other methods, like the Maxwell's stress method, the equivalent charge method and the equivalent current method will also be addressed. Since only the virtual work and the average power balance methods will be used in the thesis, they will be described in more detail.

3.2. Relationship between torque and force

The average power balance method is presented as a macroscopic approach. It is macroscopic in the sense that macroscopic machine quantities, like power, voltage and current are used. From these macroscopic quantities, the average torque value can be directly obtained as will be seen in section 3.3.

Instead of average torque, instantaneous magnetic forces can be calculated by using other methods of torque calculation. In an electrical machine with a radial air gap, the forces are spread around the circumference. The true force distribution in the air gap cannot be calculated with confidence, since the different methods of force calculation (virtual work, Maxwell's stress, equivalent charges, equivalent currents) will give different force distributions, as pointed out in [Car 1959], [Sad 1992], [deM 1999]. However, all methods of force calculation studied in those references give the same total force.

Although the exact force distribution may be difficult to predict, it is reasonable to expect all pole pairs of a symmetrical machine to give a same total force per pole pair F_p as illustrated in figure 3-1.

Since the force vector $\vec{F}_p$ can be separated into a component of tangential force per pole pair F_{pt} and a component of attractive force per pole pair F_{pa}, we can write the total tangential force F_t as:

$$F_t(t) = pF_{pt}(t) \tag{3-1}$$

and the torque expression can be written as:

$$T(t) = r_g pF_{pt}(t) \tag{3-2}$$

Our approach will be to use the virtual work method for the calculation of instantaneous magnetic forces in combination with finite element analysis. In a multi-pole machine, the problem of calculating magnetic forces on the total machine is usually reduced to the calculation of forces on only one pole pair instead of the complete machine. Then the total machine torque is calculated with the use of equation (3-2). This allows much lower computing time, especially if 3-D finite element computation is required. Although we easily reduce the computation domain from the total machine to a single pole pair, the necessity of calculating the instantaneous magnetic forces still exists and this can be done with the virtual work method as it will be described further in this chapter.

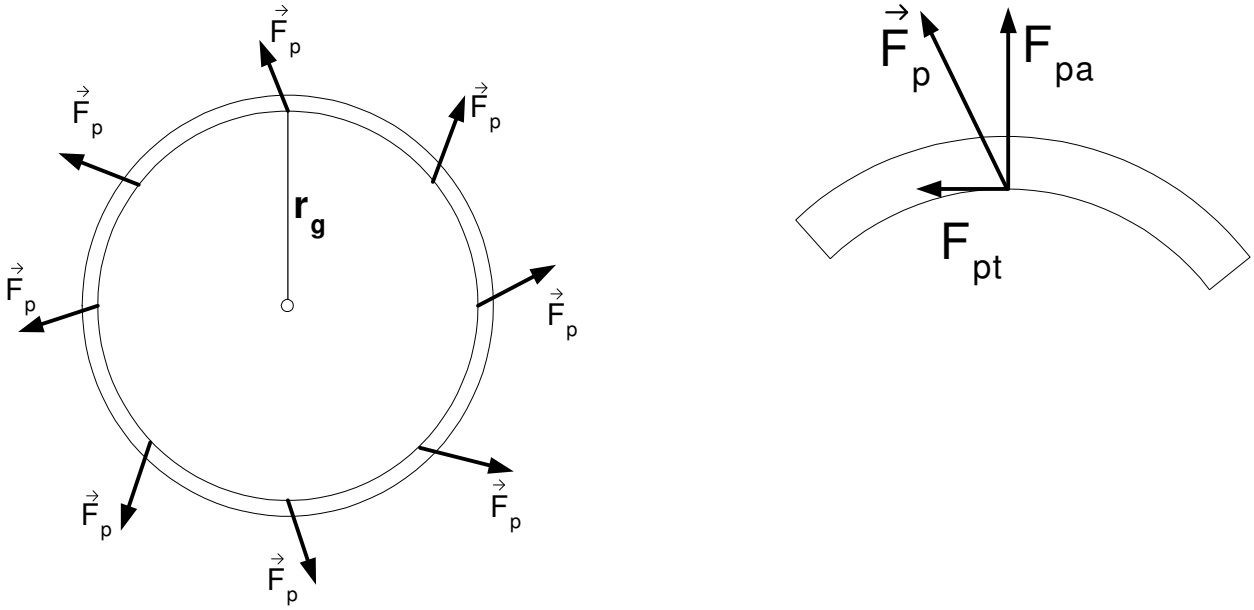

Figure 3-1: Force vectors in a multi-pole radial machine

3.3. The average power balance method

Let us assume a rotating machine with a very large diameter, such that both rotor and stator can be considered as linear. In that case, we assume that motion takes place in the x direction at a constant speed. The complete machine is enclosed within a volume V and mechanical work is performed inside V. Energy conservation allows us to write:

$$p_{elec} + \frac{dW_m}{dt} + p_{Fe} + p_{Cu} = -F_x \frac{dx}{dt} \tag{3-3}$$

where p_{elec} is the instantaneous electrical power extracted from the volume V, p_{Fe} is the instantaneous loss in iron inside volume V and p_{Cu} is the instantaneous conduction loss in copper inside volume V. It should be noted that a negative sign is given to the term on the right-hand side of equation because the force F_x opposes the direction of motion and the flow of the electrical power p_{elec} is from the inside towards the outside of the volume V.

Equation (3-3) includes the rate of change of W_m , that is stored magnetic energy. This is consistent with [Fan 1960], where the Poynting theorem is derived. The Poynting equation demonstrates that W_m must be included in the power balance and W_m is expressed as :

$$W_m + W_{mloss} = \int_V \left(\int_0^B (\vec{H} \cdot d\vec{B}) \right) dV \tag{3-4}$$

where W_{mloss} is the magnetic loss in iron (hysteresis losses and other possible magnetic losses). The problem of calculating the stored magnetic energy can be avoided, if the average force $\overline{F}_x$ is calculated instead of the instantaneous force. In that case, the following statements apply:

- 1) the magnetic energy W_m stored in the machine has the same value for any two rotor positions distant from one another by one pole pair;
- 2) the rotational speed stays constant and therefore the stored mechanical energy does not change.

In particular, the first assumption allows us to eliminate the stored energy from the problem, since the contribution of W_m to the average force is zero. We rewrite equation (3-3):

$$P_{elec} + P_{Cu} + P_{Fe} = P_{mech} = -\overline{F}_x \frac{dx}{dt} \tag{3-5}$$

In equation (3-5), all terms are average values of electrical power, copper losses, iron losses and mechanical losses. Using average values, we have eliminated the effect of the stored magnetic energy which is a significant advantage in order to simplify the calculations. We rewrite equation (3-5) in terms of the average torque $\overline{T}$ instead of forces:

$$\bar{T} = \frac{P_{elec} + P_{Cu} + P_{Fe}}{\omega_m} \tag{3-6}$$

or, if the average electrical power P_{elec} is expressed in terms of the terminal voltage and current:

$$\bar{T} = \frac{f \int_0^{1/f} vidt + P_{Cu} + P_{Fe}}{\omega_m} \tag{3-7}$$

With the help of equation (3-7), the average torque can be analytically calculated, if the amplitudes and waveforms of the terminal voltage and current are known. This method is easy to use and allows using macroscopic quantities. In this thesis, the torque calculations will be performed with the average power balance method, by using the assumption of sinusoidal no-load voltages and currents. The average power balance method has the advantage of simplicity. However, it fails to perform calculations of the cogging torque and ripple torque which are often relevant.

It must be noted that equation (3-7) now has a positive sign because we apply the generator convention, i.e. the torque opposing the direction of motion is assumed to be positive.

3.4. Virtual work method

Evaluating the maximum value of the average torque is possible by using the average power balance method. The method can easily be implemented in a design code written in C or Matlab7 language [Mat 1994] if the current and voltage amplitudes and waveforms are known. This method will be used extensively in chapter 4 for machines with longitudinal stators. In the case of transverse-flux machines, the average power balance method can also be used (and in fact it will be used in the thesis). However, in transverse-flux machines, the main limitation to the current maximum amplitude is often determined by the saturation of the stator core. In that case, the complete magnetic circuit of one pole pair of the machine must be known in order to determine the saturation point and the maximum current amplitude. In a transverse-flux machine, the pole pitches are often very short (1 - 2 cm) and the magnetic circuit becomes complex due to the presence of important leakage paths of the magnetic fields. In the thesis, the problem will be addressed by modeling the leakage paths with reluctances. This technique will enable us to estimate the maximum current amplitude and use the average power balance method.

More accurate force and torque values can be obtained with numerical techniques such as finite element methods (FEM). Contrary to the reluctances used with the average

power balance method, the FEM treats the magnetic problem in its entirety. With the reluctances, the magnetic circuit is segmented into a limited number of localized (lumped) reluctances which are rather independent from one another. If two neighbor reluctances become so close in a given space, that the fields that they model start sharing a same volume, the reluctance approach loses accuracy. In this sense, the accuracy of FEM is better because the number of elements in the problem can be much higher than with reluctances. The magnetic fields can be calculated at every point in space, for any shape of permanent magnets, ferromagnetic structure, etc. FEM computation can be made with a typical FEM simulator such as the Maxwell 3-D7 magnetostatic package of Ansoft7 [Max 2002]. Other FEM software exist which provide the same features. But in our study, this is the software package that is used for FEM computations. The value of the magnetic vector potential $\vec{A}$ can be calculated at every point in a definite region. From this result, the magnetic flux density $\vec{B}$ is computed at every point in the same region of space by using the definition of the magnetic vector potential:

$$\vec{B} = \nabla \times \vec{A} \tag{3-8}$$

The mathematical background for the calculation of $\vec{A}$ is not included in this thesis. Nevertheless, this subject is treated in other text books like [Hau 1989][Bin 1992].

In addition to the field calculation, Maxwell 3-D7 allows the calculation of magnetic forces, using the virtual work method. The virtual work method calculates the instantaneous magnetic forces F_x by computing the variation in magnetic coenergy W'_{mag} upon an infinitesimal displacement of the moving parts. [Maw 1957] shows that F_x can be written as:

$$F_x = \frac{\partial W'_{mag}}{\partial x} \tag{3-9}$$

where the partial derivative requires that the current density $\vec{j}$ remains constant at all points in space during the displacement. [Dur 1953] also shows that the coenergy function W'_{mag} can be defined by:

$$W'_{mag} = \int_V \left(\int_0^H \vec{B} \cdot d\vec{H} \right) dV \tag{3-10}$$

It must be noted that W'_{mag} includes both the coenergy W'_m stored in the volume V and the dissipation due to magnetic effects like hysteresis (see appendix II). The magnetic coenergy, expressed as a function of $\vec{B}$ and $\vec{H}$ is also used in [Str 1998] and [Med 1998]. With this definition, the magnetic forces are calculated by computing $\vec{B}$ and $\vec{H}$ everywhere in the volume V and by performing the double integral of equation (3-10). Maxwell 3-D7 performs the computation of the magnetic coenergy in one given position of the moving parts and again after the moving parts have been displaced by a very small amount dx.

The virtual work method allows calculating the instantaneous forces. Calculating the average forces (and consequently the average torque) is also possible if instantaneous forces are calculated for all positions over one pole pitch. The information of instantaneous forces provided by the virtual work method gives additional information like cogging torque and ripple torque, which does not appear in the average torque.

3.5. Other methods: Maxwell's stress, equivalent charges, equivalent currents

Other methods of force computation have been presented in literature. We may replace the permanent magnets by equivalent current and calculate the Lorentz force or we may replace the permanent magnets by equivalent virtual magnetic charges and then calculate the magnetic forces by using the equivalent of Coulomb's equation applied to virtual magnetic charges. The method of Maxwell's stress may also be used. These three alternate methods of force calculation are briefly described below.

3.5.1. Derivation of Maxwell's stress tensor

The definition of Maxwell's stress is directly derived from Maxwell's equations (see [Str 1941]). If we take a current distribution $\vec{j}$ in a medium with permeability μ_o, we can express Ampère's law in the following form:

$$\nabla \times \frac{\vec{B}}{\mu_0} = \vec{j} \tag{3-11}$$

We vectorially multiply equation (3-11) by $\vec{B}$. We obtain:

$$\frac{1}{\mu_o}(\nabla \times \vec{B}) \times \vec{B} = \vec{j} \times \vec{B} \tag{3-12}$$

In equation (3-12), the right hand term of the equality is the force per unit volume. Equation (3-11) and equation (3-12) are only presented here in order to emphasize the requirement of calculating the forces through a medium with permeability μ_o. For the rest of the derivation, it can be shown (see [Str 1941]) that a given closed surface with its contour located in a medium with constant permeability μ_o will see a tensile stress vector $\vec{t}$, where:

$$\vec{t} = \frac{1}{\mu_o}(\vec{B} \cdot \vec{n})\vec{B} - \frac{1}{2\mu_o}\left\|\vec{B}\right\|^2 \vec{n} \tag{3-13}$$

where $\vec{n}$ is a unit vector perpendicular to the surface chosen for the calculation of Maxwell's stress in the air gap.From equation (3-13), one may obtain the magnitude of the vector $\vec{t}$, which for any orientation of $\vec{t}$ gives the same result:

$$|\vec{t}| = \frac{1}{2\mu_o} B^2 \tag{3-14}$$

The total magnetic force can be obtained by integrating equation (3-13) over the complete closed surface.

3.5.2. Method of equivalent current

In most PM machines, force is created by the interaction between the magnetic field of the PMs and the magnetic field of the armature reaction created by the stator. The method of equivalent current suggests that PMs can be replaced by coils, which create fields similar to those created by the PMs outside their volume. With such virtual coils, the well-known Lorentz force may be used to calculate magnetic forces. In its more general form, the virtual "coils" can be extended to a current distribution, where the permanent magnets are replaced by an equivalent current distribution. The equivalent distribution consists of a volume current distribution $\vec{J}'$ and a surface current distribution $\vec{K}'$, the mathematical derivation is given in [Str 1941], [Dur 1953].

$$\vec{J}' = \nabla \times \vec{M} \tag{3-15}$$

$$\vec{K}' = -\vec{n} \times \vec{M} \tag{3-16}$$

where $\vec{M}$ is defined as the magnetization vector of the permanent magnet. $\vec{M}$ is related to $\vec{B}$ and $\vec{H}$ everywhere in space by:

$$\vec{B} = \mu_0(\vec{H} + \vec{M}) \tag{3-17}$$

If equation (3-17) is considered inside the permanent magnet volume and if the permanent magnet has rigid magnetization, i.e. $\vec{M}$ = constant, the volume current distribution $\vec{J}'$ will be equal to 0 at all points inside the permanent magnet. In that case, only the surface current distribution $\vec{K}'$ remains on the border of the magnet. The total force experienced by this surface current is obtained from:

$$\vec{F}_s = \iint_S \vec{K}' \times \vec{B} ds \tag{3-18}$$

where $\vec{B}$ is the total flux density field created by the sum of the stator current and the current distribution applied on the surface element *ds*.

3.5.3. Method of equivalent magnetic charges

It is also possible to replace the permanent magnets by a set of magnetic charges distributed inside the magnet volume and on their surface. It must be noted that the concept of magnetic charges is only a mathematical tool which allows modeling permanent magnets and their fields outside their volume. Such magnetic charges do not exist in reality and the fields inside the permanent magnets may not be derived with the use of magnetic charges, because Maxwell's laws are then violated. So, if we accept the fact that force is created in a machine due to the interaction of the fields, we may set a virtual magnetic charge distribution which replaces the PM so that it creates outside the magnet a field equivalent to the one created by the magnet. Then we may calculate the force on each charge by using the equivalent of Coulomb's law applied to magnetic charges. This method is inspired by electrostatic, where electrical charges create electric fields and are subjected to forces.

This method is described briefly in [deM 1999] and in detail in [Dur 1955]. The method is also largely used in [Dur 1968][Mar 1979]. As discussed in [Blo 1919][Car 1954], we are in magnetism (with permanent magnets) in the same situation as if only polarized dielectrics would exist in electricity and where isolated electric charges would not exist. In the latter case, the electrostatic force obtained on an isolated charge could not be described, and only rotation of dipoles in an electric field could be described. Due to this similarity between a magnet and an electric dipole, it is mathematically possible to replace the permanent magnet by a set of magnetic charges. Each of those equivalent magnetic charges are subjected to a force $\vec{F}_{mc}$ [Blo 1919][Car 1954][Dur 1968]:

$$\vec{F}_{mc} = q^* \vec{H} \tag{3-19}$$

where $\vec{H}$ is the total magnetic field, which sums the externally applied magnetic field and the field created by the magnetic charge distribution. The distribution of magnetic charges is given [Dur 1968][Mar 1979][deM 1999] by:

$$\rho^* = -\mu_o(\nabla \cdot \vec{M}) \tag{3-20}$$

$$\sigma^* = \mu_o(\vec{n} \cdot \vec{M}) \tag{3-21}$$

where ρ^* is the volume distribution of magnetic charges and σ^* is the surface distribution of magnetic charges. Equation (3-21) is only applicable to the magnet surface, while equation (3-20) does not apply to the surface, but only to the volume bounded by the surface. In the case of rigid magnetization in a given volume, $\rho^* = 0$ everywhere inside the magnet and only σ^* has a value. The vector $\vec{n}$ is a unity vector, which is normal to the surface of the magnet.

Based on equation (3-19), the force on this surface distribution of magnetic charges is expressed as [deM 1999]:

$$\vec{F}_{mc} = \iint_S \sigma^* \vec{H} ds \qquad (3\text{-}22)$$

where $\vec{H}$ is the total magnetic field, which includes the contribution from the magnetic charge distribution.

3.6. Selection of a method for torque calculations: conclusions

Four methods of instantaneous force calculation have been presented and one method of average torque calculation has been presented.

The method of average power balance is a powerful tool for design optimization, because the torque calculation does not need being calculated for every electrical angle of the rotor. Only one calculation is required to obtain the average torque. However, this method is not accurate in many cases. It assumes linear material properties and a certain waveform for the voltage and currents and the average torque calculation is performed by using this assumption for the waveforms. Also, the average power balance method does not allow the calculation of cogging torque and ripple torque.

In the scope of this thesis, the focus is set to the average torque of the different machine geometries. In this respect, the average power balance method will be used for its reduced computing time. We will use it to determine the machine geometry for the lowest cost/torque and highest torque/mass. Although approximate, the average power balance method allows the detection of an "area of optimum designs" within an acceptable computation time. This is especially true in the case of transverse-flux PM machines, where analytical field calculations cannot be used due to the very complex 3-D structure and where finite element calculations must be used in the three dimensions. In such a case, the detection of an optimal geometry with the means of instantaneous force calculation in finite element softwares is a very lengthy task. Finite element methods will be used in this thesis for the calculation of instantaneous forces, but only for the validation of the results obtained with the average power balance method.

From the four methods of instantaneous force computation presented in this chapter, it has been said that all of them will give equal values of the total magnetic force [Car 1959], [Sad 1992], [deM 1999]. Only the contribution of each volume element (or surface element in the case of Maxwell's stress) to the total force will vary, depending on the method used. In this respect, the use of the virtual work method will give valid results and will be used as part of the Maxwell 3-D7 FEM software package.

Chapter 4

Comparison of PM machines

4.1. Introduction

Six PM machine topologies were selected in chapter 2 for further analysis:

- conventional PM synchronous machine;
- conventional PM synchronous machine with flux concentration;
- slotted axial-flux PM machine;
- TORUS;
- surface-mounted transverse-flux PM machine;
- flux-concentrating transverse-flux PM machine.

In this chapter, the conventional PM synchronous machine will be used as a reference for comparison. The other five topologies will be compared with it on the basis of the two criteria which were previously selected:

- torque/mass;
- cost/torque.

The abundance of machine designs presented in literature will be sufficient to establish certain trends regarding the TORUS, the transverse-flux PM machines and the conventional PM synchronous machine with flux concentration with ferrite magnets.

Concerning the slotted axial-flux PM machine and the conventional PM synchronous machine with flux concentration using rare-earth magnets, insufficient literature was found to determine whether these concepts are advantageous compared to the conventional PM synchronous machine. Therefore, models of the latter three machine topologies will be

derived in the second part of this chapter and a formal comparison will be made based on these analytical models.

The information presented in this chapter will be used to determine which of the six PM machine geometries are the most promising for the minimization of active material in direct-drive generators for wind turbines.

4.2. Trends in the performance of PM machines: a literature survey

In this section, a general discussion on the torque/mass and cost/torque of the TORUS machine (and slotless machines in general), the transverse-flux machines and the conventional PM synchronous machines with ferrite magnets (flux concentration) enables us to eliminate a few of the machine concepts for the coming investigation. Based on the concepts of force density, current loading and flux density, it is possible to rank the expected performances of those topologies.

Following that discussion on force density, the result of a literature survey is presented, showing a clear trend which confirms these observations.

4.2.1. Discussion on expected masses and force densities

The force density of an electrical machine is the total average tangential force $\overline{F}_t$ divided by the air-gap area S_g. The force density is often used as an indication for the performance of a topology because it is rather independent from the machine dimensions. It is also related to the ratio of torque over air gap volume as shown here:

$$\frac{\overline{F}_t}{S_g} = \frac{\overline{F}_t}{2\pi r_g l_s} = \frac{\overline{F}_t r_g}{2\pi r_g l_s r_g} = \frac{\overline{T}_t}{2V_g} \tag{4-1}$$

In most cases, a machine with high force density will also have a high value of torque density (torque divided by machine volume). Since volume and mass are related, a high force density is expected to give good performance in terms of torque/mass and cost/torque.The force density can be related to the machine electrical parameters as follow [Mil 1989]:

$$\frac{\overline{F}_t}{S_g} = k_{exc} k_{topo} A B_g \tag{4-2}$$

where the current loading A was already defined in equation (2-2).

In equation (4-2), the factor k_{exc} depends on the waveforms of A and B_g (and consequently on the current and emf waveforms), but also on the phase angle between the emf and current fundamental frequency component. Here we assume all machine types to have similar current and voltage waveforms, with equal phase angles. Thus equal values of k_{exc} are assumed for all machine types. The parameterk_{topo} depends on the machine topology used.

For most transverse-flux PM machines, k_{topo} is lower than 1 because not all permanent magnets create a useful flux in the airgap. However, for the four longitudinal machine topologies described above, $k_{topo} = 1$.

The following comments can be made concerning the expected force density of the transverse-flux machines, the TORUS and the conventional PM synchronous machine with flux concentration using ferrite magnets.

Current loadings of transverse and longitudinal slotted stators

The current loading A of a stator with transverse orientation can be up to 10 times higher than for a longitudinal slotted stator [Weh 1986]. This is due to the large space available for copper in the slots of a transverse stator. On the contrary, in a longitudinal stator the slot area is substantially reduced as the pole pitch decreases. Although the current loading A can be made 10 times higher, k_{topo} of the transverse-flux PM machines is about half of that of a longitudinal machine. Consequently, it is expected that the force density of a transverse-flux PM machine will be up to about 5 times higher. In [Weh 1986], the force density of a transverse-flux machine is reported as being 4 - 5 times higher than for a longitudinal machine.

Based on higher force density, it is expected that transverse-flux PM machines may bring substantial mass and cost saving in the amount of active material needed.

Although high current loading is beneficial to the machine cost and mass, it is worth mentioning that, for a given pole pitch, increasing the machine current loading will also lead to a large armature reaction. In a direct-drive wind turbines, a large armature reaction will lead to a higher rating of the electronic rectifier connected to the generator, which in turn will increase the overall system costs. Whence, a complete system optimization should take the costs of power electronics into account. However, this is left out in the thesis, due to the much higher machine costs. This aspect will be discussed in more detail in chapter 6.

Mass of magnet material in a slotless machine

In appendix I, the thickness h_{PM} of PM in a surface-mounted PM machine is given by:

$$h_{PM} = g\frac{B_g}{B_r - B_g} \tag{4-3}$$

assuming that all magnetic fluxes travel in straight line. In a slotless machine, the no-load flux density B_g will often be lower than for a slotted machine. The airgap g of a slotless machine is substantially thicker, which will lead to thicker magnets (higher values of h_{PM}). Consequently, we can expect the mass and cost of a slotless machine to be slightly higher than that of a slotted machine due to the increase in the mass of PM and considering the high specific cost of rare earth PM material.

Since this thesis is concerned with the reduction of mass and cost of active material, the TORUS machine and other slotless machines are not favorable options. The amount of PM material necessary will make it a more costly option.

Ferrite magnets used in flux-concentration

A flux-concentrating rotor structure can "magnify" the magnets remanent flux-density. A high flux density B_g can be obtained even with low values of remanent flux densities B_r. Also, the specific cost of ferrite magnets is about 10 times lower than for rare-earth magnets. Thus, the use of ferrite magnets has been identified by a few authors (like in [Spo 1996]) as an interesting possibility for the conventional PM synchronous machine with flux concentration.

In [Sen 1997], it is shown that the best utilization of PM material in a flux-concentrating geometry will be obtained if the PM are used at their maximum value of $B_{PM}H_{PM}$, or energy product. It is also shown that the volume of PM material will be inversely proportional to the energy product.

In surface-mounted magnet configurations, the PM will not necessarily be operated at the energy product. The flux density in the magnet will generally be determined from the machine optimization process. However, in a flux-concentrating rotor, the flux density in the PM and the flux density in the air gap can be different. In such conditions, it may be relevant to operate the PM at its energy product.

The energy product of a ferrite magnet is about 12 times less than that of a Nd-Fe-B magnet [Dex 2002]. Consequently, the volume of ferrite magnets will be about 12 times higher than the mass of Nd-Fe-B magnets if both PM are assumed as operating at their energy products. Thus, we can expect the mass of the conventional PM synchronous machine with flux concentration to be higher if ferrite magnets are used instead of Nd-Fe-B magnets. Also, we can expect the cost of the two machine configurations to be more or less the same.

Based on this reasoning, there is no advantage expected from the use of ferrite magnets for mass and cost reduction.

4.2.2. Literature survey of the prototypes built and optimized designs

The discussion on the expected mass and cost for a given force density suggests that the TORUS and the conventional PM synchronous machine with flux concentration using ferrite magnets are not suitable for cost reduction in direct-drive generators. Also, the discussion suggested that the transverse-flux PM machines may bring substantial cost and mass savings compared to the conventional PM synchronous machine. In fact, machine designs taken from a literature survey will also confirm these trends, as discussed below.

Designs of the conventional PM synchronous machine have been proposed in [Spo 1992a][Lam 1996][Zha 1996][Gra 1996b][Gra 1997][Lan 2000a][Mit 2002].

Designs of TORUS have been presented in [DiN 1991][Hon 1991][Spo 1992a][Spo 1992b][Sti 1992][Car 1994][Car 1997][Cha 1997][LoB 1997][Söd 1997][Car 1999a][Car 1999b][Cha 1999][Bro 2002].

Designs of conventional PM synchronous machines with flux concentration (ferrite magnets) have been presented in [Spo 1992a][Spo 1996].

Designs of transverse-flux PM machines have been presented in [Weh 1988a][Mec 1996][Hen 1997][Har 1998][Mad 1998][Bli 2000][Lan 2000a].

Appendix III lists all the PM machine designs reported in those references, with their performance. The torque/mass ratios of those PM machine designs are shown in figure 4-1 and the cost/torque ratios are shown in figure 4-2. The mass and cost of all the machines listed in appendix III and represented in figure 4-1 and figure 4-2 are obtained from the dimensions stated in literature.

It must be noted that such comparison has a limited value, because all machine designs found in past literature and listed in Appendix III have different speeds, efficiencies and cooling methods. As pointed out in [Nie 1992] and as discussed in section 4.3, efficiency plays a dominant role on the machine specific power. Therefore, the graphs of figure 4-1 and figure 4-2 are not presented here as a justification to the PM machines selected or discarded. However, these two graphs give a confirmation to the analysis based on force density and discussed previously.

The following conclusions are drawn. In average, the TORUS has slightly lower torque/mass and much higher cost/torque than the conventional PM synchronous machine. In average, TFPM machines have a higher torque/mass and lower cost/torque than the conventional PM synchronous machine. In average, conventional PM synchronous machine with flux concentration (ferrite PM) has slightly lower torque/mass and comparable or higher cost/torque than the conventional PM synchronous machine.

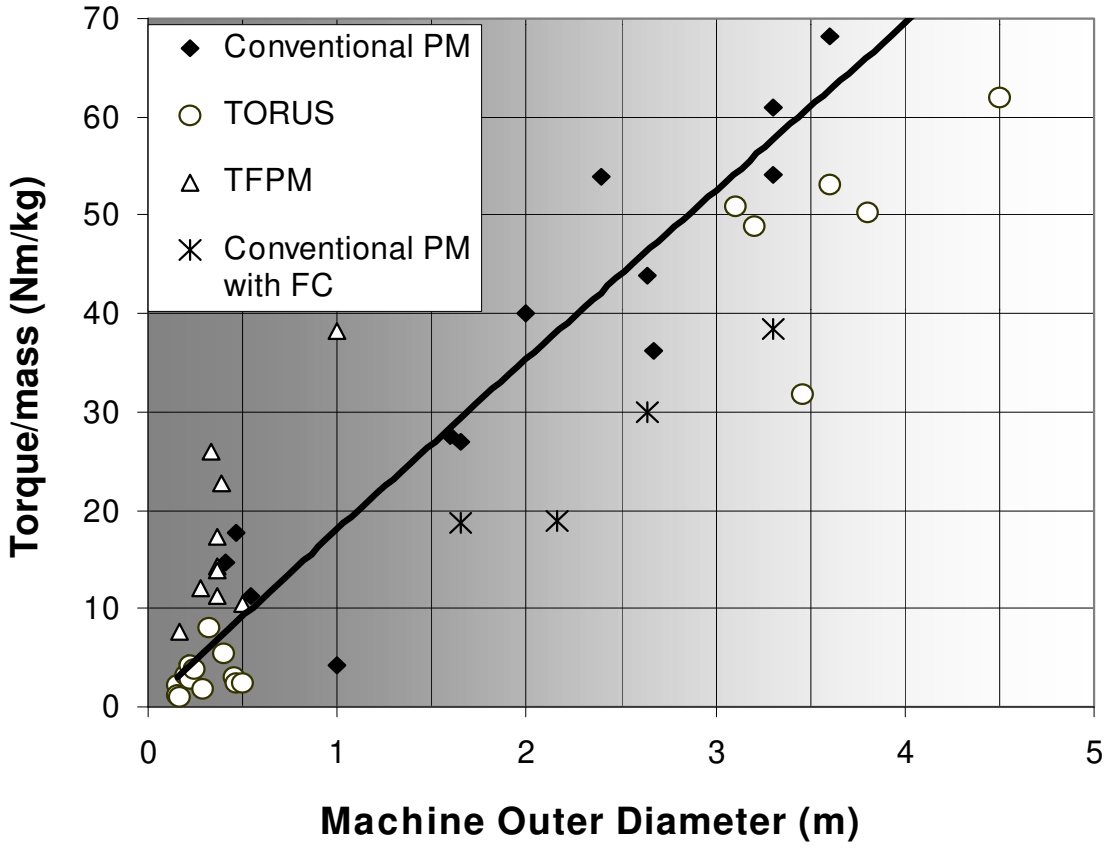

Figure 4-1: Torque/mass of PM machine designs found in literature. Only mass of active material is considered. The solid line illustrates the average torque/mass of the conventional PM synchronous machine.

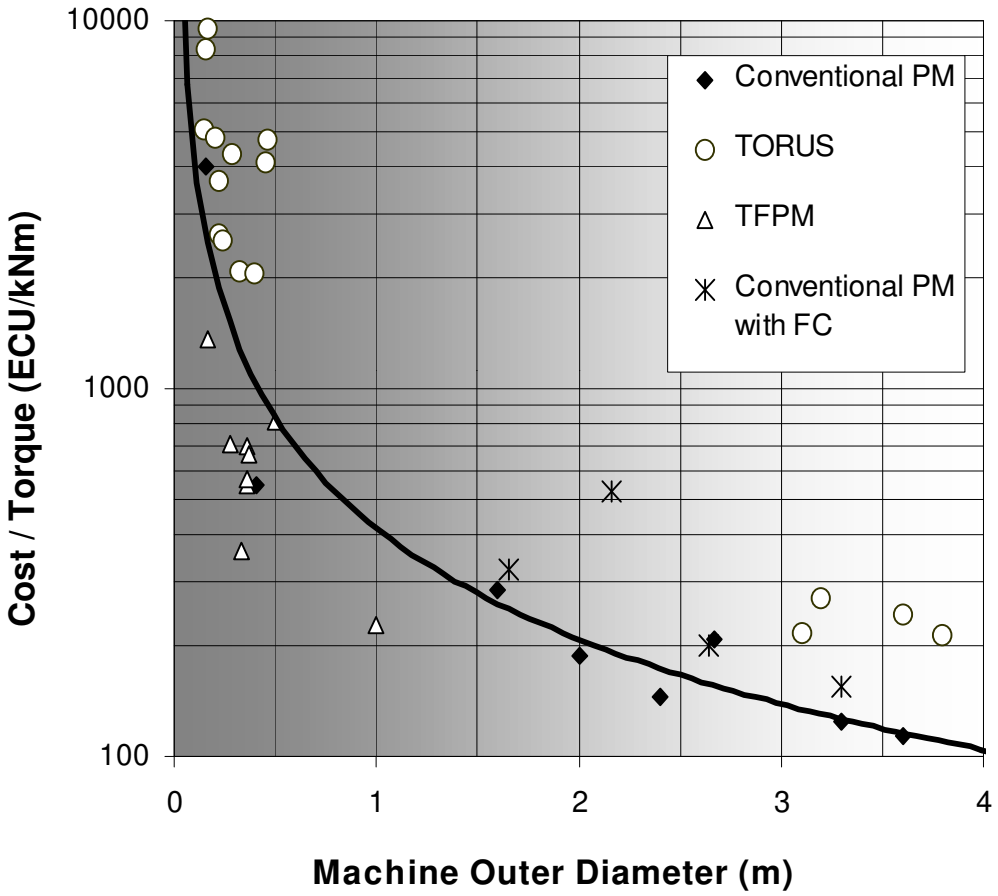

Figure 4-2: Cost/torque of PM machine designs found in literature. Only cost of active material is considered. The solid line illustrates the average cost/torque of the conventional PM synchronous machine.

4.3. Calculated performances of the conventional PM synchronous machine with/without flux concentration (rare earth PM) and the slotted axial-flux PM machine

In section 4.2, no conclusion has been drawn on the following PM machine topologies:

- slotted axial-flux PM machine;
- conventional PM synchronous machine with flux concentration (rare-earth PM).

Since no obvious conclusion can be drawn for these two machine geometries, analytical models will be derived in this section for these two PM machines. In section 4.2, the conventional PM synchronous machine was used as a basis for comparison. It is also the case in section 4.3 and consequently an analytical model is also developed for the conventional PM synchronous machine.

4.3.1. Optimization methods and analytical models

Method of optimization

An optimization program was developed for each of the three PM machine topologies. First, the optimization program calculates the cost/torque of thousands of slotted axial-flux PM machine designs. The programs identify the design having the lowest cost/torque. As a result of the optimization, the optimal design of the slotted axial-flux PM machine is given a torque value by the program. Then, the program calculates thousands of designs of the conventional PM synchronous machine with and without flux concentration having the same torque value. The program identifies the design having the lowest cost of active material. In all cases, efficiencies of 90% and 95% are set as inputs to the program. The same process is repeated for the optimization of torque/mass at efficiencies of 90% and 95%. In the optimization program, the following parameters are given as constant inputs of the optimization process:

- machine outer radius r_{out};
- efficiency η at full load.

The iron losses will depend on the machine rotational speed, which must be specified. Certain assumptions are made concerning the generator diameters and rotational speeds as a function of the machine power range, as indicated in table 4-1. These speeds and machine diameters are the same as those used in [Gra 1996b].

The following parameters are used as variable inputs of the optimization process:

- current density *J;*
- pole pitch τ_p (pole pitch τ_{po} at the outer radius for the slotted axial-flux PM machine);
- ratio of slot width/ tooth width (b_s/b_t) (ratio b_s/b_{to} at the outer radius for the slotted axial-flux PM machine);
- no-load flux density B_g in the air gap;
- ratio of stator axial length / outer radius $K_{rad} = l_s/d_{out}$ (ratio of inner lamination radius over outer lamination radius $K_{ax} = r_{li}/r_{lo}$ for the slotted axial-flux PM machine);
- in the conventional PM synchronous machine with flux concentration, the flux density B_m in the magnets;

Table 4-1. Machine rotational speed as a function of the generator outside diameter.

Generator outside diameter (m)	1.0	2.0	3.0	4.0
Wind turbine power range (kW)	30 - 100	100 - 200	400 - 600	700 - 1000
Nominal rotational speed *n* (rpm)	75	46	34	26

The five variable inputs (six variables for the conventional PM synchronous machine with flux concentartion) are varied within a certain range. The aim of the optimization programs is to identify the combination of these variable inputs providing the highest torque/mass and the lowest cost/torque, for as long as the two constant inputs are met.

For each radius r_{out} and efficiency η, the optimization program of the slotted axial-flux PM machine will identify a first torque rating $\overline{T}$ corresponding to the maximum torque/mass and a second torque rating corresponding to the minimum cost/torque. To obtain a useful comparison, the conventional PM synchronous machine and the conventional PM synchronous machine with flux concentration (Nd-Fe-B magnets) will be given the same torque rating as for the slotted axial-flux PM machine.

Assumptions

Analytical models are created for each of the three machine topology, in which the following assumptions are used:

1) the number of phases is 3 for the three machine types (m = 3);

2) the three machine types have sinusoidal terminal voltage *v(t)*, no-load voltage *e(t)* and phase current *i(t)*;

3) the number of slots per pole per phase is q = 1 and the winding is a two-layer full-pitched winding;

4) in the conventional PM synchronous machine and the slotted axial-flux PM machine, the PM cover a pole arc of 126 degrees (k_{mag} = 0.7). In the conventional PM synchronous machine with flux concentration, the flux concentrators have a width of $k_{conc}\tau_p$ near the air gap (see figure 4-5) and k_{conc} = 0.7;

5) for each phase, all the stator coils are connected in series;

6) the rotor saliency is neglected;

7) the stator slots are skewed by one slot pitch;

8) the slots are open and a non-magnetic wedge of thickness h_w = 5 mm is inserted in the opening;

9) the slots are deep with a ratio h_s/b_t = 4. For mechanical reasons, the ratio of slot depth over tooth width is limited to 4, which prevents excessive tooth mechanical vibrations from occurring;

10) the maximum flux density in the stator yoke and the rotor back iron are set to $B_{sy} = B_{rbi}$ = 1.2 T, in order to reduce the drop in magnetomotive force in those parts. This also reduces the iron losses in the stator yoke;

11) iron losses in the rotor are neglected;

12) the machine rotational speed ω_m is constant;

13) sufficient forced air or liquid cooling is provided to maintain the PMs and copper within their operating temperature range. In the calculation of copper losses, the resistivity value for copper assumes a copper temperature of 100 degrees Celcius;

14) the flux linkage under full-load condition is made equal to the no-load flux linkage;

15) all PMs are Nd-Fe-B with rigid remanent flux density B_r = 1.1 T and linear recoil permeability $\mu_{rec} = \mu_0$;

16) all steels have linear $B(H)$ characteristics with slope μ_{rFe} = 1000 up to the point of saturation where $B = B_{Fesat}$ = 1.8 T;

17) the air gap thickness g is equal to $1/1000^{th}$ of the machine outside diameter;

18) the slot filling factor is set to a constant value, i.e. k_{sfill} = 0.6 for diameters larger than 2 meters. In the latter case, square conductors are used. Below 2 meters, round conductors are assumed and k_{sfill} = 0.4;

19) the specific eddy current losses in Fe-Si laminations at 50 Hz/1.5 T is set to $k_{eddysteel}$ = 0.5 W/kg;

20) the specific hysteresis losses in Fe-Si laminations at 50 Hz/1.5 T is set to $k_{hysteel}$ = 2.0 W/kg;

21) additional iron losses due to the punching and soldering process on the stator laminations are taken into account by multiplying all iron losses by a factor $k_{addloss}$ = 2. This factor also takes into account the additional losses caused by the frequency harmonics in the phase current and no-load flux density.

Stator dimensions and basic dimensions

From the seven input variables (eight for the conventional PM synchronous machine with flux concentration), we can calculate the machines basic dimensions. The stator dimensions are summarized in table 4-2. Some of the expressions in table 4-2 are derived in appendix IV .

Phase emf E

The average power balance method is used to predict the average rated torque $\overline{T}$. We rewrite equation (3-7) for sinusoidal voltages and currents:

Table 4-2. Analytical expressions for the machines basic dimensions.

	Conventional PM synchronous machine with / without flux concentration	**Slotted axial-flux PM machine**
Slot depth	$h_s = \left(\left[\frac{h_s}{b_t}\right]\left[\frac{b_t}{b_s}\right]\frac{\tau_p}{mq}\right) / \left(1 + \frac{b_t}{b_s}\right)$	$h_s = \left(\left[\frac{h_s}{b_{ti}}\right]\frac{\tau_{po}}{mq}\right)\left(K_{ax} - \frac{1}{1 + \left[\frac{b_{to}}{b_s}\right]}\right)$
Slot width	$b_s = h_s / \left(\left[\frac{h_s}{b_t}\right]\left[\frac{b_t}{b_s}\right]\right)$	$b_s = \tau_{po} / mq\left(1 + \left[\frac{b_{to}}{b_s}\right]\right)$
Length of the conductors in the end windings per turn	$l_{ew} = \frac{h_s + \tau_p}{2}$ $l_{Cuew} = 2\sqrt{2}\tau_p + 2h_s$	$l_{ewo} = \frac{h_s + \tau_{po}}{2}$ $l_{ewi} = \frac{h_s + \tau_{pi}}{2}$ $l_{Cuew} = \sqrt{2}(\tau_{po} + \tau_{pi}) + 2h_s$
Inner and outer lamination radii	Not applicable	$r_{lo} = r_{out} - l_{ewo}$ $r_{li} = K_{ax} r_{lo}$
Axial length of stator laminations	$l_s = 2K_{rad} r_{out}$	Not applicable
Area of one pole	$A_p = l_s \tau_p$	$A_p = (r_{lo}^2 - r_{li}^2)\frac{\tau_{po}}{2r_{lo}}$
Stator yoke thickness	$h_{sy} = \frac{B_g A_p k_{mag}}{2B_{sy} l_s}$	$h_{sy} = \frac{B_g A_p k_{mag}}{2B_{sy}(r_{lo} - r_{li})}$
Air-gap radius	$r_g = r_{out} - h_{sy} - h_s$	Not applicable
Number of pole pairs	$p = \frac{\pi r_g}{\tau_p}$	$p = \frac{\pi r_{lo}}{\tau_{po}}$
Electrical frequency	$f = \frac{n}{60} p$	
Angular electrical frequency	$\omega = 2\pi f$	
mass of stator yoke	$m_{sy} = \pi(r_{out}^2 - (r_g + h_s)^2) l_s \rho_{Fe}$	$m_{sy} = 2pA_p h_{sy} \rho_{Fe}$
mass of stator teeth	$m_{st} = 2ph_s(A_p - mql_s b_s)\rho_{Fe}$	$m_{st} = 2ph_s(A_p - mqb_s(r_{lo} - r_{li}))\rho_{Fe}$

$$\bar{T} = \frac{3EI\cos\psi + P_{Fe}}{\omega_m} \tag{4-4}$$

where E is the rms value of the no-load voltage, I is the rms value of the phase current. P_{Fe} is the average sum of the hysteresis and eddy current losses in the stator core. Copper losses are not directly stated in equation (4-4), because they are already included in the term $3EI\cos\psi$. Obviously, the use of equation (4-4) alone for the maximization of torque tends to favor those designs with higher iron losses. However, this problem is circumvented if a constraint is imposed on the machine efficiency, as done here. Thus, those machine designs with high iron losses, high mechanical torques and poor efficiencies will be rejected.

From Faraday's law, the phase emf E may be written as:

$$e(t) = pN_{slot}\frac{d}{dt}\Phi_{pnl}(t) \tag{4-5}$$

In the current analysis, the emf $e(t)$ was assumed to be sinusoidal. Consequently, the no-load flux $\Phi_{pnl}(t)$ flowing in each pole is also a sinusoidal function of time. Since the machine rotational speed is constant, the air gap flux density of a sinusoidal $\Phi_{pnl}(t)$ is sinusoidally distributed in space with amplitude $\hat{B}_1$. The rms value E can be written:

$$E = \frac{4}{\sqrt{2}}pN_{slot}k_{ws}k_pk_dA_p\hat{B}_1 f \tag{4-6}$$

where k_{ws} is the skewing factor, which takes into account the reduction of emf due to slot skewing. N_{slot} is the number of conductors inserted in one slot. The factors k_p and k_d are the pitch factor and the distribution factor. k_p and k_d are equal to 1, because of the assumption of a two-layer full-pitched winding with one slot per pole per phase ($q = 1$).

In reality, the air-gap flux density is not sinusoidally distributed in space. If the flux density is assumed as crossing the air gap perpendicularly, we obtain a rectangular space distribution of the flux density of amplitude B_g. If the rectangular space distribution is expressed as a Fourier series, we can express the amplitude of the first space harmonic as:

$$\hat{B}_1 = \frac{4}{\pi}B_g\sin\left(\frac{\pi}{2}k_{mag}\right) \tag{4-7}$$

In this section, we assume that only the first space harmonic gives a contribution to power and losses. The effect of all other space harmonics is neglected.

Saturation and flux density in steel laminations

The flux densities $\hat{B}_{st1}$ and $\hat{B}_{sy1}$ are the amplitudes of the fundamental harmonic components of flux density in the teeth and in the stator yoke. The assumption was made that the terminal voltage under full-load condition is approximately equal to the no-load voltage. Consequently, the flux linkage in the stator winding will be approximately the same both at no-load and full-load conditions. In such conditions, the amplitude of the fundamental component of the flux-density in the stator yoke will be:

$$\hat{B}_{sy1} = \frac{\hat{B}_1}{\pi}\frac{\tau_p}{h_{sy}} \tag{4-8}$$

In the conventional PM synchronous machines with/without flux concentration, the amplitude of the flux-density in the stator teeth will be:

$$\hat{B}_{st(rad)} = B_g\left(1 + \frac{b_s}{b_t}\right) \tag{4-9}$$

Equation (4-9) is used to check saturation. From equation (4-9), if $\hat{B}_{st(rad)}$ is larger than $B_{Fe\text{-}sat}$, the design saturates and it is rejected. For the calculation of losses in the teeth, the amplitude of the fundamental component of the flux-density in the stator teeth is given by:

$$\hat{B}_{st1(rad)} = \hat{B}_1\left(1 + \frac{b_s}{b_t}\right) \tag{4-10}$$

In the slotted axial-flux PM machine, the flux density in the teeth will be higher on the inner radius and lower on the outer radius due to the variation in tooth width. The peak flux density at the inner radius will be:

$$\hat{B}_{sti(ax)} = B_g\left(1 + \frac{mqb_s}{K_{ax}\tau_{po} - mqb_s}\right) \tag{4-11}$$

To calculate the losses in the teeth of the slotted axial-flux PM machine, we will need to average the squares of the fundamental components of the flux density on the inner and outer radii. This is necessary because the losses are proportional to the square of the flux density.

$$\overline{B}_{st1(ax)} = \frac{\hat{B}_1}{\sqrt{2}}\sqrt{\left(1 + \frac{b_s}{b_{to}}\right)^2 + \left(1 + \frac{mqb_s}{K_{ax}\tau_{po} - mqb_s}\right)^2} \tag{4-12}$$

Equation (4-11) will be used to check saturation in the teeth of the slotted axial-flux PM machine. If saturation occurs at the inner radius, it may be the case that saturation does not occur at the outer radius as depicted in figure 4-3.

K_{axsat} is the ratio of the radius from which saturation occurs over the outer lamination radius r_{lo}. It can be determined from:

$$K_{axsat} = \frac{mqb_s}{\tau_{po}}\left(\frac{B_{Fesat}}{B_{Fesat} - B_g}\right) \tag{4-13}$$

In the case where the teeth at the inner radius saturate and the teeth at the outer radius do not saturate, the r.m.s. no-load voltage E is calculated with equation (4-14) instead of equation (4-6).

$$E \cong \frac{4}{\sqrt{2}} pN_{slot}k_{ws}k_pk_d[A_{po}B_1 + (A_{pi} - mq(r_{lo}K_{axsat} - r_{li})b_s)B_{Fesat}]f \tag{4-14}$$

where A_{po} is the area covered by one pole where no saturation occurs. A_{pi} is the area covered by one pole where saturation occurs. They are given by:

$$A_{po} = A_p\left(\frac{K_{ax}}{K_{axsat}}\right)^2 \tag{4-15}$$

$$A_{pi} = A_p - A_{po} \tag{4-16}$$

The calculation of E with equation (4-14) is based on the idea that the flux density is limited to the value B_{Fesat} in the region where saturation occurs.

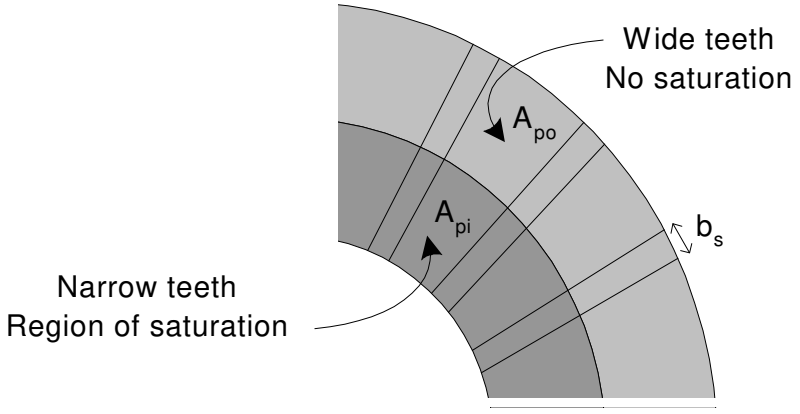

Figure 4-3: Slotted axial-flux PM machine with saturation in the teeth at the inner radius and no saturation in the teeth at the outer radius.

The calculation of the fundamental harmonic component in the region of saturation depends on the level of saturation and will be more difficult than the expression used in the case of no-saturation (equation (4-6)). Here, the calculation is simplified by assuming the flux density as varying sinusoidally with time in the saturating region and having a maximum value B_{Fesat}. Although equation (4-14) is an approximation, it gives an insight whether saturation needs to be included in the model. A complete modeling of the slotted axial-flux PM machine would require the calculation of the fundamental harmonic component in the saturating region. This is left for further investigation.

Nominal rms current I

There are three limits imposed to the amount of current I to be fed into the stator winding:

- desired efficiency η;
- temperature limits (type of cooling);
- PM demagnetization;
- stator saturation;
- desired stator reactance $X_{s\,p.u.}$.

It was already assumed in the beginning of this analysis that cooling was sufficient to prevent PM demagnetization under nominal load conditions. Also, we assumed that the machine output voltage was approximately equal to the no-load voltage. Thus, the stator flux density at full-load can be considered as equal to the stator flux density under no-load conditions. If saturation is checked for no-load conditions, the stator core will not saturate at full-load conditions. This assumption will also dictate the value of $X_{s\,p.u.}$.

In low-speed machines, if sufficient cooling is provided, the first point is usually the limiting factor. To obtain low-speed machines with acceptable power efficiencies (around 95%) at nominal load, the nominal rms current density J will be in the area of 3 - 6 A/mm^2 as it is the case in [Gra 1996b].

In our analysis, the efficiency target η is set constant and the current density J is a variable to optimize. The current is written as a function of the slot cross-section A_{Cus} and current density J.

$$I = JA_{Cus} \tag{4-17}$$

$$A_{Cus} = k_{sfill}\left[\frac{b_s(h_s - h_w)}{N_{slot}}\right] \tag{4-18}$$

Then the PM demagnetization under short-circuit conditions is checked. The short-circuit current i_{sc} is calculated from the no-load voltage E, the stator inductance L_s calculated in table 4-4 and the stator resistance R_s.

$$\hat{i}_{sc} = 2\frac{\sqrt{2}E}{\sqrt{R_s^2 + (2\pi f L_s)^2}} \tag{4-19}$$

The factor 2 in equation (4-19) accounts for the peak value that can be reached by the current in the transient period just after short-circuit. In the case of large machines, the time constant will in most cases be sufficiently large to allow the current to double, as described in [Seb 1987]. Once the peak short-circuit current is known, Ampère's law is applied on the equivalent magnetic circuit of figure 4-4, which determines the flux density created by the armature reaction and opposing the PM flux density. If the resulting flux density inside the PM is lower than 0.1 T, then the machine design is rejected.

Power losses

The conduction losses P_{Cu} are written as:

$$P_{Cu} = \frac{J^2}{\sigma_{Cu}} V_{Cu} \tag{4-20}$$

In the conventional PM synchronous machines, copper volume V_{cu} will be given by:

$$V_{cu(rad)} = 2mqpk_{sfill}b_s(h_s - h_w)\left[l_s + \frac{l_{Cuew}}{2}\right] \tag{4-21}$$

In the slotted axial-flux PM machine, the total copper volume is given by:

$$V_{cu(ax)} = 2mqpk_{sfill}b_s(h_s - h_w)\left[r_{lo} - r_{li} + \frac{l_{Cuew}}{2}\right] \tag{4-22}$$

The iron losses are approximated with Steinmetz formula [Sen 1997]:

$$P_{Fe} = k_{addloss}\left[k_{hyststeel}\left(\frac{f}{50Hz}\right) + k_{eddysteel}\left(\frac{f}{50Hz}\right)^2\right]\left[m_{st}\left(\frac{B_{st1}}{1,5T}\right)^2 + m_{sy}\left(\frac{B_{sy1}}{1,5T}\right)^2\right] \tag{4-23}$$

where $k_{hyststeel}$ and $k_{eddysteel}$ are the specific hysteresis loss and the specific eddy current loss (in W/kg) in the laminated stator core, for a frequency of 50 Hz and a flux density of 1.5 T.

Magnetic equivalent circuit and magnet dimensions

The magnetic circuit used to establish the magnet thickness h_m is illustrated in figure 4-4. Figure 4-4 is applicable for the conventional PM synchronous machine and slotted axial-flux PM machine. The left-hand side of figure 4-4 illustrates the equivalent reluctance diagram for both machine types and the right-hand side of figure 4-4 shows the flux circulation considered in the analysis for both machine topologies. As shown in the right-hand side of figure 4-4, the flux is assumed as traveling in straight line in the air gap and the leakage flux of the PM is neglected.

Figure 4-5 illustrates the equivalent magnetic circuit used for the conventional PM synchronous machine with flux concentration. The expressions used for the reluctances of figure 4-4 and figure 4-5 are given in table 4-3. In both figures, the magnetic circuit illustrates the reluctances through which half of the flux goes. This is why the magnet reluctance, the air gap reluctance and the stator teeth reluctance are multiplied by two. The reluctance of the stator yoke and the rotor back iron are divided by two because the mean distance of the flux path is about equal to half the pole pitch. The magnetic circuit of figure 4-4 can easily be solved and the value of h_m can be obtained. In the conventional PM synchronous machine and the slotted axial-flux PM machine, the flux-density B_m in the PM is equal to the air-gap flux density B_g.

In the conventional PM synchronous machine with flux-concentration, B_m and B_g may have different values. Also, the leakage of the magnetic flux between each flux concentrator is taken into account.

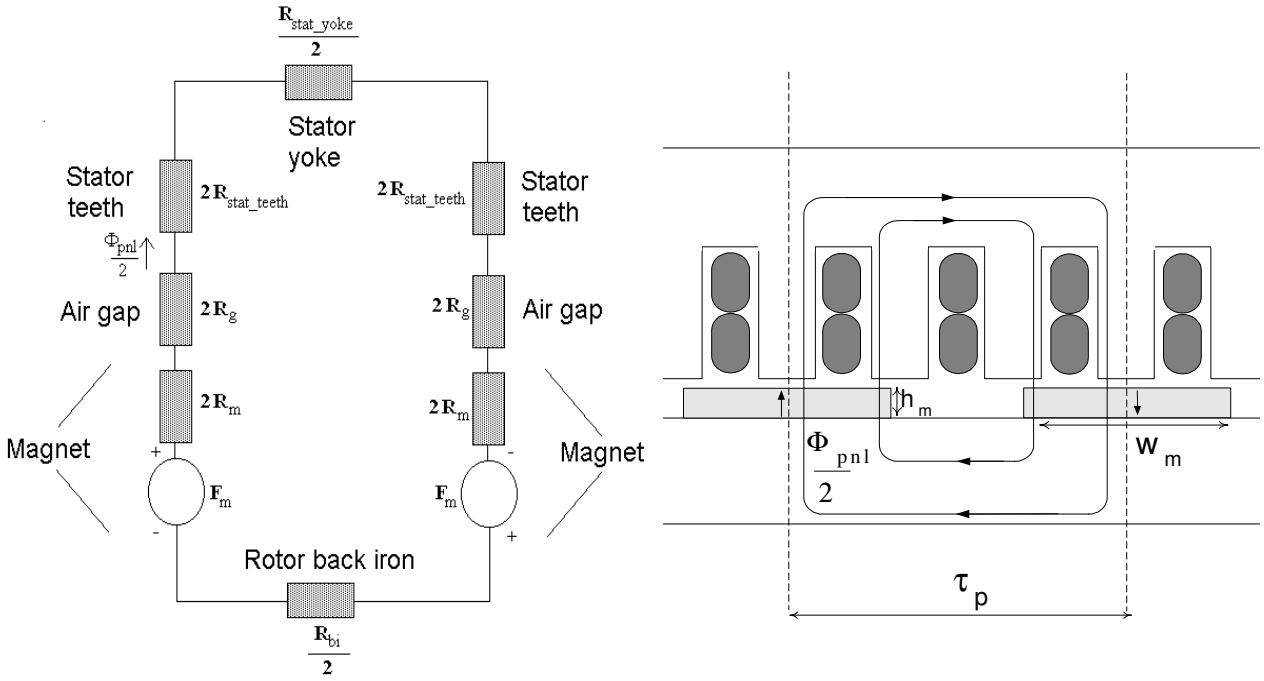

Figure 4-4: Equivalent magnetic circuit for the conventional PM synchronous machine and the slotted axial-flux PM machine.

This leakage flux travels through the air around the flux concentrators and is modeled by the equivalent reluctance $\mathcal{U}_{leak}$. The leakage reluctance is more difficult to model, due to its path through air which is not clearly bounded in space. This reluctance is modeled by form factors β_{lkside} and β_{lktop}, which are defined from the analysis in chapter 7.

$$\beta_{lkside} = 4,45 - 1,92\left(\frac{k_{conc}\tau_p}{h_m}\right) + 0,22\left(\frac{k_{conc}\tau_p}{h_m}\right)^2 + 0,27\left(\frac{w_m}{h_m}\right) - 0,02\left(\frac{w_m}{h_m}\right)^2 \tag{4-24}$$

$$\beta_{lktop} = 4,45 - 1,92\left(\frac{k_{conc}\tau_p}{h_m}\right) + 0,22\left(\frac{k_{conc}\tau_p}{h_m}\right)^2 + 0,27\left(\frac{l_s}{h_m}\right) - 0,02\left(\frac{l_s}{h_m}\right)^2 \tag{4-25}$$

In the conventional PM synchronous machine with flux-concentration, the selection of the PM flux density is done by adjusting the PM width w_m.

The no-load flux Φ_m flowing in the magnet is half the no-load airgap flux Φ_{pnl} minus the rotor pole leakage. Thus, we write:

$$\Phi_m = \frac{\Phi_{pnl}}{2} - \Phi_{leak} \tag{4-26}$$

Writing equation (4-26) in terms of the flux densities,

$$B_m l_s w_m = \frac{B_g}{2} k_{conc}\tau_p l_s - \frac{B_r h_m}{2\mu_0 \Re_{leak}} \tag{4-27}$$

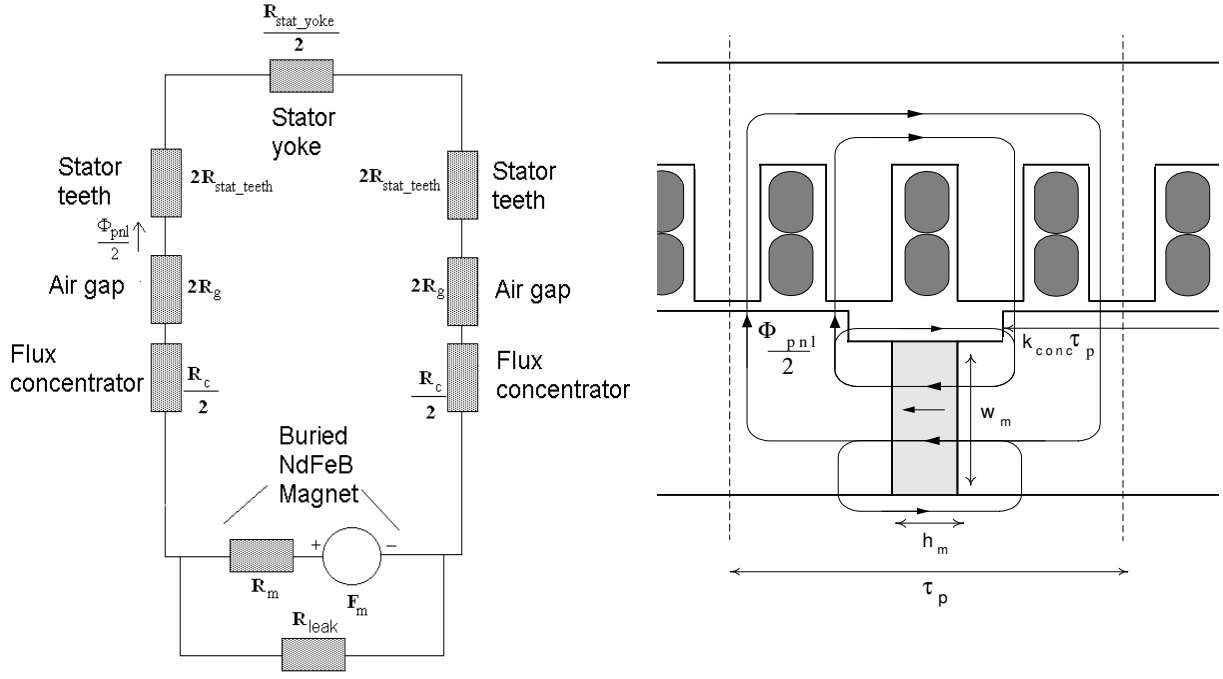

Figure 4-5: Equivalent magnetic circuit for the conventional PM synchronous machine with flux concentration (rare-earth PM).

Table 4-3. Analytical expressions for the machines reluctances.

	Conv. PM synch. Mach.	Conv. PM synch. Mach. flux conc.	Slotted axial-flux PM machine
Reluctance Stator yoke	$\Re_{statyoke} \cong \frac{\tau_p}{\mu_{rFe}\mu_0 l_s h_{sy}}$		$\Re_{statyoke} \cong \frac{\left(\frac{\tau_{po}+\tau_{pi}}{2}\right)}{\mu_{rFe}\mu_0 h_{sy}(r_{lo}-r_{li})}$
Reluctance Stator teeth	$\Re_{statteeth} = \frac{h_s}{\mu_{rFe}\mu_0 mqb_t l_s}$		$\Re_{statteeth} = \frac{h_s}{\mu_{rFe}\mu_0(A_p - mqb_s)}$
Reluctance Air gap	$\Re_g = \frac{g}{\mu_0 l_s k_{mag}\tau_p}$		$\Re_g = \frac{g}{\mu_0 k_{mag} A_p}$
Reluctance PM	$\Re_m = \frac{h_m}{\mu_{rec} l_s k_{mag}\tau_p}$	$\Re_m = \frac{h_m}{\mu_{rec} l_s w_m}$	$\Re_m = \frac{h_m}{\mu_{rec} k_{mag} A_p}$
Reluctance flux conc.	Not applicable	$\Re_c \cong \frac{w_m}{2\mu_{rFe}\mu_0 l_s k_{conc}\tau_p}$	Not applicable
Reluctance leakage flux conc.	Neglected	$\Re_{leak} = \frac{1}{2\mu_0}\left[\frac{\beta_{lkside}}{w_m} + \frac{\beta_{lktop}}{l_s}\right]$	Neglected
Reluctance rotor back iron	$\Re_{bi} \cong \frac{\tau_p}{2\mu_{rFe}\mu_0 l_s h_{sbi}}$	Not applicable	$\Re_{bi} \cong \frac{\left(\frac{\tau_{po}+\tau_{pi}}{2}\right)}{2\mu_{rFe}\mu_0 h_{bi}(r_{lo}-r_{li})}$
MMF Magnet	$\Im_m = \frac{B_r h_m}{\mu_{rec}}$		

We write,

$$w_m = \frac{B_g}{2B_m} k_{conc}\tau_p - \frac{h_m}{\mu_0 l_s \Re_{leak}} \qquad (4\text{-}28)$$

The PM thickness h_m can be determined from the equivalent magnetic circuit of figure 4-5.

Inductance and phase angle

The assumption was made that the machine flux linkage under full-load condition is equal to the no-load flux linkage in the stator winding. This is achieved by making the terminal voltage V nearly equal to the no-load voltage E. Figure 4-6 illustrates the machine phasor diagram. If the stator resistance R_s is neglected, equal values of flux linkage under no-load and full-load conditions will be obtained for equal values of E and V, as shown on the left-hand side of figure 4-6.

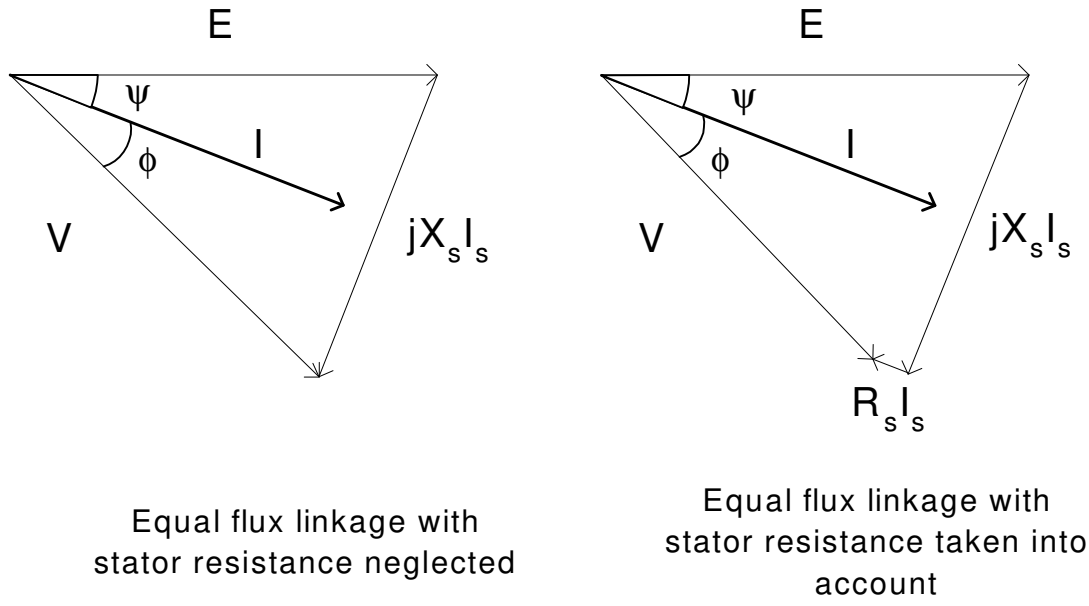

Figure 4-6: Typical phasor diagrams of three machine types considered.

By keeping the flux linkage at the same value under no-load and full-load conditions, the iron losses stay the same and saturation of the stator teeth can be neglected which brings substantial simplification in the analysis. This is accomplished by varying the phase angle ψ as the machine is loaded. If the machine per unit reactance $X_{s\ p.u.}$ is kept below 1, which is usually the case in longitudinal machines, the cosine of ψ remains will remain close to 1 and this practice will not substantially decrease the machine nominal power.

On the right-hand side of figure 4-6, the phasor diagram is drawn where R_s is taken into account. It shows that the terminal voltage V should be made slightly lower than the no-load voltage E to obtain the same flux linkage. According to figure 4-6, the phase current I must lag the no-load voltage E in order to keep the flux linkage constant in the stator winding. In that case, the phase angle ψ depends upon the value of the stator inductance L_s. The phasor diagram of figure 4-6 allows to write [Gra 1996b]:

$$\cos\psi = \cos\varphi = \sqrt{1 - \left(\frac{\pi f L_s I}{E}\right)^2} \qquad (4\text{-}29)$$

where the inductance L_s and its components are defined in table 4-4. In table 4-4, the expressions for the leakage inductances of the two conventional PM synchronous machines are taken from [Ric 1967]. The expression for the total stator inductance L_s is taken from [Gra 1996b]. All expressions for the inductances in the case of the slotted axial-flux PM machine are derived by simple substitution of the pole areas A_p from the radial case to the axial case, or by substituting the axial length l_s by the difference between the outer radius r_{lo} and the inner lamination radius r_{li}.

It should be noted that the power electronics connected to the generator output will need to be slightly increased in rating as a result of a *cos* ϕ lower than 1.

Table 4-4. Analytical expressions for the machine inductances (for q = 1).

	Conventional PM synchronous machine	Conventional PM synchronous machine with flux concentration	Slotted axial-flux PM machine
Total stator inductance L_s	$L_s = \frac{4}{3}L_{mq} + L_{\sigma ew} + L_{\sigma s} + L_{\sigma g}$		
Magnetizing inductance L_{mq} in the quadrature axis	$L_{mq} = \frac{\mu_0 \pi N_{slot}^2 l_s r_g}{2 g_{eff}}$	$L_{mq} \cong \frac{\mu_0 p N_{slot}^2 l_s}{\frac{2 g_{eff}}{\tau_p} + \frac{h_m}{\mu_{rec} w_m}}$	$L_{mq} = \frac{\mu_0 \pi N_{slot}^2 (r_{lo}^2 - r_{li}^2)}{4 g_{eff}}$
Leakage Inductance in the end windings $L_{\sigma ew}$	For a double-layer winding with $N_{slot} = 2$ ([Gra 1996b]) $L_{\sigma ew} \cong p \mu_0 \tau_p$		For a double-layer winding with $N_{slot} = 2$ ([Gra 1996b]) $L_{\sigma ew} \cong p \mu_o \left(\frac{1}{2} (\tau_{po} + \tau_{pi}) \right)$
Slot Leakage Inductance $L_{\sigma s}$	$L_{\sigma s} = 2 p \mu_o l_s N_{slot}^2 \left(\frac{h_s + 2h_w}{3 b_s} \right)$		$L_{\sigma s} = 2 p \mu_o (r_{lo} - r_{li}) N_{slot}^2 \left(\frac{h_s + 2h_w}{3 b_s} \right)$
Intertooth Leakage Inductance $L_{\sigma g}$	$L_{\sigma g} = 2 p \mu_o l_s N_{slot}^2 \left(\frac{5 \frac{g_{eff}}{b_s}}{5 + 4 \frac{g_{eff}}{b_s}} \right)$		$L_{\sigma g} = 2 p \mu_o (r_{lo} - r_{li}) N_{slot}^2 \left(\frac{5 \frac{g_{eff}}{b_s}}{5 + 4 \frac{g_{eff}}{b_s}} \right)$
Total air gap g_{tot}	$g_{tot} = g + \frac{h_m}{\mu_{rec}}$	$g_{tot} = g$	$g_{tot} = g + \frac{h_m}{\mu_{rec}}$
Effective air gap g_{eff}	$g_{eff} = g_{tot} k_{Carter}$		$g_{eff} = g_{tot} k_{Carterave}$
Carter factor k_{Carter}	$k_{Carter} = \frac{(\tau_p / m)}{(\tau_p / m) - \gamma g_{tot}}$ $\gamma = \frac{4}{\pi} \left[\frac{b_s}{2 g_{tot}} \operatorname{atan} \frac{b_s}{2 g_{tot}} - \log \sqrt{1 + \left(\frac{b_s}{2 g_{tot}} \right)^2} \right]$		Same Carter factor as the conventional PM synchronous machine. The pole pitch value used is: $\frac{\tau_{pi} + \tau_{po}}{2}$

Final mass, cost and efficiency calculations

Up to this point, sufficient information has been provided to calculate the machine output power and losses. Only the total active mass, total cost of the active material and efficiency need to be calculated. The total machine efficiency is given by:

$$\eta = \frac{\bar{T}\omega_m - P_{Cu} - P_{Fe}}{\bar{T}\omega_m} \tag{4-30}$$

and inserting equation (4-4) into equation (4-30), we obtain:

$$\eta = \frac{3EI\cos\psi - P_{Cu}}{\bar{T}\omega_m} \tag{4-31}$$

The total mass and cost of active material are given by:

$$m_{act} = m_{sy} + m_{st} + m_{bi} + m_c + m_{Cu} + m_{pm} \tag{4-32}$$

$$C_{act} = c_{Fe}(m_{sy} + m_{st} + m_{bi} + m_c) + c_{Cu}m_{Cu} + c_{pm}m_{pm} \tag{4-33}$$

where the different masses are given in table 4-5. These two last expressions allow to obtain the ratios of cost/torque and torque/mass.

4.3.2. Optimization results

The optimization method is applied to the three machine types. The detailed results are given in appendix V. Figure 4-7 and figure 4-8 summarize the performances obtained after optimization of the three machine types.

Table 4-5. Expressions for the calculation of mass.

	Conventional PM synchronous machine	**Conventional PM synchronous machine with flux concentration**	**Slotted axial-flux PM machine**
Mass of PM m_{pm}	$m_{pm} = 2\rho_m h_m k_{mag} p A_p$	$m_{pm} = 2\rho_m h_m w_m l_s p$	$m_{pm} = 2\rho_m h_m k_{mag} p A_p$
Mass of back iron m_{bi}	$m_{bi} = 2\rho_{Fe} p A_p h_{bi}$	$m_{bi} = 0$	$m_{bi} = 2\rho_{Fe} p A_p h_{bi}$
Mass of flux concentrator m_c	$m_c = 0$	$m_c = 2\rho_{Fe} p w_m (A_p - h_m l_s)$	$m_c = 0$
Mass of copper m_{Cu}	$m_{Cu} = \rho_{Cu} V_{Cu}$		

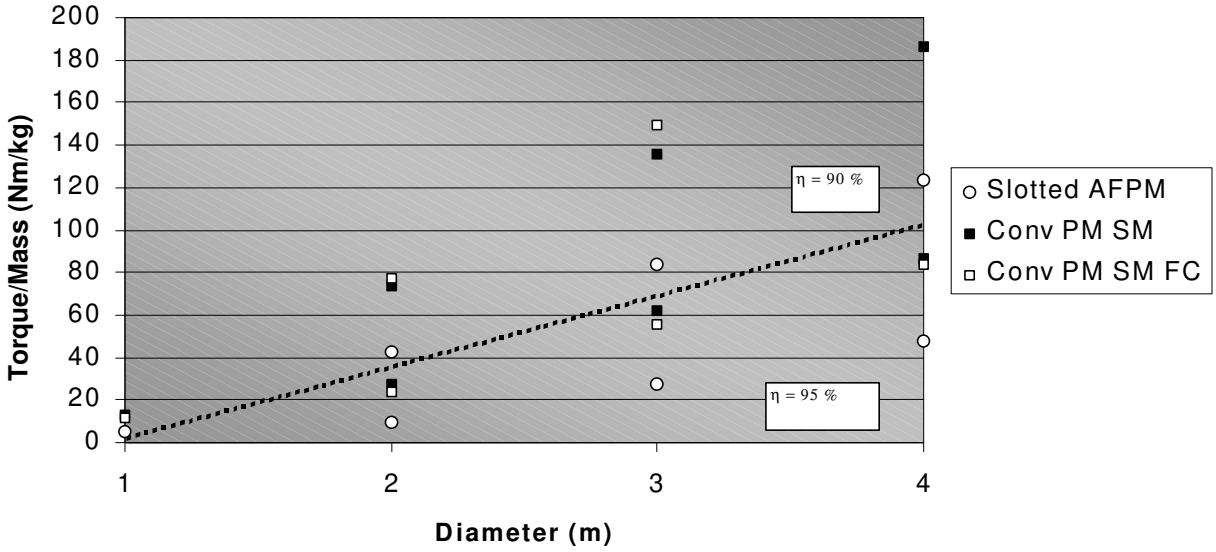

Figure 4-7: Torque/mass performance after optimization of the slotted axial-flux PM machine, the conventional PM synchronous with/without flux concentration. Optimization target: highest torque/mass. Above dotted line = designs with 90% efficiency. Below dotted line = designs with 95% efficiency.

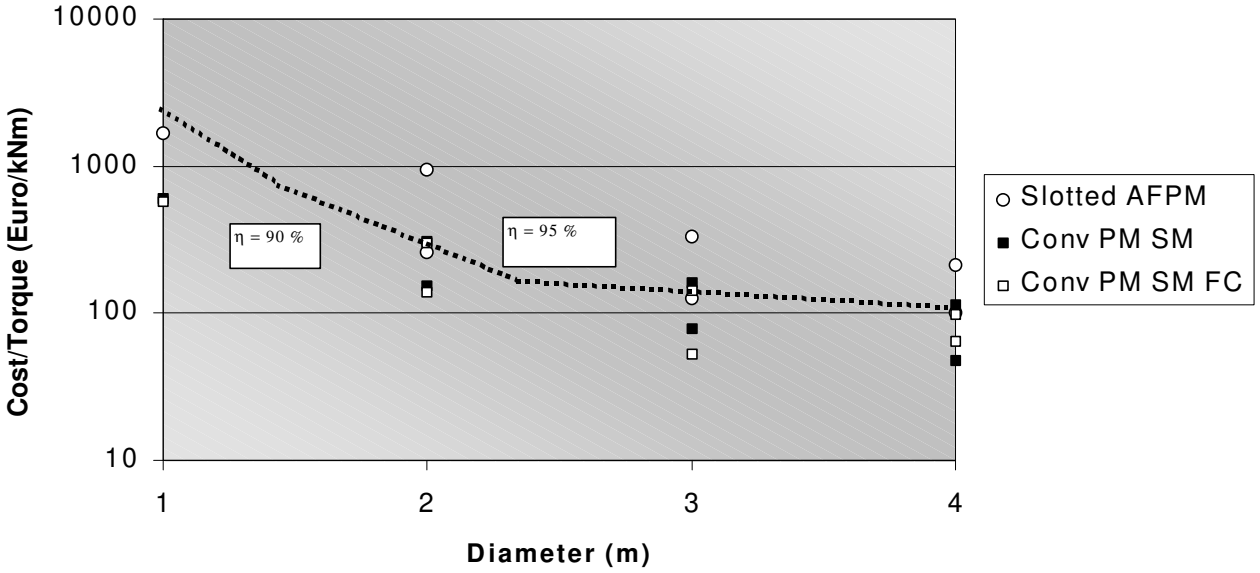

Figure 4-8: Cost/torque performance after optimization of the slotted axial-flux PM machine, the conventional PM synchronous with/without flux concentration. Optimization target: lowest cost/torque. Above dotted line = designs with 95% efficiency. Below dotted line = designs with 90% efficiency.

Figure 4-7 illustrates the torque/mass performance as a function of the machine outside diameter, when torque/mass is set as the optimization target. Figure 4-8 illustrates the cost/ torque performance as a function of the machine outside diameter, when cost/torque is set as the optimization target

On both graphs, the machine performance is shown for efficiencies of 90% and 95%. From these two graphs, we can conclude that reducing the efficiency from 95% to 90% brings substantial improvement in the torque/mass and cost/torque of the three machine types. Lower efficiencies favor light and inexpensive machine designs. Also, the improvement in torque/mass and cost/torque related to a change in efficiency is more significant for small diameters. After the optimization process, the torque/mass and cost/torque are improved by a factor 2 to 4 at 2-meter diameter. At a 4-meter diameter, reducing the efficiency from 95% to 90% will improve the torque/mass and cost/torque by a factor of about two. This difference between small diameters and large diameters can be explained by the variation in the ratio of current density at 90% over the current density at 95%.

It must be noted that the machine designs with 95% efficiency are not shown in figure 4-7 and figure 4-8 for a 1-meter diameter. This is due to the absence of a slotted axial-flux PM machine design that meets the 95% efficiency requirement. The pole pitches obtained in the optimization process are shown in figure 4-11 and figure 4-12. Those trends indicate a wider pole pitch at 95% efficiency (e.g. about 6 -7 cm for the conventional PM synchronous machines) and a shorter pole pitch at 90% efficiency (e.g. about 3 - 5 cm for the conventional PM synchronous machines).

Inspecting the results of torque/mass and cost/torque optimisation of figure 4-7 and figure 4-8, we conclude that the conventional PM synchronous machine is 1.5 to 3 times lighter and cheaper than the slotted AFPM machine for the conditions imposed by our optimization program. Regarding the difference between the two types of conventional PM synchronous machines, the torque/mass and cost/torque performances of the conventional PM synchronous machines are more or less equal to the conventional PM synchronous machine with flux concentration.

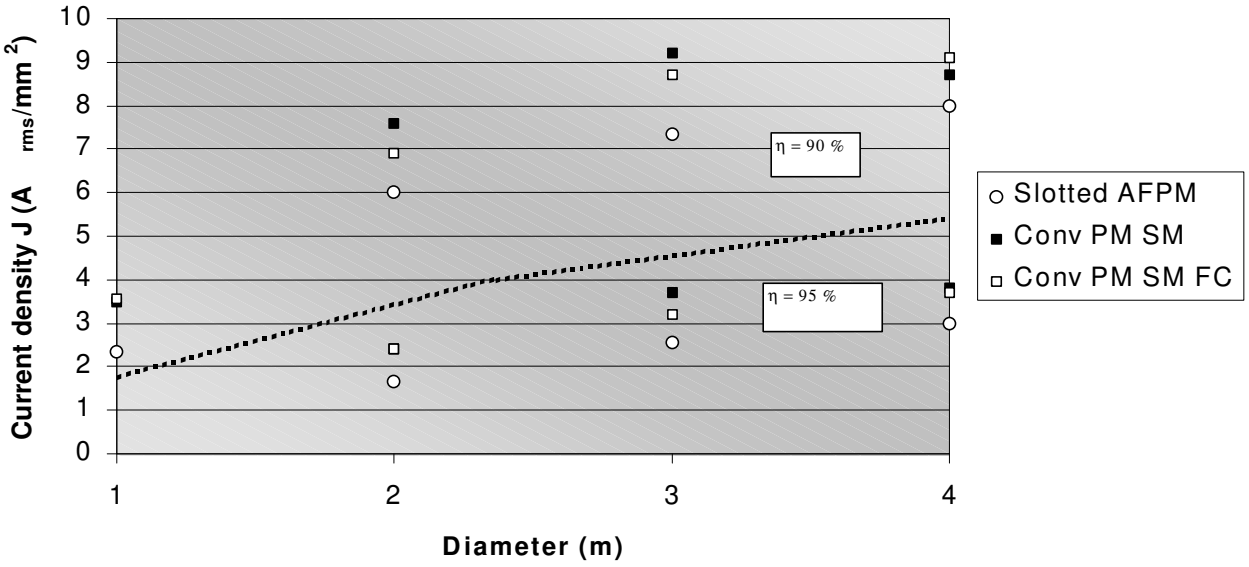

Figure 4-9: Current density J after optimization of the slotted axial-flux PM machine and the conventional PM synchronous with/without flux concentration. Optimization target: highest torque/mass. Above dotted line = designs with 90% efficiency. Below dotted line = designs with 95% efficiency.

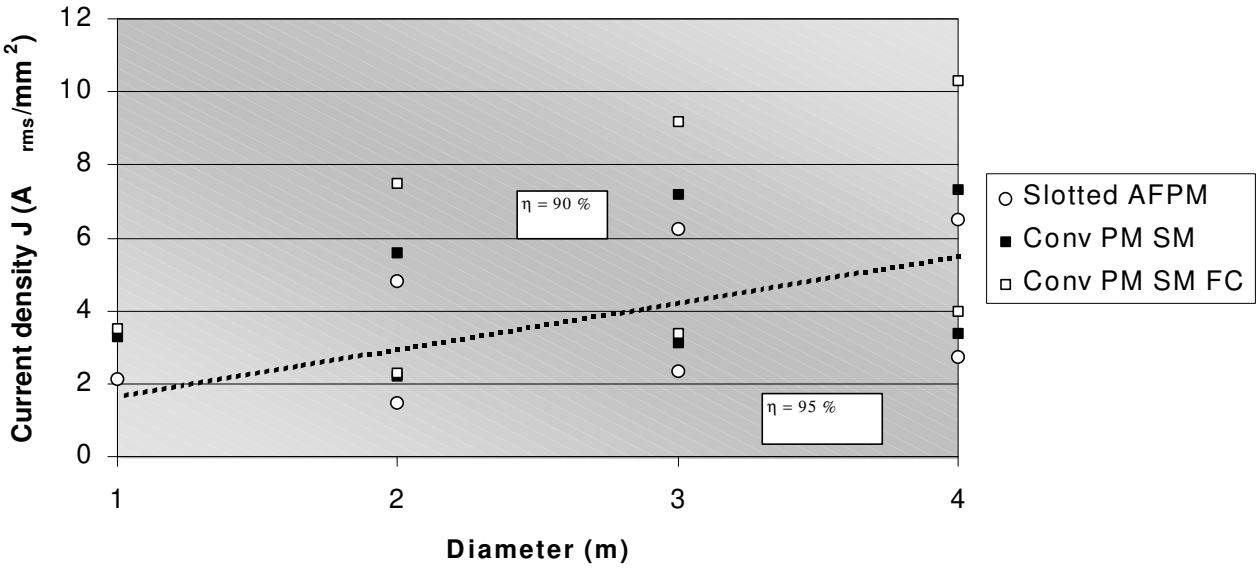

Figure 4-10: Current density J after optimization of the slotted axial-flux PM machine and the conventional PM synchronous with/without flux concentration. Optimization target: lowest cost/torque. Above dotted line = designs with 90% efficiency. Below dotted line = designs with 95% efficiency.

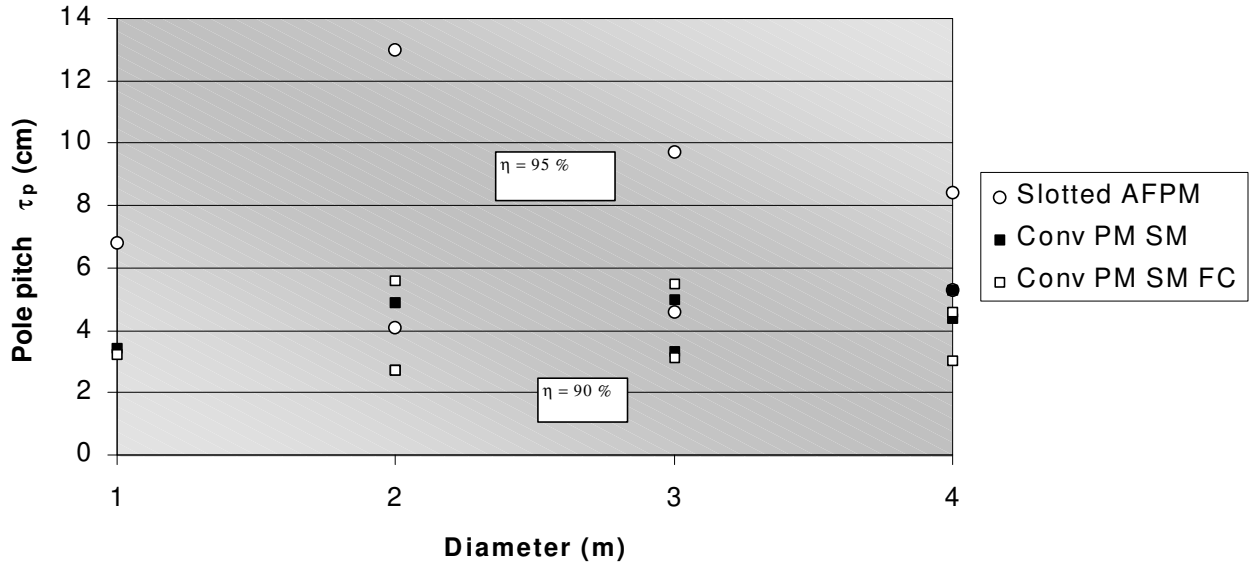

Figure 4-11: Pole pitch τ_p after optimization of the slotted axial-flux PM machine and the conventional PM synchronous with/without flux concentration. Optimization target: highest torque/mass. Above dotted line = designs with 95% efficiency. Below dotted line = designs with 90% efficiency.

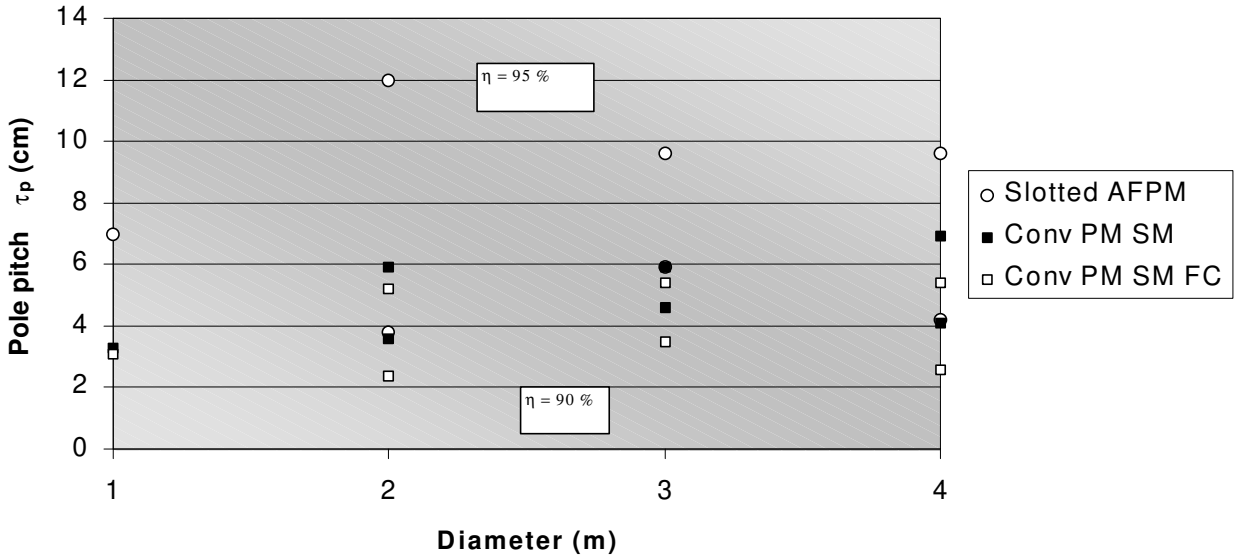

Figure 4-12: Pole pitch τ_p after optimization of the slotted axial-flux PM machine and the conventional PM synchronous with/without flux concentration. Optimization target: lowest cost/torque. Upper points = designs with 95% efficiency. Lower points= designs with 90% efficiency.

When the results of figure 4-7 and figure 4-8 are compared to the designs presented in literature, the graphs of figure 4-13 and figure 4-14 can be extracted. Figure 4-13 and figure 4-14 are the same as figure 4-1 and figure 4-2 with the addition of the results of the optimization process presented in this section. Also, the TORUS and the conventional PM synchronous machine with ferrite magnets have been discarded for better clarity.

In the same way as presented earlier, the points of figure 4-13 and figure 4-14 showing the performance of the TFPM machines and conventional PM synchronous machine are taken from the scientific literature (see appendix III). In both figure 4-13 and figure 4-14, it appears that the results predicted from the optimization process match the performances obtained in literature. At larger diameters, the designs presented in scientific literature (and reported in appendix III) have efficiencies around 95%. The torque/mass and cost/torque of those designs meet the performances predicted with our model at 95% efficiency. For smaller diameters, the designs presented in the scientific literature have lower efficiencies. For example, a design presented in [Gra 1996b] and identified in figure 4-14 has an outer diameter of 1.60 m and an efficiency of 93%. Figure 4-14 shows that the cost/torque of the 1.60-meter design is located between the cost/torque values predicted with our model for 90% and 95% efficiency.

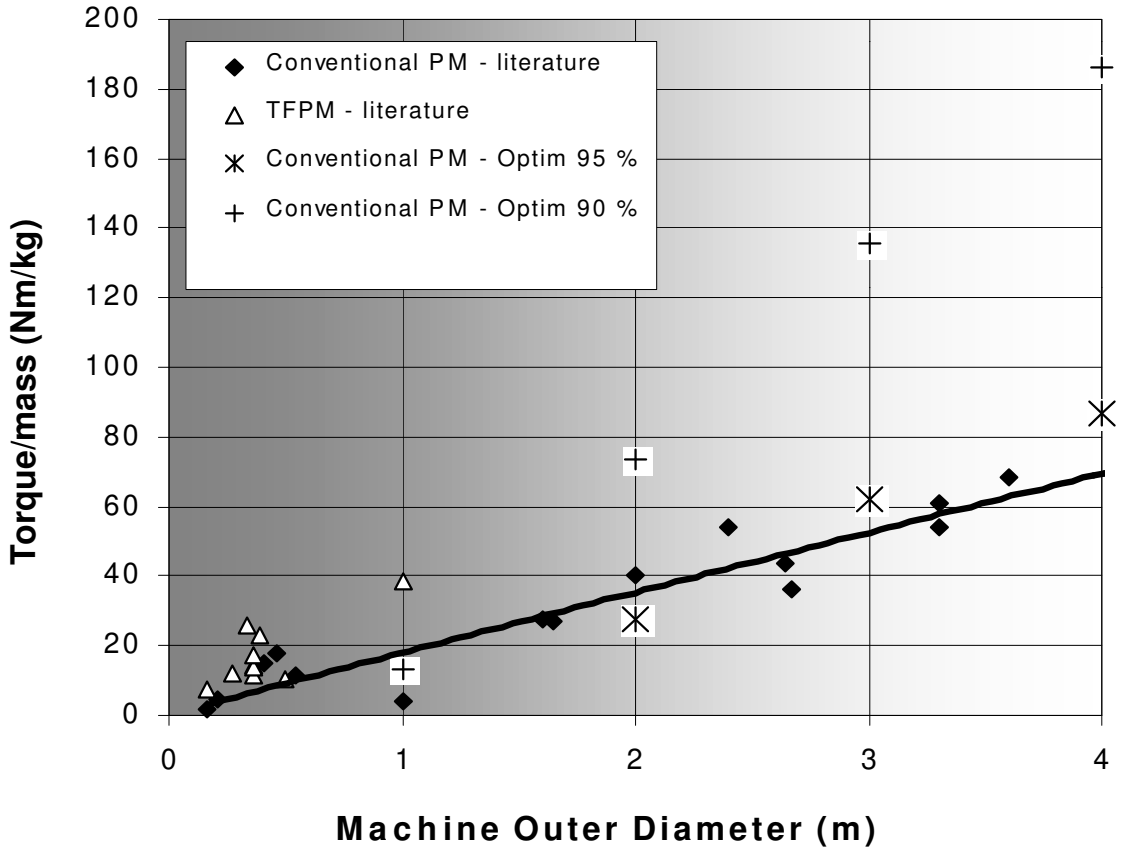

Figure 4-13: Torque/mass of conventional PM synchronous machine designs optimized at 90% and 95% efficiencies compared to designs of TFPM machines and conventional PM synchronous machines found in literature. Only mass of active material is considered. The solid line illustrates the average torque/mass of the conventional PM synchronous machines found in literature.

4.4. Conclusion

The comparison of the six machine topologies identified in chapter 2 has been discussed. Among the four longitudinal machines analyzed, the conventional PM synchronous machines with rare-earth surface magnets or with rare-earth flux concentration obtain the lowest cost/torque and the highest torque/mass. Concerning the TORUS and the conventional PM synchronous machine with flux concentration (ferrite magnets), this conclusion was confirmed by a literature survey of PM machine designs. For the other machine types (slotted axial-flux PM machine and conventional PM synchronous machine with or without flux concentration (Nd-Fe-B)), optimization programs were developed in this chapter which confirmed this conclusion.

In the work presented here, the comparison between the transverse-flux PM machines and the conventional PM synchronous machine seems to favor the transverse-flux PM machines, due to the higher current loading and force densities obtained in the latter machine types. A survey of the designs found in scientific literature also confirms that transverse-flux

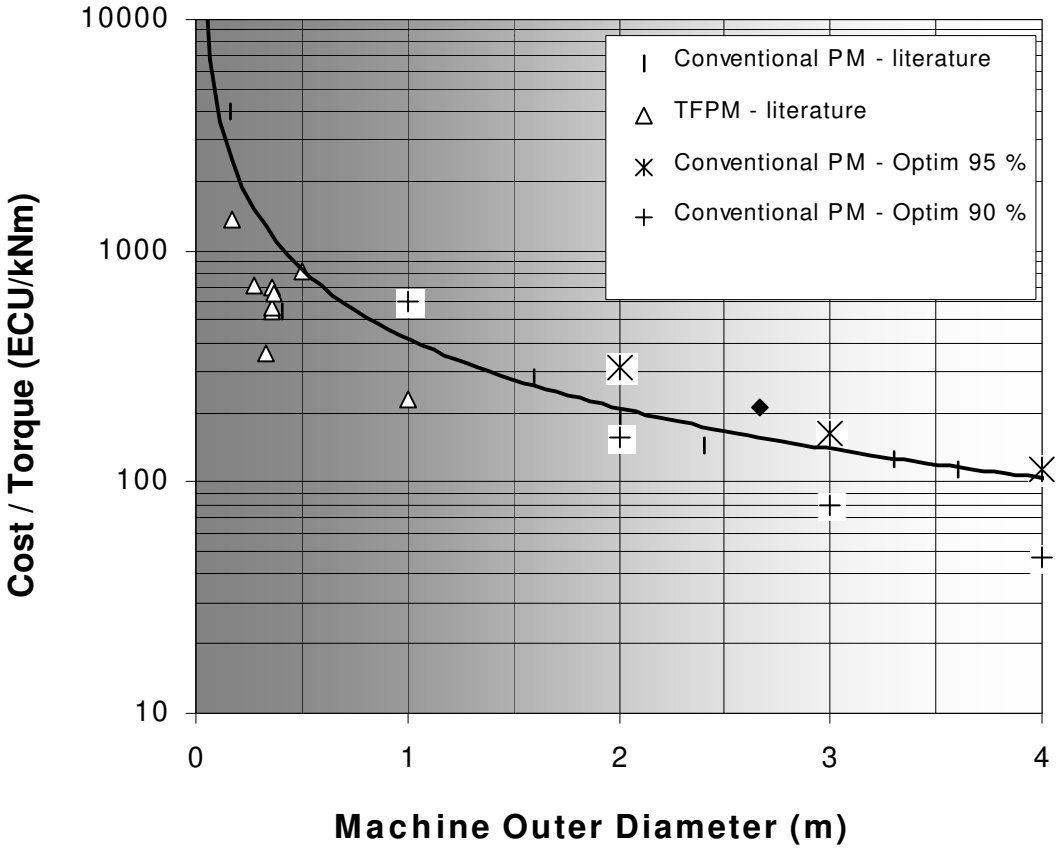

Figure 4-14: Cost/torque of conventional PM synchronous machine designs optimized at 90% and 95% efficiencies compared to designs of TFPM machines and conventional PM synchronous machines found in literature. Only cost of active material is considered. The solid line illustrates the average cost/torque of the conventional PM synchronous machines found in literature.

PM machines may bring higher torque/mass and lower cost/torque than the conventional PM synchronous machine. However, most of the literature references where TFPM designs are presented (and reported in appendix III) do not discuss the efficiency of those TFPM designs. From the study performed in this chapter, it clearly appears that efficiency plays a dominant role in the cost and mass savings obtainable for a given machine type. In the comparison of costs between TFPM machines and conventional PM synchronous machines, efficiency will be included in the analysis.

It was mentioned that TFPM machines often have lower power factor, as described in [Har 1998]. This will contribute to increase the costs of a TFPM generator with rectifier, due to the higher rating of the power electronics.

Chapter 5

Minimization of magnet material in PM machines

5.1. Introduction

The analysis of four machine topologies using longitudinal stator configurations has enabled us to keep the conventional PM synchronous machine as the most interesting among those longitudinal topologies. The transverse-flux PM machine has also been identified as a possible candidate for further decreasing the cost and mass of active material in direct-drive wind turbines. However, no final conclusion has been drawn until now in the thesis concerning the transverse-flux PM topologies and their performance in comparison with the conventional PM synchronous machine. This subject is discussed in the rest of this thesis.

Before investigating the TFPM machine topologies, we will introduce a method which allows reducing the volume of magnet material in PM machines. This method is based on the idea that every volume element inside a permanent magnet has a certain contribution to the flux created by that magnet. A mathematical expression is derived, which determines the contribution of each PM volume element to the total flux linking the stator coil. From this expression, we may leave out the magnet volume elements that provide a lower contribution and keep those with a high contribution. This will result in a better utilization of the magnet material and eventually lead to cost and mass reduction, which is the aim of this thesis.

The chapter is divided as follows. First a mathematical expression is derived, which expresses the no-load flux linkage in the coil of a stator winding in terms of the volume elements in the magnet. Secondly, a shaping method is developed and applied to a conventional PM synchronous machine and to a transverse-flux PM machine. Thirdly, the transverse-flux machines with surface-mounted magnets and flux-concentrating magnets are compared in terms of the contribution of their magnets to the no-load flux linkage.

5.2. PM local contribution to flux linkage

The step towards light and efficient electrical machines has been pushed by the use of PM materials with a high remanent flux density. In synchronous machines, bulky rotor windings can nowadays be successfully replaced by rare earth PM material. Although smaller in size than conventional rotor electromagnets, PMs have a much higher specific cost (in Euro/kg) than laminated steel and copper. In many cases, the cost of PM material is a significant part of the total machine costs.

Is it possible that some part of the PM volume bring a high contribution to the no-load voltage, while other parts would bring a lower contribution? In this section, the aim is to identify which parts of the PM volume have a high contribution to the total magnetic flux linkage induced in the stator winding at no-load.

In order to obtain the local PM contribution to the total flux linkage, a mathematical expression is derived for the flux linkage generated by a PM. This expression integrates a function over the sole volume of all the PMs considered in the machine. Usually, the flux linking a coil is obtained by computing the flux density over the area bounded by the coil. In this chapter, the no-load flux linkage is obtained by calculating field values over the PM geometry, rather than the coil geometry. Using the resulting mathematical expression, we can attribute to each volume element *dv* inside the PM a local contribution to the no-load flux linkage.

5.2.1. Problem definition, general case and assumptions

In section 5.2.2, we will derive a mathematical expression for the flux linkage induced by the PMs through the area of a coil at no-load. The derivation is meant to be general and can be applied to various geometries of PM machines. A generalized PM machine is shown in figure 5-1, where the shapes of iron, PM and coil inside the machine boundaries are arbitrary.

In figure 5-1, all PM material in the machine is contained inside the volume V_{pm}. All steel is contained inside the volume V_{iron}, and the space remaining within the machine boundary is contained inside the volume V_{air}. Outside the machine boundary, the vector quantities $\vec{B}$, $\vec{H}$ created by the coil and by the PMs are negligible. Also, the PMs and coils possibly existing outside the machine boundary create a magnetic field that is negligible inside the machine boundary. In itself, we define the machine boundary as a region in space containing most of the magnetic flux coming from the machine coil and the machine PM, and inside of which the externally created magnetic fields have a negligible effect.

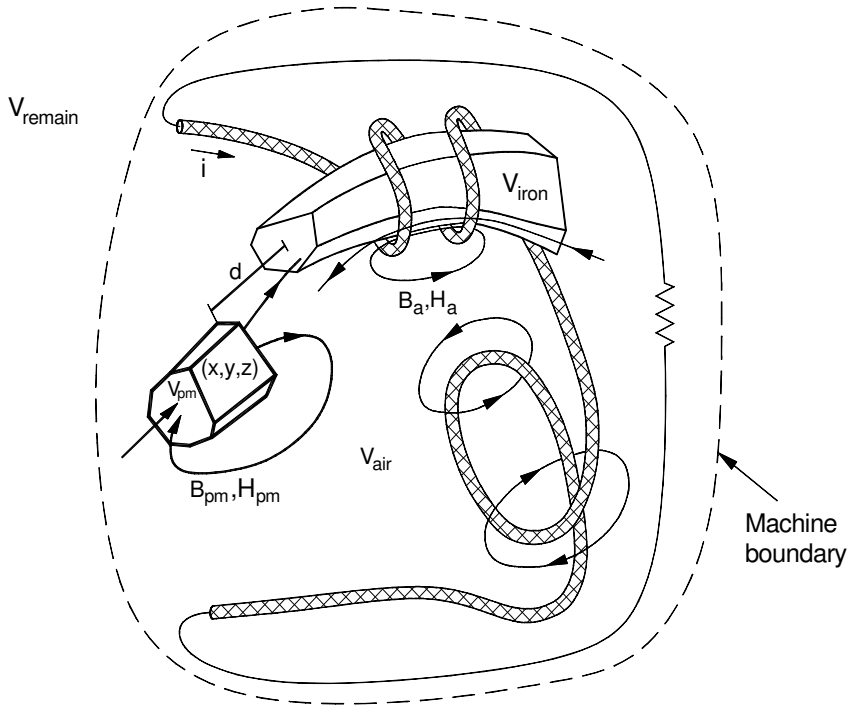

Figure 5-1: Generalized PM machine, with arbitrary iron, PM and coil shapes.

The first step in the elaboration of a shaping method for PM blocks is the derivation of an expression for the no-load flux linkage. Before going through the details of this mathematical derivation, a few assumptions must be defined.

• 1) Assumption of rigid magnetization for PMs

For the rest of this analysis, we will assume all PMs inside the machine boundary to have rigid magnetization, i.e. $\vec{B}(\vec{H})$ characteristics of the PM are defined by equation (5-1).

$$\vec{B} = \mu_{rec}\mu_0\vec{H} + \vec{B}_r \qquad (5\text{-}1)$$

In equation (5-1), $\vec{B}$ and $\vec{H}$ are respectively the flux density and magnetic field intensity inside the PMs. $\vec{B}_r$ is the PM remanent flux density and is assumed to have a constant magnitude. The relative recoil permeability μ_{rec} of these ideal magnets is assumed to be 1. These two assumptions are not serious limitations to the derivation exposed further, if PM material like Nd-Fe-B is used. "Real-life" Nd-Fe-B magnets have typical values of their recoil relative permeability in the area of 1.0 to 1.1 and have a $\vec{B}(\vec{H})$ characteristic which is approximately linear from $B = B_r$, down to $B = 0$ T.

As mentioned in the last paragraph, $\vec{B}_r$ is assumed to be independent of $\vec{H}$. It means that for any local point inside the PMs, we assume the remanent flux density $\vec{B}_r$ to have a

constant magnitude, no matter the intensity of the magnetic field $\vec{H}$ at this location. However, we leave the possibility of varying the orientation of $\vec{B}_r$ for different locations inside the PM, which will be useful in the analysis.

- ***2) Assumption of perfect ferromagnetic material for steel***

It is assumed that all iron parts are perfect: they have infinite permeability and are non-saturable. Standard "real-life" cold-rolled silicon-steel materials have a relative magnetic permeability many orders of magnitude higher than unity below their saturation point. As a consequence, the assumption of perfect iron will not harm the derivation shown below, as long as saturation does not occur in the steel parts. The validity of the proposed method would need to be carefully analyzed in those cases where saturation occurs. This is not done here.

- ***3) Assumption of constant magnetic vector potential A throughout the conductors cross-section***

The magnetic vector potential $\vec{A}$ is assumed to have constant magnitude and direction throughout any given cross-section of a conductor. This is the theoretical case of filamentary conductors, which have currents flowing through an infinitely small cross-section.

In practice, the variation of the magnetic vector potential $\vec{A}$ is very small when the conductors are wound around a ferromagnetic core, as in most electrical machines. In the latter case, most of the magnetic flux flows inside the iron, and the variation of $\vec{A}$ through the conductor cross-section may be considered as negligible compared to the absolute value of $\vec{A}$ on that conductor. However, there are cases, like in the rotor bars of large induction machines, where the conductors cross-section is large and the assumption of filamentary conductors cannot be used.

For conductors in empty space (or air), the variation of $\vec{A}$ through the conductor cross-section may be considered as negligible if the conductor cross-section is made sufficiently small.

5.2.2. Mathematical derivation

In the system of figure 5-1, we consider a coil made of several turns, where a current i is allowed to flow. We write the product $i\lambda$ "seen" by that coil.

$$i\lambda = \left[\iint_{S_{con}} \vec{j} \cdot d\vec{s}_{con}\right]\left[\iint_{S_{coil}} \vec{B} \cdot d\vec{s}_{coil}\right] \qquad (5\text{-}2)$$

where λ and $\vec{B}$ are the flux linkage and flux density linking the coil, including the flux created by the PM and the flux created by current i.

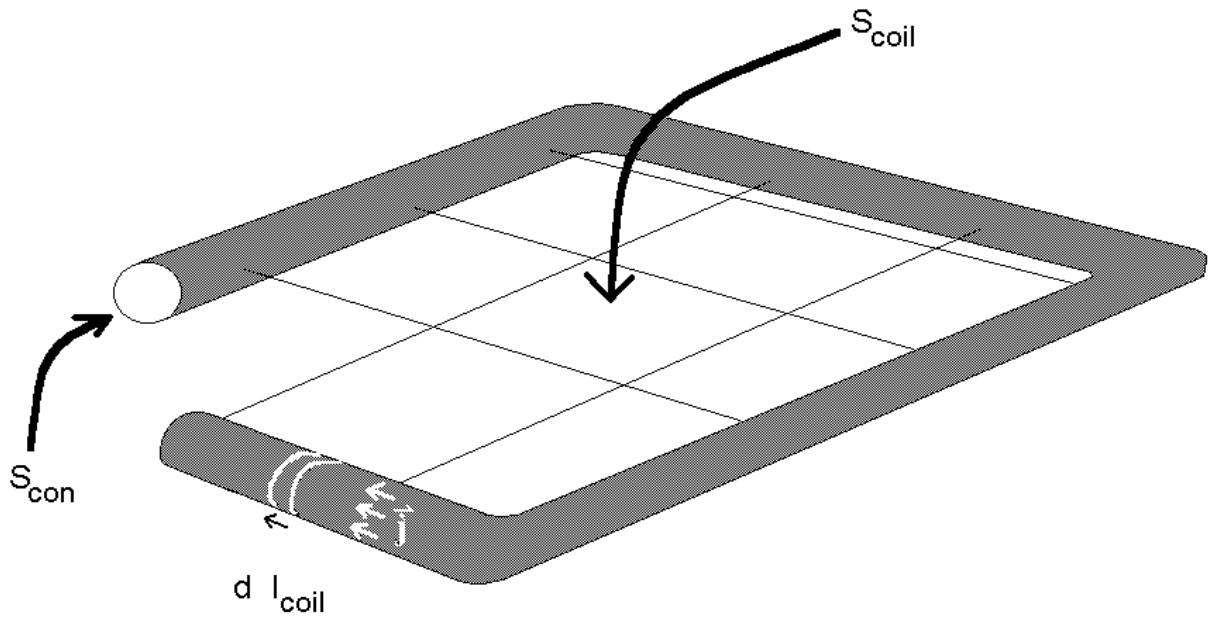

Figure 5-2: S_{coil} and S_{con} for one turn of the coil.

$\vec{j}$ is the current density vector inside the conductor, S_{coil} is a surface bounded by the complete coil and S_{con} is the cross-section of the conductor, as shown in figure 5-2. As discussed in [Maw 1957] and as shown in appendix II, $i\lambda$ is the sum of the magnetic energy and magnetic coenergy "seen" by the coil. It may look like an unusual starting point, but it will appear to be useful later in this derivation.

In appendix II, we show that the product $i\lambda$ may be written as:

$$i\lambda = \iiint_{V_{universe}} (\vec{B} \cdot \vec{H}) dv \qquad (5\text{-}3)$$

only if the variation of $\vec{A}$ throughout the conductor cross-section is negligible (assumption 3). If this assumption is met, then the coil is considered as “filamentary” and the flux linkage λ flowing through the area bounded by the coil conductor will be independent from the boundary chosen. For example, if the flux linkage λ is the same when the boundary used for the calculation of the flux linkage is the outer or the inner coil limits, the variation of $\vec{A}$ is negligible through the conductor cross-section. In any case, it becomes very difficult to define the flux of this coil if assumption 3) is not met.

The three variables λ, $\vec{H}$ and $\vec{B}$ of equation (5-3) are created by the current in the coil and by the PMs. Assumptions 1) and 2), where the PM and the iron are linear materials, allow us to subdivide λ, $\vec{H}$ and $\vec{B}$ into λ_a, $\vec{H}_a$, $\vec{B}_a$ (component created by the current flowing in the coil) and λ_{PM}, $\vec{H}_{PM}$ and $\vec{B}_{PM}$ (component created by the PM alone). The components $\vec{H}_a$, $\vec{B}_a$, $\vec{H}_{PM}$ and $\vec{B}_{PM}$ are shown in figure 5-1. We rewrite equation (5-3):

$$i\lambda = \iiint_{V_{universe}} (\vec{B}_a + \vec{B}_{PM}) \cdot (\vec{H}_a + \vec{H}_{PM}) dv \tag{5-4}$$

From Maxwell's equations, we have:

$$\nabla \cdot \vec{B}_{PM} = 0 \tag{5-5}$$

$$\nabla \cdot \vec{B}_a = 0 \tag{5-6}$$

$$\nabla \times \vec{H}_{PM} = 0 \tag{5-7}$$

As demonstrated in [Bro 1962], the integral taken over the entire universe of the dot product of two vectors is zero, if the curl of the first vector is zero and the divergence of the second vector is also zero. Whence,

$$i\lambda = \iiint_{V_{universe}} (\vec{B}_a + \vec{B}_{PM}) \cdot \vec{H}_a dv \tag{5-8}$$

Let us focus on the flux linkage λ_{PM} created by the PM in the coil. To obtain λ_{PM}, we use equation (5-8) from which is substracted $i\lambda_a$. This is easily obtained from equation (5-4), by considering the case where the only fields and flux linkage found within the machine boundary are created by the current flowing in the coil. We express $i\lambda_a$ as:

$$i\lambda_a = \iiint_{V_{universe}} \vec{B}_a \cdot \vec{H}_a dv \tag{5-9}$$

Inserting equation (5-9) into equation (5-8), we obtain:

$$i\lambda_{PM} = \iiint_{V_{universe}} \vec{B}_{PM} \cdot \vec{H}_a dv \tag{5-10}$$

This result is also obtained in [Bro 1962]. In equation (5-10), the domain of integration is still the entire universe. It is possible to simplify this expression further, if we divide the total universe into four sub-domains, which are shown in figure 5-1:

- volume V_{PM} of the PMs in the machine;
- volume V_{iron} of iron in the machine;

- volume of air V_{air} inside the machine. It must be noted that V_{air} contains not only air, but all material for which permeability is close to unity (like coils, insulators, empty space, etc.);
- volume of all universe V_{remain} outside the machine boundary.

Subdomain V_{PM}

Inside the PM, the constitutive relation is given by equation (5-1). μ_{rec} is equal to unity, as indicated by assumption 1). We rewrite equation (5-10) for the PM volume:

$$\iiint_{V_{PM}} \vec{B}_{PM} \cdot \vec{H}_a dv = \iiint_{V_{PM}} \mu_0 \vec{H}_{PM} \cdot \vec{H}_a dv + \iiint_{V_{PM}} \vec{B}_r \cdot \vec{H}_a dv \qquad (5\text{-}11)$$

$\vec{H}_a$ is the field obtained when B_r is zero. In the latter case, we consider the magnets as replaced by vacuum since the recoil permeability of PMs is the same as empty space. Therefore, we rewrite equation (5-11):

$$\iiint_{V_{PM}} \vec{B}_{PM} \cdot \vec{H}_a dv = \iiint_{V_{PM}} \vec{H}_{PM} \cdot \vec{B}_a dv + \iiint_{V_{PM}} \vec{B}_r \cdot \vec{H}_a dv \qquad (5\text{-}12)$$

Subdomain V_{iron}

Inside the iron, the magnetic fields $\vec{H}_a$ and $\vec{H}_{PM}$ are zero, because of assumption 2). We can write:

$$\iiint_{V_{iron}} \vec{B}_{PM} \cdot \vec{H}_a dv = \iiint_{V_{iron}} \vec{B}_a \cdot \vec{H}_{PM} dv = 0 \qquad (5\text{-}13)$$

Subdomain V_{air}

The subdomain of air also shows a reciprocity relation between $\vec{H}_a$, $\vec{B}_{PM}$ and $\vec{B}_a$, $\vec{H}_{PM}$. We can write:

$$\iiint_{V_{air}} \vec{B}_{PM} \cdot \vec{H}_a dv = \iiint_{V_{air}} \mu_0 \vec{H}_{PM} \cdot \vec{H}_a dv = \iiint_{V_{air}} \vec{B}_a \cdot \vec{H}_{PM} dv \qquad (5\text{-}14)$$

Subdomain V_{remain}

As defined previously, the vector quantities $\vec{H}_a$, $\vec{B}_{PM}$, $\vec{B}_a$, $\vec{H}_{PM}$ are zero outside the machine boundary. We can write:

$$\iiint_{V_{remain}} \vec{B}_{PM} \cdot \vec{H}_a dv = \iiint_{V_{remain}} \vec{H}_{PM} \cdot \vec{B}_a dv = 0 \tag{5-15}$$

Summing the four subdomains, we obtain the entire universe. We insert equation (5-12), equation (5-13), equation (5-14) and equation (5-15) into equation (5-10), and write:

$$i\lambda_{PM} = \iiint_{V_{universe}} \vec{H}_{PM} \cdot \vec{B}_a dv + \iiint_{V_{PM}} \vec{B}_r \cdot \vec{H}_a dv \tag{5-16}$$

Again, the integral taken over the entire universe of the dot product of two vectors is zero, if the curl of the first vector is zero and the divergence of the second vector is also zero. Hence, the first term on the right-hand side of equation (5-16) is equal to zero. We obtain:

$$i\lambda_{PM} = \iiint_{V_{PM}} \vec{B}_r \cdot \vec{H}_a dv \tag{5-17}$$

From equation (5-17), we obtain an expression for λ_{PM}:

$$\lambda_{PM} = \iiint_{V_{PM}} \left[\frac{\vec{H}_a}{i}\right] \cdot \vec{B}_r dv \tag{5-18}$$

Equation (5-18) expresses the flux linkage created by the PM through a coil in terms of a function which is integrated over the sole volume of the PMs interacting with the coil. It gives every volume element *dv* inside the PMs a contribution to the magnetic flux linking the coil under no-load condition.

In a PM machine, one may inject a current *i* in the coil and compute $\vec{H}_a$ in the volume of the PM. Integrating the dot product of $\vec{H}_a$ with $\vec{B}_r$ over the PM volume gives the no-load flux linking the coil into which the current was injected. This method is valid for any rotor position.

There is a reciprocity relationship between equation (5-18) and the conventional definition of no-load flux linkage given by equation (5-19).

$$\lambda_{PM} = \iint_{S_{coil}} \vec{B}_{PM} \cdot d\vec{s}_{coil} \tag{5-19}$$

In equation (5-19), the flux linkage at no-load is defined as a magnetic quantity created by the PM ($\vec{B}_{PM}$) acting on the geometry of the coil (S_{coil}), while in equation (5-18), λ_{PM} is expressed as a magnetic quantity created by the coil ($\vec{H}_a$) and acting on the geometry of the PM (V_{PM}).

5.3. Shaping of PM for cost reduction

It is possible to use equation (5-18) not only to identify the contribution of each volume element inside V_{PM}, but also to select the areas inside the PM which have the highest contribution and leave out the areas with the lowest contribution. Doing so, the PMs are shaped in order to increase the total flux linkage created through the stator coil at no-load, per cubic millimeter of PM material.

5.3.1. Selection of useful material in PM

The shaping method may either use finite element analysis (FEA) or analytical calculation in the following manner:

- consider the rotor position for which the PM faces the stator pole completely;
- replace all PM by vacuum in the FEA model, or in the analytical calculation;
- inject a current $i = I$ in the coil through which we want to calculate the flux linkage;
- calculate the field $\vec{H}_a$ inside the volume that would be filled by PMs;
- do the dot product of $\vec{H}_a$ with $\vec{B}_r$ inside all the PM volume in the machine. This will give out the contribution of each volume element inside the PM;
- remove the volume elements with the lowest values of $\vec{H}_a \cdot \vec{B}_r$.

The method is applied to various configurations in the next two subsections.

5.3.2. Example of PM shaping in a conventional PM synchronous machine

In this section, the proposed method is used to optimize the shape of PM in the conventional PM synchronous machine of figure 5-3.

It must be noted that the shaping method discussed here gives the possibility of increasing the ratio flux linkage/magnet volume, but it does not say anything about the waveform. It may be the case that the optimal magnet shape obtained with this method becomes an uninteresting choice due to the harmonics it creates in the stator core. The effect of PM shapes on voltage harmonics has been discussed in [DeL 1991], [DeL 1992], which address a finite number of discrete PM shapes and discuss the frequency spectrum obtained at no-load for each shape. It would be interesting to consider the possibility that each volume element of a PM contributes to modifying the frequency spectrum at no-load. Such analysis would add greatly to the theory exposed here. This is left for further studies.

In figure 5-3, a linear version of the conventional PM synchronous machine is shown where the distance between two adjacent PMs is zero. However, it is common practice to keep a certain distance between two adjacent PMs, where it is expected that an important leakage flux is found near the boundary between two magnets. In such an area, the flux created by the PMs does not contribute significantly to the magnetic flux in the stator coil.

Machine designers consider the frontier area of two PMs as less useful PM material and therefore remove PM material in that region. The magnets usually have a rectangular shape with a distance between adjacent magnets equal to 0.1 to 0.3 times the pole pitch. In this section, we give ourselves more freedom in the types of PM shapes. Non-rectangular shapes are also considered.

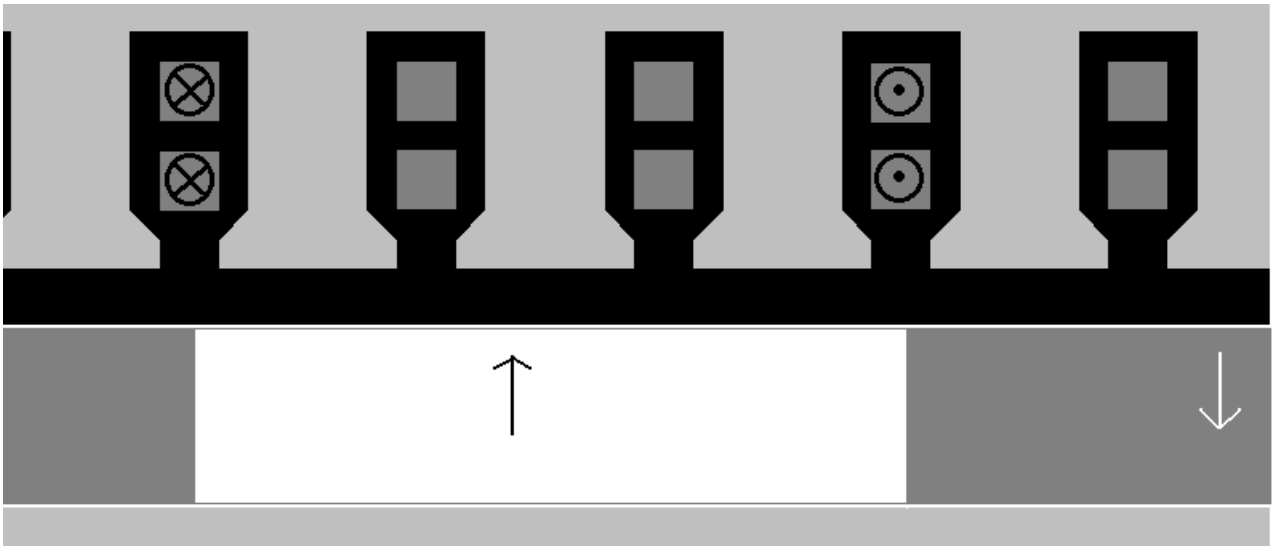

Figure 5-3: Stator and rotor of a three-phase linear conventional PM synchronous machine. Only phase A is fed as shown here.

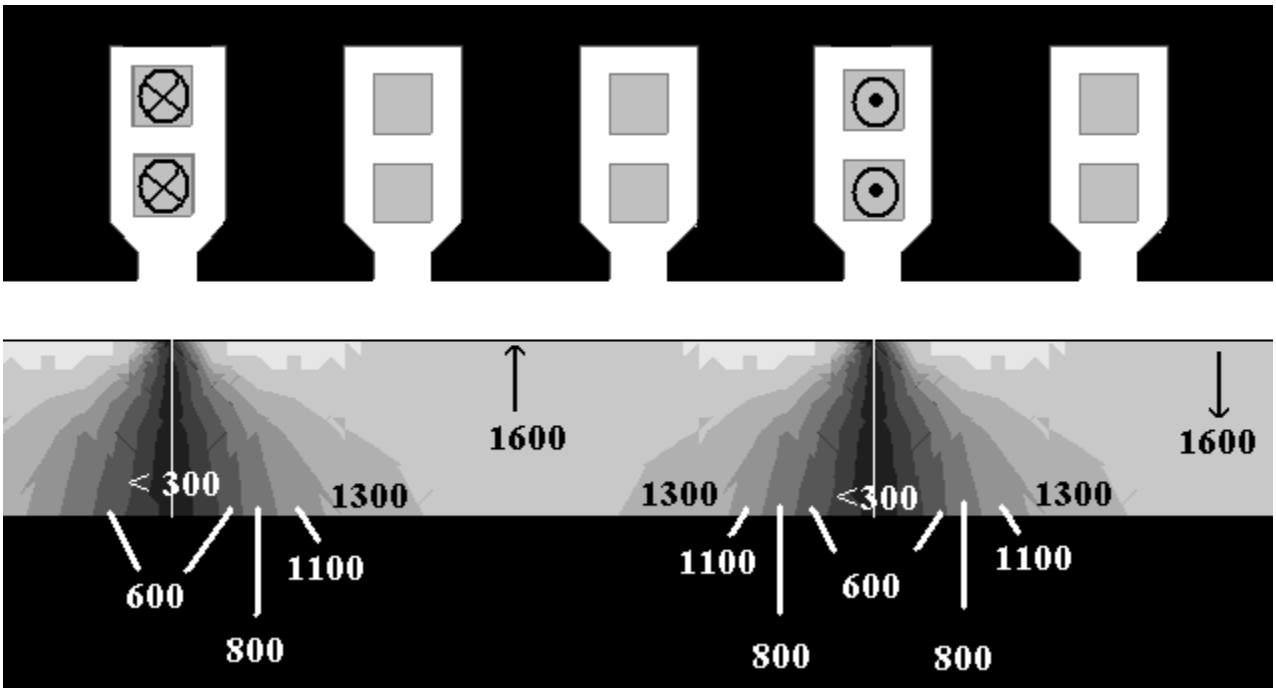

Figure 5-4: Dot product of $\vec{H}_a \cdot \vec{B}_r$ (in J/m^3) computed with finite element analysis (FEA). $\vec{B}_r$ is constant and homogeneous throughout the volume of each PM. Coil current i = 10 A.

In the proposed method, all PMs of figure 5-3 are replaced by vacuum. A current i = 10 A is injected in the coil. The dot product of $\vec{H}_a$ and $\vec{B}_r$ is computed inside the volume of the PMs by using a 2-D FEA software. The distribution of $\vec{H}_a \cdot \vec{B}_r$ is shown inside the PM in figure 5-4, which represents the contribution of each PM volume element dv to the no-load flux linkage λ_{PM} in the coil.

The linear machine has the following dimensions: air gap thickness = 2 mm, pole pitch = 2.4 cm, magnet thickness = 6 mm. The magnets are made of Nd-Fe-B and have a remanent flux density of 1.23 T and a recoil permeability equal to μ_0. It must be noted that in this example, the current is injected in all the coils of one phase. The other two phases are not excited. As a result, the magnetic field $\vec{H}_a$ is symetrically spread throughout all the PMs in the machine and the volume integration may take place on the PM of only one pole.

As expected, the region of figure 5-4 on the boundary between two PMs has the lowest contribution to the no-load flux linkage in that position. If PM elements are to be removed from the PM volume, they should indeed be taken from that region near the frontier between neighbour magnets. However, figure 5-4 suggests that PMs should not be cut in rectangles, as is usually done, but rather with a V-shape. The PM could be shaped as shown on figure 5-5. In figure 5-5, the section of PM material with the new V-shape has an area of 120 mm^2 per magnet, compared to 144 mm^2 per magnet for the initial block shape of figure 5-3. The no-load flux linkage for the new V-shape in the rotor position shown in figure 5-5 is 16.5 mWb/m, compared to 17.5 mWb/m with the initial block shape. The decrease in PM volume is 17 % and the decrease in flux linkage only 6 %. The amount of Wb/m^3 generated by the PM at no-load has increased by 13 % with the new V-shape. Table 5-1 shows the no-load flux linkage for the two PM shapes.

Equation (5-18) gives each volume element inside the PM a contribution to the no-load flux linkage. However, if equation (5-18) is used to calculate the contribution of each PM volume element to the no-load voltage e, the time-dependence must be carefully analyzed. From Faraday's law, we know that the no-load voltage is time-dependent and in fact results from the motion of all these PM volume elements. Equation (5-18) is written as a time-independent expression, which is not satisfactory when it comes to the calculation of e. In [Dub 2003a], it is shown that the contribution of each PM volume element to the no-load voltage is time-dependent, and that this contribution is constantly changing inside the volume of the PM while the rotor is moving. At some location inside the PM, the contribution to the no-load voltage changes from high to low upon the rotor translation, while at another location, it changes from low to high.

Since the shape of the PM cannot be modified during its motion, the knowledge of the instantaneous local contribution to e has little practical interest, because it is changing constantly with the motion of the rotor. As described in more detail in [Dub 2003a], it is more practical to obtain the local contributions of PM elements to the average no-load voltage $\overline{E}$, because the average no-load voltage is time-independent. Over one electrical period, the average no-load voltage is of course zero for a symmetrical machine. However, it is possible to define the average no-load voltage over one half-period.

Columns 3 in table 5-1 is computed using the method shown in section 5.3.1, with equation (5-18). Column 2 gives the no-load flux linkage obtained, by integrating $\vec{B}_{PM}$ over the coil area (conventional method expressed by equation (5-19)). The difference between

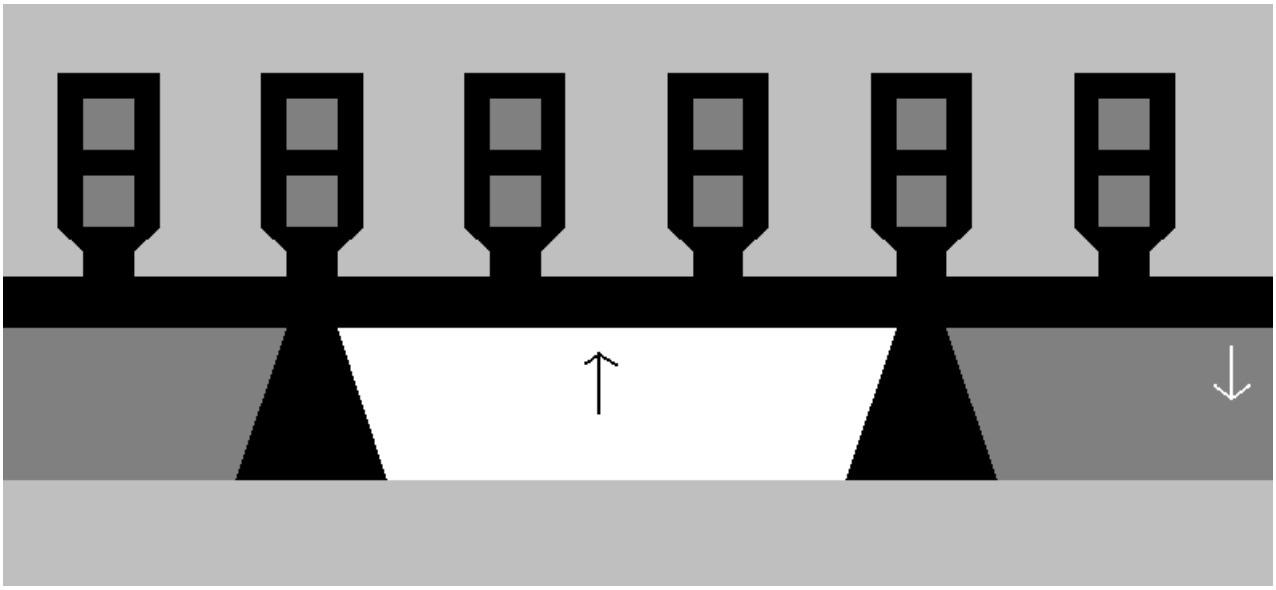

Figure 5-5: New PM shapes obtained with the method.

Table 5-1. FEA results for two different PM shapes.

PM Shape	λ_{PM} given by equation (5-19) (mWb/m)	λ_{PM} given by equation (5-18) (mWb/m)	λ_{PM}/V_{PM} (Wb/m^3)
Square (figure 5-3)	17.5	17.6	122
V-shape (figure 5-5)	16.5	16.6	138

the conventional way of computing the no-load flux linkage (column 2) and the method proposed here (column 3) is below 0.6% and can be explained by the limited accuracy of the FEA computations.

Another interesting variant of this method would consist in exciting two phases simultaneously with the same current in the case of a star-connected stator winding. In that case, we want to increase the ratio of no-load flux per magnet volume for a star connection. It may be the case that the optimal magnet shape obtained will be different from the one obtained here in a delta configuration. Also, a distributed winding with $q > 1$ will probably give a different magnet shape. This would also need to be investigated in more depth.

In conclusion, the method described here for the shaping of permanent magnets will allow some material saving in conventional PM synchronous machine in the transition between two neighbour magnets. However, a thin air-gap and a large pole pitch will result in very little possible improvement of the amount of Wb/mm^3. This is due to the presence of a largely 1-D magnetic field, which according to equation (5-18) will give a homogenous contribution for the PM volume elements. However, a thick air-gap and a short pole pitch will see a large part of the magnetic field created by the stator winding fringing the PM border.

In such cases, the shape optimization process described here may bring good PM material savings. In chapter 4, section 4.3.2, designs of conventional PM synchronous machines with 90% and 95% efficiency were presented. For 95 % efficiencies, pole pitches of about 6 cm were used, which reduce the gains obtainable by V-shape magnets. However, designs with 90 % efficiency had pole pitches around 3 cm. On the other hand, the example shown previously indicates that the benefit in PM material saving will be around 10%, which will not improve so much the total mass and cost of the machine.

5.3.3. Example of PM shaping in a TFPM machine

We have indicated that the shaping method developed in this chapter will be mainly beneficial in the case of PM machines with short pole pitches and containing large amounts of fringing fields. This is especially the case in surface-mounted transverse-flux PM machines. For this study, a pole pitch of 1 cm is used, which is also the value used in [Har 1996].

A current i = 10 A is injected in the stator coil of the machine and three cases of PM configurations are investigated:

- PMs with no clearance between them;
- PMs with a clearance of 0.2 times the pole pitch between them;
- PMs with areas of lower $\vec{H}_a \cdot \vec{B}_r$ removed.

The 3 PM shapes with the corresponding plots of $\vec{H}_a \cdot \vec{B}_r$ are shown in figure 5-6, figure 5-7 and figure 5-8. It must be noted that a same magnet height is used for the 3 shapes

.

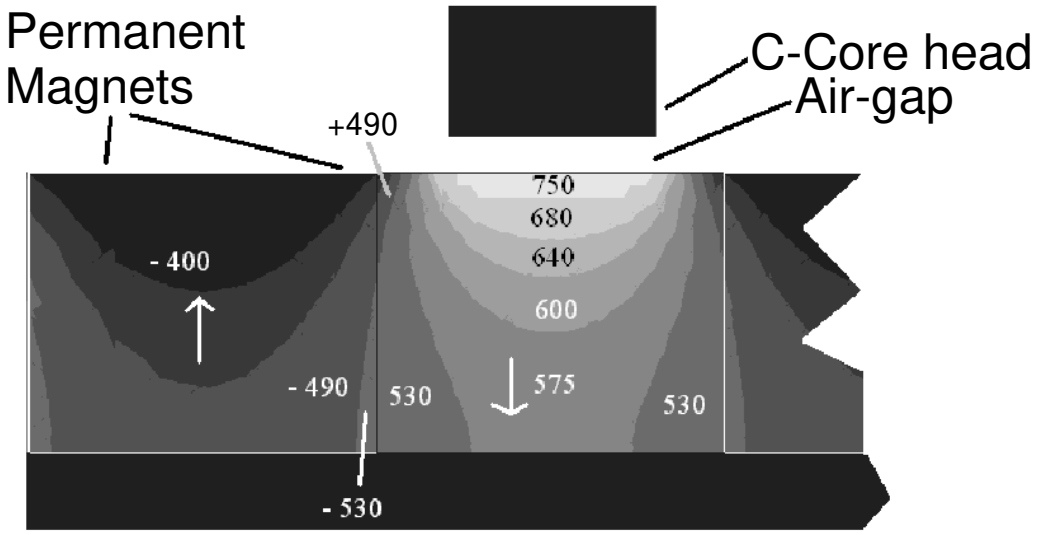

Figure 5-6: Dot product of $\vec{H}_a$ and $\vec{B}_r$ inside the cross-section of adjacent block Nd-Fe-B magnets of a surface-mounted TFPM machine. Current injected in the stator is i = 10 A. Number of turns n = 1; width of PM = 10 mm; distance between PM = 0 mm; height of PM = 8 mm; total area of PM per magnet = 80 mm^2; B_r = 1.23 T.

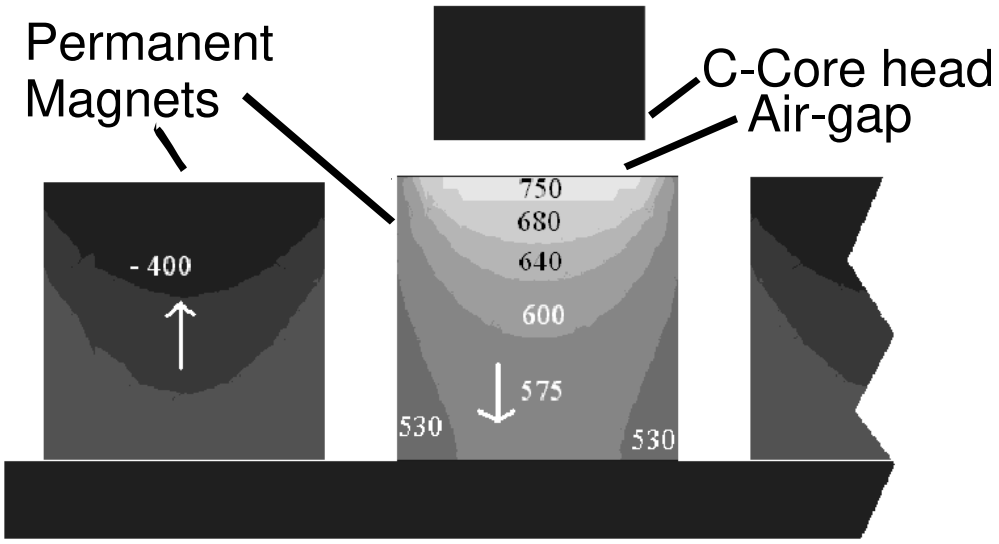

Figure 5-7: Dot product of $\vec{H}_a$ and $\vec{B}_r$ inside the volume of rectangular Nd-Fe-B magnets. Current injected in the stator is i = 10 A. Number of turns n = 1; width of PM = 8 mm; distance between PM = 2 mm; height of PM = 8 mm; total area of PM per magnet = 64 mm^2; B_r = 1.23 T.

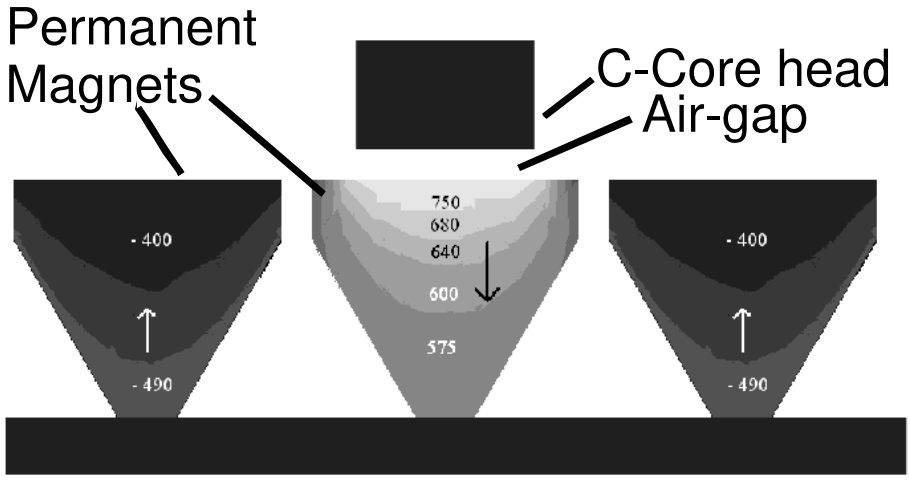

Figure 5-8: Dot product of $\vec{H}_a$ and $\vec{B}_r$ inside the volume of the PM of V-shape Nd-Fe-B magnets. Current injected in the stator is i = 10 A. Number of turns n = 1; distance between PM in the top part= 1 mm; width of PM in the bottom part = 2 mm; distance between PM in the bottom part = 8 mm; total Height of PM = 8 mm; height of the top (rectangular) part of the PM = 2 mm; total area of PM per magnet = 51 mm^2; B_r = 1.23 T.

It must be remarked that further optimization of magnet material utilization could be achieved if the magnet height was allowed to vary, which is not done here. The no-load flux linkage λ_{PM} and the PM area are computed for the 3 shapes and displayed in table 5-2. The ratio of λ_{PM} over PM volume gives the highest value for the V-shape PM. The V-shape is 37 % more volume effective than the square magnets with no clearance and 14 % more volume effective than the rectangular magnets with clearance.

Table 5-2. FEA results for three different PM shapes.

PM Shape	λ_{PM} (mWb/m)	PM surface (mm^2)	λ_{PM}/V_{PM} (Wb/m^3)
Square 100 % (figure 5-6)	1.98	80	24.8
Rectangular 80 % (figure 5-7)	1.90	64	29.7
V-shape (figure 5-8)	1.73	51	33.9

This example shows how the shaping method can be applied to surface-mounted machines with short pole pitches to minimize their PM material. As stated in the last section, the method is especially useful for the case of short pole pitches.

The two examples of PM shaping presented in this section and in the last section are no more than what is presented herein: examples. The improvements obtained in these two cases should not be considered as absolute gain for a given machine type. In fact, the benefits obtainable from the method will depend on many geometrical parameters like air gap thickness, magnet width and pole pitch. Nevertheless, these two examples were useful in showing the possibilities and the application of the method developed in this chapter.

5.3.4. Variation of $\vec{B}_r$ orientation

The shaping method described above can be enhanced with an additional step. This additional step uses the theoretical result given by equation (5-18) to further increasing the ratio of flux linkage over PM volume by varying the orientation of $\vec{B}_r$ inside the PM, as described in [Dub 2003b]. Equation (5-18) describes the flux linking the stator coil at no-load as the integral of a dot product of $\vec{H}_a$ and $\vec{B}_r$. In machines with large pole pitches, the field $\vec{H}_a$ is aligned with $\vec{B}_r$. However, in machines with short pole pitches, like TFPM machines, a large part of the field lines of $\vec{H}_a$ are not aligned with $\vec{B}_r$. As a consequence, the cosine of the angle between $\vec{H}_a$ and $\vec{B}_r$ gives a value below 1. This has an impact on dot product of $\vec{H}_a$ and $\vec{B}_r$.

The method can be enhanced with the inclusion of a plot of δ, as given by:

$$\delta = \frac{\vec{H}_a \cdot \vec{B}_r}{\left|\vec{H}_a\right|\left|\vec{B}_r\right|} \tag{5-20}$$

where δ is the cosine of the angle between $\vec{H}_a$ and $\vec{B}_r$ at any given point inside the PM. For example, when $\vec{H}_a$ and $\vec{B}_r$ are aligned in the same direction, δ = 1; and when the angle between $\vec{H}_a$ and $\vec{B}_r$ is 45 degrees, δ = 0.707. A plot of δ inside the volume of the PM is illustrated in figure 5-9, after injection of a current i = 10 A.

Figure 5-9 indicates values for δ varying between 0.88 and 1 in the PM facing the C-core head and values varying between -0.88 and -1 for the magnet on the left-hand side. A

value of $\delta = 0.9$ corresponds to an angle of 26 degrees between $\vec{H}_a$ and $\vec{B}_r$. With the information presented in figure 5-9, it is possible to select areas inside the PM, where a rotation of $\vec{B}_r$ will increase the product of $\vec{H}_a \cdot \vec{B}_r$. The area where $\delta = 1$ is not of interest, because δ already has the highest value. However, the upper corners are subject to a potential increase, if the angle of $\vec{B}_r$ is modified. This will increase the value of $\vec{H}_a \cdot \vec{B}_r$ in those areas and the contribution of those PM volume elements to the total flux linkage will also be increased.

Figure 5-10 illustrates a zoom in the upper corners of two adjacent magnet blocks before modification. The vectors $\vec{H}_a$ and $\vec{B}_r$ are shown inside those two corners. The contribution of the right corner is almost cancelled by the negative contribution of the left corner. In figure 5-11, the orientations of $\vec{B}_r$ inside the two corners have been modified so as to align $\vec{H}_a$ and $\vec{B}_r$ inside the corner of the PM facing the C-core.

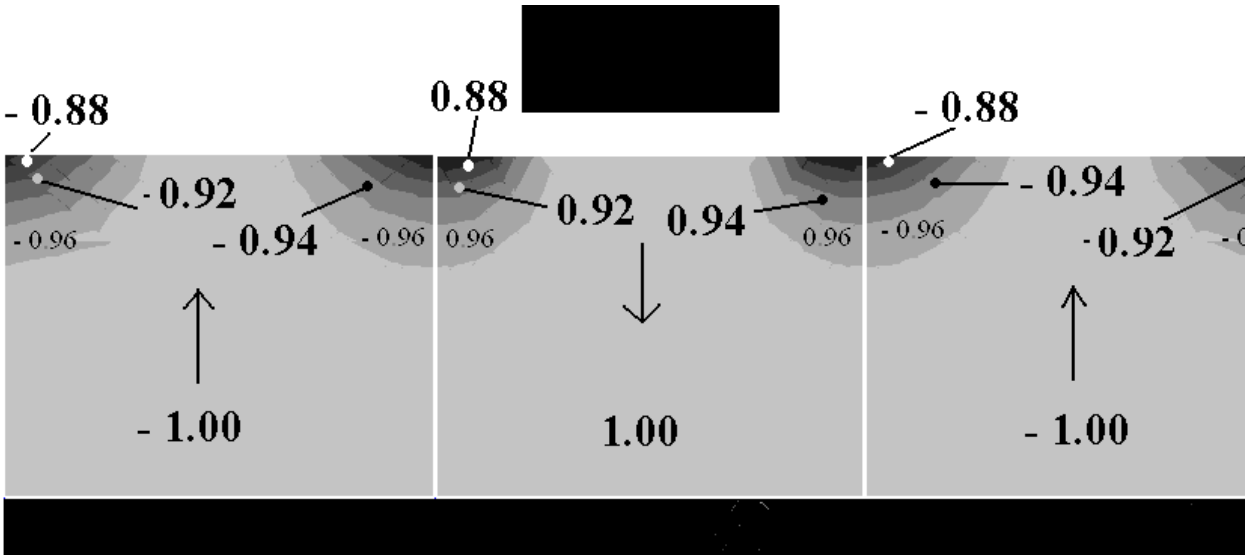

Figure 5-9: Distribution ofδ inside the PM Volume. $\vec{B}_r$ has uniform orientation.

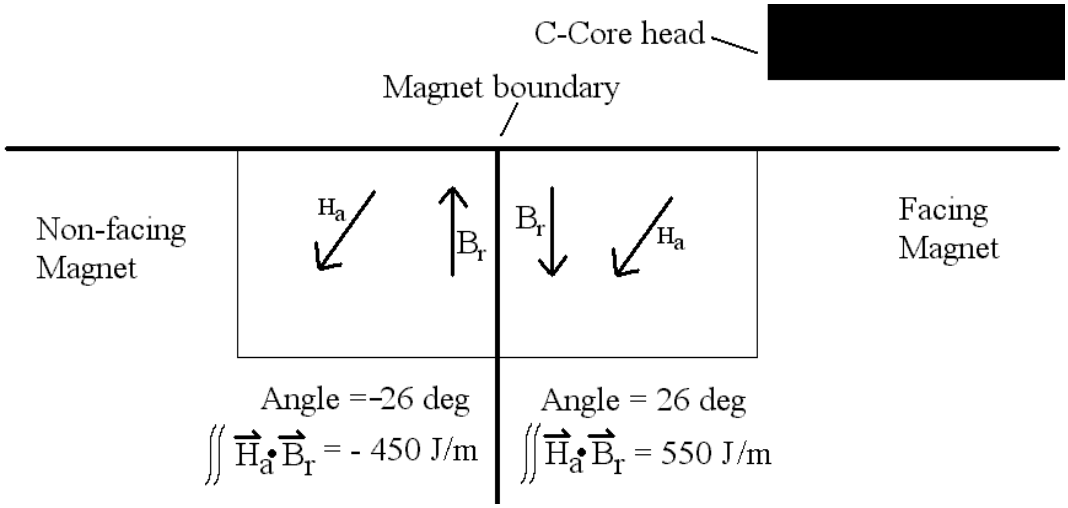

Figure 5-10: Orientation of $\vec{B}_r$ before modification. The sum of the contributions of the two corners is 100 J/m.

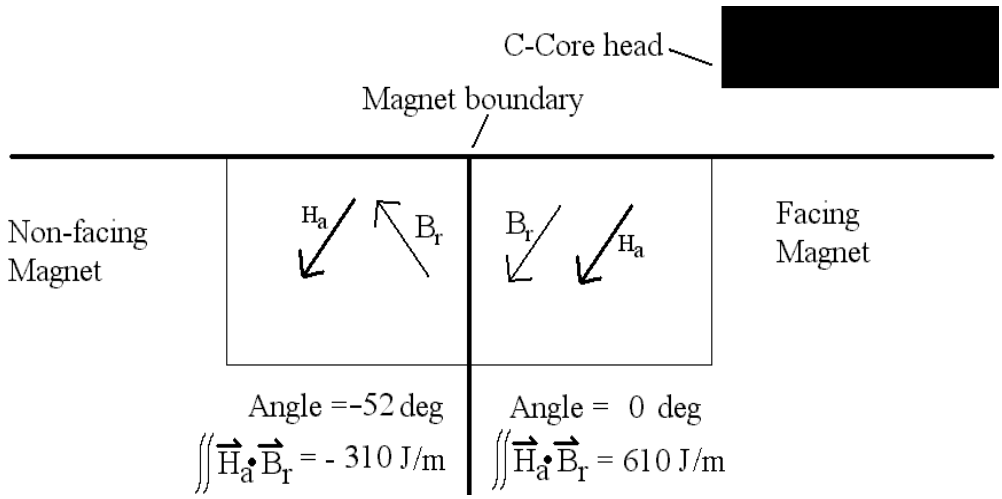

Figure 5-11: Orientation of $\vec{B}_r$ after modification. $\vec{B}_r$ is aligned with $\vec{H}_a$ in the right corner. In the left corner, the angle between $\vec{H}_a$ and $\vec{B}_r$ is increased. The total sum of $\vec{H}_a \cdot \vec{B}_r$ in that area is now 300 J/m.

By symmetry, the orientation of $\vec{B}_r$ was also modified in the corner of the PM not facing the C-core. As shown in figure 5-11, the angle between $\vec{H}_a$ and $\vec{B}_r$ has increased further on the left-hand side, reducing the negative contribution of the left corner. The change in $\vec{B}_r$ orientation brings a double improvement to the no-load flux linkage by increasing the positive contribution and reducing the negative contribution.

Figure 5-12 illustrates the proposed magnet shape and new orientation of $\vec{B}_r$ inside the magnet. Each corner of the magnets now makes an angle of 26 degrees with the main axis.

The new configuration with small magnets in the corners creates a flux linkage of 1.95 mWb/m per C-Core. The PM area per magnet is 52.5 mm^2. The ratio of no-load flux linkage over PM Volume has now increased to 37.1 Wb/m^3. This is an increase of 9% compared to

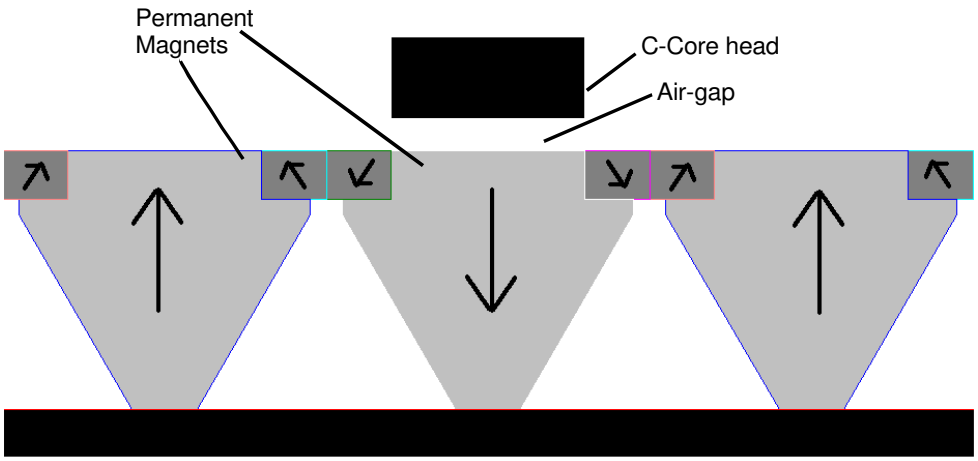

Figure 5-12: New magnet arrangement proposed to increase the flux linkage per PM volume. Small magnets are inserted in the corners of the main magnets. The angle between the $\vec{B}_r$ of each small magnet and the $\vec{B}_r$ of the main magnet is 26 degrees.

the V shape of figure 5-8 and an increase of 48% compared to the initial block magnets of figure 5-6. In fact the configuration of figure 5-12 has only 1.5% less flux linkage, for 34% less PM material than the first PM configuration.

It must be stressed that a configuration with varying angles of $\vec{B}_r$ may be difficult to accomplish in practice. For example, the small PM pieces in the corners of figure 5-12 have a cross-section of only 2 mm by 1.5 mm. It is probably not suitable to mount such small pieces in a production environment. The best choice is probably to magnetize the complete PM with a non-uniform field pattern similar to the field $\vec{H}_a$ created by the stator winding in the machine. As discussed by [Adn 1991], PM materials like ferrite, plastic-bonded Nd-Fe-B, Al-Ni-Co are isotropic and can be magnetized with various angles inside a same piece. These materials are suitable for such a magnetization inside the machine. Materials with high energy products like sintered Nd-Fe-B and Sm-Co are anisotropic and have usually one main direction of magnetization inside a given piece.

5.4. On the contribution of permanent magnets in flux-concentrating and surface-mounted TFPM machines

The comparisons between surface-mounted and flux-concentrating TFPM machines has been investigated in [Weh 1991], [Har 1996], [Paj 1997]. These authors have pointed out that flux-concentrating TFPM machines provide a significantly higher no-load flux Φ_{PM} for a given amount of PM volume. In chapter 7, section 7.2, we will show how the no-load flux Φ_{PM} influences the machine torque rating. It will become clear that a high value of Φ_{PM} per pole is advisable. Based on these remarks and based on the conclusions of these authors, the coming chapters will mainly concentrate on flux-concentrating TFPM topologies and the surface-mounted TFPM machine will not be discussed any further. Nevertheless, it is worth pointing out that such conclusions suggest that the ratio of no-load flux linkage λ_{PM} over PM volume is higher in the case of flux-concentrating TFPM machines. Hence, we can expect that this comparison can also be analyzed in terms of the volumetric contribution of the flux linkage created by the PMs in both cases.

Equation (5-18) is used to obtain the contribution of each magnet element to the stator flux linkage λ_{PM} at no-load. In the example presented below, the surface-mounted and the flux-concentrating TFPM structures will have the same pole pitch τ_p = 14 mm, the same width of the stator core leg w_{sc} = 6 mm, the same clearance gap g = 1 mm and the same magnet cross-section per pole pair S_{pm} = 108 mm^2. The method used is summarized as follows:

- in the two configurations, magnets are replaced by air;
- a current i = 10 A is injected in the stator winding;
- a magnetic field distribution $\vec{H}_a$ is obtained with 2-D finite element analysis;
- the dot product of $\vec{H}_a$ and $\vec{B}_r$ is plotted inside the magnets of each of the configuration.

The dot product of $\vec{H}_a$ with $\vec{B}_r$ inside the magnets is shown in figure 5-13 and figure 5-14 for the two TFPM configurations. This product is expressed in Joules per meter on figure 5-13 and figure 5-14 because it is a planar distribution plot. In both cases, the volume integral of equation (5-18) is calculated over the volume of four permanent magnets per stator core in order to obtain the flux linkage per pole pair. Only two of the magnets are shown in the 2-D cross-sections of figure 5-13 and figure 5-14. These transverse-flux topologies have two rows of magnets. It is reasonable to assume that the two magnets located on the other row have exactly the same contribution as the two magnets shown here on the first row.

To calculate the contribution to the flux density, the energy values per meter observed on both figures are divided by the coil current i.e. *10 ampères*. For the flux-concentrating TFPM example given here, each magnet has about the same contribution, i.e. respectively 1.53 mWb/m and 1.59 mWb/m per magnet and 6.24 mWb/m for each pole pair ((1.53 mWb/m + 1.59 mWb/m) x 2 rows). The flux is here given in Wb/m because it is a 2-D calculation. If each magnet and stator core had an axial length of 10 cm, the flux in the stator core would then be 624 μWb.

In the case of the surface-mounted TFPM structure, we observe a negative contribution of -1.25 mWb/m for the magnets not facing the stator pole, where the other magnet has a positive contribution of +3.70 mWb/m. In total the sum of the contributions of the four magnets is 4.90 mWb/m for each pole pair ((3.70 mWb/m - 1.25 mWb/m) x 2 rows).

In this example, the surface-mounted TFPM configuration gives 22% less magnetic flux in the stator core than the flux-concentrating TFPM configuration. In the surface-mounted TFPM structure, the presence of a magnet with opposite magnetization in the leakage path of the stator-created field partly cancels the contribution of the magnet facing the stator core. In other words, one magnet has a positive contribution, where the other magnet has a negative contribution. The application of this method to this example tends to confirm the results obtained by previous others. In this chapter, we give a different view on this subject by looking at the comparison between these two TFPM machines in terms of the contribution of their magnet elements.

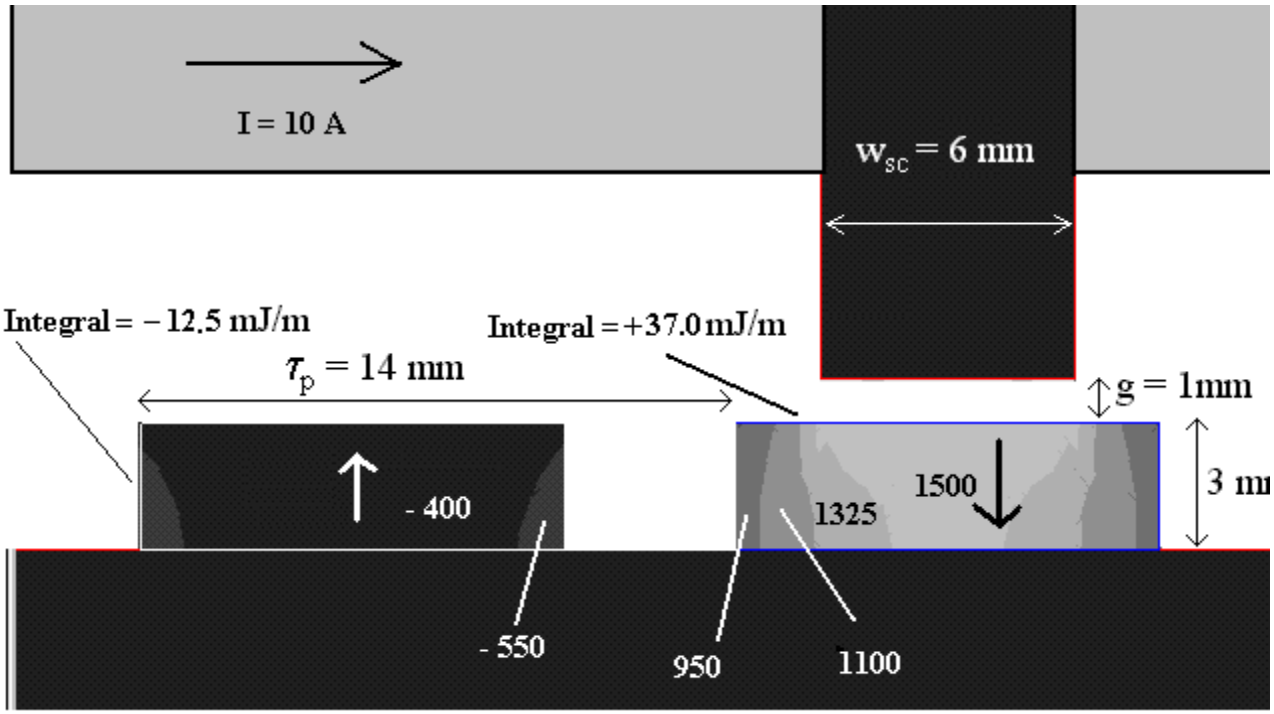

Figure 5-13: Contribution of each volume element to the no-load flux linkage in the stator winding of a surface-mounted TFPM configuration.

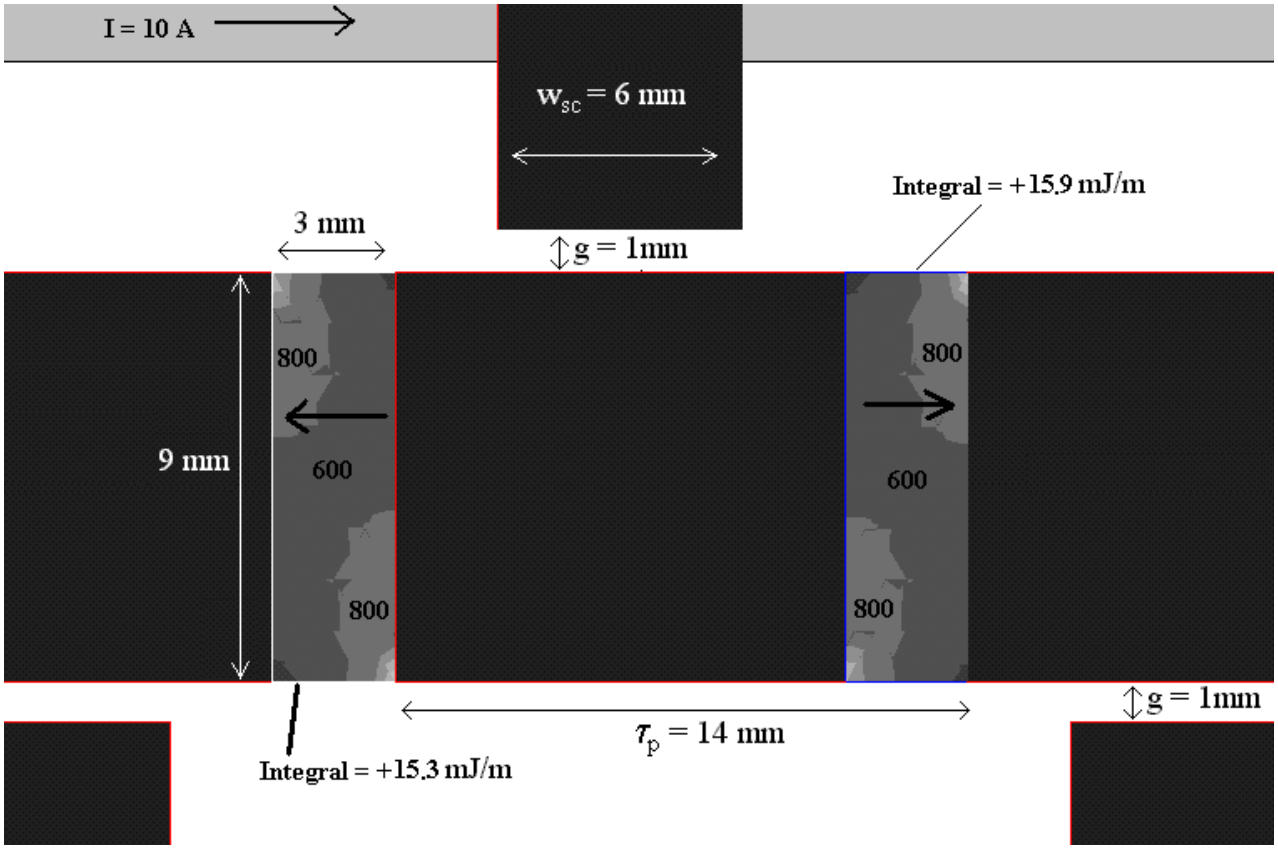

Figure 5-14: Contribution of each volume element to the no-load flux linkage in the stator winding of a flux-concentrating TFPM configuration.

5.5. Conclusions

A new expression for the flux linkage was derived. This expression describes the flux linkage in terms of a volume integral applied to the volume of the PM material located inside the machine. With such a formulation, each volume element *dv* inside the PM is given a certain contribution to the total no-load flux linkage.

With the use of this expression, a method is developed for the minimization of PM material in machines. The shaping of magnets and the variation of magnetization angle inside a given magnet is investigated more closely. The method is applied to the magnets of a conventional PM synchronous machine and to the magnets of a surface-mounted TFPM machine. The resulting PM shapes and magnetization patterns allow an increase in the amount of flux linkage per PM volume. The method of PM shaping is more beneficial in the case of a machine with short pole pitches, due to the high concentration of fringing fields. In the conventional PM synchronous machine, the improved shape can only improve the total mass or cost by a few percent, because of the wider pole pitches. However, the advantage may be more significant in the surface-mounted TFPM machine with pole pitches of 1 cm.

The same method also provides a different perspective on the advantage of flux-concentrating TFPM machines over surface-mounted TFPM machines. Several authors have argued that flux-concentrating TFPM structures are advantageous compared to the surface-mounted TFPM structure because of their higher no-load flux and higher force density for a given magnet volume. With the method developed in this chapter, the problem is treated in terms of the contribution of magnet elements *dv* to the no-load flux. With one example, we show that all magnets in the flux-concentrating TFPM structure have a positive contribution to the total no-load flux-linkage. On the contrary, half of the magnet elements in the surface-mounted TFPM structure bring a negative contribution to the total no-load flux-linkage. Such a negative contributions will partly cancel the positive contributions. In total, it leads to a lower flux linkage for a given PM volume at no-load. This confirms the superiority of flux-concentrating TFPM machine observed in the scientific literature. Since this thesis is concerned by the minimization of the cost and mass of active material, the flux-concentrating TFPM machines will be prefered in the remaining chapters.

There is a possibility that such modifications in the magnet shape and magnetization might improve the performance of the surface-mounted TFPM machine compared to the flux-concentrating TFPM machine. However, a formal comparison between a “shaped” surface-mounted TFPM machine and the flux-concentrating TFPM machine is not done in the thesis. This is left for further study.

Chapter 6

Investigation of flux-concentrating TFPM topologies

6.1. Introduction

Among the longitudinal machine concepts analyzed in chapter 4, the conventional PM synchronous machine obtained the best performance of torque/mass and cost/torque. However, the transverse-flux PM (TFPM) machines was identified as a good candidate for higher torque/mass and lower cost/torque. The TFPM structures allow a large winding window area and a short pole pitch, leading to high values of current loading and force density.

Although TFPM machines are very attractive in principle, a formal comparison with the conventional PM synchronous machine needs to be addressed before any superiority can be claimed for the TFPM machine.

In the rest of the thesis, we will focus on the flux-concentrating TFPM structures and leave out the surface-mounted TFPM topology. Various authors (see [Weh 1991][Har 1996][Paj 1997]) have pointed out the lower performance of surface-mounted geometries. In chapter 5, this was explained by the negative contribution of PMs to the no-load flux linkage. In the flux-concentrating structures, our conclusion was that all magnets contribute positively to the no-load flux linkage for a given volume of PM material. Thus, the choice is made in this chapter to pay attention only to the various structures of flux-concentrating TFPM machines.

Many variants of flux-concentrating TFPM geometries have been reported in scientific literature and we believe it is sensible at this point to describe them properly, as discussed in section 6.2. In section 6.4, the subject of powdered iron material is addressed, as many of the TFPM structures discussed require a massive use of this material. In section 6.5, we will give our view on what criteria should have a good TFPM machine and a new geometry will be derived to meet these criteria in section 6.6.

6.2. Description of existing flux-concentrating TFPM topologies

This section describes the various concepts of flux-concentrating TFPM machines proposed in literature. A comparison will be carried out between those concepts. Their advantages and disadvantages will be discussed.

6.2.1. General overview

Table 6-1 lists five different concepts of flux-concentrating TFPM machines. Six prototypes have been built and their performances are summarized in table 6-2. Table 6-2 lists the prototypes from the highest to the lowest cost/torque. In the cost calculations, the masses of active iron and copper are multiplied by 6 Euros/kg and the mass of PMs is multiplied by 40 Euros/kg. The concept of clawpole TFM is the one giving the most impressive results. However, we must be careful with the results of built prototypes since the efficiencies are not discussed in most of the publications and since the air gap thicknesses and pole pitches are not equal in all cases. In chapter 4, we pointed out how efficiency plays a significant role in the torque/mass and cost/torque performances of a machine. In the coming chapters, we will also highlight the importance of the air gap thickness and pole pitch.

It was also not clear from the scientific literature available that all machine designs were the result of a thorough optimization process. As we will see in chapter 7 and chapter 8, the optimization of TFPM machines is not straightforward.

Table 6-1. Evolution of the flux-concentrating TFPM concept.

Flux-concentrating TFPM type	Year of introduction in literature	Authors	Prototypes built
Double-sided, double-winding	1988	[Weh 1988a] [Weh 1988b]	Weh, 1988, 500 mm diameter
Double-sided, single-winding; U-core arrangement	1995	[Weh 1995] [Lan 2000a]	Lange, 2000, 370 mm diameter
Double-sided, single-winding; C-core arrangement	1995	[Weh 1995] [Mec 1996] [Mit 1997] [Voy 2000]	Mecrow, 1996, 362 mm diameter Voyce, 2000 1200 mm diameter
E-core TFPM	1995	[Weh 1995]	No prototypes reported
Clawpole TFM	1994	[Weh 1994] [Mad 1998] [Bli 2000]	Maddison, 1998, 335 mm diameter Blissenbach, 2000, 390 mm diameter

Table 6-2. Summary of performances of TFPM built prototypes.

Flux-concentrating TFPM topology and author	Diam-eter	Torque rating	Pole pitch	Mass active mate-rial	Mass PM	Torque /mass	Cost/ torque	Power factor at full load
	(mm)	(Nm)	(mm)	kg	kg	Nm/kg	Euros/ kNm	
Double-sided, single-winding; C-core arrange-ment Voyce [Voy 2000]	1200	75 960	45	N/A (Not avail-able)	N/A	N/A	N/A	N/A
Double-sided, double-winding Weh [Weh 1988a]	500	280	8	27.2	2.0	10.2	814	N/A
Double-sided, single-winding; U-core arrange-ment Lange [Lan 2000a]	370	1260	26	73	11.5	17.3	660	N/A
Double-sided, single-winding; C-core arrange-ment Mecrow [Mec 1996]	360	280	8.5	22.7	1.2	12.3	635	0.53
Clawpole TFM Blissenbach [Bli 2000]	390	2500	30.6	110	N/A	22.7	N/A	0.40
Clawpole TFM Maddison [Mad 1998]	340	540	10.7	20.8	2.0	26.0	361	N/A

The difference between an optimized machine design and a “proof of concept” machine design may be significant in terms of their respective performances. Thus, the order in which the machines are presented in table 6-2 is only representative of the performance obtained in the built prototypes. It does not necessarily reflect the true potential of each machine topology. It would require the same diameter, air gap thickness, efficiency and optimization to be used in order to assess that true potential.

The five concepts of flux-concentrating TFPM machines listed in table 6-1 are illustrated and described in the remainder of this section. It must be noted that the names given to the TFPM machines listed in table 6-1 do not always correspond to the names given in scientific literature. In many cases, the topologies discussed in past work did not have specific names or had names which applied to several geometries, e.g. the name “TFPM machine with flux concentration”. For these reasons, new names have been created in the thesis when necessary.

6.2.2. Double-sided, double-winding TFPM machine

The double-sided TFPM machine with double-winding is shown in figure 6-1. This machine was first proposed in [Weh 1988a]. It comprises a set of U-cores made of laminated steel and enclosing two stator windings, one on each side of the rotor. According to [Weh 1988a], the stator cores should be laminated with laminations parallel to the flux path in the stator core and also parallel to the direction of motion. This means that each lamination must be bent with its own radius. Other ways of laminating are possible. The two types of laminations and their respective drawbacks will be discussed in section 6.4.

The rotor is shown in figure 6-1 in between the two windings and is made of permanent magnets and flux concentrators. The PMs are magnetized parallel to the direction of motion with alternate polarities.

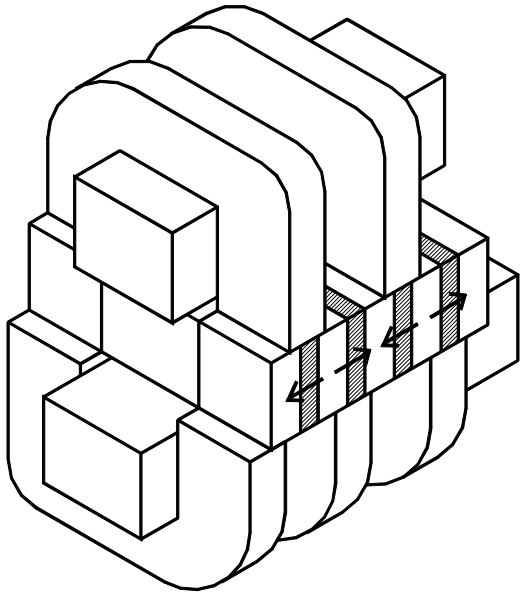

Figure 6-1: TFPM machine double-sided with double-winding.

This configuration may appear as electromagnetically interesting because each U-core encloses a winding and at the same time closes the magnetic circuit for the U-core on the other side. However, it seems that the prototype built and discussed in [Weh 1988b] does not reach such high performance in terms of cost/torque and no indication is given in [Weh 1988b] that would justify a lower performance. It is possible that the prototype presented by the author was only a proof of principle and that improved results could be obtained by optimizing the design parameters. It is also possible that the design was the result of an optimization process, with an optimization criterion other than torque/mass or cost/torque.

As a second possible explanation for the lower performances of the prototype in [Weh 1988b], we must mention the double-sided construction. From inspection of figure 6-1, we readily see how the rotor is “sandwiched” between the two stators. Although this has to do with production problems, we foresee that it may also lead to thicker air gaps. This is possibly required, in order to take into account all the possible deformations of the difficult rotor

arrangement. A thicker air gap will have an important effect on the amount of no-load flux entering the stator cores and linking the stator winding. Unfortunately, the airgap thickness of the built prototype is not mentioned in [Weh 1988b].

6.2.3. Double-sided, Single-winding; U-Core arrangement

The double-sided TFPM machine with single-winding in U-core arrangement is shown in figure 6-2.

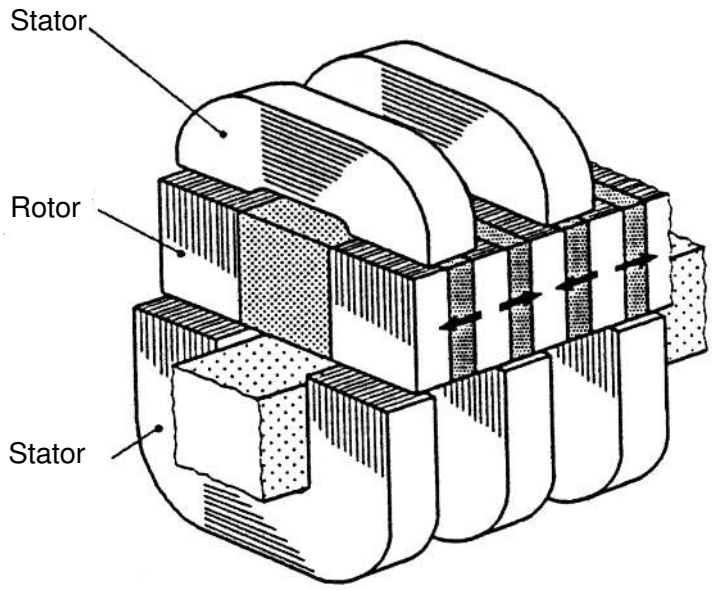

Figure 6-2: Double-sided TFPM machine with flux-concentration and single-winding in U-core arrangement .

This type of machine was discussed in [Weh 1995] and is almost identical to the double-sided TFPM machine with double-winding discussed in the previous subsection. The difference is the absence of one of the two windings. But the removal of one winding should not affect the torque rating of the machine. It will certainly create a no-load voltage twice lower than if two windings were used. However, the reluctance of the magnetic circuit is the same for one or two windings. Thus, when current flows in the two windings, saturation of the stator cores will be reached at half the current of a single winding arrangement. This is caused by the addition of the two magnetomotive forces, which are created by the two current windings sharing a same magnetic path.

If the same amount of copper is used, the length of the U-core leg is increased on one side. But this increase in stator material is compensated by a decrease in the length of the U-core leg in the top part of figure 6-2. All in all, the amount of material used for the same torque is nearly identical. Since it is reasonable to consider the leakage field through the winding windows as negligible, and as long as the copper cross-section is made equal to the copper cross-section of the two windings summed up, the performance of this single-winding machine should in principle be the same as the double-winding version of figure 6-1.

In [Weh 1995], Weh mentions two main advantages of this construction compared to the double-winding arrangement of section 6.2.2. The first advantage is the elimination of the top winding, which is difficult to mount and maintain inside the outer U-cores. The second advantage is the reduction of the machine outer diameter. This makes a better use of the inner part of the machine.

One prototype of the machine has been built and discussed in [Lan 2000a] and better performances are obtained compared to the double-winding prototype discussed in section 6.2.2. The lack of geometrical details in [Weh 1988b] prevents us from giving a good explanation for the difference in performance, since we expect the double-winding and the single-winding arrangements to give equivalent performances.

6.2.4. Double-sided, single-winding; C-core arrangement

The double-sided, single-winding TFPM machine with C-core arrangement is illustrated in figure 6-3. This design was first proposed in [Weh 1995]. Weh's idea was to start from the U-core concept of the previous subsection and reduce the rotor width in the axial direction by removing one row of permanent magnets. By making the rotor shorter, the rotor deformation due to centrifugal forces in its end parts are reduced.

Weh's machine has not been built, or at least no prototype has been formally reported in scientific literature. Weh's idea was to use laminated steel with laminations oriented as shown in figure 6-3. This construction appears as difficult. It probably explains why it was not built.

The use of powdered iron appears as a natural material for this type of construction. A variant of this machine was proposed and built in [Mec 1996].

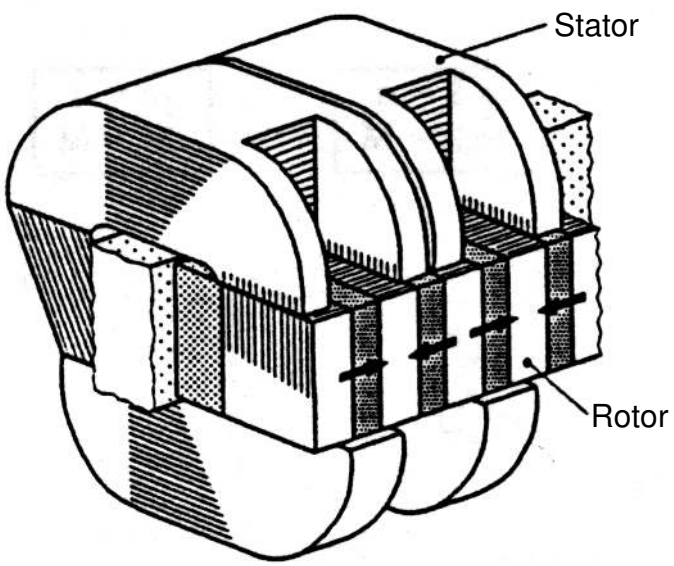

Figure 6-3: Double-sided, Single-winding TFPM machine with C-Core arrangement. Design proposed by Weh.

This variant uses powdered iron and is shown in figure 6-4. In fact Mecrow's design and Weh's design appear as equivalent, except that Weh's C-cores are linked together in Mecrow's design to form only one single stator piece. Electromagnetically speaking, this type of design uses flux concentration in the same way as with the double rows of magnet. The major difference is the removal of one row of magnets and two airgaps. The missing row of magnets with their associated airgaps have been replaced by steel or powdered iron. We expect that this machine will have comparable no-load flux linkage as the double-sided TFPM machine with single-winding in U-core arrangement discussed in section 6.2.3. However, the removal of two airgaps in the main magnetic path decreases the reluctance "seen" by the stator winding. Thus, the saturating magnetomotive force to be fed to the stator coil should also be reduced. Consequently, if the same dimensions are used in both cases, we can expect the torque density (torque per volume) to be roughly half of the torque density of the U-core version of section 6.2.3. Looking at the prototype built in [Mec 1996] with this machine configuration, a torque density of 50.8 kNm/m^3 was obtained for a diameter of 360 mm. In comparison, the prototype built in [Lan 2000a] of the TFPM machine shown in figure 6-2 gave a torque per volume of 96.3 kNm/m^3, which is about twice as high.

Regarding the amount of material required in the C-core arrangement, the amount of PM material is of course divided by two compared to the design of figure 6-2. Also, the amount of copper may be divided by two, since half the current can be fed into the machine due to the lower stator reluctance. The amount of iron material is also slightly decreased due to the smaller winding window required. Roughly, we can expect that the cost of active material will be about half, for half the torque of the TFPM machine of figure 6-2. Thus, the cost/torque and torque/mass values of this concept should be comparable to the values obtained with the U-core arrangement of figure 6-2.

Calculating the cost/torque of the prototype of the C-core arrangement built in [Mec 1996], we obtain a cost/torque of 567 Euros/kNm.

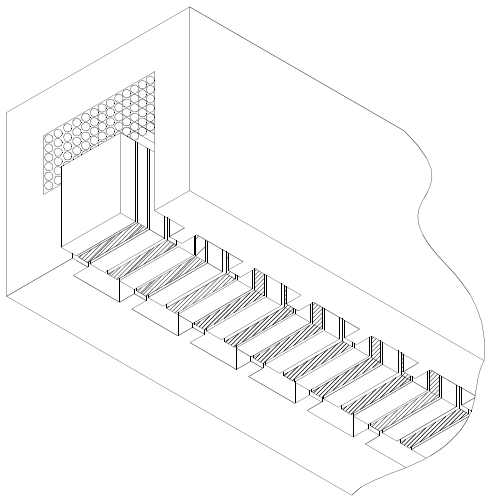

Figure 6-4: Double-sided, Single-winding TFPM machine with C-Core arrangement. Design proposed by Mecrow.

This is 14% lower than the cost/torque of the prototype of the U-core arrangement built in [Lan 2000a], which has a cost/torque of 660 Euros/kNm. Of course, it is difficult to make any final judgement on the two topologies only based on built prototypes. Differences exist, like the use of a 0.5 mm airgap in [Mec 1996], while in [Lan 2000a] a 1.2 mm airgap was used. Also, powdered iron was used in [Mec 1996], while [Lan 2000a] used laminated iron. More important, the efficiencies of the two designs are not discussed. But we believe these numbers provide a general idea on what can be expected from these machine geometries.

About the importance of the air gap thickness, calculations have been made in [Har 1998] with the same machine built in [Mec 1996] with an air gap thickness increased from 0.5 mm to 1 mm. The modified design would give 19% less torque than for the 0.5 mm airgap. This would give a cost/torque comparable to the machine reported in [Lan 2000a].

On the subject of construction, a few words have already been said about the difficulties of producing a laminated stator for this type of machine. It may seem that the construction can be simplified with the use of a powdered iron stator. However, molding a complete stator in one powdered iron piece is also a problem, due to the rating of the hydraulic press. Often, a large number of blocks will be necessary to form the complete stator. This adds to the construction complexity. The subject of powdered iron material will be addressed in section 6.4. Also, some of the problems of a double-sided air gap to be discussed in section 6.5 are also applicable to this machine topology. These problems are related to the tight mechanical tolerances and equal thermal expansion coefficients required on the stator and rotor parts for this type of "sandwiched" construction. However, it must be noted that the removal of one row of magnets will probably simplify the rotor construction.

A few construction advantages are obtained with one single row of magnets and a single-sided stator core, but increased complexity is expected due to the production of the stator winding and because of the tight tolerance of the rotor pieces. All these points being considered, it is not clear whether or not this TFPM machine will bring so much benefit compared to the double-sided/single-winding TFPM machine with U-core machine of section 6.2.3.

6.2.5. Clawpole TFM

The clawpole TFM machine was first proposed in [Weh 1994] and is illustrated in figure 6-5 according to the design in [Mad 1998]. This machine is a natural extension of the double-sided, single-winding TFPM machine with C-core arrangement discussed in the previous section. Obtaining the clawpole TFM structure of figure 6-5 from figure 6-4 is accomplished via the following steps:

- the rotor is taken out from in between the stator feet;
- the rotor width l_{rt1} is increased to match the stator width;
- the stator foot length l_f is made longer in the axial direction, in order to catch more flux from the rotor;
- the cross section (product $l_{leg}w_{sc}$) of the stator foot is made generally constant, as we move away from the airgap.

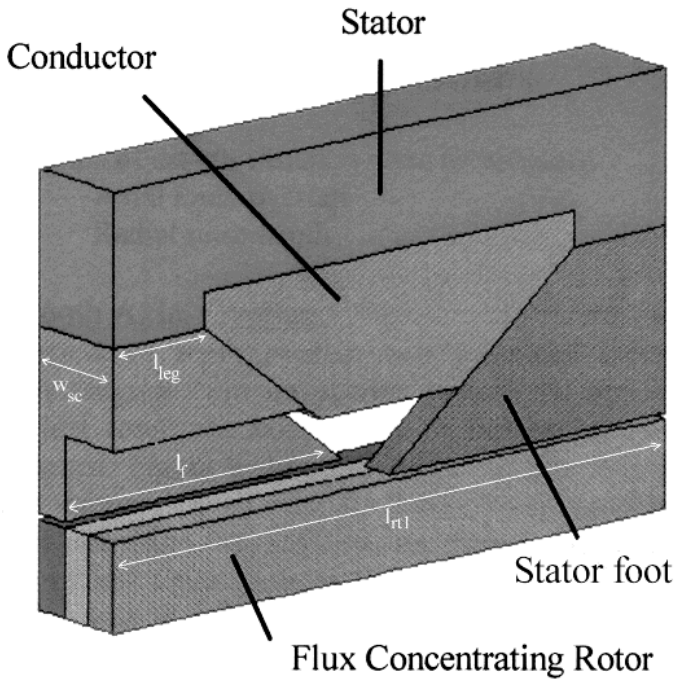

Figure 6-5: Clawpole TFM.

The last two steps are very important. It means that the stator core can be wide (large width w_{sc}) near the winding and at the same time narrow (short width w_{sc}) near the airgap. A stator core with a large cross-section (product $l_{leg}w_{sc}$) is desirable because it allows a high magnetomotive force in the stator coil before saturating the core. Moreover, if the stator core is made thin (e.g. thinner than the magnet thickness) near the air gap, the leakage in the air gap area can be kept low and the reluctance U_{up} can be kept high. The effect of the reluctance U_{up} will be seen in the next chapter, but we can already mention that the reluctance U_{up} also determines the maximum magnetomotive force in the stator coil before saturation.

The double-sided machines of section 6.2.2 and section 6.2.3 did not benefit from the advantage of a varying w_{sc}. The stator cores of these two machines had the same foot width w_{sc} both at the air gap and around the coil. Figure 6-6 shows the armature reaction and the effect of a wide stator core and its resulting leakage for the double-sided, double-winding TFPM machine and for the double-sided, single-winding TFPM machine with U-Core arrangement in the unaligned position.

If the stator core cross-section should be increased to allow a large flux linkage, it is probably desirable to keep w_{sc} thin and rather increase the foot length l_f near the air gap. However, one drawback of extending the stator foot l_f is the overlap of the two opposing feet, resulting in the increase of the stator leakage. This effect will reduce the reluctance seen by the stator and favors early saturation of the stator core. This point is extensively discussed in [Mad 1998] and [Dic 2002].

Although the stator core suffers from leakage through the overlap area between the stator feet, the clawpole TFM built in [Mad 1998] obtains an increase in total torque while the stator size and copper cross-section stay roughly the same compared to the double-sided, single-winding TFPM machine with C-core arrangement discussed in the last section and built in [Mec 1996].

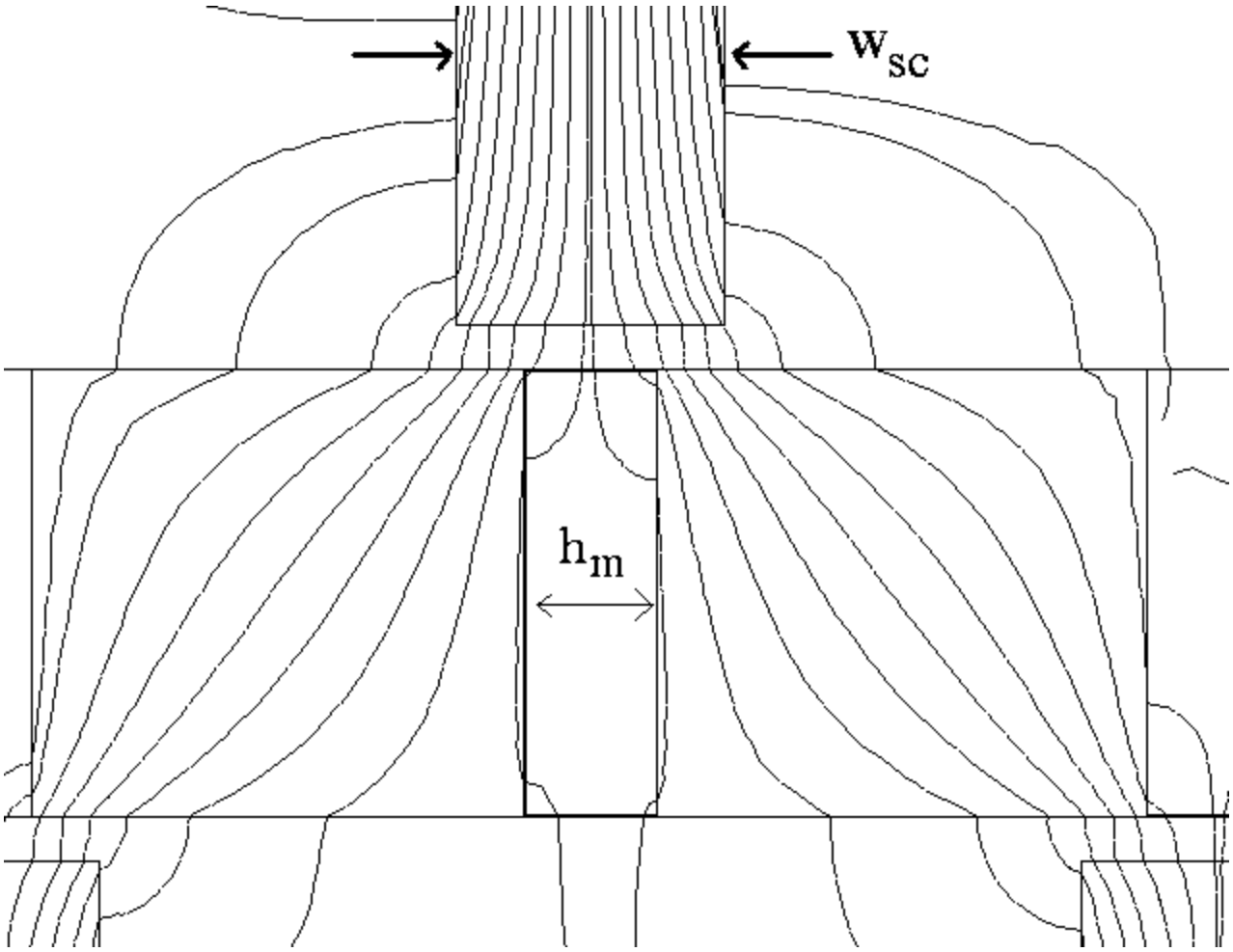

Figure 6-6: Armature reaction of a flux-concentrating TFPM machine in the unaligned position.

If we compare the latter with the clawpole TFM machine built in [Mad 1998] we notice that the two machines have almost exactly the same dimensions, i.e. diameters of 340 mm and 360 mm and an axial length of 60 mm. They both use almost the same amount of active material, i.e. 22.7 kg and 20.8 kg. They both have the same airgap thickness, i.e. 0.5 mm. The major difference lies in the rated torque and the mass of PM. The clawpole TFM machine has a rated torque of 540 Nm for a PM mass of 2.0 kg and the double-sided, single-winding TFPM machine with C-core arrangement has a rated torque of 310 Nm with a PM mass of 1.2 kg. However, it must be mentioned that the prototype of the clawpole TFM built in [Mad 1998] uses a solid steel stator with high saturation flux density and only static torque testing has been performed. In reality, this type of machine cannot easily be built with laminated steel and powdered iron should be used. This is due to the three-dimensional flow of the magnetic field inside the iron parts. If a powdered iron stator is used, it is foreseen that the torque performance will be reduced due to the lower saturating flux density.

In summary, the clawpole TFM makes a very efficient use of the stator space. In the TFPM machines of figure 6-1 and figure 6-2, there was a lot of empty space between stator

cores. In the clawpole TFM machine, the stator space is almost completely filled with ferromagnetic material. And more, this ferromagnetic material is used at its maximum flux density, by having an almost constant cross-section of the stator cores down to the airgap.

On the production level, the rotor arrangement suffers from the dependence of the PM positions on the build-up of mechanical tolerances of the rotor pieces, as with all other flux-concentrating TFPM concepts. This problem can be circumvented by using an aluminum ring with channels milled at every pole pitch around the ring. The rotor flux concentrators can then be glued or bolted inside each of these channels. Also, the problems of automating the rotor production appears in the clawpole TFM. These two problems will be discussed in detail in section 6.5. In [Dic 2002], an arrangement with surface-mounted PM with lower torque/mass performance is preferred to the high-performance flux-concentrating clawpole TFM due to the problems related to the flux-concentrating rotor. This shows how manufacturing is also very important and that torque/mass or cost/torque should not be the only criterion used for the assessment of a machine.

Lastly, it must be pointed out that the clawpole TFM has the advantage of a single-sided rotors, which makes its mechanical construction much stiffer than other double-sided TFPM machines.

6.2.6. E-core TFPM

The E-core TFPM was proposed in [Weh 1995] and is shown in figure 6-7. Weh's idea was to extend his concept of the double-sided/double-winding discussed in section 6.2.2 to a design where the rotor width in the axial direction would be reduced. As with the C-core arrangement, the idea was indeed to reduce the possible rotor deformations caused by centrifugal forces.

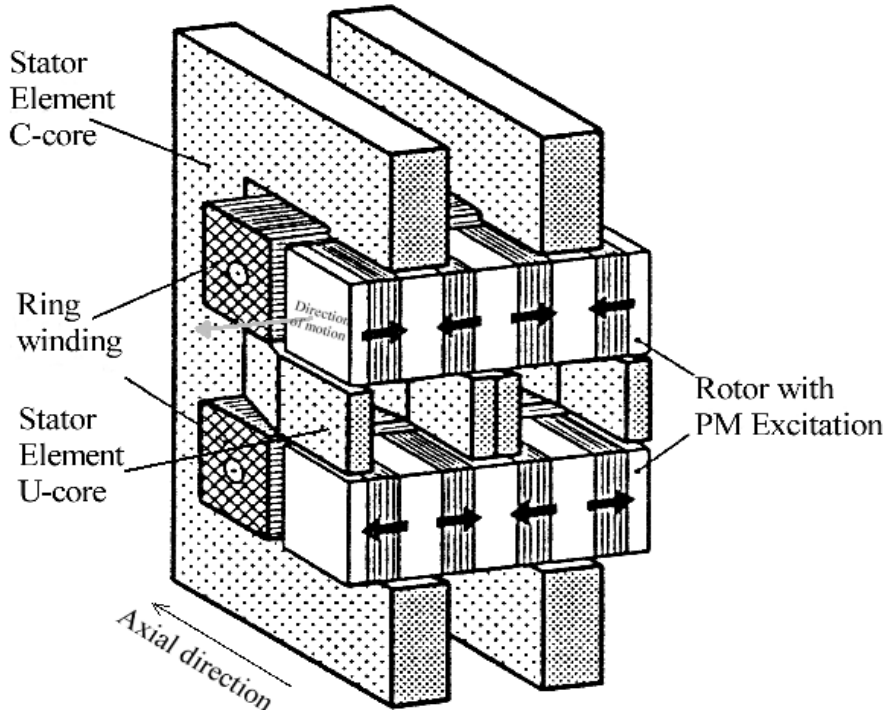

Figure 6-7: TFPM machine with E-core configuration.

This E-Core TFPM structure uses steel laminations in the stator. The stator is made of two separate parts, that is a C-core surrounding both stator windings and a U-core placed in between the two windings. Every stator winding "sees" four airgaps in the main magnetic path. Electromagnetically, this concept has the same expected performances as the double-sided, double-winding TFPM machine discussed in section 6.2.2.

In production, this type of design will also encounter the same problems as with the double-sided, double-winding TFPM machine discussed in section 6.5 with the addition of the difficulty of laminating the U-core in between the two windings. In that case, powdered iron may be used or metallic glass tape (METGLAS7). In the latter case, the cost of metallic glass material is high, which is probably not a suitable solution for cost reduction. Another major difficulty in this type of design is the presence of four air gaps, which requires a very stiff and very accurate mechanical concept. This probably explains why this machine design has never been built, or at least no reference to a built prototype is made in scientific literature.

6.3. Power factor of TFPM machines and cost of power electronics

The magnetic flux density obtained in the stator core of TFPM machines at no-load is usually much lower than the saturation flux density of the core material. This is what will happen if the cross-section of the stator core is made large enough, which is usually the case for a TFPM machine with high performance. Under nominal current conditions, the current will be sufficiently high to reach core saturation. Therefore, the magnetic flux flowing in the stator core will be much higher at full-load than under no-load conditions. This results in a terminal voltage V at full-load being much higher than the no-load voltage E. If saliency and losses are neglected, the available output power can be written as (for a three-phase system):

$$P_{out} = 3VI\cos\phi = 3EI\cos\psi \tag{6-1}$$

or

$$\cos\phi = \frac{E}{V}\cos\psi \tag{6-2}$$

Equation (6-2) readily indicates that a high ratio of output voltage over no-load voltage V/E will lead to a poor power factor $cos\phi$. In the case of a direct-drive wind turbine, where the generator output must be connected to a rectifier, the rectifier rating will need to be much higher than the generator power rating, thus increasing the rectifier cost. A low power factor will prevent the use of a diode-bridge rectifier because of the overlap of diode conduction periods. A PWM rectifier should be used instead.

Electrical machines are sized according to their nominal torque value rather than power, while the rectifier is sized according to its apparent power. Thus, applications with

low rotational speeds and high torque, as in direct-drive wind turbines, are much more sensitive to the machine costs and to a certain extent less sensitive to the cost of power electronics.

For example, let us assume a direct-drive generator of power 750 kW and rotational speed of 25 rpm. The generator must be designed for a torque of 290 kNm. If a conventional PM synchronous machine of 4-meter diameter is selected with a cost/torque of 100 Euros/kNm (as determined in section 4.3.2), the cost of active material will be about 29,000 Euros. Now, let us assume that the generator has a power factor equal to 0.5, and that its output is connected to a PWM rectifier with 6 IGBTs of rating 1700 V/2000 A each. The cost of the IGBTs will be about 750 Euros each, for a total of 4500 Euros. The extra costs of power electronics related to the use of a lower power factor will represent in that case only 5% of the generator active material costs.

6.4. Performance of powdered-iron material and laminated Fe-Si steel

Powdered iron material (or "Soft Magnetic Composite" - SMC material) has the advantage of isotropic magnetic and electrical characteristics, with a fairly high resistivity (see table 6-3). Such characteristics can be useful in the case of TFPM machine where the magnetic flux travels in the three dimensions. Since many of the flux-concentrating machine concepts discussed previously make a massive use of this material, it is important to examine how powdered iron compares to conventional laminated steel.

6.4.1. Specific iron losses of powdered iron material

From the scientific literature available, two powdered iron products have been used and described in [Per 1996], [Gel 1997]. These products are Somaloy 5007 of the company Höganäs of Sweden and Atomet EM-17 of the company Quebec Metal Powders of Canada. The characteristics of both products are generally comparable with one another.

Iron losses for the case of two-dimensional fields

If a magnetic flux flows in a planar way, i.e. in two dimensions, laminated steel is usually suitable to obtain low iron losses.

Table 6-3. Resistivity of steel and powdered iron.

	Steel Fe-Si	Powdered iron ATOMET EM-1 from [Cro 1998]
Resistivity (μΩ-cm)	10 - 50	around 15000

Laminations are insulated with insulating coating, which decreases the path of eddy currents. In powdered iron material, fine iron particles are compacted with a non-conductive compound which creates an insulating film around each particle. The reduction of iron losses is accomplished in the same way as with steel laminations, that is by reducing the path of eddy currents. Although the same principle applies, powdered iron and laminated Fe-Si steel do not exhibit the same loss characteristics. In [Per 1996][Gel 1997], the iron losses of both material are compared for the case of planar fields. In both publications, it is claimed that at low frequencies, powdered iron has specific losses higher than laminated steel. But above 100 Hz, it is claimed that powdered iron has lower losses than laminated steel. However, in both publications the comparison between powdered iron and laminated steel is carried out using laminations with a thickness of 0.8 mm or 0.9 mm. We have identified at least two manufacturers that provide laminations of much lower thicknesses. Kienle & Spiess and Mapes & Sprowl offer thicknesses of 0.35 mm and 0.50 mm as standard products. Comparing the iron losses of powdered iron with those thinner laminated steels gives different conclusions. The specific iron losses of steel laminations M-19 (taken from [Map 2001]) and powdered iron ATOMET-EM17 (taken from [Que 2001]) are shown in figure 6-8 for a peak flux density of 1.5 T.

The electrical frequencies that we expect for TFPM machines in wind turbine applications will probably range between 50 Hz and 300 Hz. In this range, powdered iron has specific losses higher than the two lamination types. According to the manufacturers data shown in figure 6-8, the 0.35 mm-thick laminations give specific losses 5 times lower than powdered iron. Thus, for two-dimensional fields, laminated steel is preferable in the range of frequencies considered for our application.

In addition to the problem of high specific losses, powdered iron shows higher losses related to the use of large blocks of this material. In principle, each metal particle is insulated with a resin boundary of higher resistivity. As illustrated in figure 6-9, small current loops will be created inside each individual particle, leading to reduced eddy current losses. However, the resin boundary does not have infinite resistivity and other paths exist for the eddy currents, as illustrated in figure 6-10. Another possible phenomenon is the absence of insulating layer between a number of iron particles, creating low resistance paths inside the powdered iron piece. For machine pieces with large volumes of powdered iron, the amount of parallel current loops created will increase with the volume, as described in [Lef 2002]. In [Lan 2000b], it is found that the losses per volume were not the same for large volumes and for small volumes. An increase of 25% is obtained in specific iron losses at a frequency of 750 Hz, for a 400% volume increase. Since wind turbine generators are usually large machines, the effect of size on powder iron specific losses must be taken into account. Using the specific losses specified by powdered iron manufacturers may lead to underestimated losses when applied to large core sizes.

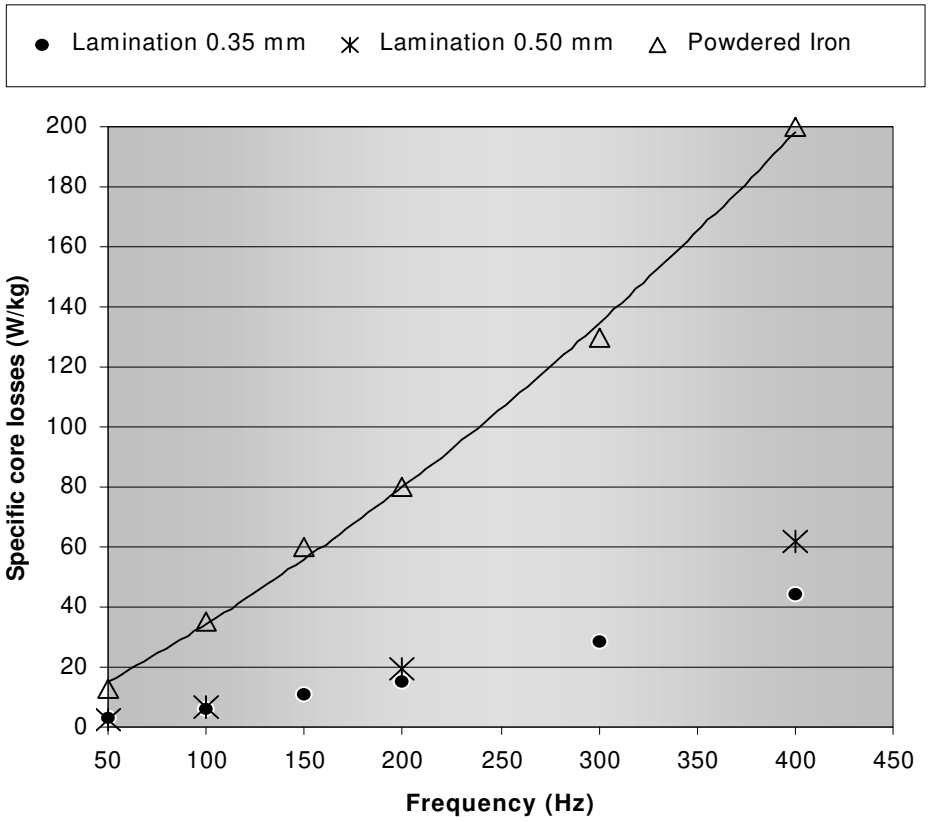

Figure 6-8: Iron losses for two lamination thicknesses and powdered iron, B = 1.5 T. Lamination type is M-19 Fe-Si steel; powdered iron is Atomet-EM17.

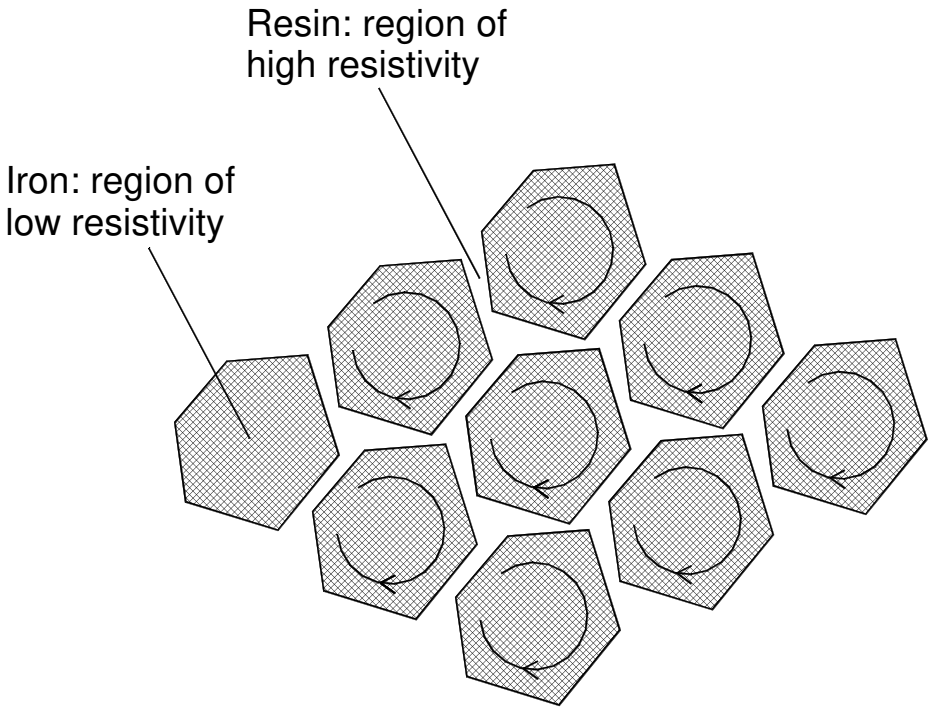

Figure 6-9: Microscopic metal particles and their insulating boundaries.

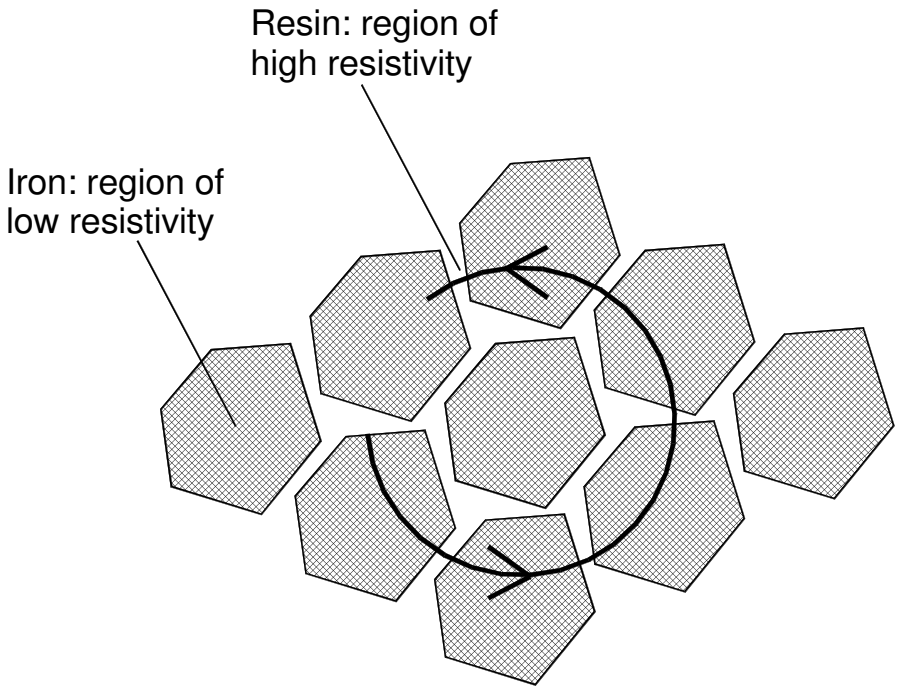

Figure 6-10: Circulation of eddy currents beyond the particles boundaries.

Iron losses for the case of three-dimensional fields

In machine topologies where the main flux travels in the three dimensions, we can expect that powdered iron will be more suitable than laminations. Varying magnetic fields will create eddy currents inside the ferromagnetic material, which will be concentrated in a thin region near the surfaces or "skin". The skin thickness or "skin depth" depends on the ferromagnetic material properties. It approaches zero as the resistivity ρ approaches zero. The skin depth δ of a material is given by:

$$\delta = \sqrt{\frac{\rho}{\pi f \mu_r \mu_0}} \tag{6-3}$$

As emphasized in [Sto 1974], the eddy currents created in a ferromagnetic core by an alternating field will be *resistance-limited* in the following condition:

$$2b < \delta \tag{6-4}$$

where $2b$ is the width of the conducting path where eddy currents are flowing. This condition is met with Fe-Si laminated steel (skin depth is about 1 mm at 50 Hz) when the main flux flows parallel to the laminations plane. In that case, the eddy current losses per volume can be calculated with the well-known formula:

$$p_{eddyloss} \cong \frac{2\pi^2 f^2}{3\rho} B^2 b^2 \qquad (6\text{-}5)$$

If the main flux flows perpendicular to the laminations plane, the path for eddy currents is much wider (*2b* much higher). The presence of coating between each lamination brings the magnetic permeability down to values around μ_r = 10 - 20, depending on the thicknesses of the coating and steel. Thus, the skin depth at 50 Hz will increase to about 1 cm and the condition stated by equation (6-4) is met in most cases. However, the eddy current losses will be substantially higher because *2b* has increased substantially.

Powdered iron material has a higher resistivity and low permeability, resulting in low losses and large skin depth. At 50 Hz, the skin depth of powdered iron is about 4 cm. This allows wide pieces of ferromagnetic core to be used and reduces the amplitude of eddy currents. This advantage can be used to create various shapes of ferromagnetic cores with larger dimensions. This is especially interesting in the case of TFPM machines such as the clawpole TFM or the double-sided, single-winding TFPM machine with C-core arrangement. In these two geometries, the main flux has a three-dimensional path and powdered iron becomes an interesting material.

Three-dimensional fields is often an inherent aspect of a TFPM geometry as in the clawpole TFM. Furthermore, more planar TFPM geometries may also exhibit a three-dimensional behavior due to the leakage fields. A very important leakage path common to most TFPM machines is the leakage between the stator core and the rotor in the unaligned position, as illustrated in figure 6-11. This leakage path will have consequences on the laminations orientation if laminated Fe-Si steel is used to carry the stator flux.

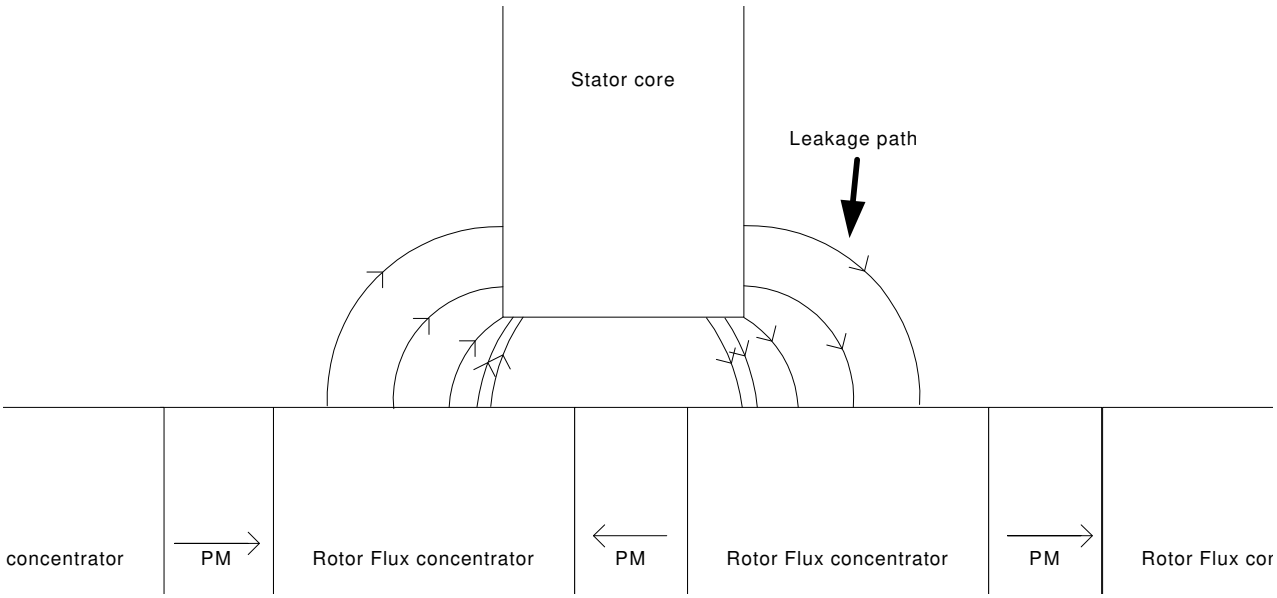

Figure 6-11: Leakage path between the stator core and the flux concentrators in the unaligned position at no-load.

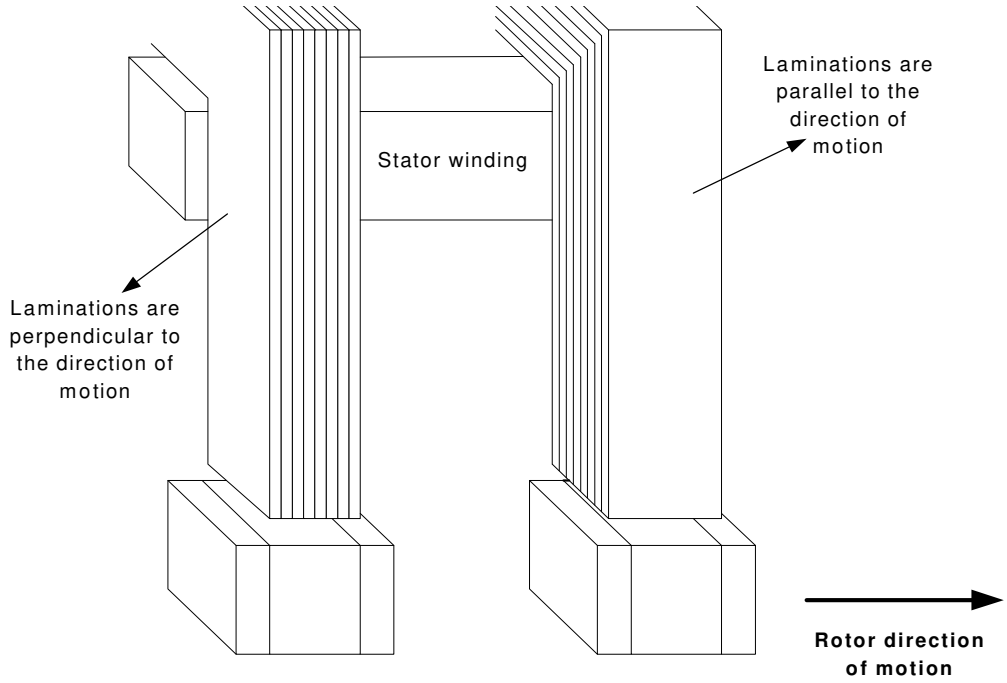

Figure 6-12: Two possible orientations of the stator laminations in a TFPM machine.

Two orientations can be used, which are illustrated in figure 6-12. If the laminations are perpendicular to the direction of motion (left-hand side of figure 6-12), the leakage flux illustrated in figure 6-11 will flow perpendicular to the laminations plane and will offer a wide path for the eddy currents. If laminations are parallel to the direction of motion (right hand-side of figure 6-12), the eddy currents created by the leakage flux will be contained within the thickness of each lamination. The eddy current losses will be the lowest if the laminations are oriented parallel to the direction of motion (right-hand side of figure 6-12). However, the stacking of identical laminations perpendicular to the direction of motion (left-hand side of figure 6-12) is much simpler than the construction on the right-hand side of figure 6-12. In the latter case, all laminations in a given C-core have a unique shape and a unique length and assembling such a C-core will be more difficult and probably more expensive.

If the C-core foot was made of powdered iron particles, we may avoid the construction problems discussed above. The eddy current losses created by this leakage flux will be lower in parallel-oriented laminations compared to powdered iron but higher in perpendicular-oriented laminations.

6.4.2. Other magnetic characteristics of SMC and laminated steel

The properties discussed here are initial relative permeability and saturation flux density and they are shown in table 6-4. Both the initial relative permeability and saturation flux density of powdered iron are lower than those obtained for cold-rolled silicon steel.

Table 6-4. Magnetic properties of Fe-Si steel laminations and SMC material.

	Cold-Rolled Silicon Steel	Powdered iron ATOMET EM-1
Maximum relative permeability (60 Hz)	1000 - 10000	about 450
Flux density (T) for a magnetic field of 5kA/m	1.7	1.1
Flux density (T) for a magnetic field of 10kA/m	1.8	1.6

For most PM machines, the low relative permeability of powdered iron will not be a problem because the MMF drop across the stator core will be much lower than the MMF drop across the PM. However, the lower saturation flux density will be a limiting factor for the amount of ampere-turns in the stator winding.

6.4.3. Manufacturing of powdered iron

This section presents the steps required for the production of powdered iron pieces. The advantages and limitations of this manufacturing technique are highlighted.

Producing powdered iron pieces is a different process from the manufacturing of steel laminations. The principle of steel lamination production is to stamp a virgin steel sheet. The shape of the stamping head determines the shape of the lamination produced.

In the case of powdered iron, it is not a stamping technique but rather a molding technique. Raw powdered iron comes in bulky fine particles, which are mixed with a few additives. This mixture is poured into a mold and compacted at high pressure. The resulting part is then solid. A heat treatment specific to the particular additives used in the powdered iron mix is then applied. The heat treatment increases the mechanical strength of the material and releases the internal stresses. A curing at 150^{o}C - 200^{o}C can be applied in the case where the binder/insulator additive is an organic material. Pyrolisis at higher temperature (300-500^{o}C) can also be applied if the insulation and mechanical strength are given by an oxide layer contained in the additive. The resulting parts have mechanical tolerances of about 0.15%. The manufacturing procedure for powdered iron parts is illustrated in figure 6-13.

As claimed in [Per 1995], one of the advantages of powdered iron is its ability to be molded in about any shapes. This is a clear advantage over steel laminations which are usually stacked in one direction. Complex 3-D shapes are more likely to be produced with powdered iron than with steel laminations. However, the compacting pressure required during the punching procedure is a limitation to the size of the parts produced. The two manufacturers of powdered iron material recommend a compacting pressures between 600 and 800 MPa. The typical punch rating available in the industry is below 1000 tons. 2000 tons presses exist, but are not common. If a 1000-ton press is used at 600 MPa, the maximum surface which can be pressed is 1540 cm^2. This is possible for the stator of a small machine.

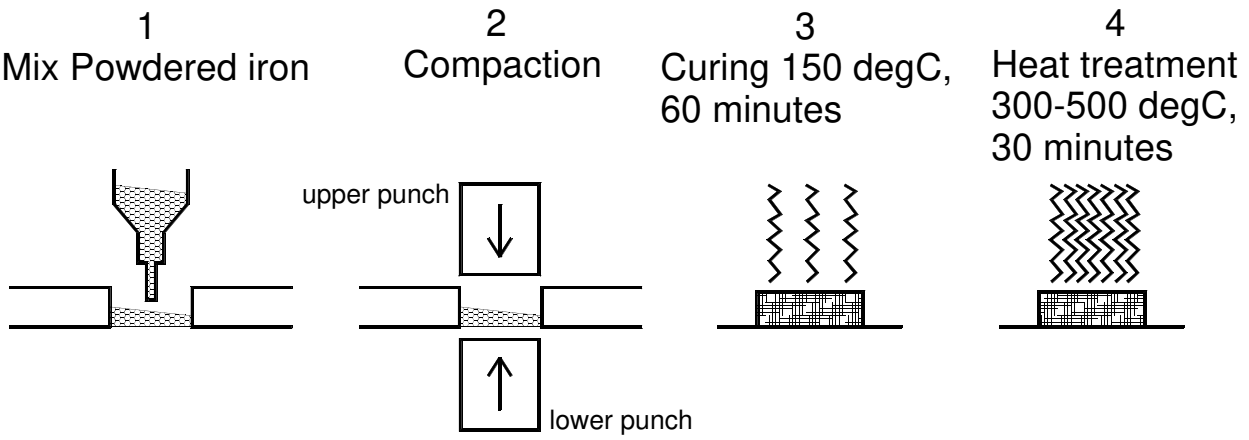

Figure 6-13: Production route for powdered iron pieces.

For wind turbine generators, the expected area of the stator is much larger. For example, a 3-meter diameter stator with a stator thickness of 25 cm and an axial length of 50 cm has an area of 140,000 cm^2. If the stator of the wind turbine generator was to be made from powdered iron, it would need to be segmented it into smaller pieces. For this design example, the stator would need to be divided into about 100 pieces. Those smaller pieces would need to be mechanically joined together by other means. This adds to the complexity of stator production.

It must be noted that conventional synchronous machines with large diameters must also be divided into smaller sections of laminations, which must be interleaved to form a complete stator. For example, Delft University of Technology was involved in the design of a 5-meter diameter direct-drive generator. The stator was made from segments of 60 cm-wide laminations. Each segment had to be mechanically joined to the next segments. With a diameter of 5 meters, the number of segments is 26.

In view of the production techniques and problems discussed in this section, it is likely that production of powdered iron pieces could be as expensive as punching and stacking steel laminations.

6.4.4. Cost of powdered iron versus steel laminations

The cost of steel laminations and powdered iron could not be obtained from any of the scientific literature available. Since cost is an important aspect of this research, several material suppliers have been contacted and the cost figures obtained are reported in table 6-5. The costs reported in table 6-5 do not include the cost of pressing or punching and the cost of lost material in the case of steel laminations.

The costs for laminated steel and powdered iron are comparable. Apparently, there is no significant advantage or disadvantage obtainable in terms of cost by using one of the two materials.

Table 6-5. Costs of laminated Fe-Si steel and powdered iron for large quantities.

Source of information	Cost of raw material (Euro/kg)
Powdered iron ATOMET EM-1	1.35
Powdered iron Somaloy 500	1.50
Transformer laminations Linto & Hirst	1.39
Transformer laminations Magnetic Metals	1.50

6.4.5. Conclusion

The comparison between powdered iron and laminated Fe-Si steel is based on losses, magnetic characteristics, manufacturing and cost.

For two-dimensional fields, the iron losses of powdered iron can be up to five time higher than Fe-Si laminations. When the main flux flows in the three dimensions, the use of powdered iron is advantageous because of its higher resistivity and larger skin depth (about 4 cm @ 50 Hz). Fe-Si laminations crossed by perpendicular fluxes will carry wide eddy current paths and lead to higher eddy current losses. The associated losses will be higher than the losses obtained with a foot made of powdered iron. Laminations oriented parallel to the direction of motion give low eddy current losses. However, this lamination configuration appears as difficult to build. The laminations are easier to stack when oriented perpendicular to the direction of motion.

The magnetic characteristics of powdered iron and Fe-Si laminations have been compared. The magnetic permeability and saturating flux density favor Fe-Si laminations.

The production of machines can benefit from powdered iron material if the machine geometry requires complex three-dimensional forms. However, the surface of the powdered iron pieces is limited due to the rating of the hydraulic punch available in the industry. For a large machine, the stator will need to be segmented into a large number of smaller pieces, as it is the case for large machines with laminations. In this respect, no advantage is expected in terms of manufacturing for simple geometries.

Finally, the price of powdered iron material has been compared to the price of standard Fe-Si laminations, which have been found to be more or less equivalent.

In conclusion, because of their lower iron losses in the range of frequencies considered in this study, Fe-Si laminations should be used as much as possible. It appears that the main interest for powdered iron is in magnetic geometries which are either difficult to produce with laminations or have an inherent three-dimensional flux path.

6.5. Construction of flux-concentrating TFPM geometries

A number of authors have emphasized the possible advantages of TFPM machines, but also the difficulties of building them. If TFPM machines are to be produced in large quantities, the manufacturing process should be carefully investigated. It is especially true in the case of flux-concentrating TFPM machines, as commented in [Dic 2002].

In most cases, the winding of conductors in TFPM machines is simpler than winding the coils of a polyphase conventional PM synchronous machine with a large number of poles. However, other parts of the TFPM machine have important production difficulties. Some of these problems are:

- presence of a double-sided stator in many flux-concentrating TFPM structures;
- dependence of each magnet location on the total build-up of mechanical tolerances due to the other rotor pieces;
- manual placement of the rotor magnets and flux concentrators.

These three points are here further discussed.

6.5.1. Double-sided stator

The double-sided stator arrangement of figure 6-1 and figure 6-2 provides very little space for mechanically retaining the magnets and flux concentrators to the rotor. One possibility is to fix each flux concentrator to a rotor disk or ring on one side, by means of screws or by gluing the flux concentrators to that rotor ring. From the production point of view, this is probably a time-consuming method. Also, the double-sided stator will give rise to some difficulties during insertion of the rotor in between the two rows of stator cores. Although many schemes can be imagined, it will be difficult to retain the magnets and flux concentrators from both sides during insertion.

Another point concerning the double-sided stator is the inherent low mechanical stiffness, due to the presence of two rows of magnets and flux concentrators. Each row can only be retained from one side, and must be mechanically joined together in the central part. The attachment of the two rows of magnets together is a difficulty which can hardly be overcome in an elegant manner and which will probably lead to a weaker machine construction.

A last point concerning the double-sided stator is the presence of two clearance air gaps radially on either side of the rotor. This complicates the mechanical design, with an additional requirement of very low thermal expansion or contraction in the radial direction. The expansion and contraction of both rotor and stator must be thoroughly equal in the radial direction, in order to avoid the rotor from touching the stator on one of the two sides. The double-sided air gap also requires lower mechanical tolerances in the radial direction, when manufacturing all the parts.

6.5.2. *Mechanical circumferential tolerances in the rotor*

All flux-concentrating TFPM machines described in the scientific literature have one or two rows of a circular arrangement of magnets and flux concentrators stacked one next to the other, as shown in figure 6-14.

Usually, the pieces of figure 6-14 are fixed one to the other with glue. Unfortunately, there are intrinsic mechanical tolerances in the circumferential direction, related to the manufacturing of either the magnets or the flux concentrators. These tolerances add up in the arrangement of figure 6-14, making the exact location of each piece of magnet or flux concentrator dependent upon the sum of the mechanical tolerances caused by all the other pieces in the ring. Of course, it is possible that such tolerances cancel one another, but this is probably not the case with pieces made in one production batch. This difficulty is also pointed out in [Bli 2000].

6.5.3. *Manual placement of rotor pieces*

The construction of a rotor ring, as the one shown in figure 6-14 is a time-consuming task. The presence of attracting and repulsive forces between magnetized pieces and flux concentrators along with the use of glue to fix the pieces together require softness, precision and adjustment. It will be difficult for a machine to perform this operation without human intervention. This is especially true when it comes to closing the ring on itself, where little space becomes available between the two ends of the rings. Then it will become difficult for a tool or a machine to work in that area.

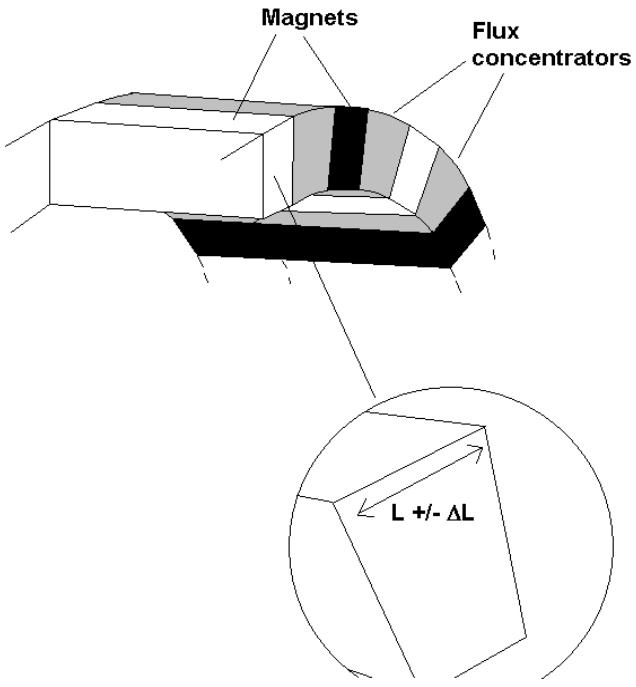

Figure 6-14: Stacking of permanent magnets and flux concentrators in most TFPM structures with flux concentration.

6.6. Derivation of a TFPM topology with toothed rotor

In chapter 4, it was expected that TFPM machines would probably offer higher torque/mass and lower cost/torque than the conventional PM synchronous machine. However, it was also indicated that more thorough comparison should be made between the two machine types. The aim of the remaining chapters of this thesis is to provide a complete performance optimization and comparison in the same way as it was done in chapter 4 for longitudinal machines. At this point, such a comparison is rather meaningless because many of the flux-concentrating TFPM machines discussed in this chapter encounter important difficulties in construction. In this context, a comparison based only on the mass and cost of active material is not sufficient. It may be the case that a given machine topology is much cheaper in active material, but very expensive in labor costs. An honest comparison should identify machine topologies that are reasonably equal in terms of construction.

Although it is not the aim of this thesis to detail the various steps of building a machine and neither to describe the construction costs, various points have been identified in this chapter:

- the stator should be single-sided;
- the rotor PM and flux concentrators should not be dependent upon the build-up of mechanical tolerances in the circumferential direction;
- the installation of rotor parts (PM and flux concentrators) should be automated as much as possible;
- the flux circulation should be such that laminated steel can be used in the stator.

Inspecting the five flux-concentrating TFPM topologies identified above, none of them meet these four characteristics. In this respect, we would like to contribute to the field of TFPM structures by deriving a new topology. The name given to that machine is TFPM machine with toothed rotor.

The starting point for the derivation of the TFPM machine with toothed rotor is figure 6-2, since the double-sided single-winding TFPM machine with U-core arrangement makes use of laminated steel and provides rather good torque performance. The topology derived here supports the two lamination orientations shown in figure 6-12. No concluding quantitative comparison between the iron losses of a perpendicular lamination and those of a parallel lamination placed in the above-stated conditions could be found in the available scientific literature. Therfore, we adopt here a lamination plane perpendicular to the direction of motion for easier construction. The comparison of iron losses for the two lamination orientations is left for further studies.

The double-sided stator is made single-sided, by moving the lower stator cores to the upper side. This first step is shown in figure 6-15. The next step is the addition of a guiding structure to the rotor. The guiding structure solves both the problems of the circumferential mechanical tolerances and automation of the rotor production process. This guiding structure is built from a stack of toothed laminations in the rotor, as shown in figure 6-16. Each magnet

piece of figure 6-15 can be cut in two magnets with the same direction of magnetization. These two magnets with identical directions of magnetization are placed on each side of the tooth, as shown in figure 6-17. One of the main problems in single-sided TFPM stators is the stator leakage flux between the stator C-core part of figure 6-17 and the I-core.

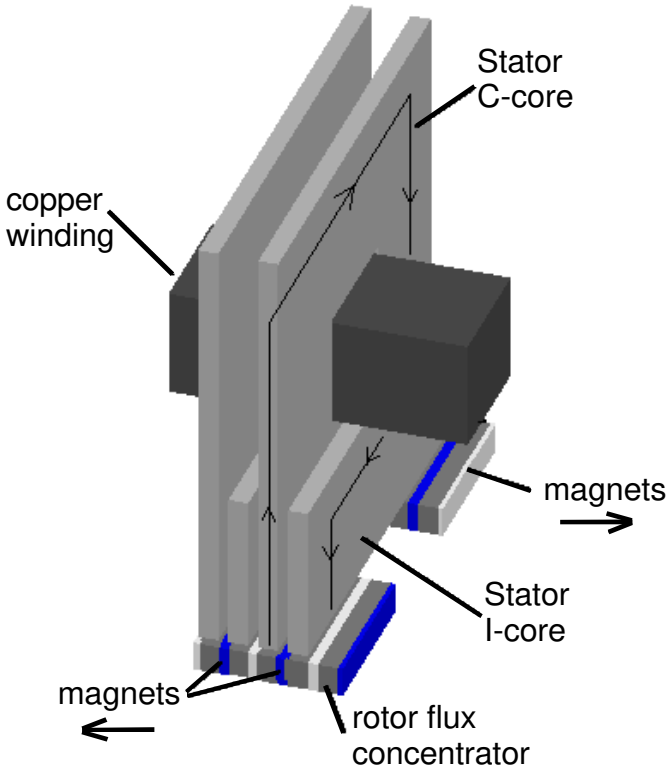

Figure 6-15: (Step 1): Single-stator version of figure 6-2.

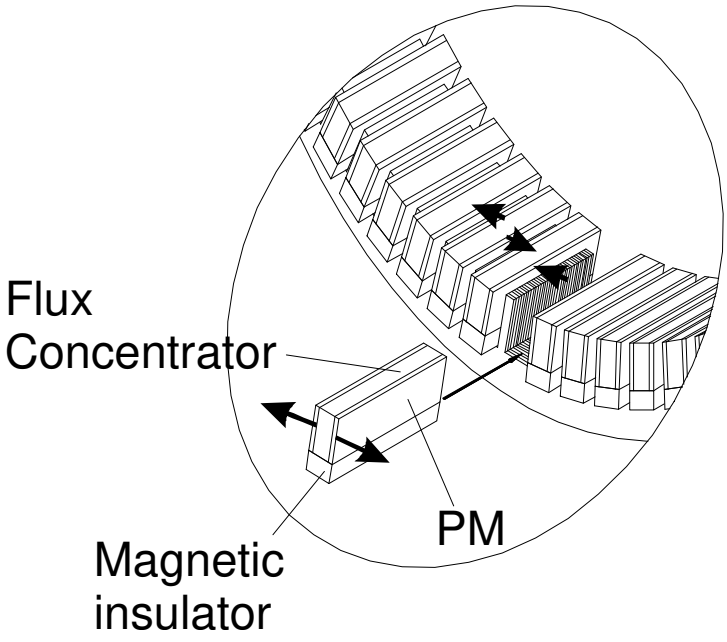

Figure 6-16: Introduction of a toothed rotor structure.

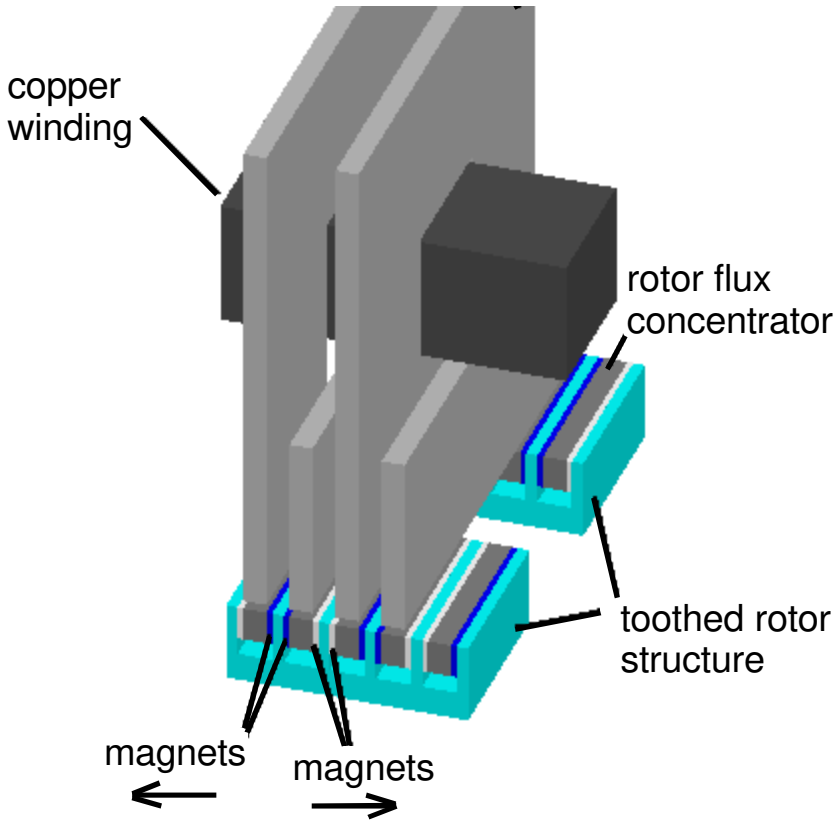

Figure 6-17: (Step 2): insertion of the toothed rotor to figure 6-15.

This can be partly overcome by forming the I-core into a trapezium and by shaping the C-core into a horseshoe with a foot, as shown in figure 6-18. This reduces the area of flux leakage between the two stator cores.The insertion of the toothed structure has formed an additional leakage path between the stator horseshoe and the trapezoidal flux return. The performance of the machine of figure 6-18 can be further increased, by slightly reducing the rotor tooth height. A factor 3-4 between the clearance air gap and the stator-tooth distance is generally sufficient to reduce the tooth leakage flux to negligible levels. The reduction of the rotor teeth height is shown in figure 6-19.

The stator leakage flux can be reduced further, if the flux concentrators and magnets are made slightly longer than the rotor stack, as shown in figure 6-20. The stator horseshoe is made a little longer, thus reducing further the leakage area between the stator horseshoe and the stator trapezium. In that case, the flux concentrators are also used to carry the flux in the axial direction. This final step is shown in figure 6-20 and figure 6-21, which display the proposed TFPM machine with toothed rotor.

Shortcomings related to the toothed rotor

Although many advantages result from the use of a toothed rotor from a construction point of view, one main shortcoming is identified. For structural requirements, the teeth used in the rotor have a minimum width of 2 - 4 mm. This additional width increases slightly the pole pitch and reduces the number of poles available in the total circumference. This reduces the

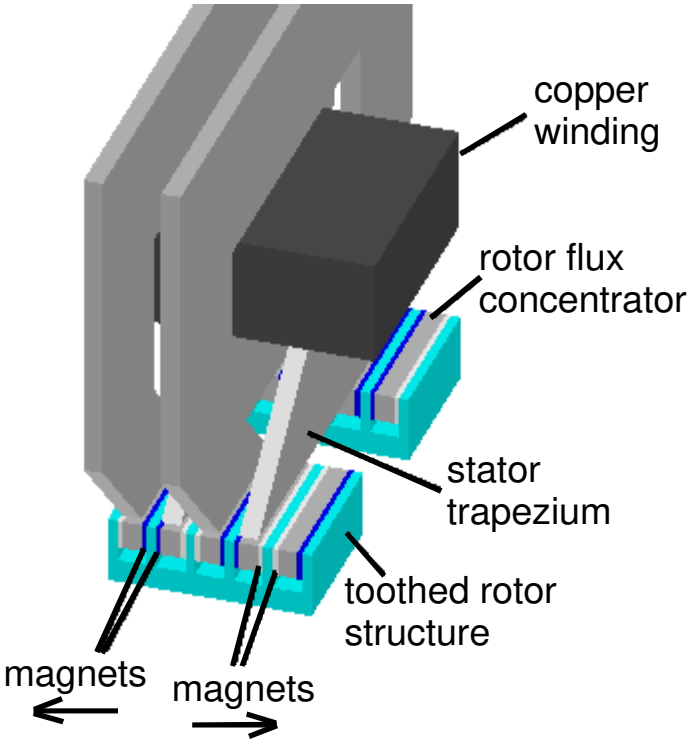

Figure 6-18: (Step 3): Reduction of stator leakage by using a stator horseshoe and a trapezoidal flux return.

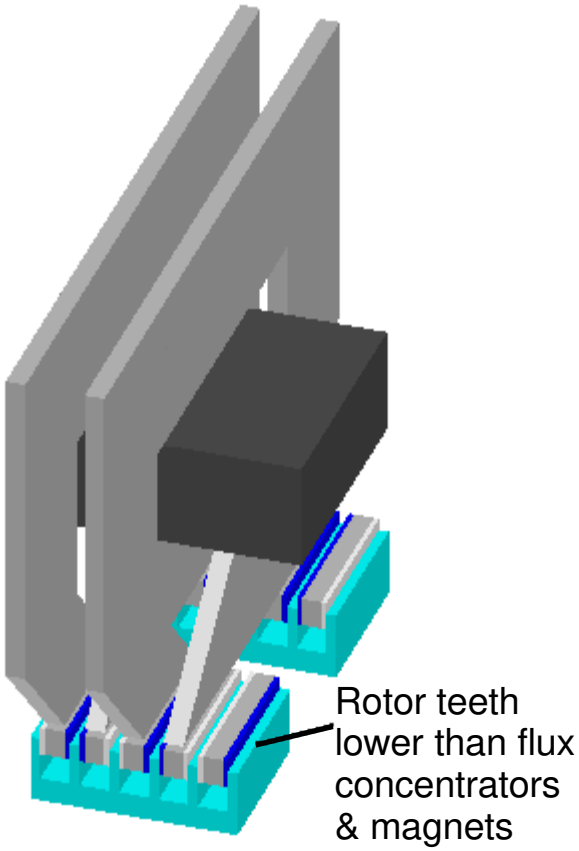

Figure 6-19: (Step 4): Reduction of the rotor teeth height.

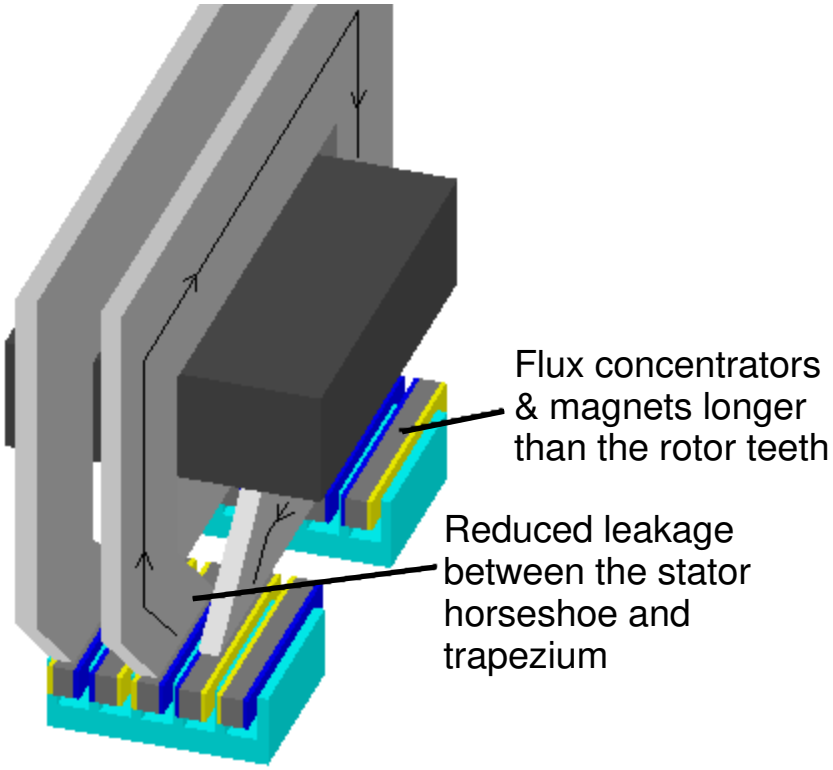

Figure 6-20: Final result: TFPM machine with toothed rotor.

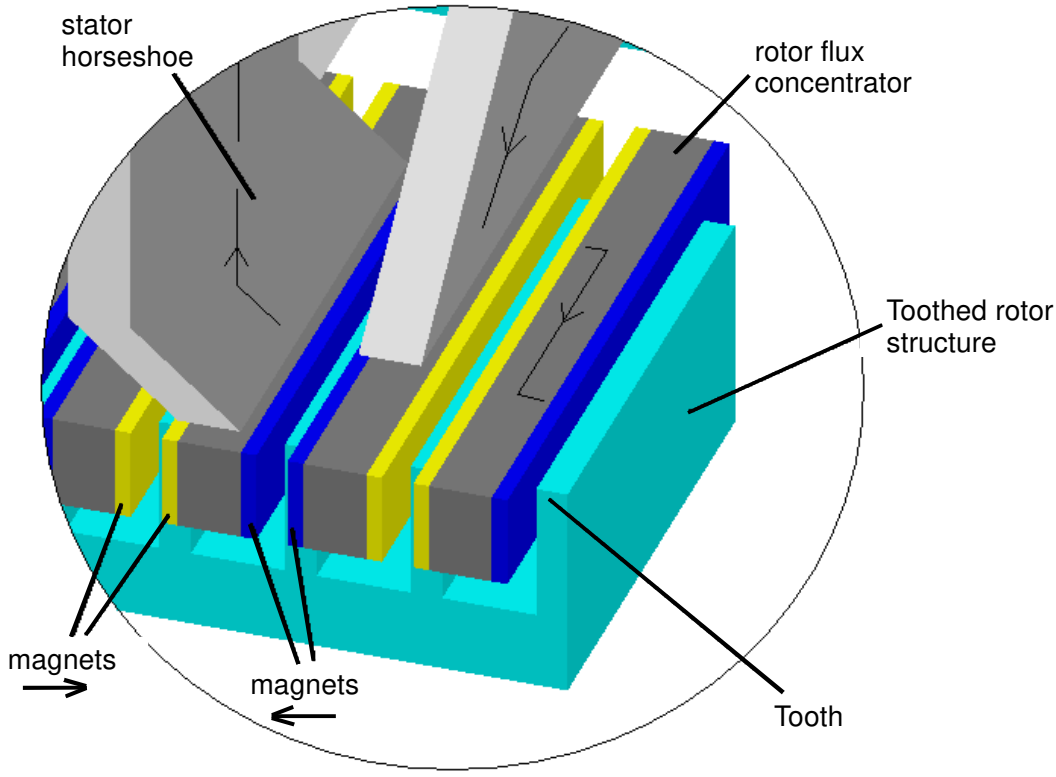

Figure 6-21: Close-up on the TFPM machine with toothed rotor.

total tangential force and gives a lower torque, compared to the machine structure of figure 6-2. This is the price to pay for a toothed rotor.

6.7. Conclusion

Five topologies of flux-concentrating TFPM machines have been reported in literature and described here. Also, six prototypes of flux-concentrating TFPM machines have been reported in past literature. Among the five topologies described in past papers, the clawpole TFM machine appears as the most promising. The torque/mass and cost/torque performance of the built prototypes also give the best value. However, the clawpole TFM machine makes a massive use of powdered iron, which has higher specific losses than 0.35 mm and 0.5 mm Fe-Si laminations. Also, the relative permeability and saturation flux density of powdered iron is lower than Fe-Si steel.

Unfortunately, among all existing concepts of flux-concentrating TFPM machines, none is satisfactory in terms of construction characteristics. Four characteristics are desirable for an improved machine version:

- the stator should be single-sided;
- the rotor PM and flux concentrators should not be dependent upon the build-up of mechanical tolerances in the circumferential direction;
- the installation of rotor parts (PM and flux concentrators) should be automated as much as possible;
- the flux circulation should be such that laminated steel can be used in the stator.

A new TFPM geometry is derived in this chapter, which fulfills these characteristics. The new concept is named TFPM machine with toothed rotor. It is not expected that the TFPM machine with toothed rotor can reach the high torque performance of the clawpole TFM, because of the use of teeth in the rotor. With such toothed rotor, the pole pitch cannot be made as low as in the case of other flux-concentrating TFPM machines. However, the expected improvement in construction makes it an attractive concept.

Chapter 7

Modeling of the TFPM machine with toothed rotor

7.1. Introduction

In the last chapter, several TFPM topologies have been discussed and a new geometry has been proposed, which fulfills the criteria of improved manufacturing and use of laminations in the stator. For the rest of the thesis, the choice is made to analyze the TFPM machine with toothed rotor in detail and ultimately investigate how it will compare to the conventional PM synchronous machine. Although, we chose to limit ourselves to one specific machine topology, we believe that the methods proposed in this chapter could also be applied to other flux-concentrating TFPM topologies.

As was done for longitudinal topologies in chapter 4, an optimization program should also be written for the TFPM machine with toothed rotor in order to obtain the machine design with the best torque/mass and cost/torque performances. Then, a valuable comparison can be achieved. The fastest way to optimize a machine design is to analytically express the machine magnetic quantities like reluctances, no-load flux, stator MMF and torque as a function of the machine geometrical parameters. Then, those analytical expressions can be implemented in a computer program, as was done in chapter 4. The various input parameters can be varied within a certain range and a large number of combinations can be tested.

In longitudinal machines, analytical expressions for the no-load flux linkage could easily be written by assuming that the magnetic fields crossed the air gap perpendicularly. However, field modeling is much more complex in a TFPM machine because the pole pitches are generally short (e.g. 10 mm) and the leakage fluxes in all three dimensions must be taken into account. This problem could eventually be addressed by solving Maxwell's equations analytically with the three-dimensional boundaries of a TFPM structure, as attempted in [Lan 2001]. We judge this as a very difficult mathematical problem and it is not the direction that is followed in this chapter. The difficulty is further increased if core satu-

ration must be included in the mathematical model. As a matter of fact, saturation is a determining limitation to the maximum torque value of a TFPM machine.

Optimization of TFPM machines has been discussed in a number of scientific publications. In [Har 1996], optimization is performed with finite element analysis (FEA), but the optimization is done by varying only the pole pitch around a certain value, while keeping constant some of the geometrical ratios. In the latter case, the objective was to increase the nominal torque value. In [Hen 1997], optimization is done with three-dimensional FEA, by defining a range of variations for the 5 geometrical parameters identified for the machine under investigation. Then a 3-D FEA is run only for the maximum and minimum values of the range (in total 2^5 simulations are required for 5 variables). The optimal design is determined by interpolating the torque value within that 5 variable space. In [Mad 1998], optimization is performed on the clawpole TFM by using 3-D FEA. However, in that case only two parameters are allowed to vary independently from one another and the optimization objective is the torque output. In [Mec 1996], an optimization is also performed using 3-D FEA. In that case, a number of geometrical parameters are kept constant while the pole pitch is allowed to vary. In [Dic 2002], optimization is performed on a surface-mounted PM clawpole machine, which is also a TFPM machine. In that case, a magnetic circuit is first derived which represents the machine geometry with its main flux path and its leakage paths. Then each reluctance is given an analytical expression relating its value to the geometrical parameters and a complete optimization is performed by using genetic algorithms. The final results were checked with 3-D FEA and refined optimization could be achieved with 3-D FEA.

From the scientific literature available, it appears that using 3-D FEA to optimize a machine geometry with a large number of variable geometrical parameters in a wide range of values is not practical. This point has been mentioned in [Har 1996] and [Hen 1997]. It is also the author's experience that if an optimization has to be carried out with 3-D FEA where all combinations of the machine geometrical data must be tested, the time required for processing all these FEA solutions will be very long (months!). The method used by all authors, except Dickinson *et al* (see [Dic 2002]) limits the number of variable parameters and uses torque as the optimization criterion. This has the following disadvantages:

- the full multi-dimensional space is not investigated for the search of the optimum. Only a thin area of that space is investigated;
- optimizing cost/torque instead of torque alone may possibly require a wider search space because of the high specific cost for PM;
- efficiency is an important parameter, which also requires that a wider search space be used. For example, a short pole pitch is often beneficial to the torque and torque/mass, but it tends to decrease efficiency;

The need to explore a wide multi-dimensional space for the identification of an optimal design in terms of cost/torque and torque/mass was addressed by the author in [Dub 2002a][Dub 2002c] and the detailed description of this method is given in this chapter.

A mathematical model is developed in this chapter in order to predict the torque of the TFPM machine with toothed rotor. The mathematical model is derived from localized (or lumped) reluctances of the magnetic circuit, as in [Dic 2002]. The originality of the method

presented in this chapter is in the way each lumped reluctance is mathematically modeled by solving a number of FEA simulations performed on simplified geometries. A linear regression is then performed on the results of FEA simulations and a descriptive law is extracted linking each lumped reluctance to the geometric data of the machine.

In section 7.2, the machine torque is expressed in terms of the pole magnetic quantities instead of the machine voltage and currents. In section 7.3, the magnetic circuit of the TFPM machine with toothed rotor is derived. In section 7.4, each reluctance of the magnetic circuit is given an expression based on a large sample of FEA simulations. In section 7.5, the validity of the model is discussed and section 7.6 describes the machine losses and efficiency.

7.2. Torque expression for a single-phase machine with saliency

This section derives a torque expression as a function of the machine macroscopic quantities like current, voltage and inductance in the case of a single-phase machine with saliency. Then, a more useful torque expression will be derived, which expresses the average nominal torque in terms of the machine magnetic quantities per pole pair.

The structure of the TFPM machine with toothed rotor implies saliency, i.e. a variation in the inductance seen by the stator winding as a function of the electrical angle. In fact, this is also the case for other flux-concentrating TFPM machines. To derive a torque expression as a function of the machine current, voltage and inductance, we make the following assumptions:

- 1) the no-load voltage is assumed as varying sinusoidally with time;
- 2) the stator current is assumed as varying sinusoidally with time;
- 3) the magnetic circuits are linear. Saturation is not considered;
- 4) the inductance seen by the stator winding is assumed as varying sinusoidally with the electric angle α as follows:

$$L_s(\alpha) = \left[\frac{L_a + L_u}{2}\right] + \left[\frac{L_u - L_a}{2}\right]\cos(2\alpha) \qquad (7\text{-}1)$$

where L_s is the inductance seen by the stator coil, L_a is the inductance seen by the stator core in the aligned position, L_u is the inductance seen by the stator core in the unaligned position and α is the electrical angle of the rotor with respect to the unaligned position.

Assumption 3) is of high importance. At this point, the stator iron will be considered as non-saturable. The linear model derived in this chapter will use this assumption. However, saturation will be introduced in chapter 8, before proceeding to the design optimization.

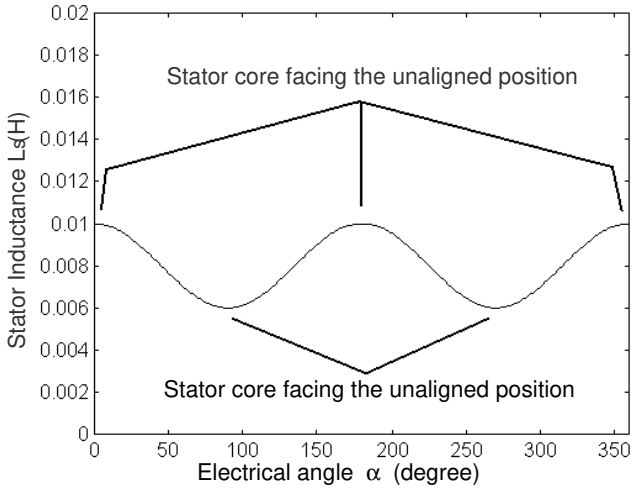

Figure 7-1: Sinusoidal variation of the stator inductance

Using these assumptions, appendix VI derives an expression (equation (VI-23)) for the average electrical power P_{elec} in the case of a single-phase, multi-pole machine with saliency. Inserting equation (VI-23) into equation (3-6), the average power balance allows writing the average torque as:

$$\overline{T} = \frac{EI\cos\psi + \frac{\pi I^2 f}{2}(L_a - L_u)\sin 2\psi + P_{Fe}}{\omega_m} \tag{7-2}$$

The second term in the numerator of equation (7-2) is the reluctance torque and is the same expression as derived in [Sen 1997] for a single-phase synchronous reluctance machine.

In the case of TFPM machines, it is more practical to express the nominal average torque $\overline{T}$ in terms of the magnetomotive force T_s and no-load flux per pole pair $\hat{\Phi}_{pnl}$, because saturation in the stator core occurs as a consequence of these two quantities. In the process, we can get rid of the number of turns in the stator coil N_s.

From Faraday's law, a sinusoidal rms no-load voltage E may be related to the amplitude of the no-load flux per pole-pair $\hat{\Phi}_{pnl}$.

$$E = \sqrt{2}\pi\frac{n}{60}p^2 N_s \hat{\Phi}_{pnl} \tag{7-3}$$

Also, the inductances L_a and L_u can be expressed in terms of their reluctances U_{ap} and U_{up} per pole pair.

$$\begin{aligned} L_a &= \frac{N_s^2 p}{\Re_{ap}} \\ L_u &= \frac{N_s^2 p}{\Re_{up}} \end{aligned} \tag{7-4}$$

Equation (7-3) and equation (7-4) are inserted into equation (7-2). We obtain*:

$$\bar{T} = \frac{p^2}{2}\left[\hat{\Im}_s\hat{\Phi}_{pnl}\cos\psi + \frac{\hat{\Im}_s^{\,2}}{4}\left(\frac{1}{\Re_{ap}} - \frac{1}{\Re_{up}}\right)\sin 2\psi\right] + \frac{P_{Fe}}{\omega_m} \tag{7-5}$$

where $\hat{\Im}_s$ is the amplitude of the stator magnetomotive force, as defined by:

$$\hat{\Im}_s = \sqrt{2}N_s I \tag{7-6}$$

7.3. 3-D magnetic circuit of one pole pair

Equation (7-5) depends upon the amplitude of the no-load flux per pole pair $\hat{\Phi}_{pnl}$, the reluctances per pole pair U_{ap} and U_{up} and the magnetomotive force $\hat{\Im}_s$. Here, the values of $\hat{\Phi}_{pnl}$, U_{ap} and U_{up} are determined from equivalent magnetic circuits obtained from localized (lumped) reluctances.

Again, we comment on the fact that the reluctances derived here have constant values and do not depend upon the current value. This is valid until core saturation is reached. In the latter case, core saturation MUST be included in the analytical model. It will be introduced in chapter 8.

7.3.1. Magnetic circuit used for $\hat{\Phi}_{pnl}$

To determine the no-load flux per pole pair $\hat{\Phi}_{pnl}$, a magnetic circuit taking into account the various leakage paths is used. The flux paths and leakage paths are modeled by reluctances. These lumped reluctances are shown in figure 7-2 and figure 7-3. These lumped parameters and their corresponding descriptions are as follows:

- $\Im_m$ = MMF of a single permanent magnet;
- U_m = reluctance of a single permanent magnet;
- U_g = lumped reluctance of the air gap;
- U_{ctc} = lumped reluctance of the leakage path between the stator horseshoe or trapezium and the rotor flux concentrator of the neighboring pole;
- U_{LEC} = lumped reluctance of the leakage between two adjacent flux concentrators through their ends on one side;
- U_{Ccore} = reluctance of the iron in the stator horseshoe;

* About equation (7-5), it must be noted that in [Dub 2002c], a similar expression is used where the two reluctances are inverted within the parenthesis. This sign difference is a consequence of the sign convention (generator or motor). In [Dub 2002c], the machine was assumed to be working as a motor, while here we assume the machine to be operated as a generator.

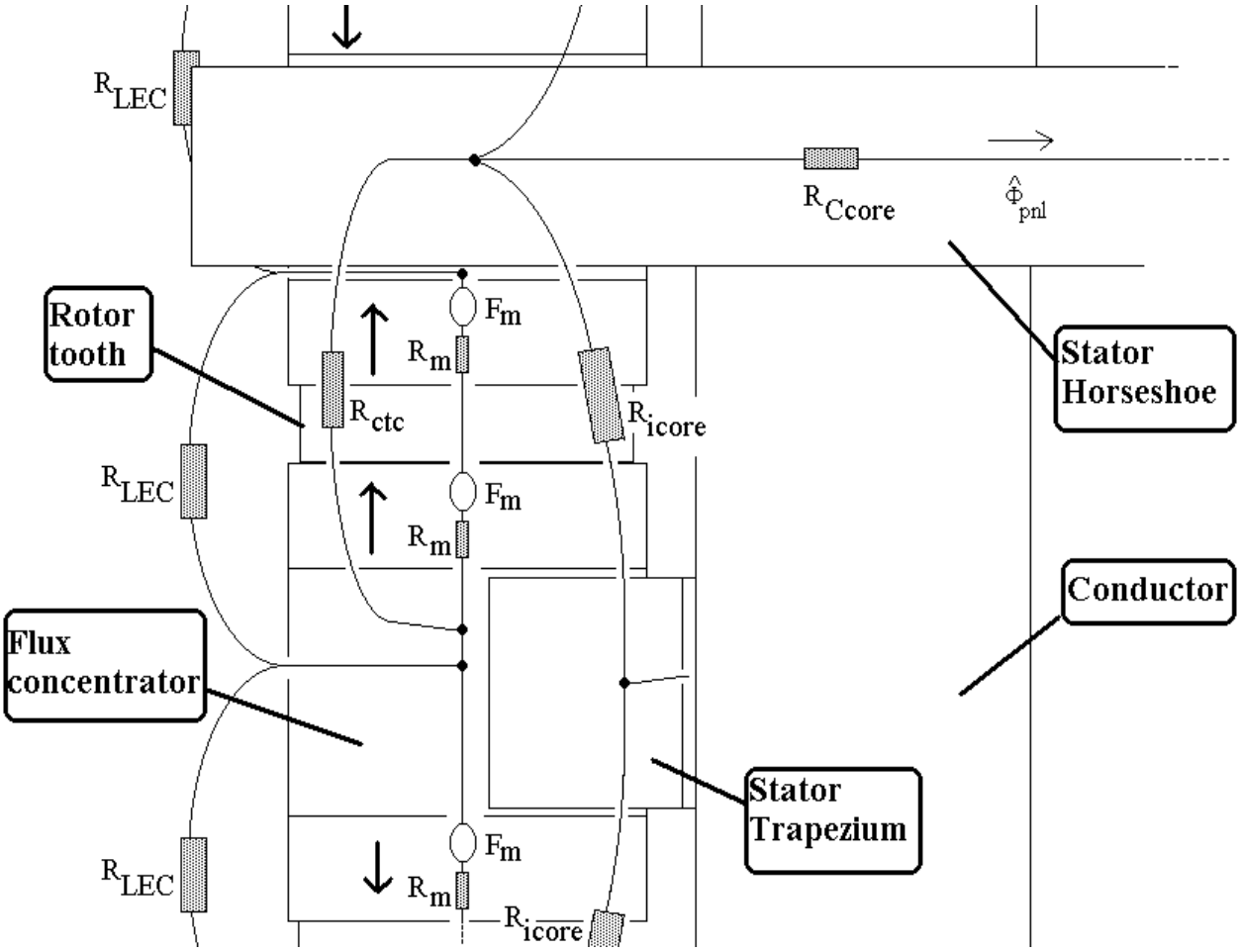

Figure 7-2: Top view of the TFPM structure with toothed rotor.

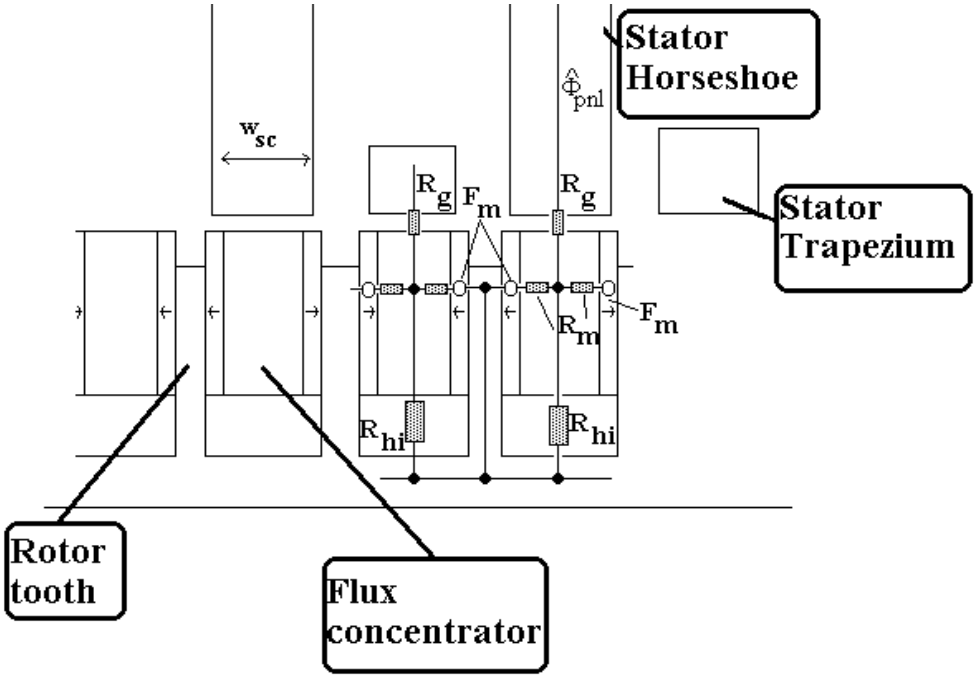

Figure 7-3: Side view of the TFPM structure with toothed rotor.

- $\mathcal{U}_{SScore}$ = reluctance of the iron in the stator trapezium;
- $\mathcal{U}_{hi}$ = lumped reluctance of the leakage between the flux concentrator and the rotor core through the slot;
- $\mathcal{U}_{icore}$ = lumped reluctance of the leakage between one stator horseshoe and one trapezoidal stator core.

From figure 7-2 and figure 7-3, an equivalent magnetic circuit is derived and is illustrated in figure 7-4. It must be noted that reluctance $\mathcal{U}_{icore}$ of the leakage path between the trapezium and the C-core is not included in the model of figure 7-4 due to the circuit symmetry. The mmf difference between the stator horseshoe and the stator trapezium is nearly zero. In fact, if the iron permeability was infinite, then the mmf difference would be equal to zero. For this reason, the leakage between the two stator cores is negligible in the calculation of the no-load flux per pole pair $\hat{\Phi}_{pnl}$ and we chose to eliminate $\mathcal{U}_{icore}$ from the magnetic circuit.

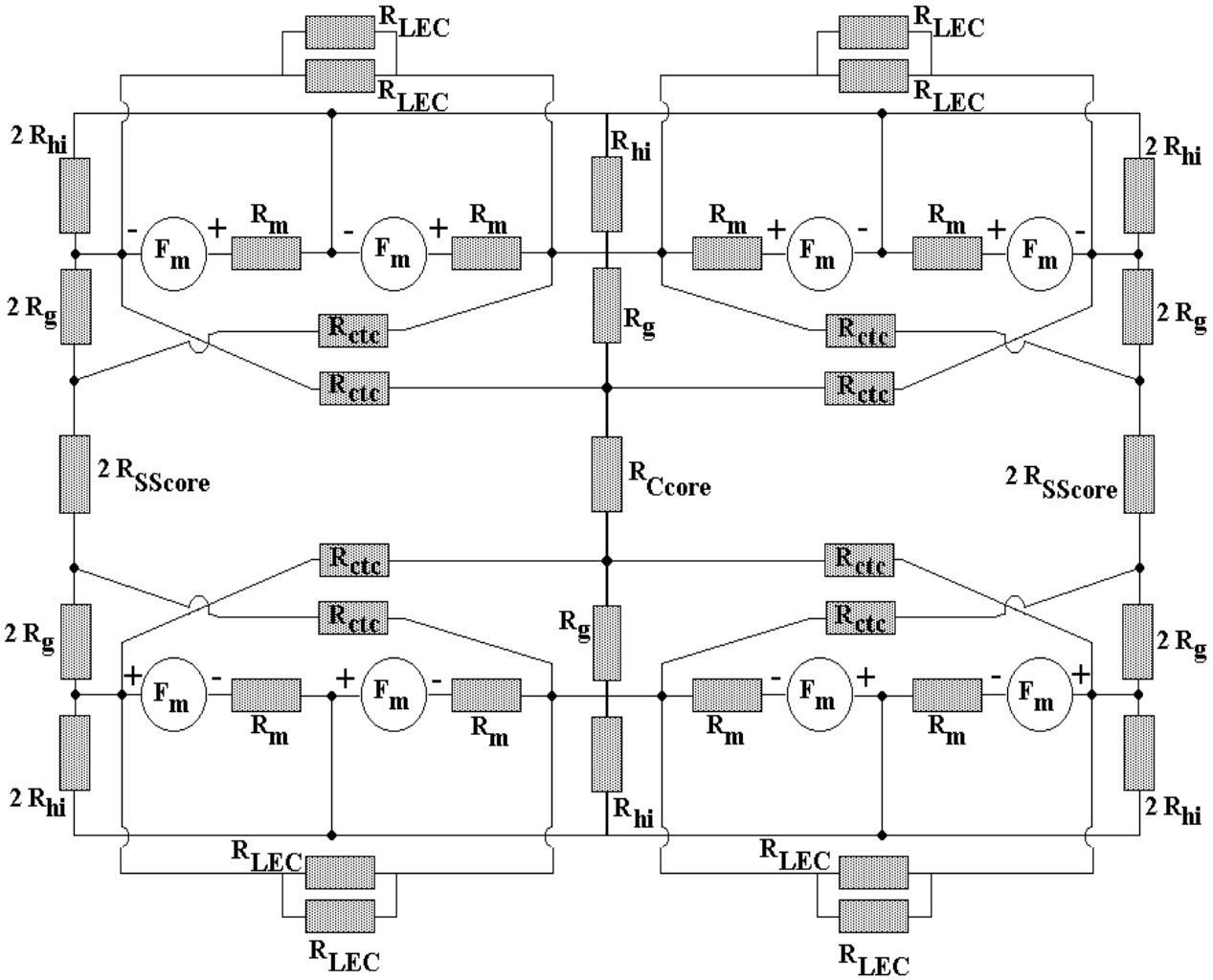

Figure 7-4: Magnetic circuit representing one pole pair in the aligned position, without current flowing in the stator winding

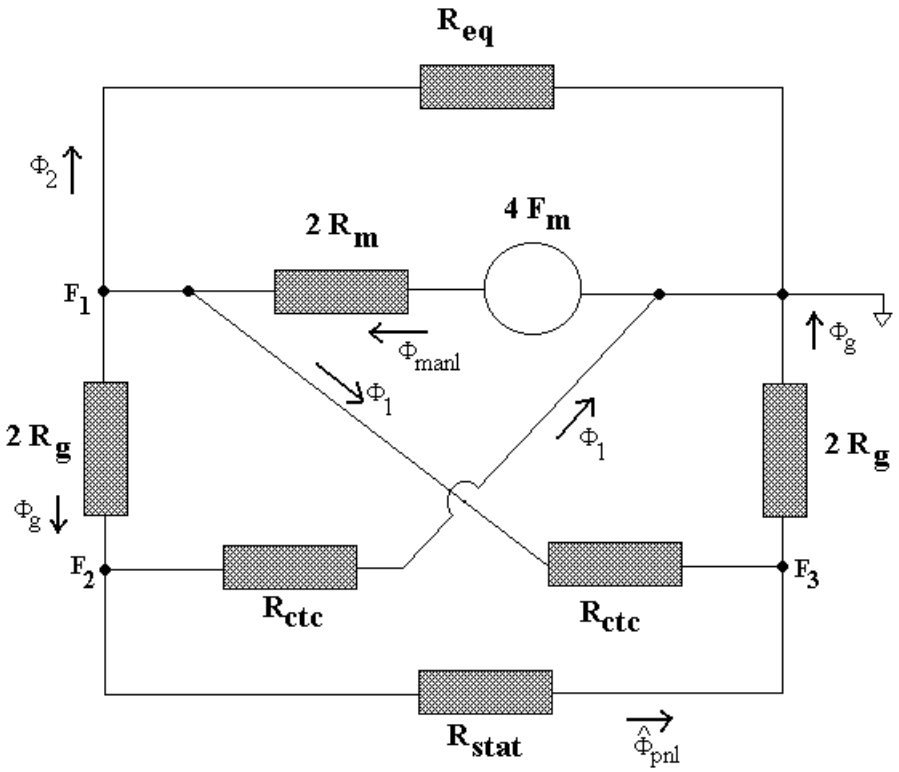

Figure 7-5: Final simplification of the magnetic circuit for the no-load flux in the stator core.

The magnetic circuit of figure 7-4 appears as complex. It can be simplified by taking symmetry into account, leading to one quarter of the circuit of figure 7-4. The resulting circuit is shown in figure 7-5.

Using basic circuit analysis, the no-load flux per pole pair $\hat{\Phi}_{pnl}$ can be derived from figure 7-5 and expressed by equation (7-7).

$$\hat{\Phi}_{pnl} = \frac{4\Im_m(\Re_{ctc} - 2\Re_g)}{4\Re_g\Re_m + 4\Re_{ctc}\left(2\frac{\Re_m\Re_g}{\Re_{eq}} + \Re_g + \frac{\Re_m}{2}\right) + \Re_{stat}\left(\frac{4\Re_g\Re_m + 2\Re_m\Re_{ctc}}{\Re_{eq}} + 2\Re_g + 4\Re_m + \Re_{ctc}\right)} \tag{7-7}$$

where U_{eq} and U_{stat} are defined as:

$$\Re_{eq} = 4\Re_{hi} \parallel \frac{\Re_{LEC}}{2} = \frac{2\Re_{hi}\Re_{LEC}}{4\Re_{hi} + \Re_{LEC}/2} \tag{7-8}$$

$$\Re_{stat} = \Re_{Ccore} + \Re_{SScore} \tag{7-9}$$

The flux flowing in the magnet in the aligned position at no-load is obtained from:

$$\Phi_{manl} = \frac{4\Im_m\left(1+\frac{\Re_{ctc}}{\Re_{eq}}\right)+\hat{\Phi}_{pnl}(\Re_{ctc}+\Re_{stat})}{2\Re_m+\Re_{ctc}+\frac{2\Re_m\Re_{ctc}}{\Re_{eq}}} \tag{7-10}$$

7.3.2. Magnetic circuit used for the reluctance per pole pair U_{ap} in aligned position

In this section, we look at the reluctance U_{ap} seen by the stator winding in the aligned position. Figure 7-6 illustrates the magnetic circuit seen by the stator winding in the aligned position for one pole pair.

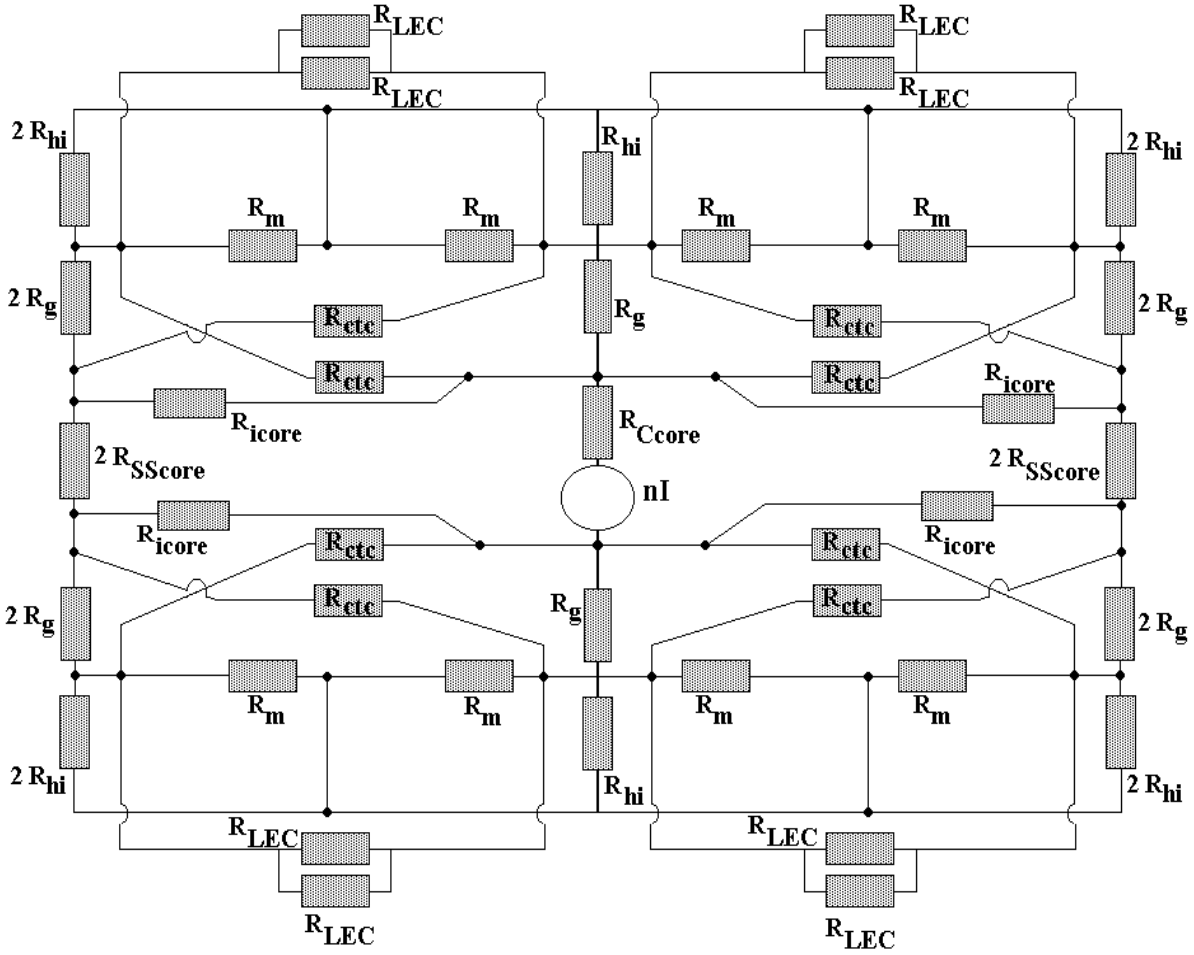

Figure 7-6: Magnetic circuit seen by the stator winding for one pole pair in the aligned position.Again, the magnetic circuit of figure 7-6 can be simplified by taking symmetry into account. Figure 7-7 shows one quarter of the magnetic circuit. Using basic circuit analysis, reluctance U_{ap} seen by the stator winding per pole pair in the aligned position can be derived as:

Again, the magnetic circuit of figure 7-6 can be simplified by taking symmetry into account. Figure 7-7 shows one quarter of the magnetic circuit. Using basic circuit analysis, reluctance U_{ap} seen by the stator winding per pole pair in the aligned position can be derived as:

$$\Re_{ap} = \frac{\Re_{eq3}\Re_{icore}}{\Re_{eq3} + \Re_{icore}} + \Re_{stat} \tag{7-11}$$

where

$$\Re_{eq3} = \Re_{T12} + \frac{(\Re_{T2} + \Re_{ctc})(\Re_{T1} + 2\Re_g)}{\Re_{T2} + \Re_{ctc} + \Re_{T1} + 2\Re_g} \tag{7-12}$$

and where

$$\Re_{T1} = \frac{4\Re_{ctc}\Re_{hi}}{4\Re_{hi} + (\Re_{ctc} + 2\Re_g)\left[\frac{8\Re_{hi}}{\Re_{LEC}} + \frac{2\Re_{hi}}{\Re_m} + 1\right]} \tag{7-13}$$

$$\Re_{T2} = \frac{8\Re_g\Re_{hi}}{4\Re_{hi} + (\Re_{ctc} + 2\Re_g)\left[\frac{8\Re_{hi}}{\Re_{LEC}} + \frac{2\Re_{hi}}{\Re_m} + 1\right]} \tag{7-14}$$

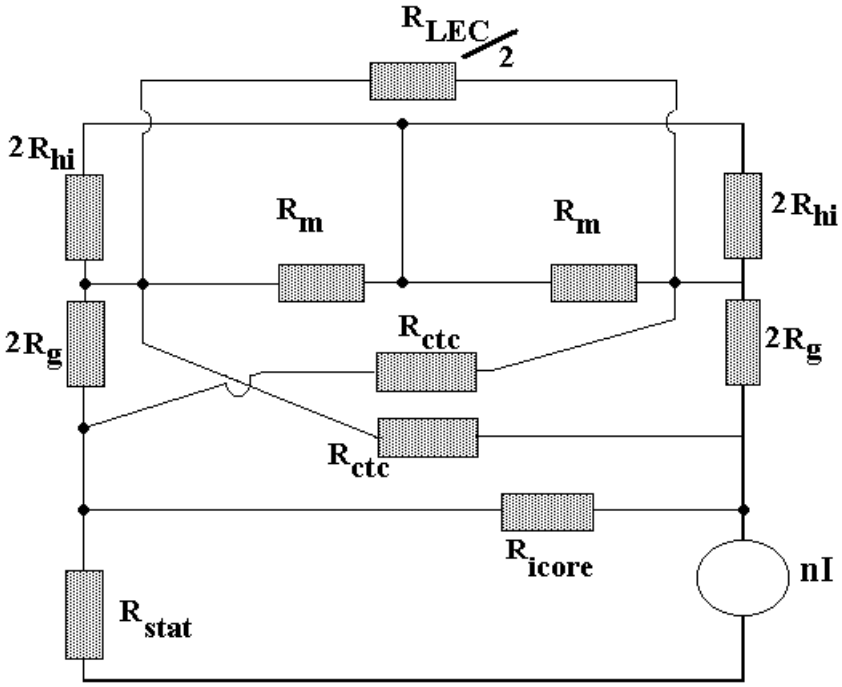

Figure 7-7: Simplified magnetic circuit seen by the stator winding for one pole pair in the aligned position. Simplified from figure 7-6.

$$\Re_{T12} = \frac{2\Re_{ctc}\Re_g\left[\frac{8\Re_{hi}}{\Re_{LEC}} + \frac{2\Re_{hi}}{\Re_m} + 1\right]}{4\Re_{hi} + (\Re_{ctc} + 2\Re_g)\left[\frac{8\Re_{hi}}{\Re_{LEC}} + \frac{2\Re_{hi}}{\Re_m} + 1\right]} \tag{7-15}$$

7.3.3. Magnetic circuit used for the reluctance per pole pair $\mathcal{U}_{up}$ in unaligned position

Figure 7-8 shows the machine stator in the unaligned position. The reluctances shown in figure 7-8 represent the various leakage paths and flux paths created by the stator mmf in the unaligned position.

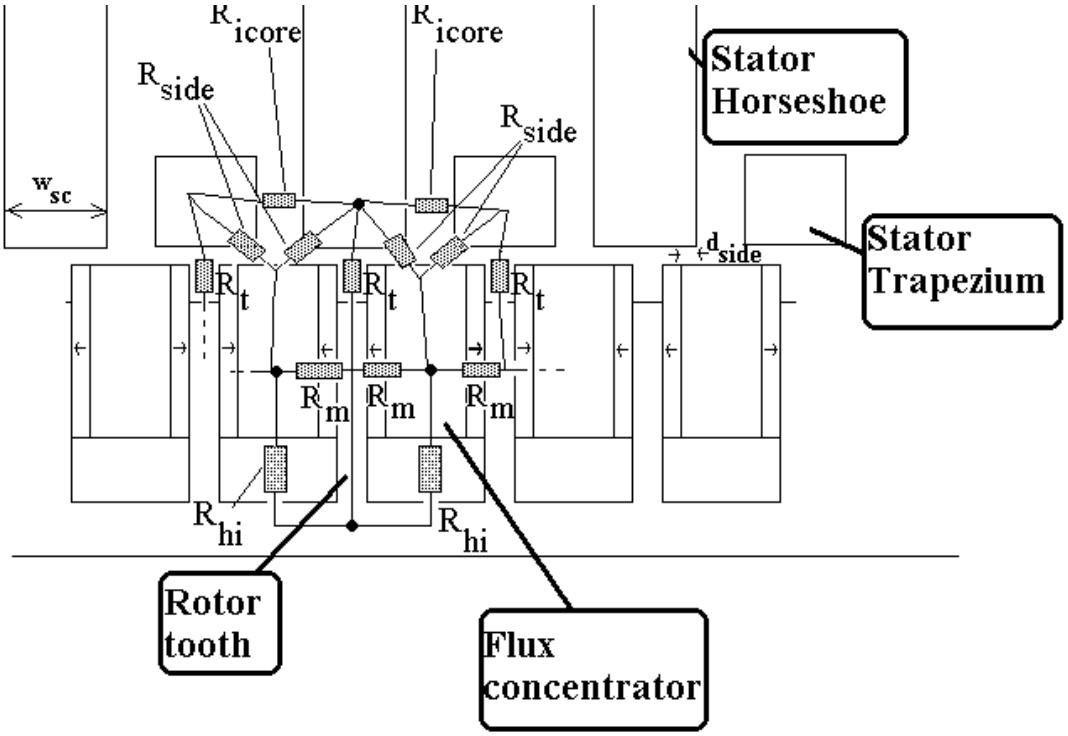

Figure 7-8: Side view of the rotor and stator of the TFPM machine with toothed rotor in unaligned position.

There are 2 new reluctances, which were not identified in the previous sections:

- $\mathcal{U}_t$ = reluctance of the gap between the stator core and the rotor teeth;
- $\mathcal{U}_{side}$ = reluctance between the stator core and the rotor flux concentrator.

The equivalent magnetic circuit is shown in figure 7-9. Here, the magnetic circuit is assumed to be linear. Consequently the flux created by the stator mmf can be considered separately from the flux created by the permanent magnets. To obtain the reluctance seen by the stator winding per pole pair $\mathcal{U}_{up}$ in the unaligned position, it was not necessary to include the permanent magnets mmf in the equivalent magnetic circuit of figure 7-9. Here, the PM are modeled with only a reluctance $\mathcal{U}_m$.

If the flux created by the PM is taken out of the magnetic circuit, the mmf difference between two neighboring flux concentrators will be zero. Therefore, the reluctance $\mathcal{R}_{LEC}$, which represents the leakage between two adjacent flux concentrators is not included in the magnetic circuit of figure 7-9. Also, we neglect the flux leakage through the stator winding window. The width of the window will be large due to the presence of a clearance between the two rows of magnets on the rotor. These two rotor rows being far apart (a distance of 20 times the air gap thickness *g* is used in the design), the two stator feet of a same horseshoe will have a certain distance and the winding window area will be rather rectangular, leading to negligible magnetic flux leakage through the stator conductor. The magnetic circuit of figure 7-9 can be simplified by taking symmetry into account, giving the magnetic circuit of figure 7-10. Using basic circuit analysis, we derive the reluctance $\mathcal{R}_{up}$ as:

$$\Re_{up} = \Re_{stat} + \frac{\Re_A \Re_B}{\Re_A + \Re_B}$$

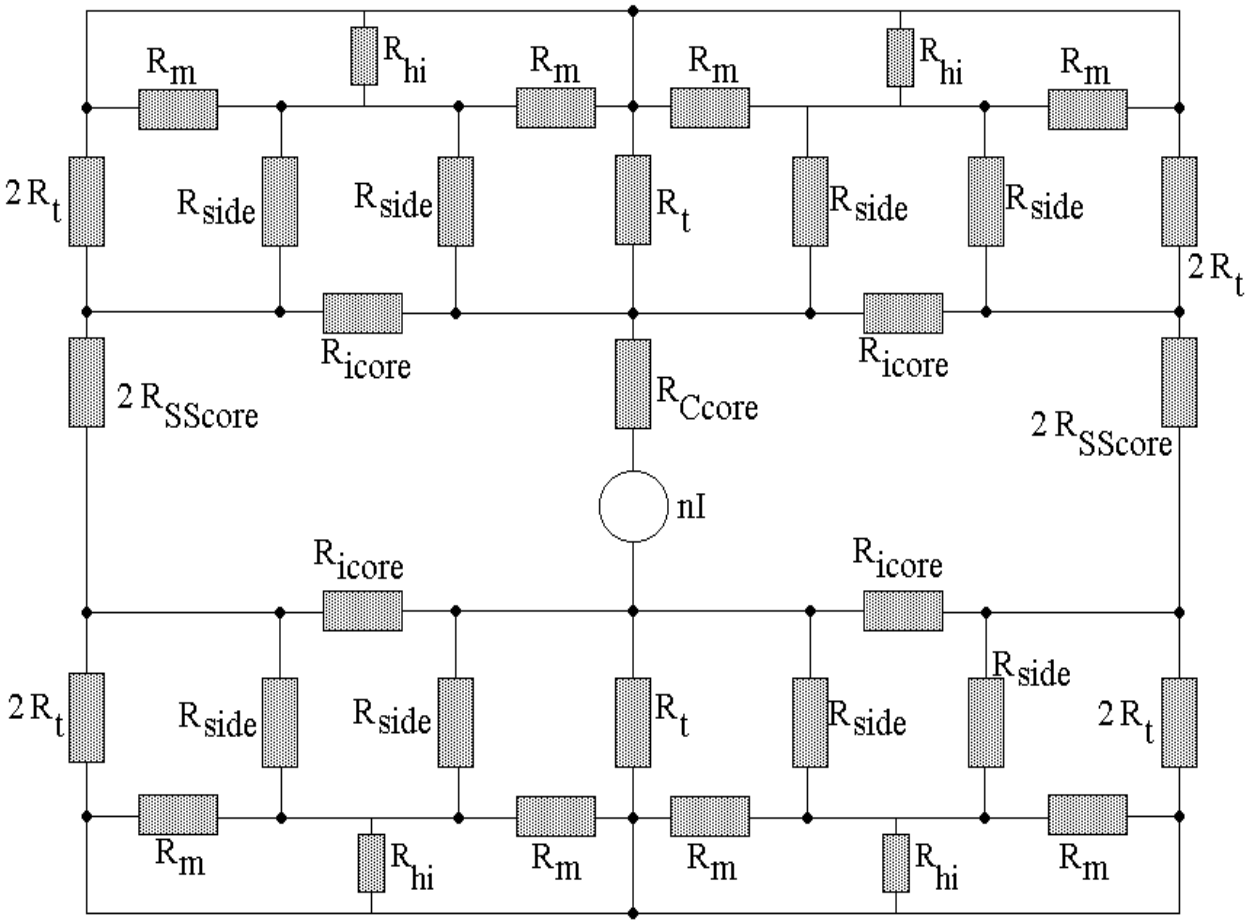

Figure 7-9: Complete magnetic circuit defining the reluctance $\mathcal{R}_{up}$ seen by the stator winding in the unaligned position, for one pole pair of the TFPM machine with toothed rotor.

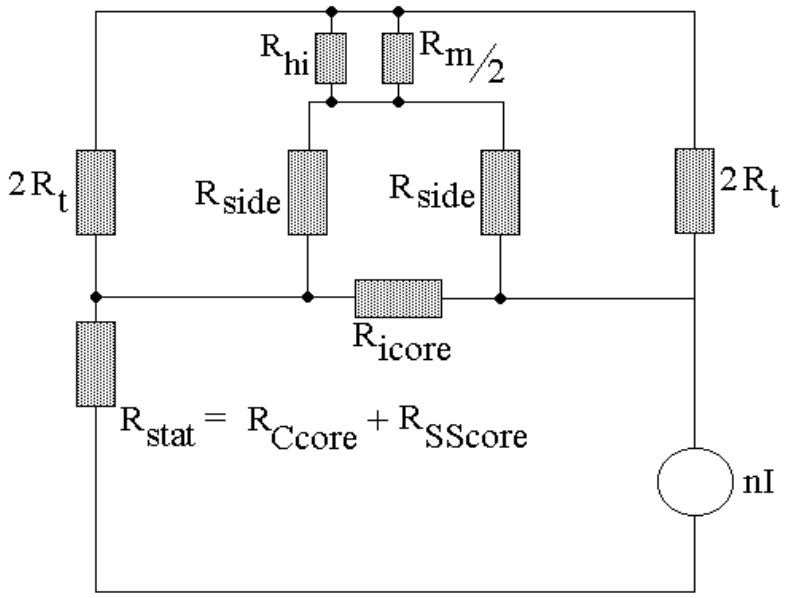

Figure 7-10: One quarter of the magnetic circuit in the unaligned position. Simplified from figure 7-9.

where

$$\Re_A = \frac{4\Re_{icore}\Re_t\left(1+\frac{\Re_t}{\Re_{hi}}+2\frac{\Re_t}{\Re_m}\right)}{\Re_{icore}+4\Re_t\left(1+\frac{\Re_t}{\Re_{hi}}+2\frac{\Re_t}{\Re_m}\right)} \tag{7-16}$$

and where

$$\Re_B = \frac{4\Re_{side}\left[\Re_t+\frac{\Re_{hi}\Re_m}{2\Re_{hi}+\Re_m}\right]}{\Re_{side}+2\Re_t+\frac{2\Re_{hi}\Re_m}{2\Re_{hi}+\Re_m}} \tag{7-17}$$

7.4. Expressions for the lumped reluctances

The equivalent magnetic circuits derived in section 7.3 give expressions relating the reluctances per pole pair U_{ap}, U_{up} (in the aligned and unaligned positions) and the no-load flux $\hat{\Phi}_{pnl}$ to the lumped reluctances of the equivalent magnetic circuits.

In this section, expressions relating the lumped reluctances and mmfs to the geometrical parameters of the TFPM machine with toothed rotor are derived.

7.4.1. Definition of $\Im_m$, $\cup_m$, $\cup_t$, $\cup_{Ccore}$, $\cup_{SScore}$ with 1-D field approximation

For four of the lumped reluctances discussed earlier and for the magnet mmf, the relationship to the machine geometry is determined by assuming that the associated magnetic field moves primarily in one dimension. These components are approximated as follows:

$$\Im_m = \frac{B_r}{\mu_0 \mu_{rec}} h_m \tag{7-18}$$

$$\Re_m = \frac{h_m}{\mu_0 \mu_{rec} l_{rt1} (w_m - h_{ru})} \tag{7-19}$$

$$\Re_t = \frac{h_{ru} + g}{\mu_0 w_{rc1} l_f} \tag{7-20}$$

where
l_{rt1} is the length of the rotor tooth in the axial direction and in this case it is assumed that magnets have the same length l_{rt1} in the axial direction;
h_{rt1} is the slot height;
h_{ri} is the thickness of the insulation layer between the flux concentrator and the slot bottom;
h_{ru} is the distance between the tip of the tooth and the top of flux concentrator
g is the thickness of the air gap;
w_{rc1} is the width of the stator teeth;
w_{rc2} is the width of the flux concentrator;
l_f is the length of the stator foot.

The different geometrical parameters are shown in figure 7-11 and figure 7-12.

Regarding the expression of the reluctance $\cup_t$ between the stator core and the rotor tooth which is given by equation (7-20), the assumption of rectilinear fields in the air gap may appear as suspicious because of the low ratio of tooth width over air gap thickness. Figure 7-13 illustrates a more realistic plot of the flux lines when only $\cup_t$ is considered. However, one consequence of using lumped reluctances is the probability of having two neighboring reluctances enclosing a common volume of the geometry.

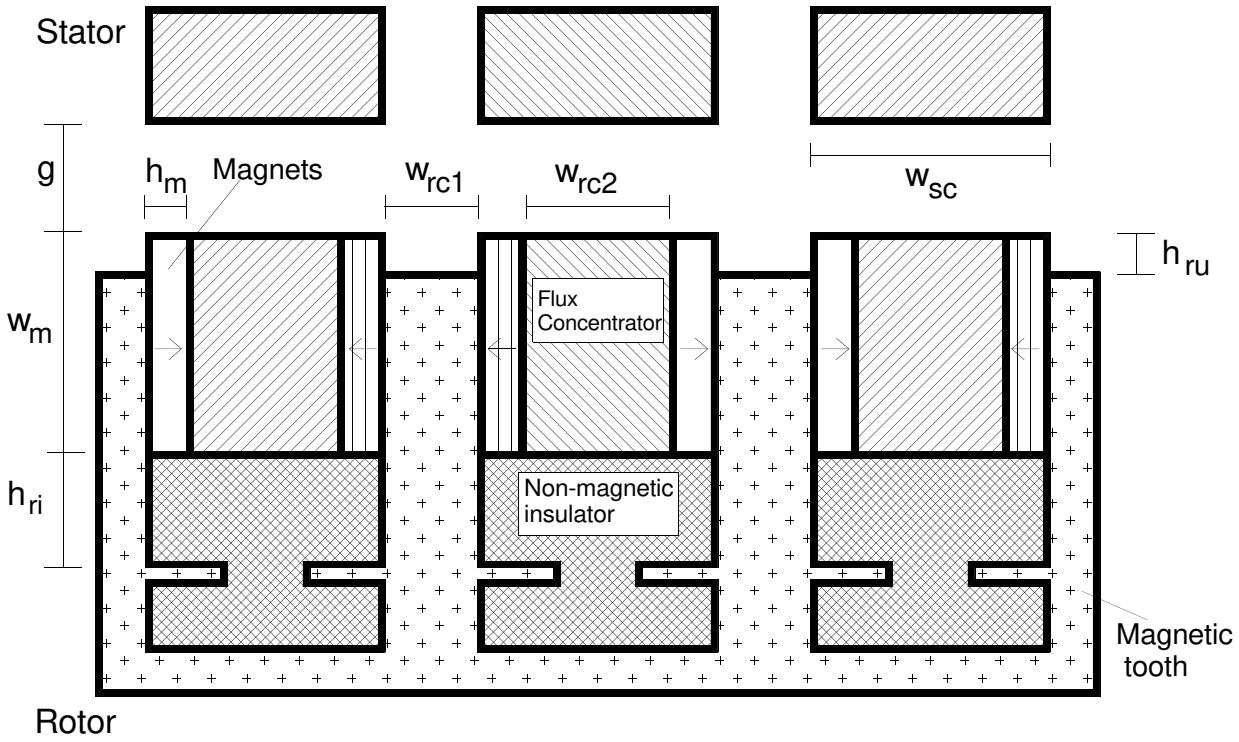

Figure 7-11: Detail of the geometrical parameters (side view).

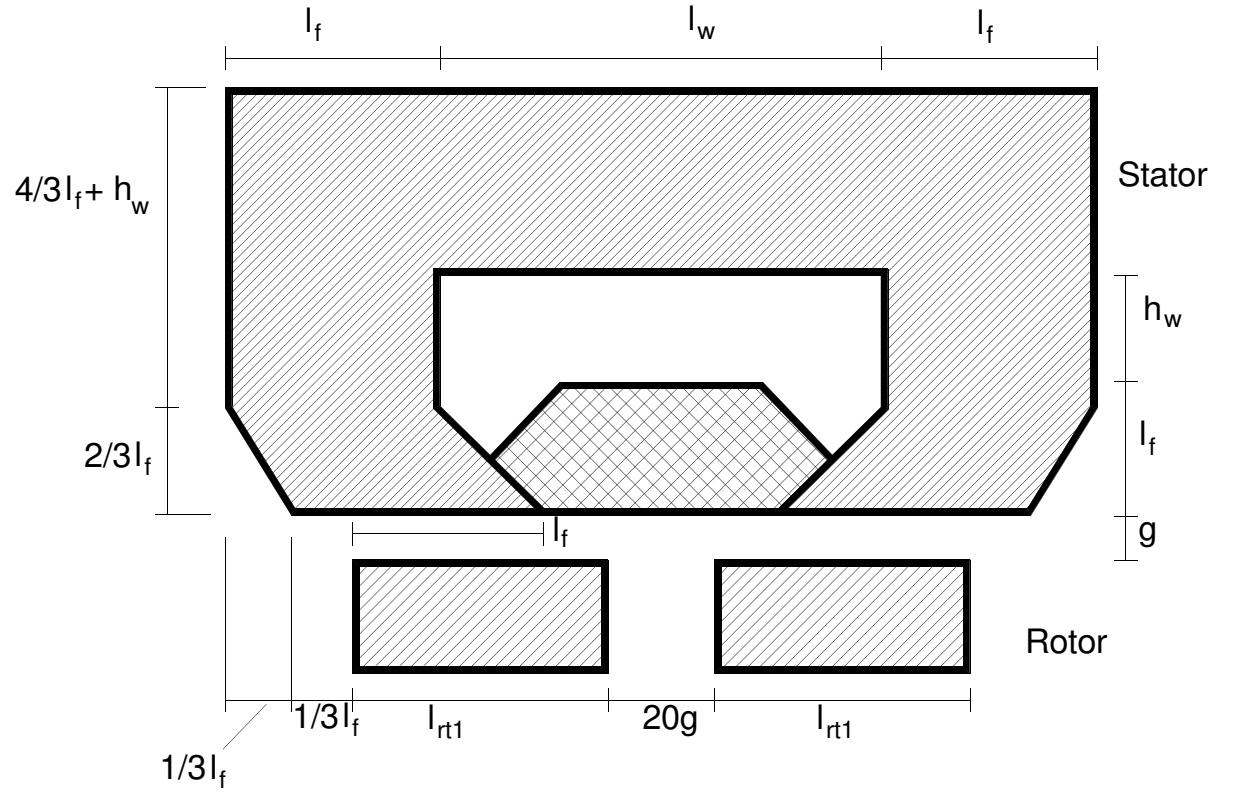

Figure 7-12: Detail of the geometrical parameters (front view).

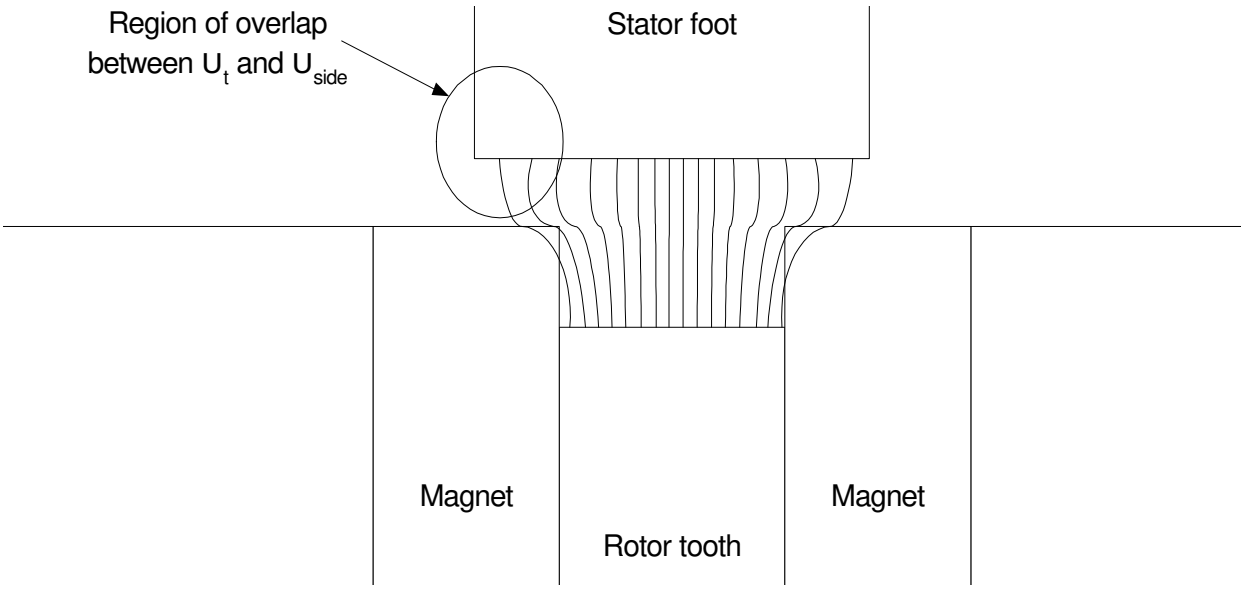

Figure 7-13: Two-dimensional plot of the magnetic flux lines above the rotor tooth.

This difficulty is one of the drawbacks of this method. Here, the reluctance U_t between the stator core and the rotor teeth and the reluctance U_{side} between the stator core and the flux concentrator in the unaligned position will enclose a region which will include flux lines of both U_t and U_{side}. Therefore, calculating separate expressions for U_t and U_{side} will result in an underestimate of the total reluctance when both reluctances are included in the magnetic circuit. To avoid this situation, we approximate U_t with its one-dimensional expression and assume the leaking flux lines to belong to U_{side} only.

The conduction path inside the two stator cores are not one-dimensional. However, the reluctances associated to these conduction paths are substantially lower than the reluctance of the air gap. We chose to express the reluctance U_{Ccore} of the stator C-core and the reluctance U_{SScore} of the stator trapezoidal core by assuming the magnetic flux as travelling parallel to the average conduction path inside these two stator cores. These two stator reluctances are defined as:

$$\Re_{Ccore} \cong \frac{l_w + 2h_w + \left(\frac{4\sqrt{2}+5}{3}\right)l_f}{\mu_{rFe}\mu_0 w_{sc} l_f} \tag{7-21}$$

$$\Re_{SScore} \cong \frac{l_w + \sqrt{2}l_f - 2l_{rt1}}{\mu_{rFe}\mu_0 w_{sc} l_f} \tag{7-22}$$

where
w_{sc} is the width of the horseshoe and trapezium stator cores;
l_w is the width of the stator winding window;
h_w is the height of the stator winding window.

The main parameter defining the window width l_w is the clearance required between the two rows of magnets on the rotor side. Such a clearance is necessary, otherwise the two rows of magnets will exchange flux through air due to their opposite magnetic polarities. We make this clearance equal to twenty times the air gap thickness so that leakage between the two rows of PM can be neglected. If the foot of the stator C-core and the stator trapezium have an angle of 45 degrees in the area near the air gap and if the same proportions shown in figure 7-12 are used, we can geometrically determine the value for l_w as:

$$l_w = 2l_{rt1} + 20g - \frac{2}{3}l_f \tag{7-23}$$

The height of the stator winding window area can be determined as:

$$h_w = \frac{\hat{\Im}_s}{\sqrt{2}Jl_w k_{sfill}} \tag{7-24}$$

where J is the current density in the stator conductors and k_{sfill} is the stator winding filling factor.

7.4.2. Determination of the geometrical relationship for 3-D reluctances

The remaining six lumped reluctances (U_g, U_{hi}, U_{icore}, U_{CTC}, U_{side}, U_{LEC}) used in the magnetic circuits exhibit a strong 2-D or 3-D flux path and the 1-D approximation cannot be used. A method is herein developed, which uses finite element analysis and curve-fitting in order to model the 2-D and 3-D behavior of these six reluctances. For each lumped reluctance, the same method is used and it is described as follows:

STEP 1) Determine a normalization reluctance U_{xxN} based on the assumption of one-dimensional fields.

STEP 2) By inspection of the geometry, determine the geometrical parameters that will affect the value of a form factor β_{xx} such that:

$$\Re_{xx} = \beta_{xx}\Re_{xxN} \tag{7-25}$$

The form factor β_{xx} is dimensionless and is introduced to take into account the 3-D dispersion of the magnetic field associated to the lumped reluctance under investigation.

STEP 3) A 3-D model is drawn on the FEA software, so that the desired reluctance is isolated and decoupled from the other reluctances.

STEP 4) Solve the 3-D problem with FEA with many combinations of the geometrical parameters affecting the reluctance.

STEP 5) Make a list of all β_{xx} obtained as a function of geometrical ratios.

STEP 6) Perform a curve-fit for β_{xx}.

In first instance, this method is described in detail for the air gap reluctance $\mathcal{R}_g$. For other reluctances, only the main results will be shown while the method will remain the same.

Determination of an expression for $\mathcal{R}_g$

The reluctance $\mathcal{R}_g$ of the field crossing the air gap is two and three-dimensional, due to the small ratio of flux concentrator width w_{rc2} over air gap thickness g. Also, the stator core and the rotor flux concentrators may have different values of stator core width w_{sc} and rotor flux concentrator width w_{rc2}.

STEP 1) Determine normalization reluctance $\mathcal{R}_{gN}$ based on the assumption of one-dimensional fields:

The air gap reluctance $\mathcal{R}_g$ can be defined as a function of a normalized reluctance $\mathcal{R}_{gN}$, such that

$$\Re_g = \beta_g \Re_{gN} \tag{7-26}$$

where the normalized reluctance is defined with the assumption of 1-D fields as:

$$\Re_{gN} = \frac{g}{\mu_0 l_f w_{rc2}} \tag{7-27}$$

A remark is made here concerning the choice of w_{rc2} as the width of the flux path. The variable used for the flux path width in the normalization reluctance could have been chosen as the stator core width w_{sc}. The choice betweenthe stator core w_{sc} and the flux concentrator width w_{rc2} is arbitrary as long as the expression of β_g takes this choice into account.

The air gap normalization factor β_g will take into account the 3-D distribution of the field. As an example illustrating the role of the form factor β_g, if all dimensions in a given air gap structure are multiplied by a factor 10, the factor β_g should not change its value, because it is a form factor which remains unchanged when the geometrical ratios in the structure stay the same. In such a case, only the value of $\mathcal{R}_{gN}$ will be modified, which in turn will

modify the air gap reluctance $\mathcal{U}_g$. But on the other hand, if the geometrical ratios in the structure are modified, then β_g should be modified. It is the relationship between β_g and the geometrical ratios that we will try to establish.

STEP 2) By inspection of the geometry, determine the geometrical parameters which will affect the value of β_g:

The value of β_g will mainly depend upon the geometrical parameters w_{sc} (stator core width), w_{rc2} (rotor flux concentrator width), g (air gap thickness), l_f (length of the stator foot).

STEP 3) A 3-D model is drawn on the FEA software. The 3-D model is chosen so that the desired reluctance is isolated.

The model used for the computation of β_g is illustrated in figure 7-14. A program is developed using the Macro7 language of Maxwell 3-D7, where the 3-D model is automatically generated with a given set of values for w_{sc}, w_{rc2}, g and l_f. This allows a great number of combinations of these 4 parameters to be used and a great number of FEA solutions can be generated automatically within a limited time.

STEP 4) Solve the 3-D problem with FEA with many combinations of geometrical values for each of the geometrical parameter affecting the reluctance.

A total of 97 combinations of the parameters w_{sc}, w_{rc2}, g and l_f were imposed to the FEA software, where a known current was fed to the winding of figure 7-14 and the flux generated was computed in the stator leg. With the knowledge of the mmf and flux, the air gap reluctance was derived. In the model of figure 7-14, all iron parts are non-saturable with infinite permeability. The 97 combinations and the values obtained for the air gap reluctance $\mathcal{U}_g$ and the air gap normalization factor β_g are listed in appendix VI.

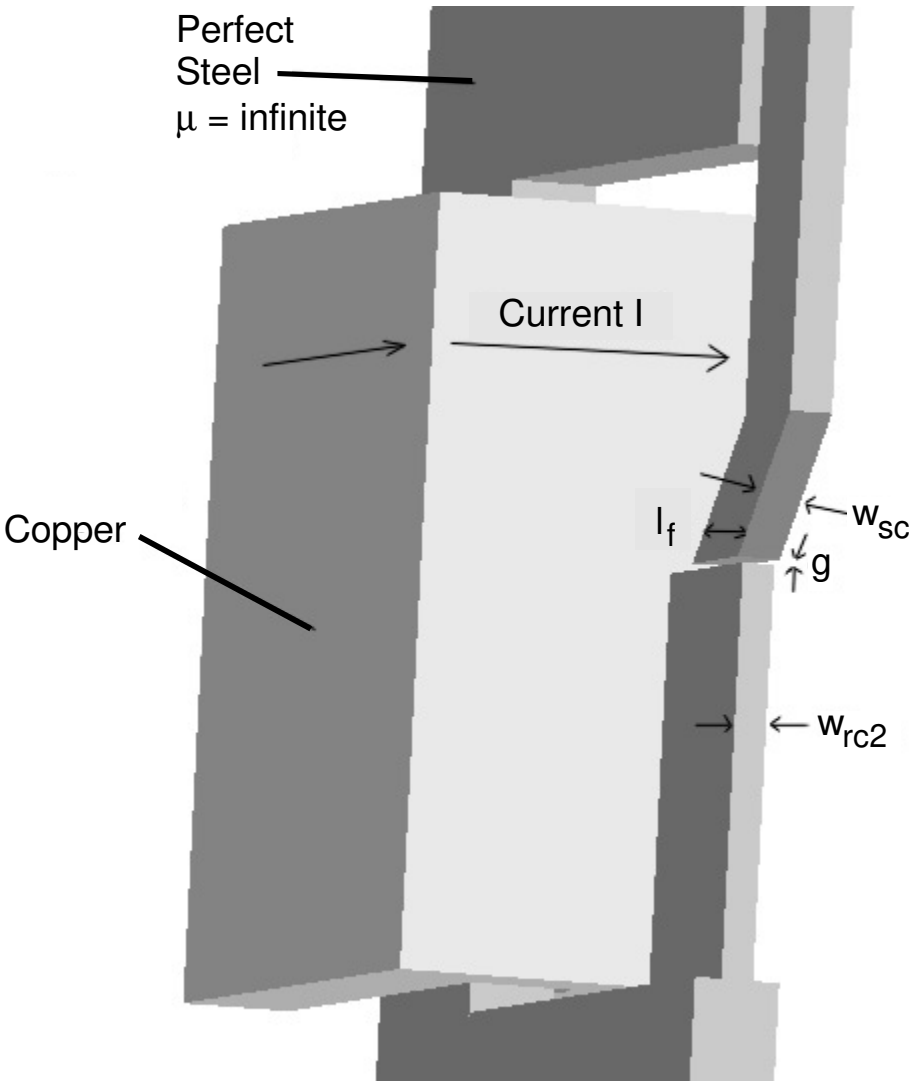

Figure 7-14: 3-D model for the computation of β_g

STEP 5) Make a list of all normalization factors β_g obtained as a function of geometrical ratios

The geometrical ratios that will affect the value of β_g are chosen as:

- ratio of stator core width over flux concentrator width w_{sc}/w_{rc2};
- ratio of flux concentrator width over air gap thickness w_{rc2}/g;
- ratio of stator foot length over air gap thickness g/l_f.

These ratios could have been chosen differently. For example, a common denominator could have been chosen for all three ratios. The ratio g/l_f could have been replaced by the ratio l_f/w_{rc2}. However, the importance of the flux leakage in the axial direction will increase as g/l_f increases. The relationship between this axial flux leakage and the ratio l_f/w_{rc2} has less physical meaning.

In other words, the ratios are chosen by inspection of the structure and selection of the most significant ratios for a given leakage behavior. The list of all values of β_g calculated is given in appendix VII as a function of w_{sc}/w_{rc2}, w_{rc2}/g, g/l_f.

STEP 6) Perform a curve-fit for all air gap normalization factors β_g.

Using all β_g listed in appendix VII as a function of the 3 ratios determined above, a curve-fit is performed to obtain a polynomial expression. The curve-fitting process used is the method of linear regression. The method of linear regression is a numerical method which allows extracting a linear mathematical expression from a set of observations. This method is well-known in the field of statistics and has been described by a number of authors in that field (see [Won 1969], [Mar 1980], [Edw 1984], [Net 1985]). In the field of electrical engineering, linear regression has been used by [Saf 1990] and [Hou 1996] for the modeling of miscellaneous magnetic behaviors in electrical machines. In [Saf 1990], linear regression is used to describe the losses in a DC machine. The author describes ten commercial DC machine designs with characteristics such as nominal speed, nominal power, size and enclosure types. Then a descriptive law is found based on these ten observations with the method of linear regression. In [Hou 1996], linear regression is used to describe the magnetic parameters of low-carbon steel. The author analyzes a sample of 17 steel plates characterized in terms of grain size, carbon content, sulfur content, nitrogen content. A mathematical relation is extracted between the iron losses and these parameters with the method of linear regression. In general, the application of linear regression to the field of electrical engineering is rather unusual. It must be noted that no mention of such linear regression in combination with FEA simulation has been found in literature.

Although the method of linear regression is well-known in other fields of science, our reader may be less familiar with its mathematical treatment. Here we give a short overview of the linear regression.

A set of n observations is described by a dependent variable Y and k independent variables X_1, X_2,...., X_k. In our application, the dependent variable is the factor β and the independent variables are the geometrical ratios. Each i^{th} point (or i^{th} observation) among the n observations has a certain position (y_i, x_{1i}, x_{2i},..., x_{ki}) in the multi-variable space. The multi-variable space has $k + 1$ dimensions. The linear regression aims at finding an estimate Y' which is a linear function:

$$Y' = b_0 + b_1 X_1 + b_2 X_2 \ldots + b_k X_k \qquad (7\text{-}28)$$

such that the sum of the differences Y - Y' squared is minimized. In other words, the coefficients b_0, b_1, b_2,..., b_k are calculated as to minimize the following function:

$$\sum_{i=1}^{n} [y_i - y_i']^2 \tag{7-29}$$

The resulting linear function (equation (7-28)) is named the function of linear regression or function of least squares. Considering the simple case of a planar set of observations ($k = 1$), the square function of equation (7-29) can be rewritten:

$$Q(b_0, b_1) = \sum_{i=1}^{n} [y_i - b_0 - b_1 x_i]^2 \tag{7-30}$$

where $Q(b_0, b_1)$ is the function corresponding to the sum of differences squared and it is the function to be minimized. The values of b_0 and b_1 are derived by equating to zero the partial derivatives of $Q(b_0, b_1)$. We write

$$\begin{aligned} \frac{\partial Q}{\partial b_0} &= -2 \sum_{i=1}^{n} [y_i - b_0 - b_1 x_i] = 0 \\ \frac{\partial Q}{\partial b_1} &= -2 \sum_{i=1}^{n} [y_i - b_0 - b_1 x_i] x_i = 0 \end{aligned} \tag{7-31}$$

We can solve for b_0 and b_1 as done in [Mar 1980] and the solutions are:

$$\begin{aligned} b_0 &= \bar{y} - b_1 \bar{x} \\ b_1 &= \frac{\sum_{i=1}^{n} x_i y_i - n \bar{x} \bar{y}}{\sum_{i=1}^{n} x_i^2 - n \bar{x}^2} \end{aligned} \tag{7-32}$$

where $\bar{x}$ and $\bar{y}$ are the average of the observed values for variables X and Y. The same principle may be applied when the number of independent variables is larger than 1 ($k > 1$): the sum of the differences squared needs to be minimized. The resulting number of partial derivatives is then equal to $k + 1$ and it becomes necessary to solve a system of $k + 1$ equations. As the number of independent variables increases, the problems becomes more complex and Gauss' elimination method is required. It is not the intention here to detail all

the necessary mathematics in the multi-variable case. The main principle highlighted above is used by the SPSS7 software [SPS 1996], which allows multiple (or multi-variable) linear regressions.
In the air gap normalization factor β_g, a few tries and errors enabled us to establish the following six independent variables for an acceptable value of r^2, which is described further by equation (7-34) and which meaning is explained further in this section. The regression function is written in the form:

$$\beta_g = b_0 + b_1\left(\frac{w_{sc}}{w_{rc2}}\right) + b_2\left(\frac{w_{sc}}{w_{rc2}}\right)^2 + b_3\left(\frac{w_{rc2}}{g}\right) + b_4\left(\frac{w_{rc2}}{g}\right)^2 + b_5\left(\frac{g}{l_f}\right) + b_6\left(\frac{g}{l_f}\right)^2 \qquad (7\text{-}33)$$

After processing the data of appendix VII in SPSS7, a curve-fitted expression for the 97 observations of β_g is found as:

$$\beta_g = 1,29 - 0,64\left(\frac{w_{sc}}{w_{rc2}}\right) + 0,17\left(\frac{w_{sc}}{w_{rc2}}\right)^2 + 0,028\left(\frac{w_{rc2}}{g}\right) - 6,41\times10^{-4}\left(\frac{w_{rc2}}{g}\right)^2 - 2,32\left(\frac{g}{l_f}\right) + 3,84\left(\frac{g}{l_f}\right)^2$$

Figure 7-15 shows a plot of equation for a constant value of air gap thickness over stator foot length g/l_f.
.

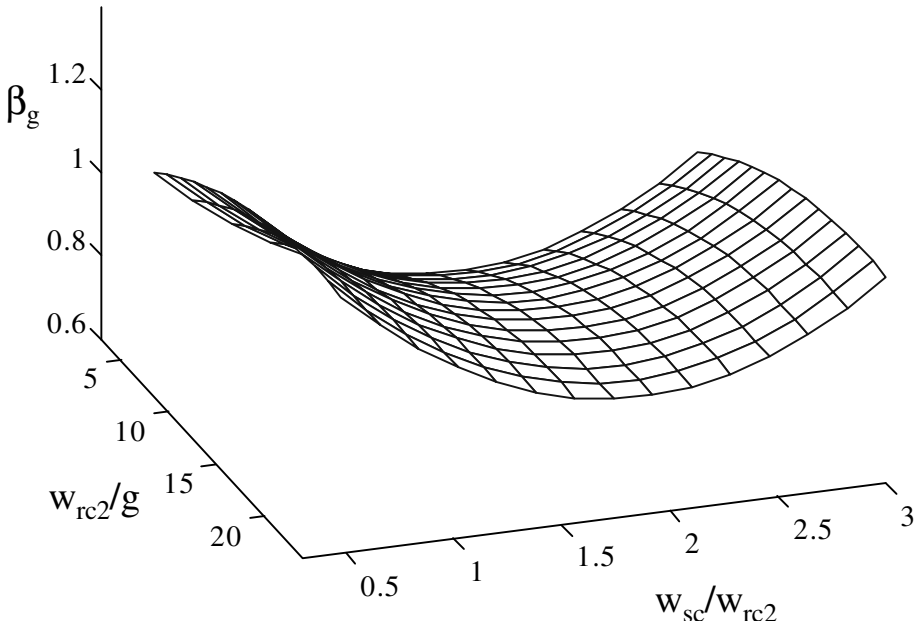

Figure 7-15: Air gap normalization factor β_g after linear regression. $g/l_f = 0.05$.

A very important issue is the question of how accurate is the curve-fit. Figure 7-16 shows "clouds" of points corresponding to the 97 observations of β_g made with the FEA software. On the same graphs, the values of β_g obtained from equation are also plotted. Each of the three graphs of figure 7-16 illustrates the same 97 points as a function of a different independent variable on the *x*-axis. Although the general shapes of the FEA "clouds" are consistent with the shapes predicted by the linear regression, substantial differences still exist between individual observations and the results of the linear regression. One example of these differences is shown in figure 7-17 which gives a closer look to a specific set of observations for a ratio of rotor flux concentrator width over air gap thickness $w_{rc2}/g = 3$ and $w_{rc2}/g = 12$ (while g/l_f is set to 0.05). The error of the curve-fit estimate vary from point to point. For some points, the estimate is excellent while for other points a difference up to 17% is observed.

Figure 7-18 gives a more complete description of the curve-fit accuracy. The error between the estimate and the observation varies from -18% to + 56%. A large occurrence of errors ranging between -4% and 18% is observed. This error on the air gap reluctance will affect the accuracy obtained on the total reluctance seen by the stator winding in the aligned position. The fact that each 3D reluctance is analytically described from a curve-fitting will inevitably introduce a cumulative error on the total reluctance calculation, as will be discussed at the end of this section.

SPSS7 gives an estimate of how well the set of observations is described (or explained) by the linear regression. The value *r* is named the multiple correlation coefficient and is defined in [Won 1969], [Mar 1980], [Edw 1984], [Net 1985] as:

$$r^2 = \frac{\sum_{i=1}^{n} [y'_i - \bar{y}]^2}{\sum_{i=1}^{n} [y_i - \bar{y}]^2} \qquad (7\text{-}34)$$

where y is the observed value, y' is the estimated value and $\bar{y}$ is the average value of the population observed (the β_g obtained from FEA in this case). r^2 is the ratio of the variance of the estimate over the variance of the population. The closer r^2 is to 1.0 the better the estimation. In the latter case, the linear regression would "explain" very well the population. In the words of Wonnacott *et al* (see [Won 1969]), "*r* is the proportion of the total variation in *Y* explained by fitting the regression".

In the case of the air gap normalization factor β_g, the output of the linear regression gives a value of $r^2 = 0.814$ for the estimate expressed by equation .

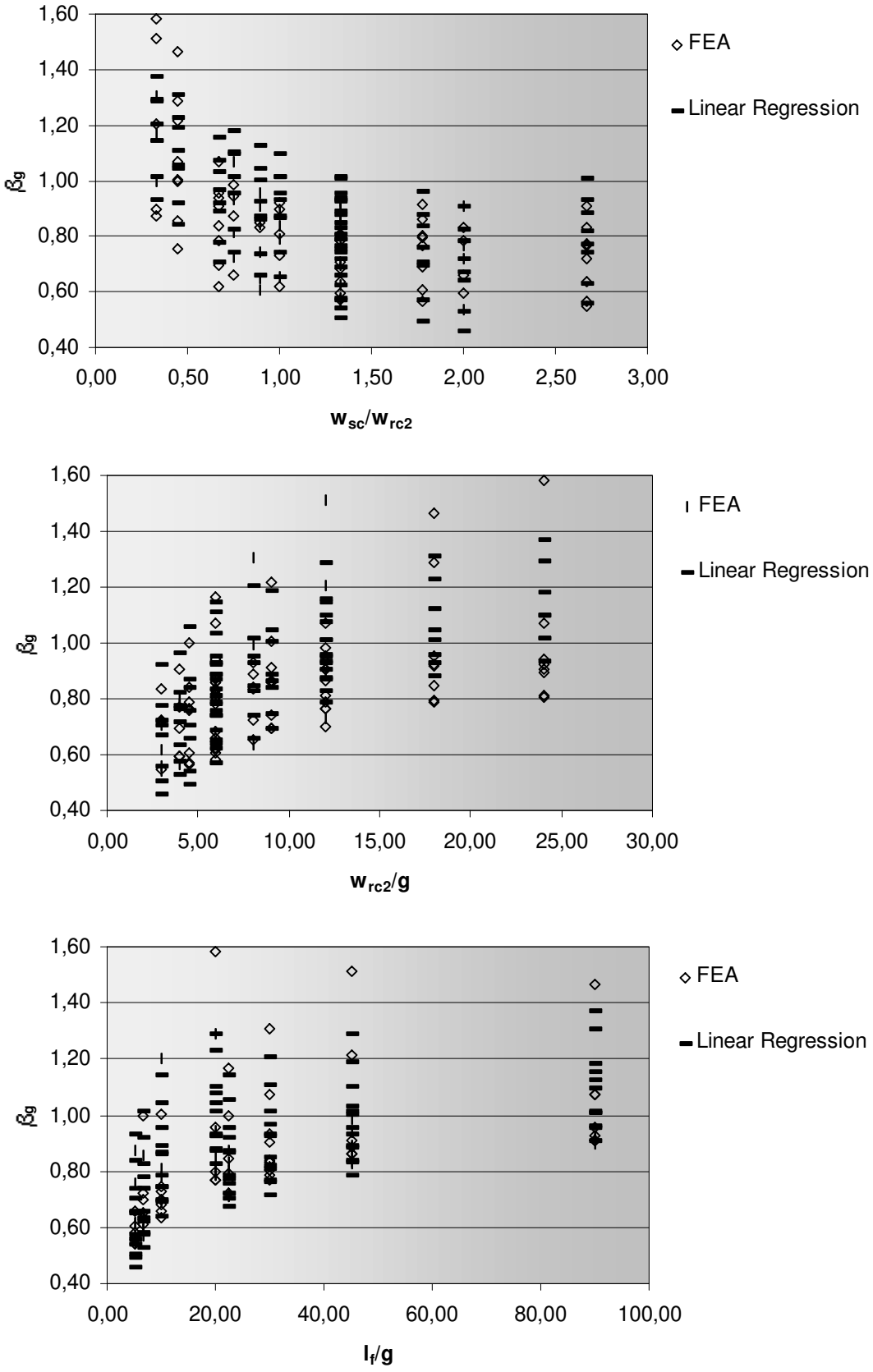

Figure 7-16: Plot of the 97 values of β_g observed as a function of the three independent variables.

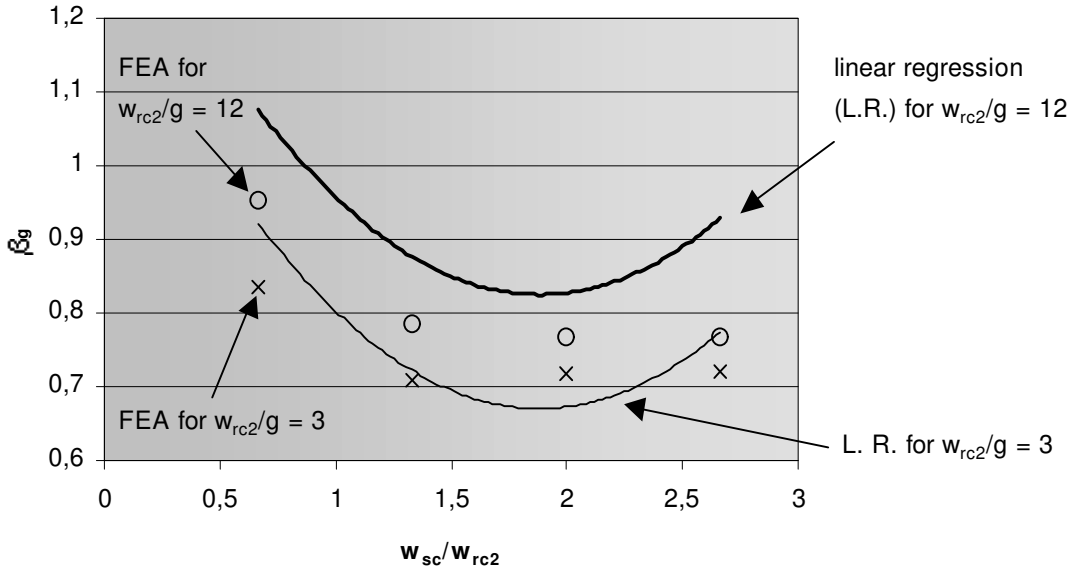

Figure 7-17: Comparison between β_g obtained from the linear regression (L. R.) curves and 8 β_g observed with FEA among the population of 97. $g/l_f = 0.05$.

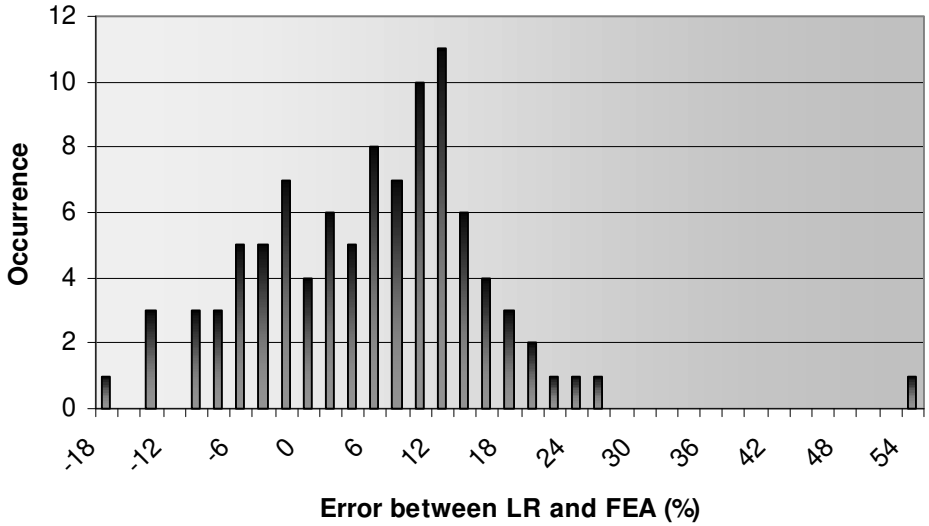

Figure 7-18: Occurrence of the error between the curve-fit estimate and the FEA observations. The error is expressed in % compared to the FEA observation while the occurrence is expressed in absolute number of occurrence in the population of 97.

Determination of an expression for U_{hi}, U_{ctc}, U_{icore}, U_{side}

The determination of U_{hi} (reluctance between the flux concentrator and the rotor slot bottom), U_{ctc} (reluctance between the rotor flux concentrator and the next stator core in the aligned position), U_{icore} (reluctance between a stator C-core and a stator trapezium), U_{side} (reluctance between the stator core and the rotor flux concentrator in the unaligned position) is done in the same way as for the air gap reluctance U_g. The same method is used, with

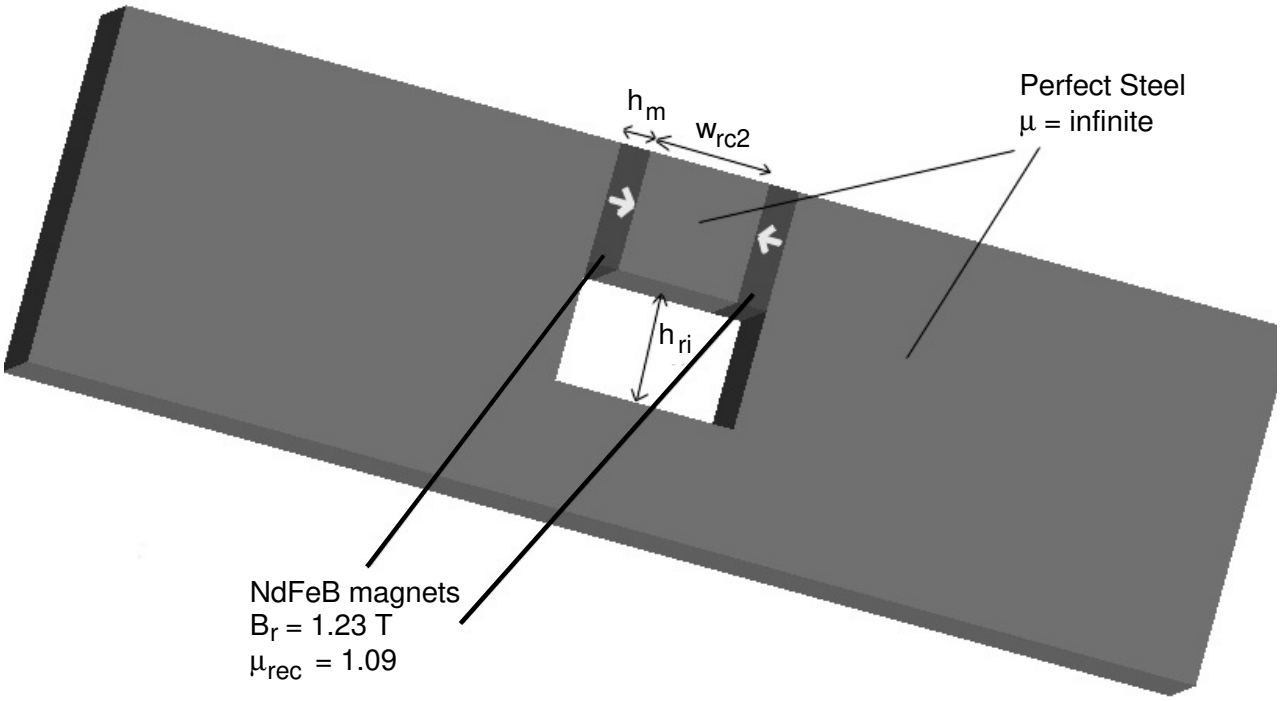

Figure 7-19: 3-D model for the computation of β_{hi}.

different variables. Figure 7-19 to figure 7-22 illustrate the FEA 3-D models used. The main results obtained with this method are shown in table 7-1 and given by equation (7-36) to equation (7-39).

For the computation of the normalization factor β_{hi}, the three-dimensional model of figure 7-19 is used. The two magnets of figure 7-19 generate a flux in the flux concentrator part. The flux traveling through the distance h_{ri} between the rotor flux concentrator and the bottom of the slot is computed with FEM. The mmf difference between the flux concentrator and the steel core is also computed. Knowing the mmf drop and the flux, the reluctance U_{hi} can be calculated. In total, the reluctance U_{hi} was calculated for 36 combinations of geometrical parameters which are listed in appendix VII.

For the computation of the normalization factor β_{icore}, the three-dimensional model of figure 7-20 is used. The magnetic permeability of the core is set equal to infinity, because we are only interested in the calculation of the inter-core reluctance. It must be noted that infinite magnetic permeability for iron is used solely for the purpose of modeling the individual lumped reluctances. The copper winding generates a flux in the leg. The flux is calculated with FEA in the upper part of the leg, near the copper winding and also in the bottom part of the model (where a thin path is formed below the hole). The difference between these two fluxes is equal to the flux leaking through the distance τ_p-w_{sc} separating a stator C-core from a trapezium.

Since the steel core has infinite permeability, the reluctance U_{icore} can be directly obtained by dividing the winding mmf by this flux difference. In total, the reluctance U_{icore} was calculated for 45 combinations of geometrical parameters which are listed in appendix VII.

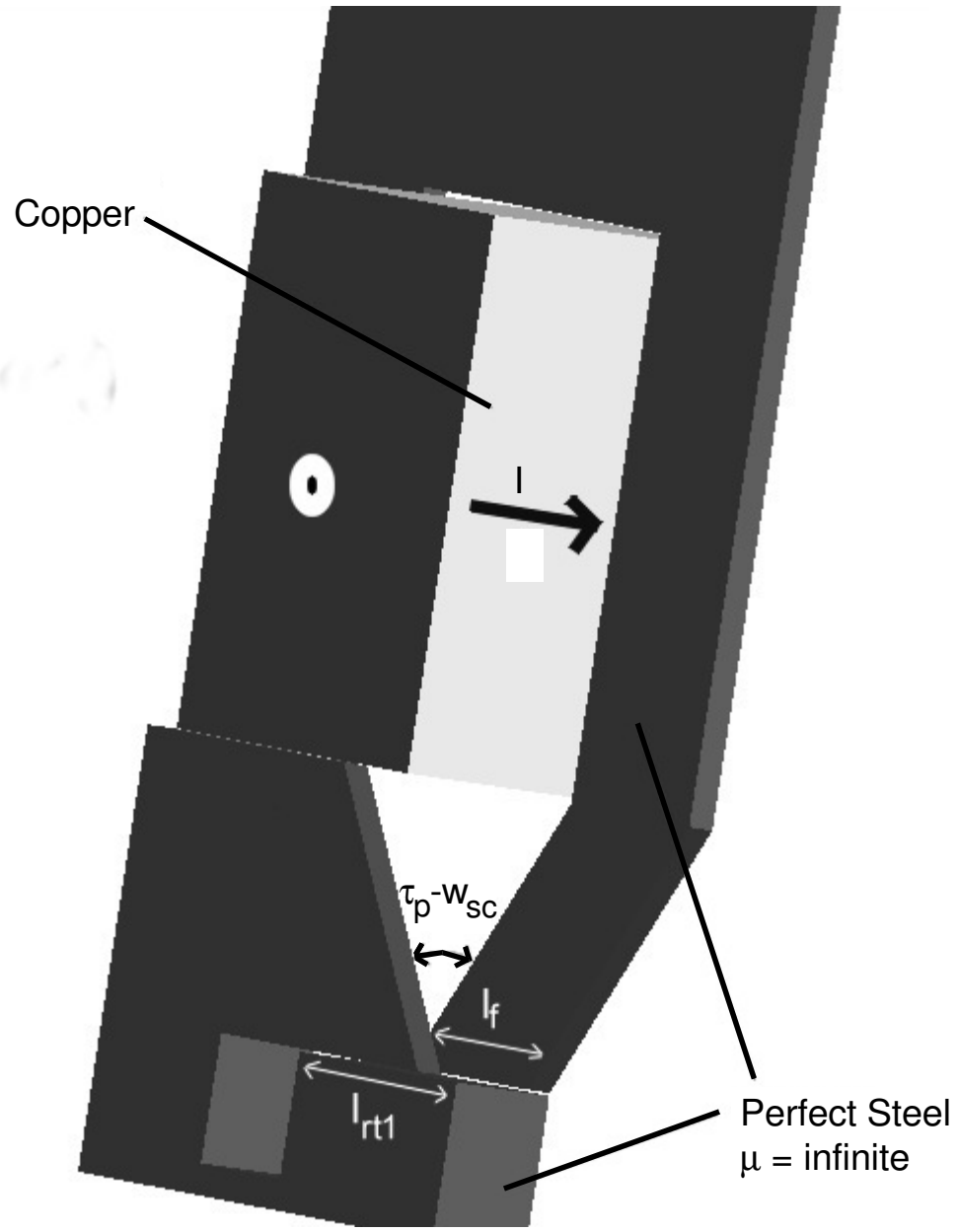

Figure 7-20: 3-D model for the computation of β_{icore}.

The computation of the normalization factor β_{ctc} is the most difficult of all normalization factors described in this chapter. The three-dimensional model of figure 7-21 is used. Each magnet generates a flux in the flux concentrator part. This flux crosses the air gap and penetrates the stator foot. Part of this flux leaks between the stator core and the next flux concentrator. This is the flux that is computed with FEM. To do so, the flux in the magnet is computed. Assuming the magnet mmf and reluctance as defined by equation (7-18) and equation (7-19), we can establish the mmf difference across a given magnet. In the model of figure 7-21, the mmf across a magnet also corresponds to the mmf difference between two flux concentrators. Secondly, the flux leaving the flux concentrator is computed by integrating the flux density over the window shown in figure 7-21. This integrating window is located just above the flux concentrator. The flux is also computed in the stator leg far above

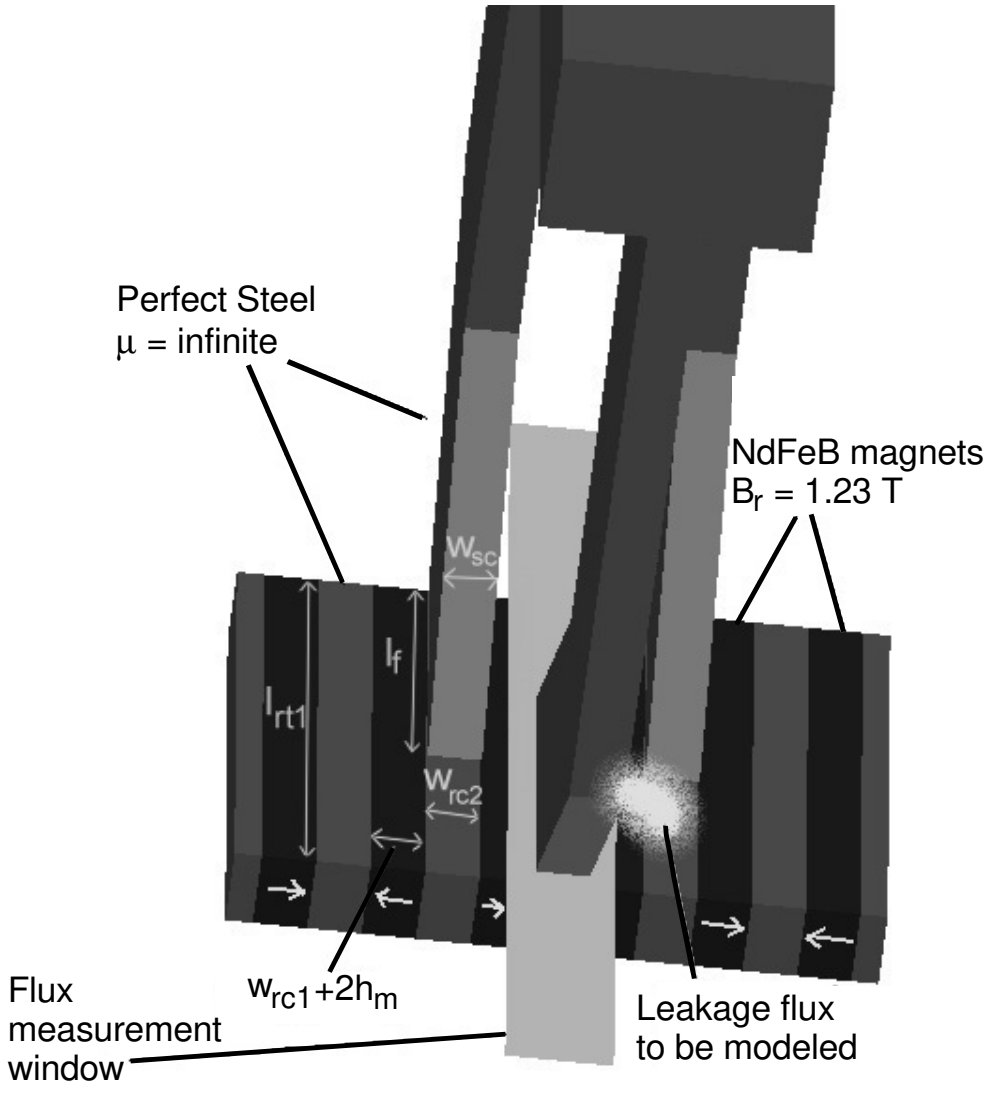

Figure 7-21: 3-D model for the computation of β_{ctc}.

the air gap. The difference between these last two fluxes will give the total flux leaking from one stator core to the next flux concentrator.

Knowing the mmf difference between two flux concentrators and the reluctance of the air gap, the reluctance U_{ctc} can be calculated. The reluctance U_{ctc} represents the leakage occuring between a rotor flux concentrator and a stator core in the aligned position. The air gap reluctance is calculated using equations developed previously in this chapter. In total, the reluctance U_{ctc} was calculated for 39 combinations of geometrical parameters which are listed in appendix VII.

Because of the location of the integration window (just above the flux concentrator), the flux calculation also includes the flux leaking from one concentrator to another through the air gap and which does not penetrate the stator foot. Clearly, this is a limitation of our model, since the latter assumes that all the flux leaking from one flux concentrator to another also penetrates the stator foot. In reality, most of the flux indeed crosses the air gap reluctance

entirely before penetrating the stator foot, while part of the flux crosses the air gap reluctance partially before leaking to the next flux concentrator. At some point, the air gap reluctance $\mathcal{U}_g$ is mixed with the leakage reluctance. A solution could be to include an additional lumped reluctance to model the flux leakage which does not penetrate the stator foot. However, this also increases the model complexity. Since it was found that for thin air gaps, most of the leakage flux penetrates the stator foot, we have chosen to assume all the leakage flux as penetrating the stator foot.

For the computation of the normalization factor β_{side}, the three-dimensional model of figure 7-22 is used. The copper winding generates a flux in the leg. The flux is calculated in the lower part of the leg. This flux is equal to the flux leaking through the distance d_{side} between a stator core in the unaligned position and the rotor flux concentrator. Since steel has infinite permeability, the reluctance $\mathcal{U}_{side}$ can be calculated by dividing the winding mmf by this flux. In total, the reluctance $\mathcal{U}_{side}$ was calculated for 20 combinations of geometrical parameters which are listed in appendix VII, where d_{side} is the distance between the stator core and the flux concentrator in the rotor, as shown in figure 7-8. It is defined as:

$$d_{side} = \frac{1}{2}(\tau_p - w_{rc2} - w_{sc}) \tag{7-35}$$

The value of d_{side} can either be positive or negative. In the case of a negative d_{side}, there will be a flux flowing through the air gap. In that case, the computation of $\mathcal{U}_{side}$ also includes the air gap flux.

It must be noted that the presence of the tooth with a thicker air gap in the model aims at representing the real conditions found in the machine. In this case, the thickness of the air gap above the tooth was set constant to 3 mm. Nevertheless, the flux flowing through the tooth was not included in the computation of $\mathcal{U}_{side}$ because this flux is modeled by the reluctance $\mathcal{U}_t$, which represents the flux between the stator core and a rotor tooth in the unaligned position and which is already included in the magnetic circuit.

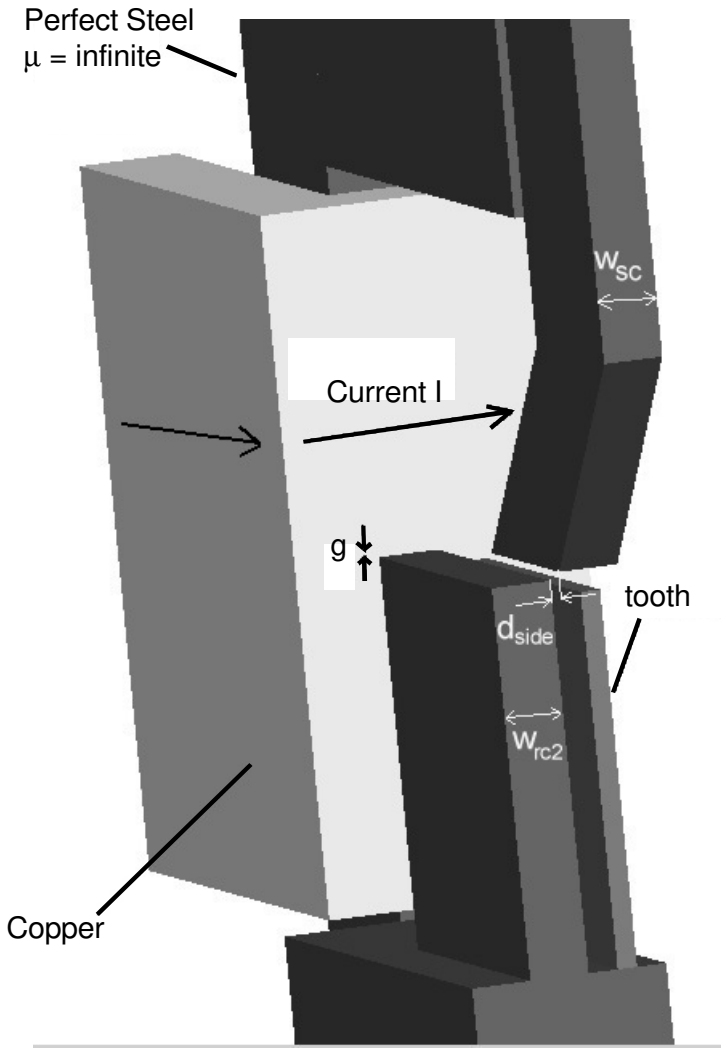

Figure 7-22: 3-D model for the computation of β_{side}.

Table 7-1. Main results of the curve-fitting of U_{hi}, U_{ctc}, U_{icore} and U_{side}.

	U_{hi}	U_{icore}	U_{ctc}	U_{side}
Expression for U	$\Re_{hi} = \beta_{hi}\Re_{hiN}$	$\Re_{icore} = \beta_{icore}\Re_{icoreN}$	$\Re_{ctc} = \beta_{ctc}\Re_{ctcN}$	$\Re_{side} = \beta_{side}\Re_{sideN}$
Normalized reluctance	$\Re_{hiN} = \frac{h_{ri}}{\mu_0 l_{rt1} w_{rc2}}$	$\Re_{icoreN} = \frac{(\tau_p - w_{sc})}{\mu_0 l_f^2}$	$\Re_{ctcN} = \frac{1}{\mu_0 l_{rt1}}$	$\Re_{sideN} = \frac{g}{\mu_0 l_f w_{rc2}}$
Geometric parameters affecting β	h_{ri}, w_{rc2}, h_m	τ_p-w_{sc}, l_f, l_{rt1}	l_f, l_{rt1}, g, w_{sc}, w_{rc2}, w_{rc1}	d_{side}, w_{sc}, w_{rc2}, g, (l_f is not included for simplification)
Ratios of geometric parameters chosen as variables	$(2h_m + w_{rc2})/h_{ri}$, h_m/w_{rc2}	l_f/l_{rt1}, $(\tau_p\text{-}w_{sc})/l_f$	l_f/g, l_{rt1}/l_f, w_{sc}/w_{rc2}, $(2h_m + w_{rc1})/l_{rt1}$	d_{side}/g, d_{side}/w_{rc2}, w_{sc}/w_{rc2}, w_{sc}/g
r^2	0.986	0.801	0.455	0.971

$$\beta_{hi} = -0,042 + 0,30\left(\frac{2h_m + w_{rc2}}{h_{ri}}\right) - 2,73\times10^{-2}\left(\frac{2h_m + w_{rc2}}{h_{ri}}\right)^2 + 0,075\left(\frac{h_m}{w_{rc2}}\right) \quad (7\text{-}36)$$

$$\beta_{icore} = 8,0 + 9,68\left(\frac{\tau_p - w_{sc}}{l_f}\right) - 1,24\left(\frac{\tau_p - w_{sc}}{l_f}\right)^2 - 14,9\sqrt{\frac{\tau_p - w_{sc}}{l_f}} - 1,92\left(\frac{l_f}{l_{rt1}}\right)^2 \quad (7\text{-}37)$$

$$\beta_{ctc} = 11,64 - 72,53\left(\frac{g}{l_f}\right) + 4,63\left(\frac{l_f}{l_{rt1}}\right) + 1,58\left(\frac{w_{sc}}{w_{rc2}}\right)^2 \quad (7\text{-}38)$$

for a distance between the stator core and the rotor flux concentrator in the unaligned position $d_{side} > 0$,

$$\beta_{side} = 1,66 + 0,48\left(\frac{d_{side}}{g}\right) - 0,89\left(\frac{d_{side}}{w_{rc2}}\right) - 1,07\left(\frac{w_{sc}}{w_{rc2}}\right) + 0,17\left(\frac{w_{sc}}{g}\right) \quad (7\text{-}39)$$

for $d_{side} < 0$,

$$\beta_{side} = 1,64 + 0,35\left(\frac{d_{side}}{g}\right) - 1,32\left(\frac{d_{side}}{w_{rc2}}\right) - 1,06\left(\frac{w_{sc}}{w_{rc2}}\right) + 0,14\left(\frac{w_{sc}}{g}\right) \quad (7\text{-}40)$$

Determination of an expression for U_{LEC}

The determination of the reluctance U_{LEC} (reluctance representing the flux leakage between two adjacent flux concentrators) is done in the same way as for the air gap reluctance U_g, with the difference that U_{LEC} is composed of two sub-reluctances U_{LEC1} and U_{LEC2}, as depicted in figure 7-23.

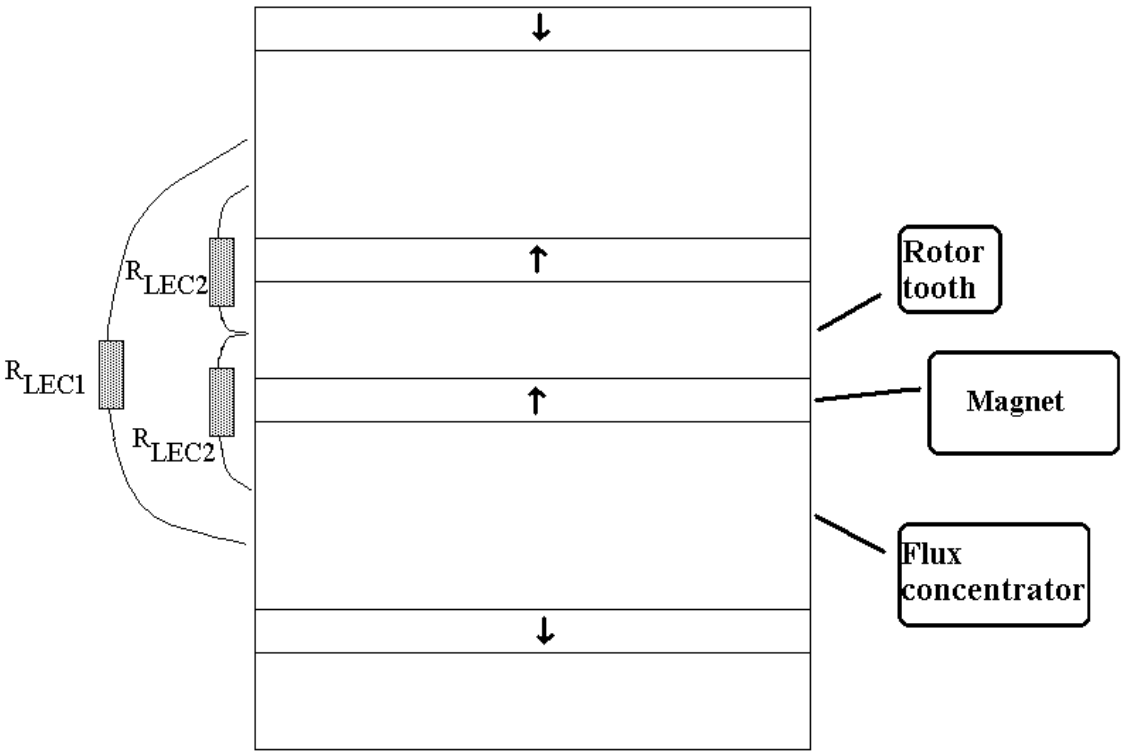

Figure 7-23: Top view of the rotor toothed structure. Division of $\mathcal{R}_{LEC}$ into two sub-reluctances $\mathcal{R}_{LEC1}$ and $\mathcal{R}_{LEC2}$.

The reluctance $\mathcal{R}_{LEC}$ can be expressed as a combination of $\mathcal{R}_{LEC1}$ and $\mathcal{R}_{LEC2}$ as:

$$\Re_{LEC} = \frac{2\Re_{LEC2}\Re_{LEC1}}{\Re_{LEC1} + 2\Re_{LEC2}} \tag{7-41}$$

Figure 7-24 illustrates the FEA 3-D model used and the main results obtained with this method are shown in table 7-2. The linear regression provides an expression for the factor β_{LEC} as:

$$\beta_{LEC} = 4,45 - 1,92\frac{w_{rc2}}{d} + 0,27\frac{w_m}{d} + 0,22\left(\frac{w_{rc2}}{d}\right)^2 - 0,02\left(\frac{w_m}{d}\right)^2 \tag{7-42}$$

where d is the distance between two adjacent flux concentrators (in the case of β_{LEC1}) given by:

$$d = 2h_m + w_{rc1} \tag{7-43}$$

and the distance between a flux concentrator and a tooth (in the case of β_{LEC2}) given by:

$$d = h_m \tag{7-44}$$

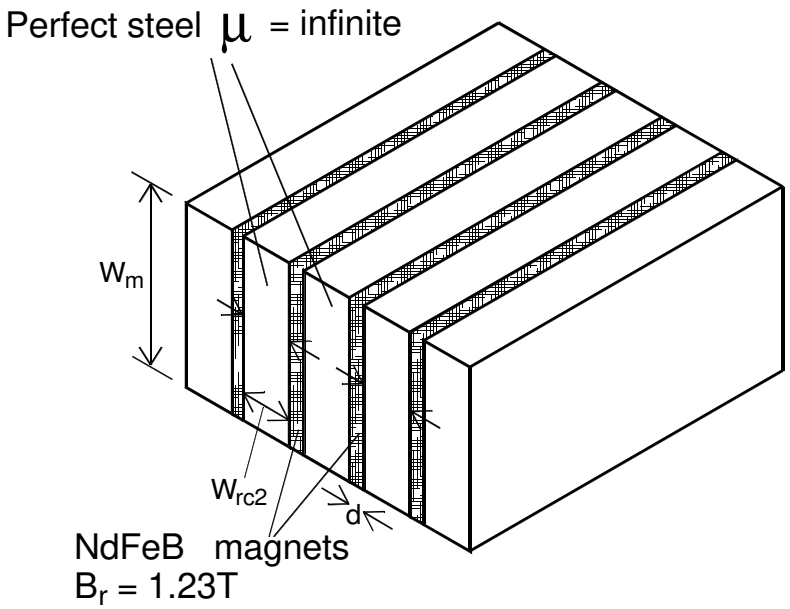

Figure 7-24: 3-D model for the computation of β_{LEC}.

For the computation of β_{LEC}, the three-dimensional model of figure 7-24 is used. Each magnet generates a flux in the flux concentrator part. The flux traveling through the surface defined by the dimensions w_{rc2} and w_m is computed with FEM. By computing the flux in the magnets, the mmf difference between two adjacent flux concentrators can be obtained and the reluctance $\mathcal{U}_{LEC}$ can be calculated. In total, the reluctance $\mathcal{U}_{LEC}$ was calculated for 51combinations of geometrical parameters which are listed in appendix VII.

Table 7-2. Main results of the statistical derivation of $\mathcal{U}_{LEC}$.

Expression for $\mathcal{U}_{LEC}$	$\Re_{LEC1} = \beta_{LEC1}\Re_{LEC1N}$ $\Re_{LEC2} = \beta_{LEC2}\Re_{LEC2N}$
Normalized reluctance	$\Re_{LEC1N} = \frac{w_{rc1} + 2h_m}{\mu_0 w_m}$ $\Re_{LEC2N} = \frac{h_m}{\mu_0 w_m}$
Geometric parameters affecting β_{LEC}	β_{LEC1}: w_{rc1}, h_m, w_m, w_{rc2} β_{LEC2}: h_m, w_m, w_{rc2}
Ratios of geometric parameters chosen as variables	w_{rc2}/d, w_m/d, β_{LEC1}: $d = 2h_m + w_{rc1}$ β_{LEC2}: $d = h_m$
r^2	0.699

7.5. Comparison between mathematical model and FEA

In this chapter, the torque rating of the TFPM machine with toothed rotor has been derived as a function of the no-load flux $\hat{\Phi}_{pnl}$, the reluctance seen by the stator winding in the aligned position $\mathcal{U}_{ap}$ and in the unaligned position $\mathcal{U}_{up}$. Then, the three parameters $\hat{\Phi}_{pnl}$, $\mathcal{U}_{ap}$ and $\mathcal{U}_{up}$ have been expressed as a function of the 11 lumped reluctances and mmfs of the magnetic circuit. Expressions were derived that express the 11 lumped reluctances and mmfs as functions of the geometrical parameters. We now have a model at hand which allows predicting the torque performance of the TFPM machine with toothed rotor from the geometrical parameters.

In this section, ten design configurations of the machine are investigated where the values of the parameters $\hat{\Phi}_{pnl}$, $\mathcal{U}_{ap}$ and $\mathcal{U}_{up}$ obtained with the model are compared with the results of FEA for each given configuration. The 10 TFPM machines used for the comparison have the design characteristics listed in table 7-3 and the result of the comparison is given in table 7-4. These geometric parameters are chosen more or less arbitrarily and give a broad range of possible size, air gaps, etc.

It must be noted that the mathematical model developed in the last section is derived from a set of FEA computations. But there is a substantial difference between the model-derived values of $\hat{\Phi}_{pnl}$, $\mathcal{U}_{ap}$ and $\mathcal{U}_{up}$ in table 7-4 and the FEA-derived values of $\hat{\Phi}_{pnl}$, $\mathcal{U}_{ap}$ and $\mathcal{U}_{up}$. The FEA computations used to obtain the mathematical model in the last section were drawn in such a way to isolate one lumped parameter to obtain the magnetic flux and the mmf created by this lumped parameter. In the FEA-derived values of $\hat{\Phi}_{pnl}$, $\mathcal{U}_{ap}$ and $\mathcal{U}_{up}$ in table 7-4, the complete TFPM structure with toothed rotor was drawn and the quantities $\hat{\Phi}_{pnl}$, $\mathcal{U}_{ap}$ and $\mathcal{U}_{up}$ were computed as a whole.

Table 7-3. Geometric parameters of the 10 TFPM machines with toothed rotor simulated with FEA.

Machine Number	w_{sc}	w_{rc2}	g	l_{rt1}	l_f	w_m	h_m	h_{ri}	h_{ru}	w_{rc1}	τ_p
	(mm)	(mm)	(mm)	(mm)	(mm)	(mm)	(mm)	(mm)	(mm)	(mm)	(mm)
1	8	8	1	72	45	12	2	5	3	4	16
2	8	8	2	72	45	12	2	5	3	4	16
3	8	8	1	72	45	20	2	5	3	4	16
4	8	6	1	72	50	15	1	5	4	3	11
5	6	8	1	60	45	15	2	5	3	3	15
6	12	12	1	75	60	20	3	8	3	3	21
7	12	12	2	75	60	20	3	8	3	3	21
8	3	4	1	30	20	12	1	8	3	3	9
9	8	6	1	40	25	12	1	5	3	3	11
10	9	12	1	75	50	20	3	5	3	4	22

Table 7-4. Comparison between model and FEA results for the 10 geometries of table 7-3.

Machine Number	$\hat{\Phi}_{pnl}$ FEA	$\hat{\Phi}_{pnl}$ model	$\Delta\ \hat{\Phi}_{pnl}$	U_{ap} FEA	U_{ap} Model	$\Delta\ U_{ap}$	U_{up} FEA	U_{up} model	$\Delta\ U_{up}$
	μWb	μWb	%	MA/ Wb	MA/ Wb	%	MA/ Wb	MA/ Wb	%
1	355	352	- 1	6.51	5.69	- 13	7.21	4.88	- 32
2	206	227	+ 10	7.68	6.62	- 14	8.45	5.55	- 34
3	423	452	+ 7	5.70	5.36	- 6	6.92	4.79	- 31
4	191	237	+ 24	4.74	3.59	- 24	4.57	3.07	- 33
5	343	352	+ 3	6.94	5.70	- 18	6.99	5.02	-28
6	957	930	- 3	3.57	3.35	- 6	3.53	2.65	- 25
7	564	633	+ 12	3.91	3.84	- 2	4.25	3.11	- 27
8	50	54	+ 8	20.72	16.68	- 20	22.34	15.08	- 32
9	98	116	+ 18	8.83	8.47	- 4	9.85	6.77	- 31
10	718	755	+ 5	4.84	4.79	- 1	5.41	4.22	- 24
		avg Δ	+ 8		avg Δ	- 11		avg Δ	- 30

In fact, the comparison performed in table 7-4 evaluates how much accuracy has been lost by decoupling all lumped reluctances one from the other and by processing the lumped reluctance values through a set of linear regressions. Both in the model-derived and FEA-derived calculations of the no-load flux per pole pair $\hat{\Phi}_{pnl}$, the reluctance per pole pair in the aligned and unaligned position U_{ap} and U_{up}, the steel relative permeability has been assumed as 1000 and the remanent flux density of the permanent magnets used with both methods is equal to 1.23 T.No saturation is yet taken into account in the FEA calculations at this point. Saturation will be taken into account in the design and optimization in chapter 8.

From table 7-4, we observe that the model predicts the no-load flux $\hat{\Phi}_{pnl}$ and the reluctances U_{ap} with an accuracy of about 10% in the ten examples selected. However, the reluctance U_{up} is significantly underestimated by the method. This is due to the overlapping fields represented by the reluctances U_{side} and U_{icore} in the unaligned position. These two reluctances represent respectively the leakage between the stator core and the flux concentrator in the unaligned position and the leakage between the stator C-core and the stator trapezium. Since these two leakage fields are located in the same area, the two reluctances calculated separately and then grouped together in the equivalent circuit tend to overestimate the total leakage flux in the unaligned position.

Concerning the aligned position, we must point out the poor r^2 ratio obtained in the linear regression performed on the normalization factor β_{ctc}. This means that the independent variables chosen in equation (7-38) do not explain satisfactorily the 39 observations obtained with FEA. In fact, for all normalization factors β's, the selection of the independent variables (whether the independent variable should be chosen as the square root, the square, the cube, the log, etc. of a geometrical ratio) was done arbitrarily by trial and error. A more systematic

mathematical method should be developed in order to find the independent variables more accurately.

Even for variables where a higher value of r^2 is obtained from the linear regression process, there may remain an important error on the reluctance value calculated with the curve-fit. In the example of the air gap normalization factor β_g, one of the points showed an error of 56% compared to the β_g obtained with the FEA software.

In conclusion, it appears that the only use of this model for the accurate prediction of the machine torque is not enough. In the optimization process, it is necessary to recalculate the torque capabilities of the machine design obtained from the model with a complete three-dimensional FEA computation.

7.6. Losses and efficiency

A simplified description of the losses is proposed with the following assumptions:

- 1) the flux densities in the stator cores and the rotor flux concentrators are assumed as varying sinusoidally with time at all points and for all load conditions. The amplitude of the flux densities are made equal to $B_{Fesat} = 1.8\ T$ inside laminated steel and to 1.5 T inside flux concentrators, which are assumed to be made of powdered iron material;
- 2) the iron losses in the rotor teeth are neglected;
- 3) the machine rotational speed ω is constant;
- 4) the specific eddy current losses in the stator laminations at 50 Hz/1.5 T is set to $k_{eddysteel} = 0.5$ W/kg;
- 5) the specific hysteresis losses in the stator laminations at 50 Hz/1.5 T is set to $k_{hyststeel} = 2.0$W/kg;
- 6) additional iron losses due to the punching and soldering process on the stator laminations are taken into account by multiplying all iron losses by a factor $k_{addloss} = 2$. This factor also takes into account the additional losses caused by the frequency harmonics in the phase current and no-load flux density. This factor also takes into account the non-uniform flux density distribution in the stator core;
- 7) the specific iron losses inside the rotor flux concentrators are set to $k_{pow\text{-}iron} = 13$ W/kg at 50 Hz/1.5 T. The losses in powdered iron are assumed as proportional to the frequency;
- 8) in the unaligned position, the flux components travelling perpendicular to the laminations plane are contained inside the stator foot and trapezium in a thickness equal to 3 times the thickness of the air gap. It is also assumed that the losses caused by perpendicular fields under full load conditions are equal to the losses obtained under no-load conditions;

- 9) the proximity losses in the stator coil are neglected. This assumption is reasonable for a wide window area, as it is the case here.

Considering the above mentioned assumptions, the copper losses P_{Cu} may be written as:

$$P_{Cu} = \frac{J^2}{\sigma_{Cu}} V_{cu} \tag{7-45}$$

where the copper volume V_{cu} is approximated by:

$$V_{cu} \cong 2p\tau_p l_w h_w k_{sfill} \tag{7-46}$$

The masses of stator laminations are given by:

$$m_{Ccore} = \rho_{Fe} p w_{sc} l_f (l_w + 2h_w + 4l_f) \tag{7-47}$$

$$m_{SScore} = \rho_{Fe} p w_{sc} l_f (l_f + 20g) \tag{7-48}$$

The iron losses in the stator steel laminations are approximated with Steinmetz formula [Sen 1997]:

$$P_{Fes} = [m_{Ccore} + m_{SScore}] k_{addloss} \left[k_{hyststeel} \left(\frac{f}{50Hz} \right) + k_{eddysteel} \left(\frac{f}{50Hz} \right)^2 \right] \left(\frac{B_{Fesat}}{1,5T} \right)^2 \tag{7-49}$$

The iron losses P_{Fes} do not include the losses inside the rotor flux concentrators nor the losses caused by the flux perpendicular to the laminations plane which are described by $P_{powiron}$ and $P_{eddyperp.}$

As defined per assumption 1),

$$P_{powiron} = m_{fluxconc} k_{powiron} \left(\frac{f}{50Hz} \right) \left(\frac{1,5T}{1,5T} \right)^2 \tag{7-50}$$

The mass of the rotor flux concentrators is given by:

$$m_{fluxconc} = 4\rho_{powiron} p w_{rc2} l_{rt1} w_m \tag{7-51}$$

The eddy current losses created by the field travelling perpendicular to the laminations plane in the unaligned position are contained within a thickness $2b_{perp}$:

$$2b_{perp} = 3g \tag{7-52}$$

Figure 7-25 shows an example of how the flux density is distributed in the C-core foot, where most of the flux traveling perpendicular to the laminations plane is located within a thickness 3 times the airgap thickness.

The magnetic flux Φ_{perpnl} flowing through the stator foot and the base of the trapezium is approximated with the following expression:

$$\Phi_{perpnl} \cong \frac{\Im_m}{\Re_m + \Re_{side}} \tag{7-53}$$

and the flux density B_{perpnl} of the perpendicular component is assumed as uniform within the thickness $2b_{perp}$ and is approximated by:

$$B_{perpnl} \cong \frac{\Phi_{perpnl}}{2b_{perp} l_f} \tag{7-54}$$

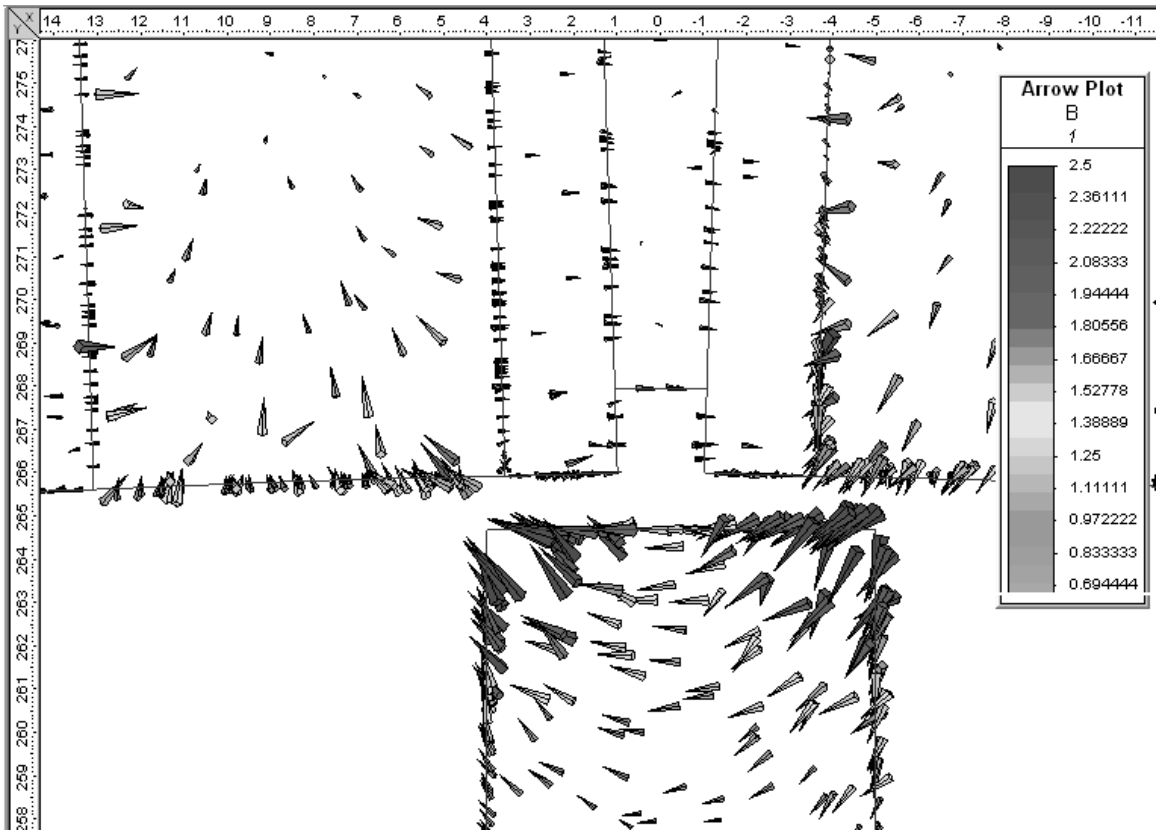

Figure 7-25: Arrow plot of the stator foot of the TFPM with toothed rotor in the unaligned position. The stator current is equal to zero. Dimensions in mm.

The losses $P_{eddyperp}$ per volume are given by equation (6-5). The volume of stator laminations involved in the calculations of eddy current losses caused by perpendicular fields is given by:

$$V_{Feperp} = 8pb_{perp}l_f w_{sc} \tag{7-55}$$

A simplified loss model

As mentioned above, the loss model presented in this section is simplified. A few remarks are made here on how the model should be improved. Those improvements are not included in this thesis because of the complexity of deriving such an exact model, which would substantially increase the length of the document. At this moment, the complete description of losses is left for further studies and this simplified model is adopted.

Firstly, the losses created by the magnetic flux traveling perpendicular to the plane of the stator laminations as proposed in our assumption 8) contains several approximations.

- It was assumed that the perpendicular component of flux density was uniformly distributed throughout the stator foot within a thickness of 3 times the thickness of the air gap. Such an approximation is very rough. In reality, the perpendicular component of flux density extends beyond a thickness of 3g. The flux density has its highest value near the air gap and decays progressively as we move away from the air gap;
- when d_{side} is negative, which corresponds to an overlap of the stator foot and the rotor flux concentrator in the unaligned position as depicted in figure 6-11, a large part of the perpendicular flux flowing through the reluctance $\mathcal{U}_{\text{side}}$ will not enter all laminations. In this loss model, we have assumed that all laminations will see the same flux density, which will overestimate the losses in that case;
- the eddy current losses calculated at no-load for the perpendicular flux density is made equal to the losses obtained under full-load conditions. Preliminary calculations and FEA simulations allowed us to verify that the no-load component constitutes the main parts of these losses. Although the losses under full-load conditions are only slightly higher than the no-load losses, the extra losses are not zero. As a matter of fact, a complete loss model should calculate the additional losses due to the perpendicular flux in full-load conditions. Such a model should also take into account the phase angle ψ, which adds to the model complexity.

Secondly, a complete loss model should accurately determine the loss distribution inside the rotor flux concentrators. It is not correct to assume that all parts of the flux concentrators "see" the same amplitude of the flux density, as we state in assumption 1). In reality, each volume element inside the flux concentrators has a different flux density and thus a different

power loss. A few attempts have been made before the completion of this study, to include the concentrators flux distribution in this analysis. However, it is a complex subject which requires deeper analysis and many more pages of this thesis. The choice was made not to include it in the thesis. In our simplified model, we have chosen to use assumption 1), which will certainly overestimate the losses in the flux concentrators.

Thirdly, a complete loss model should carefully consider all harmonics of the fundamental frequency. Assumption 1) implies that all flux densities will vary sinusoidally with time. However, we will see in chapter 9 that measurements on a rotating TFPM machine with toothed rotor may provide a non-sinusoidal waveform. A complete loss model should predict the flux density harmonics and corresponding losses.

Efficiency

Although the simplified model is rather imperfect as noted above, it gives a quick first approximation. The results obtained with the model are compared with experiments in chapter 9. The resulting efficiency at full load will be:

$$\eta = \frac{|\bar{T}|\omega - (P_{Cu} + P_{Fes} + P_{powiron} + P_{eddyperp})}{|\bar{T}|\omega} \qquad (7\text{-}56)$$

7.7. Summary

A model was developed for the TFPM machine with toothed rotor. The model allows an analytical prediction of the nominal average torque, the machine losses and efficiency. This model is based on three equivalent linear magnetic circuits that establish the following quantities:

- no-load flux $\hat{\Phi}_{pnl}$ per pole;
- reluctance $\mathcal{U}_{ap}$ seen by the stator winding in the aligned position;
- reluctance $\mathcal{U}_{up}$ seen by the stator winding in the unaligned position.

These three parameters are determined from a number of lumped reluctances, which are expressed as a function of the machine geometrical parameters. These expressions are obtained after curve-fitting a large number of reluctance values obtained from finite element computations. The quantities $\hat{\Phi}_{pnl}$, $\mathcal{U}_{ap}$, $\mathcal{U}_{up}$ obtained analytically are compared with the results of finite element analysis in the case of ten machine designs chosen arbitrarily. The model appears to be good enough as a first approximation, but it is not expected that it will lead to an accurate prediction of the torque. Due to the difficulty of analytically predicting the nominal average torque in a TFPM machine, we chose to keep this method for the optimization process. To compensate for the lack of precision of the method, a torque computation with finite element analysis should be performed on the resulting machine design to obtain the accurate torque value, as will be done in chapter 8 for in the process of design optimization.

The analytical model developed in this chapter did not include saturation. However, core saturation is a very important limit to the torque obtainable. Therefore, any TFPM design procedure must include saturation. This will be introduced in chapter 8.

A model for predicting the power losses was also developed. The model is said to be "simplified". The development of a complete loss model for the TFPM machine with toothed rotor still needs to be addressed properly. A complete model should calculate more accurately the eddy current losses in the stator laminations caused by the perpendicular vector component of the flux density. It should also determine the true distribution of the flux density vector inside the rotor flux concentrators. Finally, the model should take into account the time harmonics of the flux density in both laminated steel and powdered iron.

Chapter 8

Cost and mass optimization of direct-drive TFPM machine with toothed rotor

8.1. Introduction

Optimization is a key step in the design of electrical machines. A thorough comparison between machine topologies should result from an optimization process. Here, the model developed for the TFPM machine with toothed rotor is enhanced with the inclusion of core saturation and the resulting model is implemented in a computer program. This program is used to generate a very large number of machine designs, as it was the case in chapter 4 for the conventional PM synchronous machine. Then, the designs of TFPM machine with toothed rotor with the best cost/torque or torque/mass are retained. Our aim is to evaluate how the best designs of TFPM machine with toothed rotor compare with the best designs of conventional PM synchronous machine.

In section 8.2, the optimization method is presented. In section 8.3, a comparison is made between optimized TFPM machines with toothed rotor and optimized designs of the conventional PM synchronous machine. In section 8.4, the resulting optimized designs of the TFPM machine with toothed rotor are briefly compared with other TFPM topologies.

8.2. Optimization of the TFPM machine with toothed rotor

The optimization of the TFPM machine with toothed rotor uses the model developed in chapter 7. Two optimization runs are performed. The first run finds the maximum of the torque/mass function. The second one finds the minimum of the cost/torque function.

8.2.1. Optimization parameters and variables

The following parameters are set constant during the optimization process:

- outside diameter d_{out};
- rotational speed n;
- magnet remanent flux density B_r= 1.1 T;
- PM relative recoil permeability μ_{rec}= 1.09;
- rotor tooth clearance h_{ru}= 3 mm;
- relative permeability of stator laminations μ_{rFe} = 1000;
- stator winding filling factor k_{sfill}= 0.6 for diameters d_{out} = 1.0 m and above;
- stator winding filling factor k_{sfill}= 0.4 for diameter d_{out} = 0.5 m;
- air gap thickness g= d_{out} /1000.

Design optimization is done for outside diameters of d_{out} = 0.5 m, 1.0 m, 2.0 m and 3.0 m. For each value of d_{out}, a corresponding rotational speed n is assigned as follows: 130 rpm, 75 rpm, 46 rpm and 34 rpm.

The following parameters are allowed to vary:

- magnet thickness h_m;
- stator core width w_{sc};
- flux concentrator width w_{rc2};
- rotor tooth width w_{rc1};
- flux concentrator length l_{rt1};
- ratio of stator foot length over flux concentrator length l_f/l_{rt1};
- magnet radial dimension w_m;
- conductor current density J;
- phase angle ψ.

The following constraints are used:

- efficiency η = 90% and η = 95%;
- rotor tooth width w_{rc1} $ 2 mm;
- flux concentrator length l_{rt1} $30 mm.

The nine variables listed above are varied between a lower value and an upper value, using ten intermediate values for each variable. In total, 10^9 machine designs are calculated with a computer program which uses the model of chapter 7.

8.2.2. Amplitude $\hat{\Im}_s$ of the sinusoidal magnetomotive force and core saturation

The torque expression described by equation (7-5) requires that the amplitude of the stator mmf $\hat{\Im}_s$ be known. As previously remarked, the high per-unit value of the stator inductance

requires that TFPM machines be connected to an PWM rectifier (e.g. a voltage-source inverter used as rectifier). Here, the assumption is made that a PWM rectifier is used for this purpose. With such a rectifier, the current waveform injected in the phase winding may be chosen more or less arbitrarily. The limitation to the possible current shapes comes mainly from the rectifier DC voltage and switching frequency and from the machine inductance and back e.m.f. The use of non-sinusoidal current waveforms may bring higher average torque and lower ripple torque, as discussed in [Fre 2002]. Although non-sinusoidal m.m.f.'s may bring interesting benefits, they may also bring higher iron losses. Therefore, the assumption of sinusoidal mmfs is made here. The design optimization of TFPM machines fed with non-sinusoidal m.m.f. waveforms is left for further research.

With the assumption of sinusoidal m.m.f., the torque of the TFPM machine can be predicted from equation (7-5). But the amplitude $\hat{\Im}_s$ of the sinusoidal function $\mathsf{T}_s(t)$ yet needs to be expressed. To determine $\hat{\Im}_s$, we use the expression of $\lambda_s(t)$ developed in appendix VI and expressed by equation (VI-11). $\lambda_s(t)$ is the flux linkage created by the armature reaction in the cores of a salient TFPM machine fed with a sinusoidal current. Inserting equation (7-4) into equation (VI-11), we rewrite $\lambda_s(t)$:

(8-1)

$$\lambda_s(t) = \frac{pN_s^2\hat{i}_s}{4}\left(\sin\psi\left[-\left(\frac{1}{\Re_{up}}+\frac{3}{\Re_{ap}}\right)\sin\omega t+\left(\frac{1}{\Re_{ap}}-\frac{1}{\Re_{up}}\right)\sin(3\omega t)\right]+\cos\psi\left[\left(\frac{1}{\Re_{ap}}+\frac{3}{\Re_{up}}\right)\cos\omega t+\left(\frac{1}{\Re_{up}}-\frac{1}{\Re_{ap}}\right)\cos(3\omega t)\right]\right)$$

or we may also get rid of the number of turns N_s and the number of pole pairs p by writing the flux $\Phi_{ps}(t)$ per pole pair*:

(8-2)

$$\Phi_{ps}(t) = \frac{\hat{\Im}_s}{4}\left(\sin\psi\left[-\left(\frac{1}{\Re_{up}}+\frac{3}{\Re_{ap}}\right)\sin\omega t+\left(\frac{1}{\Re_{ap}}-\frac{1}{\Re_{up}}\right)\sin(3\omega t)\right]+\cos\psi\left[\left(\frac{1}{\Re_{ap}}+\frac{3}{\Re_{up}}\right)\cos\omega t+\left(\frac{1}{\Re_{up}}-\frac{1}{\Re_{ap}}\right)\cos(3\omega t)\right]\right)$$

Contrary to the longitudinal machines (chapter 4) where the stator m.m.f. was mainly limited by copper losses, the value $\hat{\Im}_s$ of flux-concentrating TFPM machines will in most cases be limited by saturation of the stator core. In most cases, increasing the stator m.m.f. above the point of core saturation will only marginally increase the average machine torque, while increasing the copper losses substantially. Here, the value $\hat{\Im}_s$ is chosen so that the flux in the stator core closely approaches saturation but never exceeds it. In addition to moderate copper losses, this choice has the advantage of mathematical linearity which substantially simplifies our model.

* The reader will note that equation (8-2) is different from the expression of $\Phi_{ps}(t)$ given in [Dub 2002c]. This is a consequence of expressing the no-load voltage by $e(t) = \hat{e}\cos(\omega t)$ instead of $e(t) = \hat{e}\sin(\omega t)$. The first expression is easier to work with and is preferred in the thesis. Also, the generator convention is preferred in the thesis. In [Dub 2002c], the motor convention was used.

The flux in the stator core is obtained by subtracting the flux $\Phi_{ps}(t)$ to the no-load flux $\Phi_{pnl}(t)$. This is a consequence of equation (VI-12). In this respect, we can express the total flux per stator pole as:

$$\Phi_{ptot}(t) = \hat{\Phi}_{pnl}\sin(\omega t) - \Phi_{ps}(t) \tag{8-3}$$

Inserting equation (8-2) into equation (8-3), we obtain:

(8-4)

$$\Phi_{ptot}(\theta) = \hat{\Phi}_{pnl}\sin\theta + \frac{\hat{\Im}_s}{4}\left\{\sin\psi\left[\left(\frac{1}{\Re_{up}}+\frac{3}{\Re_{ap}}\right)\sin\theta+\left(\frac{1}{\Re_{up}}-\frac{1}{\Re_{ap}}\right)\sin 3\theta\right]-\cos\psi\left[\left(\frac{1}{\Re_{ap}}+\frac{3}{\Re_{up}}\right)\cos\theta+\left(\frac{1}{\Re_{up}}-\frac{1}{\Re_{ap}}\right)\cos 3\theta\right]\right\}$$

where

$$\theta = \omega t \tag{8-5}$$

If the saturation flux Φ_{psat} is defined as:

$$\Phi_{psat} = B_{Fesat} w_{rc2} l_f \tag{8-6}$$

Equation (8-4) can be solved by implementing a numerical algorithm which varies θ between 0 and 2π. Equation (8-4) is used to find the highest value of $\hat{\Im}_s$ for which $\Phi_{ptot}(\theta)$ does not exceed Φ_{psat}. This is the value that will be used in the torque calculation. Higher values of $\hat{\Im}_s$ will saturate the stator core deeper at certain electric angles.

It must be noted that the phase angle ψ plays an important role both in the torque calculation and in the calculation of $\hat{\Im}_s$. According to equation (7-5), the average torque will be maximized for a certain combination of ψ and $\hat{\Im}_s$. Here, the phase angle ψ is varied between -45 degrees and + 45 degrees and for each value of ψ, a value of $\hat{\Im}_s$ is calculated by scanning θ between 0 and 2π. During this scan, ψ is held constant. The combination retained will be chosen based on the maximum average torque corresponding to a machine design which also meets the efficiency target.

8.2.2. Optimization results and FEA verification

The results of the design optimization are given in appendix VIII. Because the model developed in chapter 7 is not accurate, the output of the optimization program was also entered in the Maxwell7 FEA software and the average torque was calculated with the virtual work

method. To reduce the FEA calculation burden, only one pole pair of the machine was modeled with surface boundaries at the two ends of the pole pair. The two surface boundaries were given equal values and directions of the magnetic field.

For each of the optimized designs listed in appendix VIII, the magnetic force could be calculated with Maxwell7 FEA software for twelve rotor positions. For each rotor position, the stator current is varied as to follow a sinusoidal function of the rotor position. The average force per pole pair was obtained by averaging the twelve force values obtained.

Appendix VIII lists the output of the optimization process. The resulting geometry is then processed through a FEA software, and the resulting torque obtained from the FEA calculation is also indicated in appendix VIII. The average torque calculated with the analytical model is about 30 to 40% higher than the average torque calculated with finite element methods. In the remainder of this chapter, the value used for the comparison is the one resulting from the FEA calculation. We comment on the fact that the efficiency target was first set to either 90% or 95%, but needed to be corrected to a lower value for all machine designs as a result of lower machine torque.

The error of 30 to 40% between the torque predicted by the linear model and the FEA calculation can be explained by the local saturation of the stator core in the unaligned position. In the FEA simulation, where the non-linear *B(H)* characteristics of the stator laminations is taken into account, we observed that the total magnetic flux flowing in the stator core passes through the corner of the stator foot near the air gap. The latter corner is much narrower than the stator core cross-section and therefore local saturation is obtained. Such local saturation appears as the limiting factor for the torque increase, rather than the saturation of the total cross-section that is used in the estimation of the maximum magnetomotive force, as described in section 8.2.2.

8.3. Comparison between TFPM machine with toothed rotor and conventional PM synchronous machine

The performances of the TFPM with toothed rotor from the FEA program are compared to those of the conventional PM synchronous machine. To ensure a valuable comparison, the same torque values, efficiency constraint, outside diameter, rotational speed, air gap thickness, steel and magnet characteristics are used in both machine types. Also, the optimization method developed in chapter 4 is used for the conventional PM synchronous machine. The results are presented in figure 8-1 and figure 8-2.

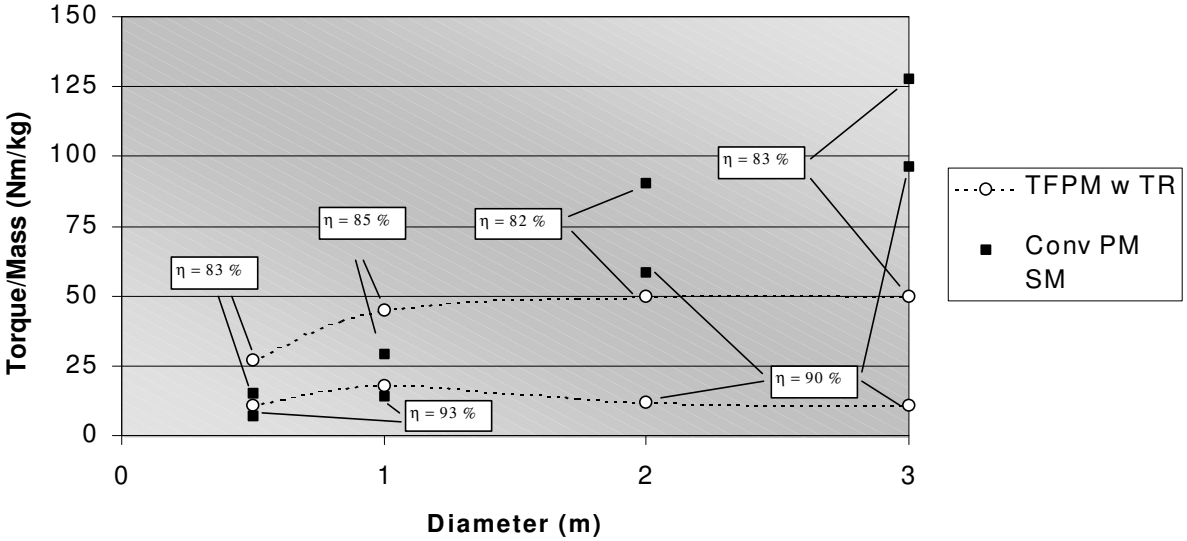

Figure 8-1: Torque/mass performance after optimization of the TFPM machine with toothed rotor and conventional PM synchronous. Results on the TFPM machine are taken from FEA calculations. Optimization target: highest torque/mass. Dotted lines = torque/mass of the TFPM machine with toothed rotor.

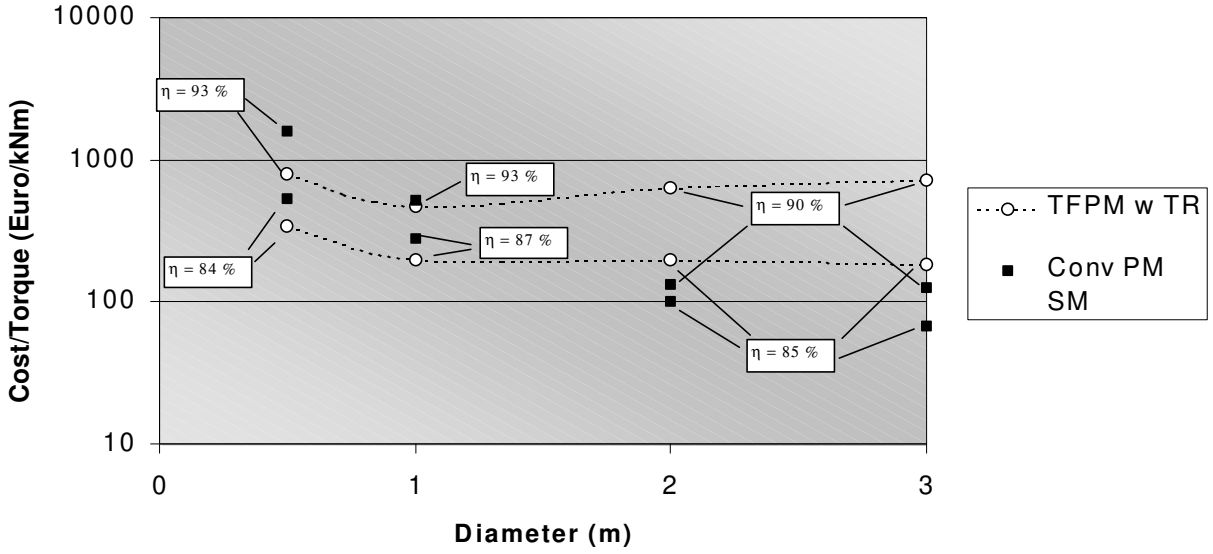

Figure 8-2: Cost/torque performance after optimization of the TFPM machine with toothed rotor and conventional PM synchronous. Results on the TFPM machine are taken from FEA calculations. Optimization target: lowest cost/torque. Dotted lines = cost/torque of the TFPM machine with toothed rotor.

According to the optimization results obtained in appendix VIII and depicted in figure 8-1 and figure 8-2, the TFPM machine with toothed rotor obtains favorable performance for

diameters of 1 m and below. Above 1 meter, the conventional PM synchronous machine obtains better performance and the advantage increases as the diameter increases.

This is consistent with the conclusions obtained in [Dub 2002a], which compared the conventional PM synchronous machine to another TFPM machine type, that is the double-sided TFPM machine with single winding. In [Dub 2002a], the analysis concludes that larger diameter favors the conventional PM synchronous machine. However, the comparison carried out in [Dub 2002a] compares machines fed with the same current density and efficiency is not used directly as a basis for comparison. A more accurate comparison is performed in this thesis, where current density is allowed to vary independently in both machine topologies and where equal efficiencies are targeted. It appears that current density alone is not sufficient, because most losses in the conventional PM synchronous machine are copper losses, while the TFPM machines with toothed rotor has higher iron losses.

Although the analysis presented in this chapter appears as more thorough than the comparison done in [Dub 2002a], the overall general conclusions remain more or less the same: large diameters favor the conventional PM synchronous machine. The reason for the bad performance of TFPM machine with toothed rotor with large diameters is the need for a thicker air gap and larger pole pitch as depicted in figure 8-3.

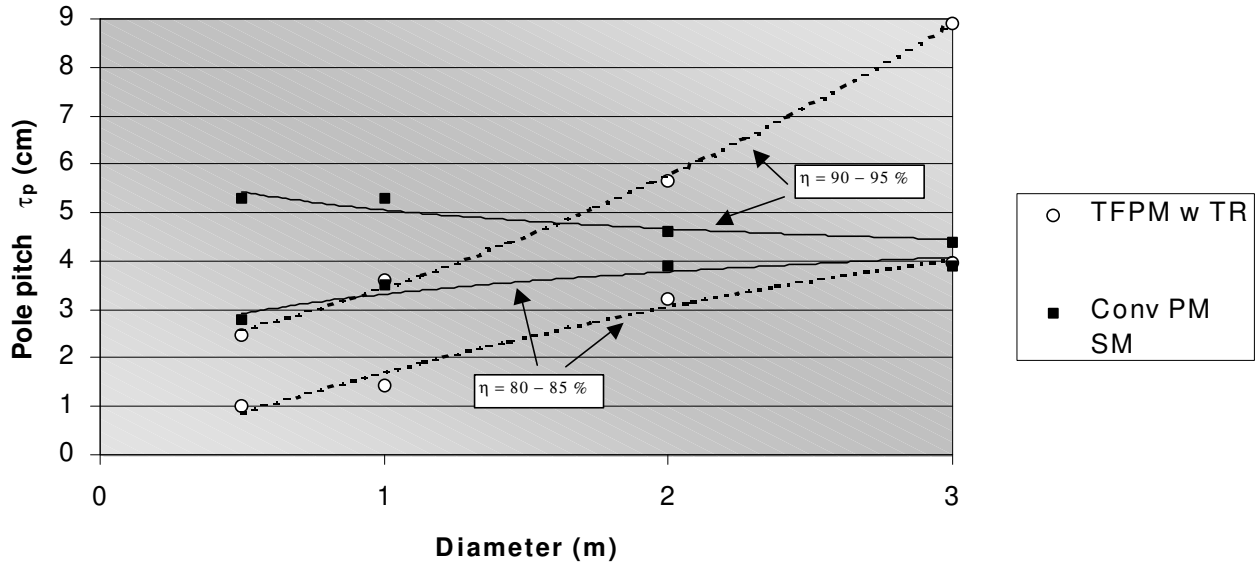

Figure 8-3: Pole pitch τ_p after optimization of the TFPM machine with toothed rotor and the conventional PM synchronous machine. Optimization target: lowest cost/torque. Upper points = designs with 90 - 95% efficiency. Lower points= designs with 80 - 85% efficiency. Dotted lines = TFPM machine with toothed rotor. Solid lines = conventional PM synchronous machine.

8.4. Comparison between TFPM machine with toothed rotor and other TFPM machines

It is relevant to determine how the TFPM machine with toothed rotor compares to the other TFPM configurations described in section 6.2. As stated in section 4.4, any valid comparison between electrical machine topologies must be made with equal efficiencies and equal rotational speeds. Because most TFPM machine designs proposed in the scientific literature do not address suitably that issue, it is not possible to draw any valid conclusion on how the TFPM machine with toothed rotor compares to other TFPM machine designs. To gather such a comparison, the various TFPM topologies must be optimized with the same constraints as those expressed in section 8.2.1. Nevertheless, the torque/mass and cost/torque performance obtained in the last section are given as indications of what can be expected. Figure 8-4 and figure 8-5 illustrate the cost/torque and torque/mass of active material obtained in this chapter for the TFPM with toothed rotor. These two figures also show the same points illustrated previously in figure 4-1 and figure 4-2 for the TFPM machine designs obtained from past literature.

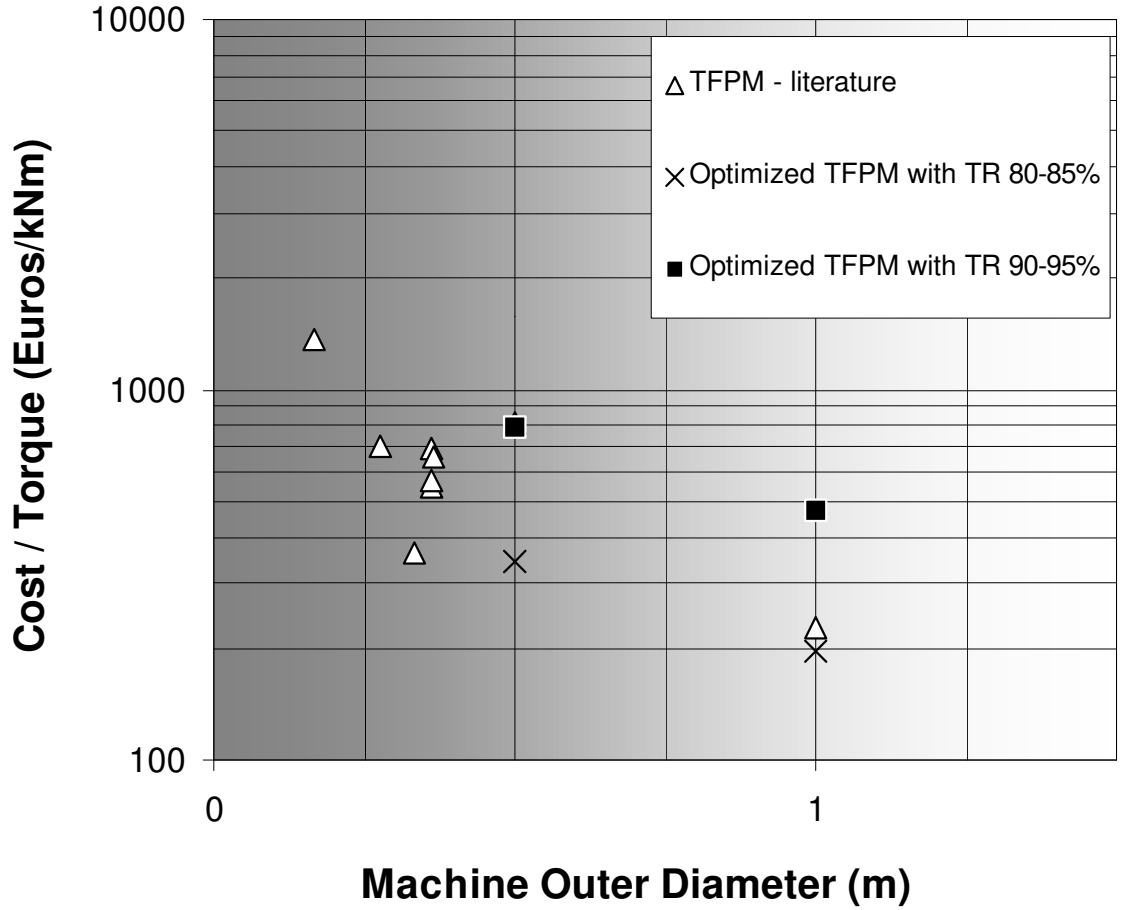

Figure 8-4: Cost/torque of active material for the optimized designs of the TFPM with toothed rotor and the other TFPM topologies discussed in past literature.

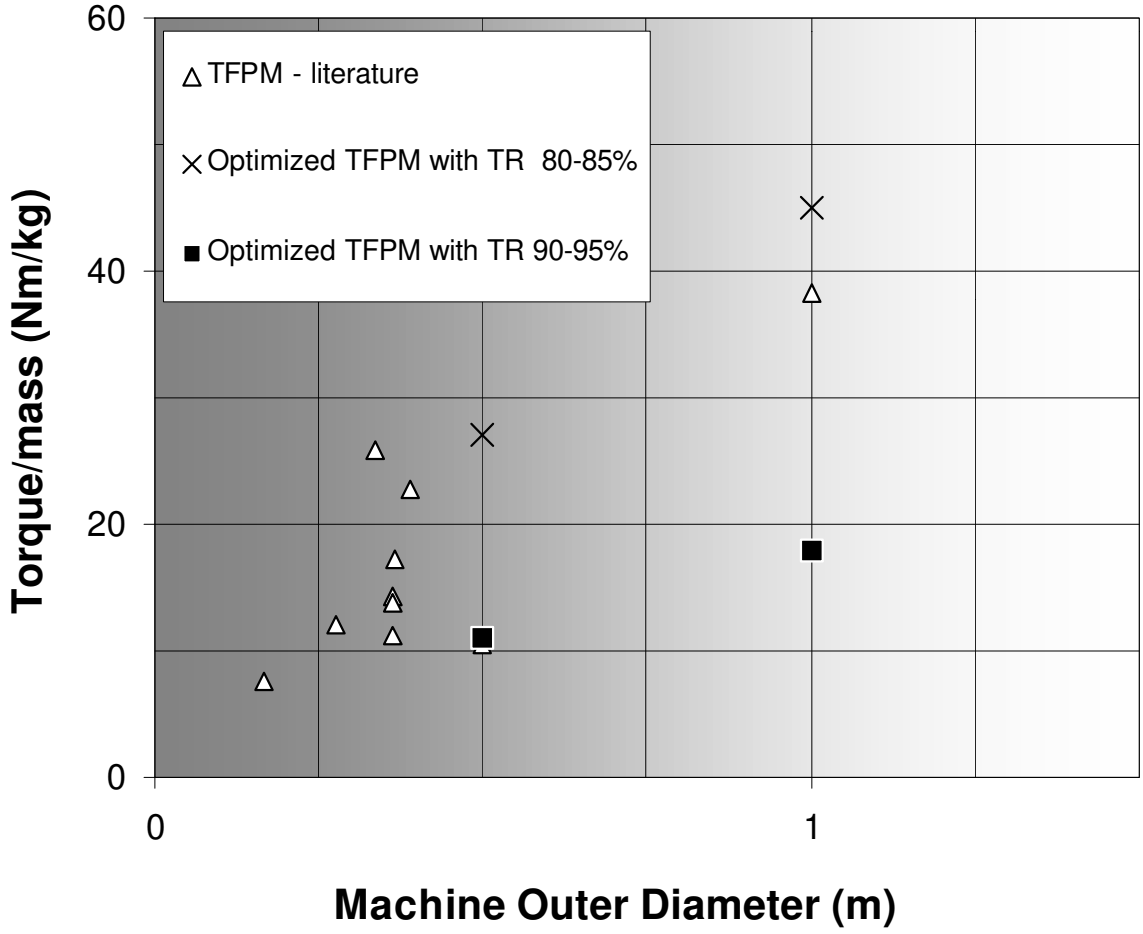

Figure 8-5: Torque/mass of active material for the optimized designs of the TFPM with toothed rotor and the other TFPM topologies discussed in past literature.

8.5. Summary and discussion

The comparison between TFPM machines with toothed rotor and conventional PM synchronous machines was discussed. To allow a valuable comparison, the two machine topologies were optimized with the same constraints, that is efficiency, average nominal torque, outside diameter, rotational speed, air gap thickness and material properties. Optimization of the TFPM machine with toothed rotor was based on the analytical model developed in chapter 7. The resulting torque values were validated with a FEM check. It was found that our analytical model of the TFPM machine with toothed rotor gives an average nominal torque value 30% to 40% too high compared to the results obtained with FEM. The FEM-derived torque was used as the reference for comparison. The conventional PM synchronous machine was optimized with the mathematical model and assumptions of chapter 4 to obtain the lowest cost/torque and the highest torque/mass. Comparison of the cost/torque and torque/mass of the two machine topologies for diameters ranging between 0.5 m and 3.0 m showed favor-

able expected performances of the TFPM machine with toothed rotor for diameters of 0.5 m and 1.0 m. Diameters of 2.0 m and above favored the conventional PM synchronous machine. This is due to the larger air gap used in the calculations for larger diameters.

Larger air gaps create significant flux leakage in the TFPM machine with toothed rotor. To compensate the increase in flux leakage, a larger pole pitch is required. It appears that the TFPM machine with toothed rotor is a valuable option as long as its optimized pole pitch can be kept significantly lower than the pole pitch of the conventional PM synchronous machines.

It was already mentioned that the analytical model used for the optimization of the TFPM machine with toothed rotor is rather inaccurate, tending to overestimate the average torque value. It is expected that the "optimized" designs found with the optimization process are not truly optimal due to this inaccuracy. Hence, we must highlight the possibility that better designs of the TFPM machine with toothed rotor could be identified with a more accurate model. This model is yet to be derived.

Chapter 9

Experimental results on TFPM machines with toothed rotor

9.1. Introduction

This chapter introduces some experimental results in order to validate the concept of TFPM machine with toothed rotor. The first part of this chapter presents a linear version of the TFPM machine with toothed rotor. This is the subject of section 9.2.

The second part of this chapter presents a rotating machine using the TFPM topology with toothed rotor. This is the subject of section 9.3, which puts more emphasis on the measurements of the machine parameters. Comparison with the model developed in chapter 7 is also addressed in section 9.3.

9.2. Measurements on a linear TFPM actuator with toothed rotor

Practically, building a first prototype of TFPM machine can become a very costly exercise. In the TFPM machine with toothed rotor, three lamination types are needed: the toothed rotor structure, the stator C-core and the stator trapezoidal core. These lamination patterns are not available on the market. Laminations must be cut in one way or another. The most common method is the use of a die specifically built for these shapes. Then the laminations are stamped with a punch press. Also, the flux concentrators must be built from powdered iron material pressed at high pressure. This also requires a mold. All these elements are expensive, not to mention the assembly of all the components and the other inactive mechanical components that need to be machined. To reduce the investment necessary for conducting the first experiments, a linear actuator was built with the geometry of the TFPM machine with toothed rotor.

The objectives of building the linear actuator were:

- 1) validate the construction principle and advantages claimed for the TFPM structure with toothed rotor with only a few poles;
- 2) verify that a tangential force can be obtained from the TFPM structure with toothed rotor;
- 3) become more familiar with the use of powdered iron material.

The experimental set-up used is shown in figure 9-1. The materials used for the construction were Nd-Fe-B for the magnets, fully-processed M-45 electric steel with 0.35 mm thickness for the stator horseshoes, trapeziums and the rotor toothed structure, and ATOMET-EM1 powdered iron for the flux concentrators. The dimensions of the linear actuator are given in table 9-1.

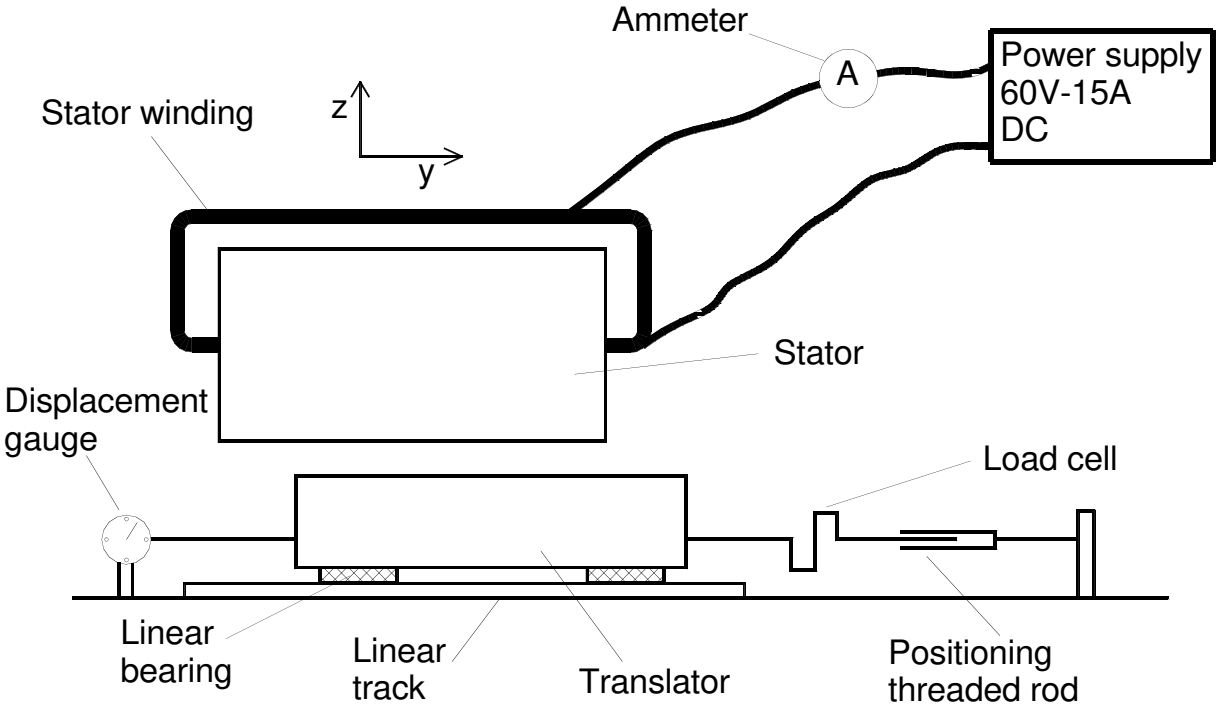

Figure 9-1:Linear actuator using the TFPM structure with toothed rotor: test set-up.

The linear actuator was operated in a static way and only static tangential forces were recorded. Figure 9-3 shows the forces measured as a function of the translator position for a constant current of 2.5 A. Figure 9-3 also shows the result of a finite element analysis performed on the exact same geometry, having the same number of poles (16 poles). Figure 9-4 shows the force obtained for several constant currents between 0 A and 8.5 A. In figure 9-4, the results were filtered with a 6^{th} order polynomial curve-fitting. Some of the points of figure 9-3 show a difference between the measured value and the value calculated with FEA. To explain these differences, it must be mentioned that a small error on the position measurement may lead to a substantial variation in the force measurement where the slope is steeper as it is the case for the positions 8 mm and 10 mm.

Table 9-1. Main geometrical parameters of the linear TFPM actuator with toothed rotor built (x, y, z coordinate system refers to figure 9-1).

Actuator geometrical parameter	Data
Pole pitch (y - axis)	16 mm
Number of poles	16
Number of turns in the stator winding	538
Magnet thickness (y - axis)	2 mm
Length of magnets - flux concentrators (x - axis)	72 mm
Width of magnets - flux concentrators (z - axis)	12 mm
Thickness of flux concentrators (y - axis)	8 mm
Rotor tooth width (y-axis)	4 mm
Rotor tooth width (x - axis)	48 mm
Slot depth (z-axis)	14 mm
Air gap (z-axis)	1 mm
Stator - tooth distance (z-axis)	4 mm
Stator core thickness (y-axis)	8 mm
Length of the stator core foot (x-axis)	42 mm

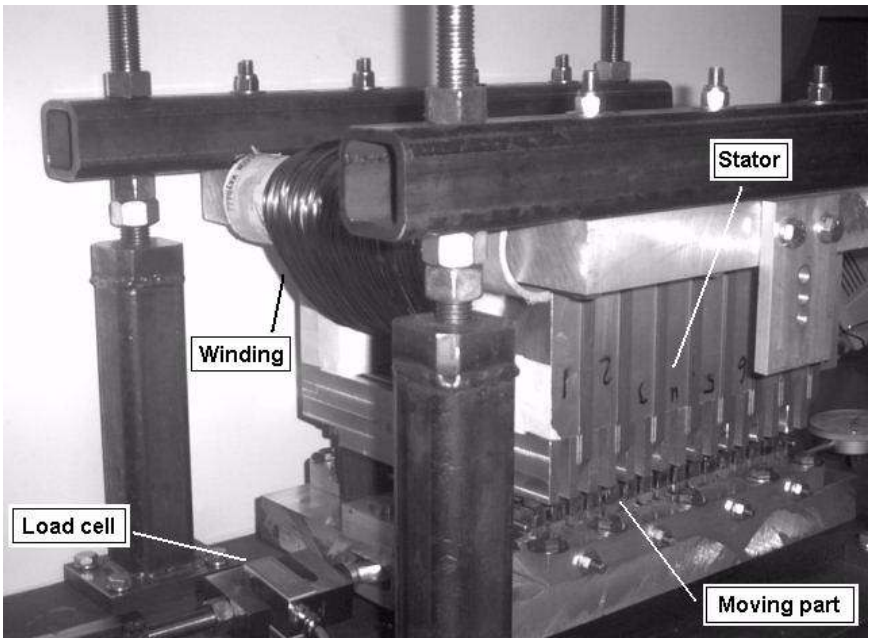

Figure 9-2:Linear actuator using the TFPM structure with toothed rotor; picture.

Another possible explanation can be related to the effect of hysteresis in the *B(H)* curve of the magnetic material, which is not taken into account in the FEA software. However, little effort was made to explain those differences because the correlation between the force values

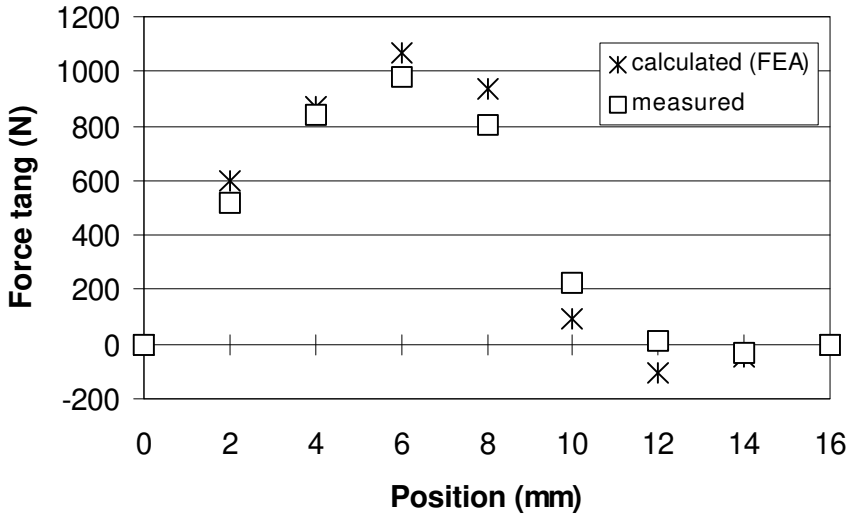

Figure 9-3: Static force versus position, for i = 2.5 A, and number of turns = 538.

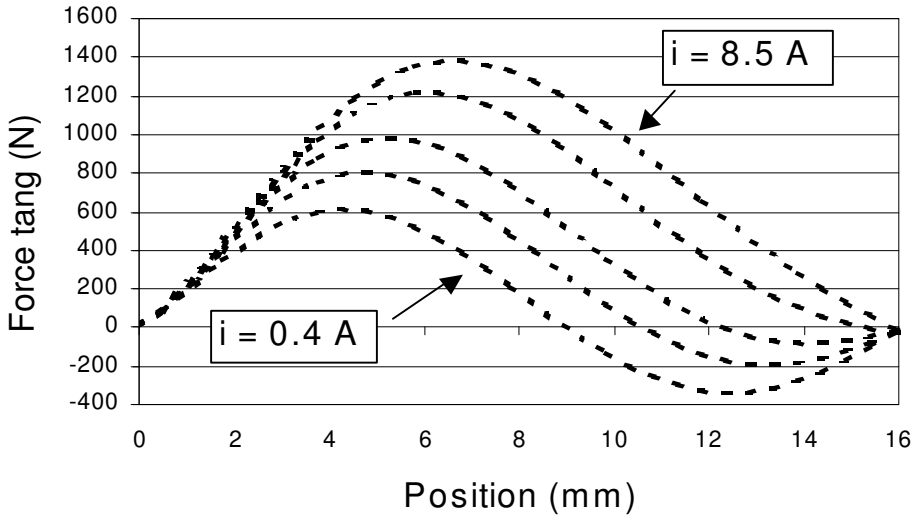

Figure 9-4: Static force measured experimentally versus position, for i = 0.4 A, 1.5 A, 2.5 A, 4.5 A, 8.5 A. Number of turns = 538. The experimental results are filtered with a 6^{th} order polynomial curve-fitting for clearer illustration.

measured and those predicted with the finite element analysis computation are acceptable and prove that the TFPM structure with toothed rotor can generate tangential forces.

Problems encountered during construction

The sub-assembly composed of one flux concentrator and two magnets could easily be mounted. The magnets were glued to the concentrators and each concentrator was glued to an aluminum block. The aluminum block is necessary to keep the magnet field from leaking

into the bottom of the slot and is also used to retain the concentrator to the toothed rotor structure. The sub-assembly formed by the magnets, the flux concentrator and the aluminum block was then inserted into the toothed structure. For the linear actuator, this whole process was done manually but it could easily be automated. The main problem encountered was the weak mechanical bonding between the flux concentrator and the aluminum block, which could be solved by proper selection of the glue type.

Another point concerns the production of the flux-concentrators. Laminated steel M-45 was first used for this purpose by stacking and welding them together. In a second step, this production process could be improved by making the flux concentrators from molded powdered iron. The static forces obtained were also slightly higher with powdered iron. This last result was more surprising since the permeability of powdered iron is much lower than that of laminated steel. However, the first flux concentrators were built with isolated laminated steel which were oriented parallel to the magnet plane. With such orientation, a large part of the magnet flux was flowing perpendicular to the lamination plane, in a direction where the average permeability was lower than that of powdered iron, due to the laminations coating.

A key point in this investigation is the thickness of the airgap. The number of mechanical pieces and their respective geometrical tolerances made it very difficult to maintain a uniform air gap thickness over the whole air gap area. This problem could be solved by machining both the stator and the translator. It is expected that the problem will also arise in the rotary version and machining both the rotor and stator should also be included in the production process.

One of the targets in developing the TFPM machine with toothed rotor is simplifying the production of flux-concentrating TFPM machines. During the construction of the linear actuator, the different production advantages described in chapter 6 could successfully be tested. Considering the 3 objectives discussed earlier, the linear actuator has confirmed all expectations and enough confidence was acquired for the construction of a rotary version of the TFPM machine with toothed rotor.

9.3. Measurements on a rotating TFPM machine with toothed rotor

The 6 objectives of building a rotary version of the TFPM machine with toothed rotor are:

- 1) measure the machine torque, inductances, no-load flux and losses.
- 2) compare the measurements with the model developed in chapter 7;
- 3) compare the torque measurements with finite element simulations;
- 4) check the assumption of sinusoidal voltage waveform;
- 5) check that temperatures stay within acceptable range;
- 6) obtain experience with the construction in the rotary version.

9.3.1. Selection of the machine geometrical parameters

The design of a rotating TFPM machine with toothed rotor has been guided by the application as a direct-drive generator for a 25-kW wind turbine. The nominal speed was chosen as 100 rpm and the generator outside diameter was chosen as 53 cm. The number of phases was 3 and the generator was built with three single-phase generators stacked on the same shaft. Each phase was shifted by 120 degrees with respect to the two other phases. This phase shift was made by aligning the stator cores and by phase shifting the rotor rings.

The machine was built before the analytical modeling and optimization was completed. Thus, the design presented here is not optimized. The machine was built according to the geometry described in table 9-2. Also, the following values were used: J = 4.0 A/mm^2, k_{sfill} = 0.5, B_r = 1.10 T, μ_{rFe} = 2000, μ_{rm} = 1.09, B_{Fesat} = 1.8 T. Pictures of the TFPM machine with toothed rotor are shown in figure 9-5 and figure 9-6.

The prototype was built with an inner stator and an outer rotor. The stator C-core and trapezoidal laminations were cut using a punch press. Four retaining disks were mounted to the stator shaft and each C-core was inserted between the retaining disks. The stator was then moved onto a lathe and the stator winding could be rolled inside the C-cores.

The rotor structure was built from laser-cut laminations. Laminations were stacked together and six rotor rings were assembled.

Table 9-2. Main geometrical parameters of the TFPM machine with toothed rotor built.

Air gap diameter d_g	46 cm
Pole pitch τ_p	14 mm
Number of pole pairs p per phase	52
Number of turns in the stator winding N_s per phase	27
Magnet thickness h_m	2 mm
Length of magnets and flux concentrators l_{rt1}	48 mm
Width of magnets and flux concentrators w_m	12 mm
Thickness of flux concentrators w_{rc2}	6 mm
Rotor tooth width w_{rc1}	4 mm
Thickness of the insulating block under the flux concentrator h_{ri}	5 mm
Slot depth	14 mm
Air gap g	1 mm
Stator - Tooth distance $h_{ru} + g$	4 mm
Stator core thickness w_{sc}	8 mm
Length of the stator core foot l_f	40 mm
Mass of PM material per phase	3.6 kg
Mass of active material per phase (without the rotor ring)	68 kg
Cost of active material per phase	530 Euros

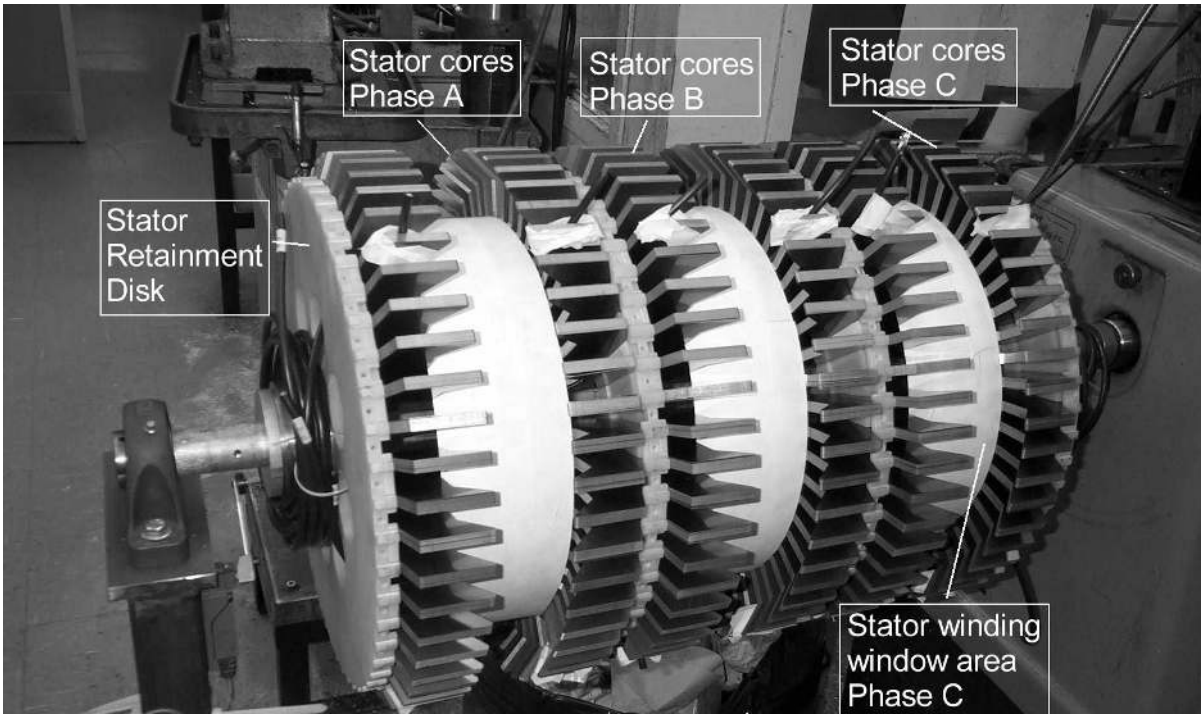

Figure 9-5: Stator cores before winding. Rotor and trapeziums not mounted.

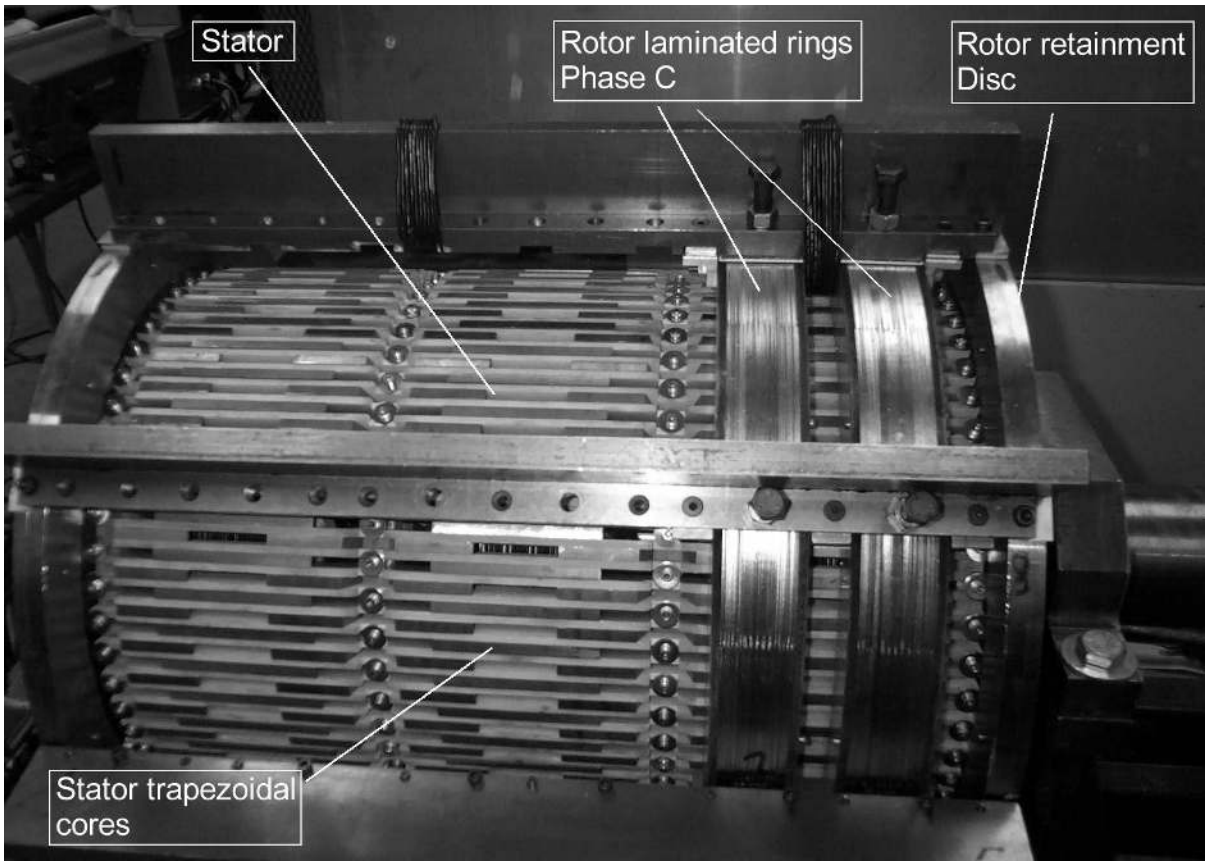

Figure 9-6: Prototype of the TFPM machine with toothed rotor. Three stator phases and one rotor phase are shown.

The magnets were glued to their powdered-iron flux concentrator, thus forming 624 sub-assemblies composed of one flux concentrator and two magnets. The 624 pieces were inserted inside the guiding structure of the toothed rotor, forming the six magnetized rotor rings. The six rings were inserted around the stator body and fixed to two rotor retainment disks located at both ends, by using 8 transversal aluminum bars.

9.3.2. Performance obtained and comparison with the model

Experiments on the TFPM machine with toothed rotor have been conducted with one phase mounted as illustrated in figure 9-6. The experimental set-up used was composed of a motor drive controlling an induction motor with a synchronous speed of 1800 rpm. A gearbox with gear ratio 18:1 was mounted on the shaft of the induction motor, providing a rotational speed of 100 rpm. The TFPM machine with toothed rotor was mechanically joined to the 100 rpm shaft through a flexible joint with chains. The torque was measured with a strain gauge coupled to a 60 cm-long arm welded onto the stator of the TFPM machine with toothed rotor. The strain gauge provided a force measurement, which multiplied by the arm length gave the mechanical torque.

The terminals of the TFPM generator with toothed rotor were connected to a bank of capacitors and resistors. The test set-up is shown in figure 9-7. Figure 9-8 shows the simplified equivalent circuit of the TFPM with toothed rotor with the capacitive and resistive load connected to its terminals. The capacitor and resistor values shown in figure 9-8 represent one load example, for which the maximum power could be extracted from the TFPM generator feeding a linear load.

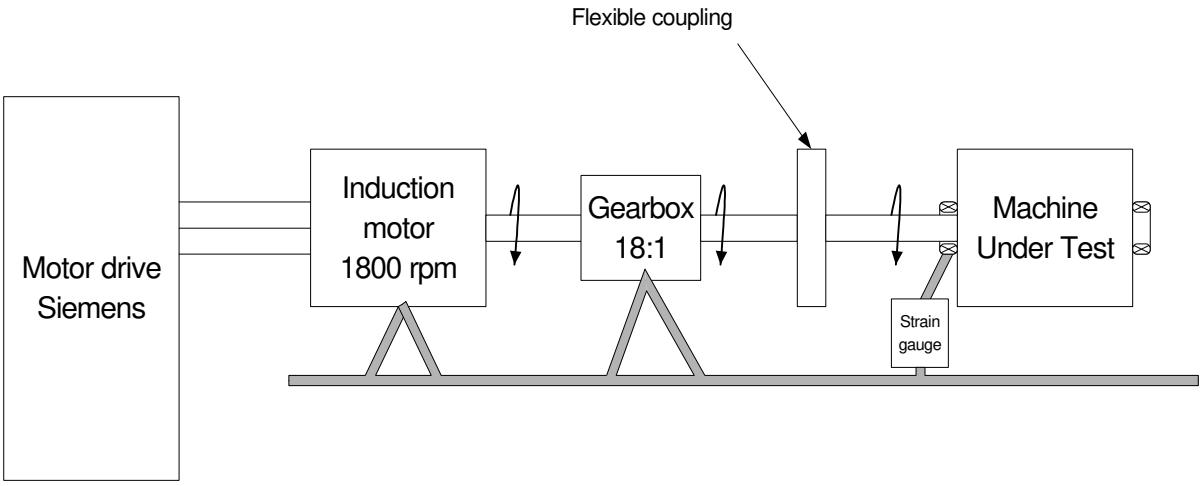

Figure 9-7: Experimental set-up for the TFPM generator with toothed rotor.

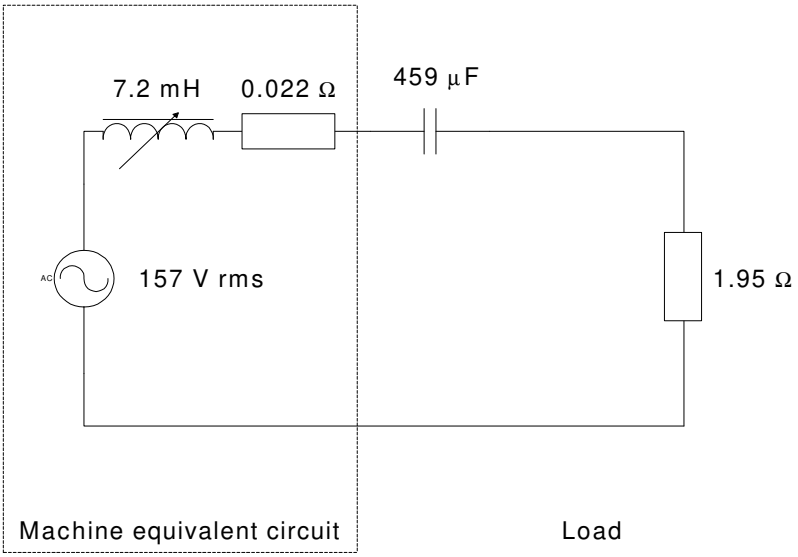

Figure 9-8: Connection of electrical loads to the TFPM generator with toothed rotor.

No-load voltage and flux

First, the no-load voltage was recorded. It is shown in figure 9-9. Integrating the no-load voltage over one half cycle allows us to extract the flux amplitude $\hat{\Phi}_{pnl}$ in the aligned position with the following equation:

$$\hat{\Phi}_{pnl} = \frac{1}{2pn_s} \int_{halfcycle} e\,dt \qquad (9\text{-}1)$$

The result is given in table 9-3 with a comparison between the measured values and the value predicted by the model developed in chapter 7. The agreement between the value of $\hat{\Phi}_{pnl}$ measured and the value predicted with the model is within 1%. Also, the finite element calculation gave a value of 256 µWb, which is 6% lower than these two values (experiment and model).

In chapter 7, it was assumed that all voltages and currents will have a sinusoidal waveform. Inspection of figure 9-9 clearly indicates that the no-load voltage is not sinusoidal. The shape has a some content of third harmonic. Figure 9-9 indicates that the third harmonic component of the no-load voltage has an amplitude of about 10% of the fundamental harmonic. This means that the no-load flux has a third harmonic of amplitude around 3% of the amplitude of the fundamental flux wave.

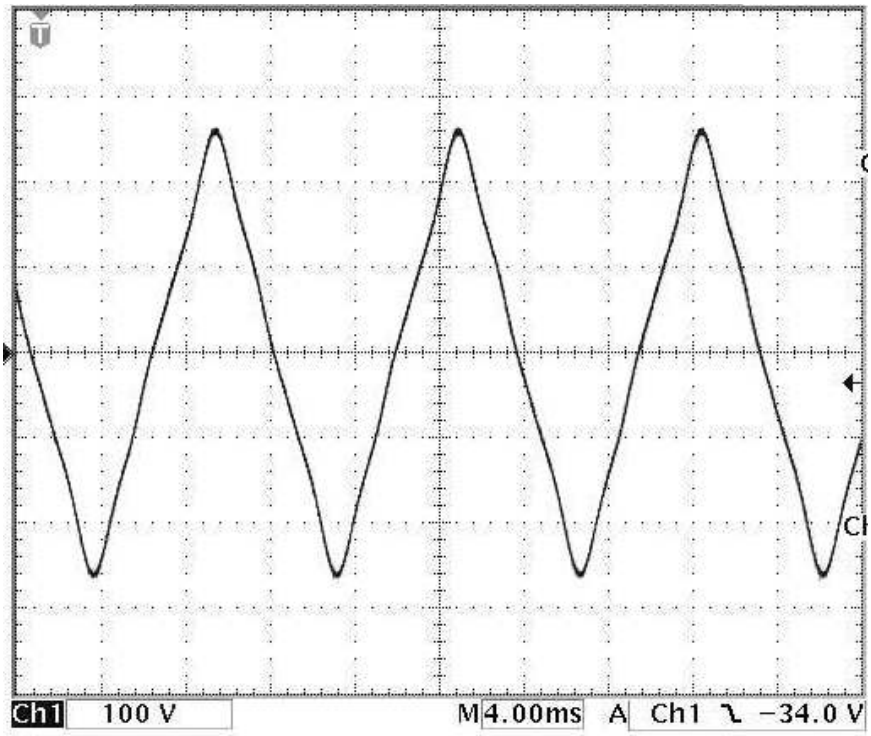

Figure 9-9: Machine terminal voltage at no-load (one phase); 100 V/div, 4 ms/div. n = 100 rpm, freq. = 87 Hz, peak-peak voltage = 530 V, rms voltage = 157 V.

Voltage and current with a linear load

Several combinations of linear loads have been experimented. Those results are not all presented here, because it would require many pages and would not add so much to the study. Here, the main results of some selected load combinations are highlighted.

When a linear load is connected to the generator as in figure 9-8, the voltage third harmonic component observed at no-load reduces strongly. In figure 9-10, a load made of a capacitor of value 224 μF in series with a resistor of value 6.71 Ω was connected to the machine terminals. The terminal voltage has become more sinusoidal. The same behavior was also observed for a very light resistive load directly connected to the machine terminals (no capacitor in the circuit in that case). It appears that the machine stator inductance quickly filters out the higher current harmonics.

In figure 9-11, the load was increased*. The machine terminals were connected to a resistive load of 1.95 Ω in series with a capacitive load of 459 μF. In the analysis of chapter 7, the reluctances $\mathcal{U}_{SScore}$ and $\mathcal{U}_{Ccore}$ were considered as constant. In reality, the relative permeability μ_{rFe} of the Fe-Si laminations reduces as the flux density level increases.

* There is an error on figure 9-11. The current clamp was placed in the wrong current direction during the measurement. The current should be leading, not lagging the terminal voltage.

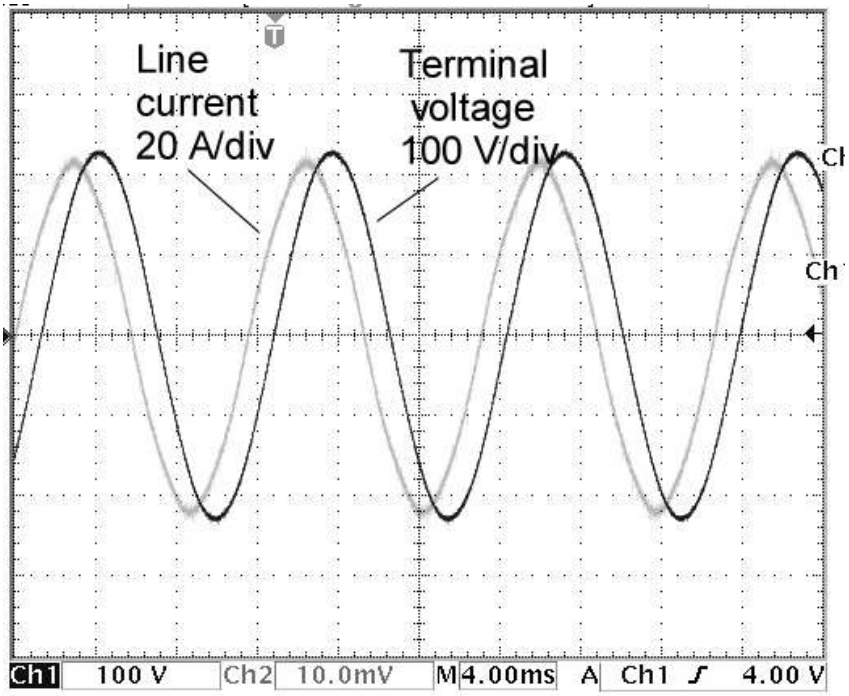

Figure 9-10: Machine terminal voltage & line current for load C_s = 224 uF, R = 6.71 Ω. n = 100 rpm, freq. = 86.84 Hz, peak-peak voltage = 468 V, rms voltage = 161 V, rms current = 30.4 A. Electrical power output = 3.7 kW (one phase). 4 ms/div.

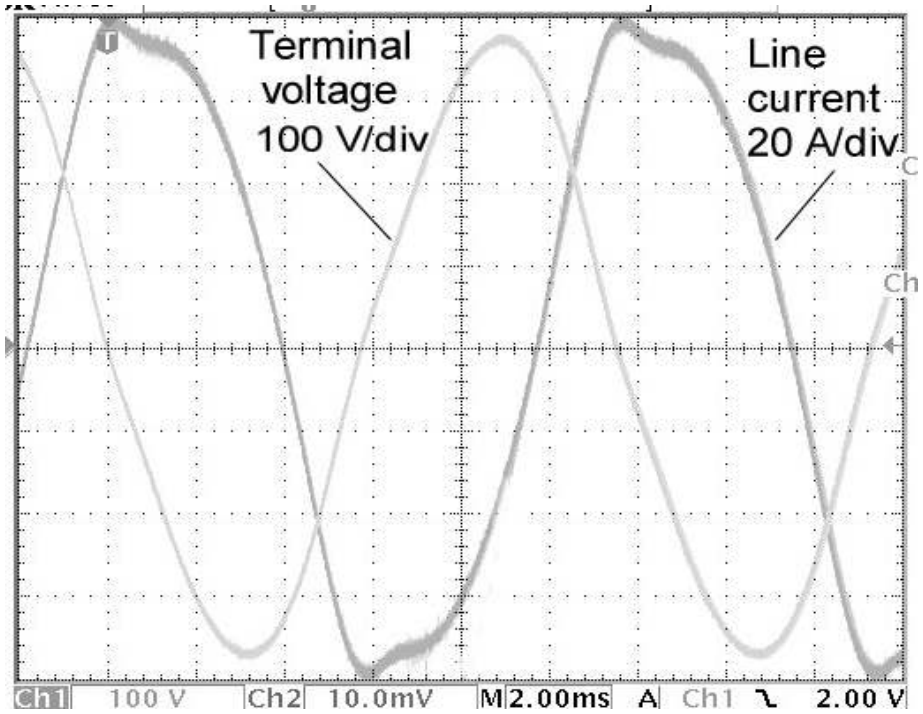

Figure 9-11: Machine terminal voltage & line current for load C_s = 459 uF, R = 1.95 Ω. n = 100 rpm, freq. = 86.80 Hz, peak-peak voltage = 756V, rms voltage = 252V, rms current = 57.6 A. Electrical power output = 6.6 kW (one phase). 4 ms/div. Current clamp was set in the wrong direction.

Consequently, these two reluctances increase as the current increases and the stator reactance decreases accordingly due to core saturation. This is why an arrow was superposed over the inductor symbol of figure 9-8, indicating that the stator inductance is in fact variable. This non-linear behavior of the stator inductance explains the waveforms observed in figure 9-11. If we trace the current cycle step by step, the current starts at 0 A with a rather constant stator inductance value. In that region, the negative reactance value of the capacitor compensates the positive reactance value of the stator inductor. As the current increases above 60 A, the stator inductance starts decreasing and the negative reactance value provided by the capacitor over-compensates the stator reactance. The result is an increasing load as the current increases above 60 A. This effect has three consequences:

- 1) current oscillation;
- 2) difficulty of extending the current amplitude above 80 A with a linear load;
- 3) shift of the current waveform so that it creates more reactive power and less active power than with sinusoidal waveforms.

The effects 2) and 3) in particular will affect the amount of electrical power and torque that can be extracted from the generator.

Figure 9-12 and figure 9-13 illustrate the results of an experiment showing the point of saturation of the machine and the inductance value in the aligned and unaligned positions. The experiment consists of charging a 30,000 µF capacitor to a voltage of 100 V DC, which is then discharged into the machine winding while the machine is at rest. The results confirm that core saturation occurs at about 80 A. The inductance values measured are reported in table 9-3.

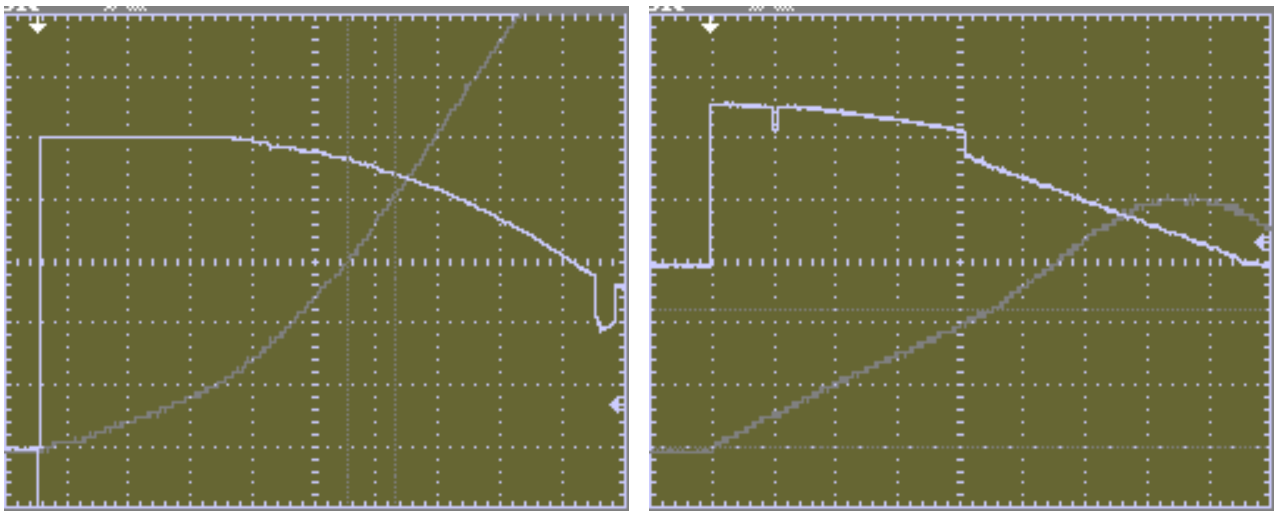

Figure 9-12: Current measured as a function of time for a winding excited with a 30,000 µF capacitor charged with 100 V. Machine in the aligned position. Left-hand side: flux adds up to the no-load flux. Right-hand side: flux opposes the no-load flux. Grey line = winding current, white line = winding voltage. Scale: current = 50 A/div, time = 2.5 ms/div, voltage = 20 V/div (left) and 50 V/div (right).

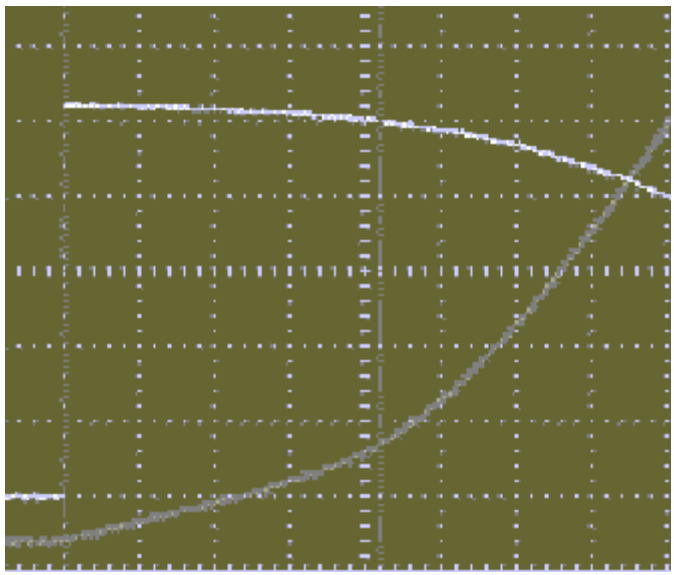

Figure 9-13: Current measured as a function of time for a winding excited with a 30,000 μF capacitor charged with 100 V. Machine in the unaligned position. Grey line = winding current, white line = winding voltage. Scale: current = 50 A/div, time = 1 ms/div, voltage = 20 V/div.

The values presented in table 9-3 indicate that the maximum torque obtained with the current machine setup is 65% of the value predicted with the model. This is consistent with the conclusion of chapter 8, which states that the model developed in the thesis overestimates the average nominal torque by 30 - 40% due to saturation. The torque value obtained experimentally is consistent with the torque value obtained with FEM. The FEM simulation gave a torque value of 722 Nm per phase while, experimentally, a torque value of 778 Nm was obtained. Table 9-3 also presents the losses measured experimentally and calculated with the model. The losses measured are 22% higher than the value predicted by the model. The lower torque and higher losses result in an overall efficiency of 81%, compared to the value of 89% predicted with the model.

Problems encountered during construction

The main problem encountered during construction was related to the air gap thickness. As it will be discussed in chapter 9, the performance of the TFPM machine with toothed rotor is very much dependent upon the air gap thickness. To meet the requirement of a 1-mm air gap, the stator was machined on a lathe. This step assured an excellent mechanical tolerance on the stator radius along the circumference. However, we discovered that it short-circuited the stator laminations on the surface which had been in contact with the lathe tool. Also, each stator core was previously soldered to maintain all laminations together. These two processes lead to additional paths for the eddy currents, resulting in an increase in eddy current losses. No further investigation of the problem was made, but we foresee that a different production method could circumvent the problem and reduce the losses presented in table 9-3.

Table 9-3. Performance predicted with the model and obtained experimentally.*

	Model prediction at nominal load	Experimental results with C_s = 459 μF / R = 1.95 Ω
Maximum average torque per phase *T*	1194 Nm / phase	778 Nm/phase
Maximum electrical power	11.2 kW	6.6 kW
No-load flux per pole $\hat{\Phi}_{pnl}$	271 μWb	272 μWb
Reluctance in the aligned position $\mathcal{U}_{ap}$	5.3 A/μWb	Can not be measured directly
Inductance in the aligned position L_a	7.2 mH	7 mH (initial induct. value)
Reluctance in the unaligned position $\mathcal{U}_{up}$	4.4 A/μWb	Can not be measured directly
Inductance in the unaligned position L_u	8.6 mH	6.5 mH (initial induct. value)
Peak stator magnetomotive force $\hat{\mathfrak{I}}_s$	3025 A-turns	2133 A-turns
Maximum losses	1250 W/phase- (does not include mechanical losses)	1530 W/phase (including mechanical losses)
Peak stator flux density	1.8 T	1.6 T (deduced from equation (9-1) and figure 9-11)
Efficiency	89%	81%
Power factor at maximum load	0.47	0.45

Thermal performance

The machine was operated as a generator with a load of C_s = 459 μF and R = 1.95 Ω. Only one phase was tested and the evolution of the temperature as a function of time is shown in figure 9-14 for five locations inside the machine. The peak temperature observed was 66 degrees Celsius which is acceptable.

* The machine prototype discussed here is the same as in [Dub 2002c]. The reader will note that the results obtained with the model and experimentally are slightly higher than in [Dub 2002c]. Further experimental work and model fine-tuning have taken place after the publication of [Dub 2002c] which lead to these new values. Although the data has changed a little, the general conclusions are the same.

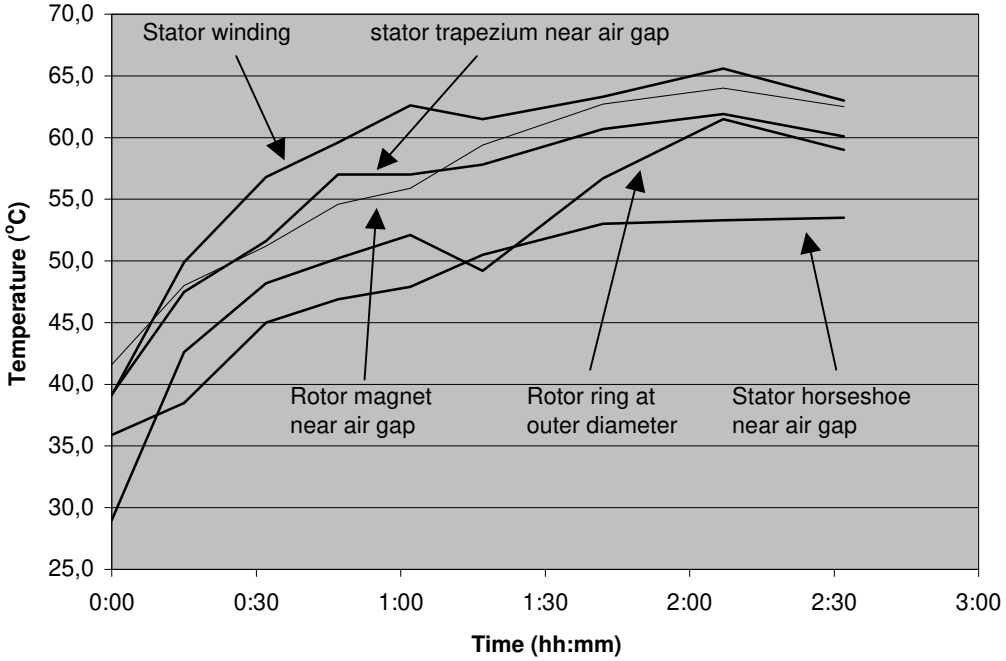

Figure 9-14: Temperatures of the TFPM machine under test at 5 different locations as a function of time. Load conditions: C_s = 459 μF, R = 1.95 Ω. Only one phase tested. The ambient temperature is 25 degrees. The machine was already warm at t = 0:00.

9.4. Conclusions

This chapter presented experimental work performed on the TFPM structure with toothed rotor derived earlier in this thesis.

First, a linear actuator was built from which static forces could be measured. The linear actuator demonstrated the ability of the TFPM topology with toothed rotor to produce a tangential force. Also, the various construction advantages claimed in chapter 6 were successfully verified. Flux concentrators made with powdered iron material were pressed, inserted in the actuator and compared to the force obtained with flux concentrators built from Fe-Si laminations. Powdered iron concentrators were much easier to build and gave a tangential force output slightly higher than with laminated flux concentrators.

Then a circular TFPM generator with toothed rotor was built. The machine was tested at no-load and then loaded with linear loads (capacitors and resistors). The agreement is excellent between the values of no-load flux $\hat{\Phi}_{pnl}$ and inductance L_a measured and predicted with the model of chapter 7. Concerning the maximum average torque $\overline{T}$ and the peak magnetomotive force $\hat{\Im}_s$, the measurements also demonstrated that the model derived in chapter 7 overestimates these two parameters by about 30 - 40%. This is due to non-linear behavior of the stator core in the unaligned position, which is not considered in the model.

The losses measured are about 20% higher than the losses predicted by the model under nominal load conditions. However, the iron losses are increased in the experimental machine due to short-circuits between the stator laminations caused by the manufacturing process. Also, the use of a capacitor to compensate the non-linear inductance generates

higher harmonics in the current waveform which adds to the iron losses. Also, the mechanical losses are measured as part of the total losses. These three effects are "parasitics" in the measurements and will certainly increase the losses, while they are not included in the loss model developed in chapter 7. Additional experimental work should be done in order to quantify or eliminate these three effects. Although the three effects mentioned above tend to increase the losses, other points will contribute to make them lower in the experiment conducted. The copper losses are lower due to lower rms current in the stator winding. Also, the peak flux density is 1.6 T where the losses predicted by the model assumed a value of 1.8 T. We may speculate what the losses would be if the laminations were not short-circuited and if a PWM voltage-source rectifier was used instead of a linear load. However, we can not conclude at this point about the correlation between the losses measured and those predicted by the model because insufficient reliable experimental work has been done on the machine. We can only say that the loss model derived in chapter 7 gives a good order of magnitude. But we cannot confirm whether or not it agrees with experiment.

The no-load voltage waveform recorded is not sinusoidal as assumed previously. It has a third harmonic component of amplitude about 10% of the fundamental component, which corresponds to a flux harmonic component of about 3% of the fundamental flux component. The current waveform was also previously assumed as sinusoidal. In the experimental work conducted here, it was not sinusoidal due to non-linearities. The use of a PWM voltage-source rectifier would be suitable to provide a sinusoidal current waveform.

Temperatures were also recorded at several locations inside the TFPM generator under test. In the maximum load configuration used, the maximum temperature recorded was 66 degrees Celsius, which is below the limits imposed by the materials inside the machine.

Concerning the construction of the TFPM machine with toothed rotor, the main problem experienced was the control of the air gap thickness. To obtain a 1-mm air gap, the stator surface had to be machined on a lathe, which short-circuited the stator laminations together thus increasing the iron losses. The suggestion of a hybrid structure is made here. In such a hybrid structure, the stator foot could be made of powdered iron material while the stator leg could be made of laminated steel. This would allow machining the stator surface and at the same time would reduce the iron losses due to the flux entering perpendicular to the lamination plane in the unaligned position.

Chapter 10

Conclusions and recommendations

The thesis deals with the issue of cost reduction in direct-drive generators for wind turbines. Today, the combination gearbox-medium-speed (1000-2000 rpm) induction generator largely dominates the market of MW-scale wind turbines. This is due to the lower costs of the gearbox option compared to the costs of gearless systems. Nevertheless, there is an acute interest among researchers and wind turbine suppliers in the possibility of removing gears and slip rings from the drive train. The main advantages of direct-driven generators are variable-speed, less maintenance (no oil is required and slip rings can be avoided) and higher reliability due to the absence of wear between gears. The direction followed by the thesis is the investigation and comparison of various permanent magnet (PM) machine topologies. The topologies investigated were:

- conventional PM synchronous machine;
- conventional PM synchronous machine with flux concentration;
- slotted axial-flux PM machine;
- TORUS;
- surface-mounted transverse-flux PM machine;
- flux-concentrating transverse-flux PM machine.

The thesis targets machine topologies with the lowest cost/torque and highest torque/mass.

10.1. Conclusions

Longitudinal PM machines

Scientific literature indicates that short pole pitches reduce the mass and cost of stator active material. A comparison was made in the thesis between the cost of wound-rotor and PM exci-

tations. It was established that PM excitation is more cost-effective for pole pitches shorter than about 10 cms. Also, PM rotors give lower machine losses lower due to the absence of rotor copper losses.

In the comparison between the TORUS and other longitudinal-flux machines, a general reasoning based on force density allowed us to conclude to the higher cost and weight of the TORUS. Also, a wide survey of PM machine designs built and proposed in the scientific literature confirmed this conclusion.

Regarding the comparison of the slotted axial-flux PM machine to the conventional PM synchronous machine with/without flux-concentration, analytical models were developed in the thesis for the three machine topologies. Based on these models, optimization of the machine designs for various diameters and low-speed conditions was made. Optimized designs of the conventional PM synchronous machine with/without flux-concentration gave the lowest costs and masses for a given average nominal torque value. The same conclusions have been obtained for all diameters and for efficiencies of 90% and 95%.

Minimization of PM material in machines

The thesis investigated the contribution of each PM volume element to the total flux in the stator windings. The question was raised to whether PMs should be rectangular, and if not, what shape is the most cost-effective. A new expression was derived, describing the flux linkage in terms of a volume integral applied over the volume of PM material. Each PM volume element dv is given a certain contribution to the total no-load flux linkage. Then, a method was developed to minimize the volume of PM material in machines. The shaping of magnets and the variation of magnetization angle inside the PM were especially investigated. The method was applied to the magnets of a conventional PM synchronous machine and surface-mounted TFPM machine. The resulting V-shapes and magnetization patterns increase the flux linkage per PM volume. However, PM shaping is found to be more beneficial for machines with short pole pitches, due to their higher concentration of fringing fields.

Contribution of PM material in surface-mounted and flux-concentrating TFPM machines

The thesis identified transverse-flux PM machines as suitable for cost reduction, from their higher current loading. A survey of the designs found in literature confirmed that transverse-flux PM machines could bring higher torque/mass and lower cost/torque compared to the conventional PM synchronous machine.

The flux-concentrating TFPM machines was chosen and surface-mounted TFPM machines were discarded, because of the higher contribution of PM volume elements to the no-load flux in the flux-concentrating TFPM machines. Thus, less PM volume is needed in flux-concentrating PM machines for a given no-load flux value.

TFPM machine with toothed rotor and analytical modeling in TFPM machines

Among the five flux-concentrating TFPM topologies described in earlier work, the clawpole TFM machine appeared as promising. However, this machine makes a massive use of pow-

dered iron, which has specific losses higher than standard Fe-Si laminations. Also, the relative permeability and saturation flux density are lower for powdered iron.

None of those flux-concentrating TFPM machines were considered as satisfactory in terms of construction characteristics. Four characteristics are preferable:

- the stator should be single-sided;
- the rotor PM and flux concentrators should not be dependent upon the build-up of mechanical tolerances in the circumferential direction;
- the installation of rotor PM and flux concentrators should be automated;
- the flux circulation should be such that laminated steel can be used in the stator.

To fulfill these requirements, a new TFPM geometry was derived, named TFPM machine with toothed rotor. An approximate three-dimensional analytical model was developed for the TFPM machine with toothed rotor. The model allows analytical prediction of the nominal average torque, losses and efficiency. This model is based on three equivalent linear magnetic circuits which establish the following quantities:

- no-load flux $\hat{\Phi}_{pnl}$ per pole;
- reluctance $\mathcal{U}_{ap}$ seen by the stator winding in the aligned position;
- reluctance $\mathcal{U}_{up}$ seen by the stator winding in the unaligned position.

These three parameters are determined from lumped reluctances, which are functions of the machine geometrical parameters. These are obtained after curve-fitting a large number of reluctance values obtained from finite element computations.

Comparison between TFPM machine with toothed rotor and conventional PM synchronous machine and experimental verifications

The comparison between TFPM machines with toothed rotor and conventional PM synchronous machines was investigated. The two machine topologies were optimized with the same constraints, that is efficiency, average nominal torque, outside diameter, rotational speed, air gap thickness and material properties. Optimization of the TFPM machine with toothed rotor was based on the analytical model described in the previous paragraph. The resulting torque values were validated with a FEM check. It was found that our analytical model of the TFPM machine with toothed rotor gives an average torque value 30% to 40% higher than the values obtained with FEM. Consequently, the FEM-derived torque was used as the reference for comparison. Comparison of the cost/torque and torque/mass of the two machine topologies showed favorable performance for the TFPM machine with toothed rotor with diameters of 1.0 m and lower. However, diameters larger than 1.0 m favored the conventional PM synchronous machine.

The degradation of performances of TFPM machines at diameters above 1.0 m is due to the larger air gap used in the calculations in those cases. Larger air gaps create significant

flux leakage. To compensate the increase in flux leakage, a larger pole pitch is required. It appears that the TFPM machine with toothed rotor is a valuable option as long as its optimized pole pitch can be kept significantly lower than the pole pitch of the conventional PM synchronous machines.

Efficiency also played a dominant role in the performance of the TFPM machine with toothed rotor. Although not formally shown in the thesis, we suggest that the same influence of efficiency is also expected for other TFPM topologies.

A prototype of the TFPM machine with toothed rotor has been built and tested in a low-speed direct-drive generator application. The measurements showed good agreement between the values of no-load flux $\hat{\Phi}_{pnl}$ and inductance L_a measured experimentally and the values predicted by the model of chapter 7. Concerning the maximum average torque $\overline{T}$, experimental results matched the finite element analysis computation within 7%. However, both finite element analysis and experimental values were 35% lower than the value predicted with the analytical model. This confirmed the low accuracy of the linear model.

A simplified loss model was developed in the thesis. The losses measured experimentally were about 20% higher than the losses predicted with the model under nominal load conditions. However, iron losses were higher in the experimental machine due to short-circuits between the stator laminations caused by the manufacturing process.

Expected mass and costs for a MW-scale and for a 10-kW scale wind turbine

The comparison between geared and direct-drive concepts carried out in [Böh 1997] and presented in our introduction estimated the generator costs to be 36% of a complete direct-drive wind turbine. We conclude from the thesis that the best option for a MW-scale direct-drive generator was the conventional PM synchronous machine with a large diameter. If a generator of 4-meter diameter is used with an efficiency of 95%, its expected cost/torque would be around 100 Euros/kNm. For a 1.5 MW wind turbine rotating at 22 rpm with a torque of 650 kNm, we can expect a generator cost of about 65 000 Euros in active material. With an approximate cost of 1 Euro/Watt for a complete wind turbine, a 1.5-MW wind turbine would cost around 1 500 000 Euros. Therefore, the cost of the generator active material would represent about 5% of the total turbine cost, which is much lower than the ratios described in [Böh 1997].

There are many remote applications where a low-power wind turbine may be used in combination with battery storage. If a diameter of 50 cms is used for the generator, the TFPM machine with toothed rotor appears as a lighter and more cost-effective solution than the conventional PM synchronous machine. In that case, the cost/torque of the TFPM machine with toothed rotor will be around 800 Euros/kNm. For a 10 kW wind turbine, we can expect a cost of about 600 Euros in active material. With an approximate costs of 2 Euros/Watt for a complete 10-kW wind turbine, which would amount to about 20 000 Euros, the cost of the generator active material would represent about 3% of the total turbine cost.

10.2. Recommendations for further research

Need for research on mechanical and manufacturing concepts

A wind turbine direct-drive generator is a heavy component which requires a lot of mechanical material and intense manufacturing. The numbers obtained in the thesis for costs and masses of active material indicate that further optimization and reduction of active material is maybe not a priority. It is widely accepted that the cost of a wind turbine direct-drive generator is well above 3- 5% of the total turbine cost, as indicated in [Böh 1997]. Therefore we recommend that more attention be paid to the optimization of the mechanical design and manufacturing costs of those generators. For example, the optimal magnetic design obtained in the thesis for the conventional PM synchronous machine gave stator yoke thicknesses in the order of 5 mm for the active material. It is likely that the mechanical material providing sufficient mechanical stiffness to the stator yoke will require more material than the stator yoke ferromagnetic material itself. In this context, a complete model requires that the magnetically inactive material also be taken into account.

Concerning the manufacturing process, we believe that the cost of assembling PM machines and especially winding the stator conductors can not be neglected. It is likely that the costs of winding the copper conductors could be higher than the costs of the copper material.

It must be noted that the possibility exists that additional research on the subject of direct-drive generators which would include manufacturing and inactive material could conclude to the use of smaller diameters. In the latter case, the further optimization of active material would then become more sensible. But again, this would be a result of considering active material, inactive material and manufacturing as a whole.

Recommendations for further research on TFPM machines

The TFPM machine was identified as an interesting direct-drive solution for low power applications. The main limitation to the use of TFPM machines in higher power applications is the use of large machine diameters with thick air gaps. One of the assumptions used in this thesis for all machines is the use of an air gap thickness of $1/1000^{th}$ of the machine outside diameter. In the case of the TFPM machine, this assumption has important consequences. Thick air gaps lead to increased pole leakage and requires that wider pole pitches be used. However, the air gap thickness ratio used in the thesis is rather arbitrary and is not substantiated by any convincing arguments. We believe that such an important parameter should be analyzed more closely. Again, this is a matter that belongs to the mechanical design and we suggest that the complete TFPM machine be optimized in all its magnetic, mechanical and production aspects.

Looking at the construction of the TFPM machine with toothed rotor, the main problem experienced during the experimental phase of this research was the control of the air gap thickness. To obtain a 1-mm air gap, the stator surface had to be machined on a lathe, which short-circuited the stator laminations together, thus increasing the iron losses. The suggestion

of a hybrid structure is made here. In such a hybrid structure, the stator foot could be made of powdered iron material while the stator leg could be made of laminated steel. This would allow machining the stator surface and at the same time would reduce the iron losses due to the flux entering perpendicular to the lamination plane in the unaligned position.

It was already mentioned that the analytical model used for the optimization of the TFPM machine with toothed rotor was rather inaccurate, tending to overestimate the average torque value. It is expected that the "optimized" designs found with the optimization process in the thesis are not truly optimal due to this inaccuracy. Hence, we must highlight the possibility that better designs of the TFPM machine with toothed rotor could be identified with a more accurate model. We must stress the need for an optimization method that would include non-linear magnetic behaviors. Maybe a combination of analytical models and finite element analysis computation controlled by genetic algorithms and/or fuzzy logic would be an interesting area of investigation. In any case, the design method should include saturation of the stator core in the unaligned position.

On many occasions, we mentioned the great dependence of the optimal design solution on the machine efficiency. A model for predicting the power losses of the TFPM machine with toothed rotor was developed in the thesis. The model was said to be "simplified". The development of a complete exact model for the TFPM machine with toothed rotor still needs to be addressed properly. A complete model should calculate more accurately the eddy current losses in the stator laminations caused by the perpendicular vector component of the flux density. It should also determine the true distribution of the flux density vector inside the rotor flux concentrators. Finally, the model should take into account time harmonics of the flux density in both laminated steel and powdered iron.

References

[Aca 1997] P.P. Acarnley, B.C. Mecrow, J.S. Burdess, J.N. Fawcett, and P.G. Dickinson, "An integrated flywheel/machine energy store for road vehicles," in *Proc. 1997 IEE Colloquium on New Topologies for Perm. Mag. Mach.*, pp. 9/1 - 9/6.

[Adn 1991] A. K. Adnanes, "High Efficiency, High performance permanent magnet synchronous motor drives," Ph. D. dissertation, Univ. of Trondheim, Norway, 1991.

[Ark 1992] A.A. Arkadan, R. Vyas, J.G. Vaidya, and M.J. Shah, "Effect of toothless stator design on core and stator conductors eddy current losses in PM generators," *IEEE Trans. Energy Conversion*, vol. 7, pp. 231-237, March 1992.

[Bau 2003] P. Bauer, S.W.H. DeHaan, and M.R. Dubois, "Introduction to Windenergy and Offshore Windparks Problematic," in *Proc. 2003 Int. Conf. Pow. Conv., Intelligent Motion and Pow. Quality*, Nuremberg.

[Bin 1992] K.J. Binns, P.J. Lawrenson, and C.W. Trowbridge, *The analytical and numerical solution of electric and magnetic fields,* Chichester: Wiley, 1992.

[Bir 1991] M.J. Birks, "Directly Coupled, Slow Speed Wind Turbine Alternators," in *Proc. 1991 Symposium Electr. Syst. for Wind Turbines with Constant and Variable Speed*, Göteborg, pp. 15-24.

[Bli 2000] R. Blissenbach, G. Henneberger, U. Schäfer and W. Hackmann, "Development of a transverse flux traction motor in a direct drive system," in *Proc. 2000 Int. Conf. on Elec. Mach.*, pp. 1457-1460.

[Blo 1919] L. Bloch, *Précis d'Électricité Théorique*, Paris: Gauthier-Villars, 1919. [In French]

[Böh 1997] G. Böhmeke, R. Boldt and H. Beneke, "Geared Drive Intermediate Solutions-Comparisons of Design Features and Operating Economics," in *Proc. 1997 Europ. Wind Energy Conf.*, pp. 664-667.

[Böh 2003] G. Böhmeke, "Development and operational experience of the wind energy converter WWD-1," in *Proc. 2003 Europ. Wind Energy Conf.*

[Bor 1996] M. Bork and G. Henneberger, "New Transverse Flux Concept for an Electric Vehicle Drive System," in *Proc. 1996 Int. Conf. on Elec. Mach.*, pp. 308- 313.

[Bro 1962] W. F. Brown, *Magnetostatic Principles in Ferromagnetism*, Amsterdam: North-Holland, 1962.

[Bro 2002] P. Brooking and J.R. Bumby, "An Integrated Engine-Generator set with Power Electronic Interface for Hybrid Electric Vehicle Applications," in *Proc. 2002 Power Electronics, Machines & Drives Conf.*, pp. 153-158.

[BTM 2001] BTM Consult, "International Wind Energy Development; World Market Update 2000," March 2001.

[Car 1954] G.W. Carter, *The Electromagnetic Field in its Engineering Aspects*, London: Longmans, Green & Co., 1954.

[Car 1959] C.J. Carpenter, "Surface-Integral Methods of Calculating Forces on Magnetized Iron Parts," *IEE Monograph no. 342*, pp. 19-28, Aug. 1959.

[Car 1994] F. Caricchi, F. Crescimbini, O. Honorati and R. Vivarelli, "Prototype of a Wind-Turbine Directly-Coupled Axial-Flux PM Generator," in *Proc. 1994 Europ. Wind Energy Conf.*, pp. 492-499.

[Car 1995] R. Cardenas, W.F. Ray and G.M. Asher, "Switched Reluctance Generators for Wind Energy Applications," in *Proc. 1995 Power Elec. Specialist Conf.*, pp. 559-564.

[Car 1996] O. Carlson, J. Hylander and K. Thorborg, "Survey of Variable Speed Operations of Wind Turbines," in *Proc. 1996 Europ. Wind Energy Conf.*, pp. 406-409.

[Car 1997] F. Caricchi, F. Crescimbini, E. Santini and C. Santucci, "Influence of the Radial Variation of the Magnet Pitch in Slotless Permanent Magnets Axial Flux Motors," in *Proc. 1997 IEEE Conf. Ind. Appl. Soc.,* pp. 18-23.

[Car 1999a] F. Caricchi, V. Callea, F. Crescimbini, L. Solero and M. Falchetta, "Prototype of Variable-Speed, Direct-Drive generator for wind power exploitation in extremely cold climates," in *Proc. 1999 European Wind Energy Conf.*, pp. 821- 824.

[Car 1999b] F. Caricchi, F. Crescimbini, and O. Honorati, "Modular Axial-Flux Permanent-Magnet for Ship propulsion drives," *IEEE Trans. Energy Conversion*, vol. 14, no. 3, pp. 673-679, Sept. 1999.

[Cha 1997] B.J. Chalmers, E. Spooner, O. Honorati, F. Crescimbini, F. Caricchi, "Compact PM Machines," *Electric Machines and Power Systems*, vol. 25, pp.635-648, 1997.

[Cha 1999] B.J. Chalmers, W. Wu, and E. Spooner, "An Axial-Flux PM Generator For a Gearless Wind Energy System," *IEEE Trans. Energy Conversion*, vol. 14, no.2, pp. 251- 257, June 1999.

[Che 1996] Z. Chen and E. Spooner, "Grid Interface for a Variable-Speed, Permanent-Magnet, Wind Turbine Generator," in *Proc. 1996 Int. Conf. on Elec. Mach.*, pp. 347-352.

[Cro 1998] J. Cros, P. Viarouge and C. Gélinas, "Design of PM Brushless Motors using Iron-resin Composites for Automotive Applications," In *Proc. 1998 Conf. Industry App. Soc.*, pp. 5-11.

[deH 1994] S.W.H. de Haan, T.G. van Engelen, C.F.A. Frumau, A.T. Veltman, E.J. Wildenbeest, S.E. Childs, and D.A. Torrey, "Development of a Gearless Drive with Variable Reluctance Generator for Variable Speed Wind Turbines," in *Proc. 1994 Europ. Wind Energy Conf.*, pp. 1-4.

[deH 1995] S.W.H. de Haan, A.T. Veltman, J. Janousek, Z. Cerovsky, J. Mericka, J. Pavelka, J. Perina, and F. Petrasek, "A High Efficiency Electrical Conversion System with Variable Reluctance Generator for Variable Speed Wind Turbines," ECN, The Netherlands, Tech. Rep. ECN-C--95-033, May 1995.

[deM 1999] L.H. de Medeiros, G. Reyne, and G. Meunier, "About the distribution of forces in permanent magnets," *IEEE Trans. on Magnetics*, vol. 35, no. 3, pp. 1215-1218, May 1999.

[DeL 1991] J. De La Ree, and N. Boules, "Magnet shaping to reduce induced voltage harmonics in PM machines with surface mounted magnets," *IEEE Trans. on Energy Conversion*, vol. 6, no. 1 pp. 155-161, Mar. 1991

[DeL 1992] J. De La Ree, and N. Boules, "Induced voltage harmonic reduction of PM cylindrical machines," *IEEE Trans. on Ind. Application*, vol. 28, no. 3, pp. 619-624, June 1992.

[Dex 2002] Dexter Magnetics, Magnetic material specification data sheets, 2002.

[Dic 2002] P. Dickinson, A. G. Jack and B.C. Mecrow, "Improved Permanent Magnet Machines with Claw Pole Armatures," in *Proc. 2002 Intern. Conf. on Elec. Mach.*, paper 245.

[DiN 1991] A. Di Napoli, F. Caricchi, F. Crescimbini and G. Noia, "Design Criteria of a Low-Speed Axial-Flux PM Synchronous Machines," in *Proc. 1991 Intern. Conf. on Evolution and Modern Aspects of Synchronous Machines*, pp. 1119-1123.

[Dit 2003] A. Dittrich, and A. Stoev, "Grid Voltage Fault Proof Doubly-Fed Induction Generator System," in *Proc. 2003 Europ. Pow. Electronics Conf.*, paper 363.

[Dub 2000] M.R. Dubois, H. Polinder and J.A. Ferreira, "Comparison of generator topologies for direct-drive wind turbines," in *Proc. 2000 Nordic Countries Pow. and Indust. Elec.*, pp. 22-26.

[Dub 2001a] M.R. Dubois, H. Polinder and J.A. Ferreira, "Axial and Radial-Flux PM Generators for Direct-Drive Wind Turbines," in *Proc. 2001 Europ. Wind Energy Conf.*, pp. 1112-1115.

[Dub 2001b] M.R. Dubois, H. Polinder and J.A. Ferreira, "Generator Topologies for Direct-Drive Wind Turbines, an adapted Technology for Turbines running in Cold Climate," presented at the Conf. Wind Energy in Cold Climate, Matane, Canada, 2000. Available: http://ee.its.tudelft.nl/EPP

[Dub 2002a] M.R. Dubois, H. Polinder and J.A. Ferreira, "Influence of Air Gap Thickness in Transverse Flux Permanent Magnet (TFPM) Generators for Wind Turbine Application," in *Proc. 2002 IEEE PELS Soc. Young Researcher Symp.*, Leuven, Belgium.

[Dub 2002b] M.R. Dubois, H. Polinder and J.A. Ferreira, "Transverse-Flux Permanent Magnet (TFPM) Machine with Toothed Rotor," in *Proc. 2002 Power Electronics, Machines & Drives Conf.*, pp. 309-314.

[Dub 2002c] M.R. Dubois, H. Polinder and J.A. Ferreira, "Prototype of a new Transverse-Flux Permanent Magnet (TFPM) Machine with Toothed Rotor," in *Int. Conf. on Elec. Mach.*, paper 635.

[Dub 2002d] M.R. Dubois, H. Polinder and J.A. Ferreira, "Magnet shaping for minimal magnet volume in machines," *IEEE Trans. Magnetics*, vol. 36, pp. 2985-2987, 2002.

[Dub 2002e] M.R. Dubois, H. Polinder, and J.A. Ferreira, "Machine électrique à flux transverse à rotor dentelé", Patent pending, US patent Office, April 2002. [In French].

[Dub 2003a] M.R. Dubois, H. Polinder and J.A. Ferreira, "Contribution of permanent magnet volume elements to the no-load voltage in machines," *IEEE Trans. Magnetics*, vol. 36, pp. 1784-1792, May 2003.

[Dub 2003b] M.R. Dubois, H. Polinder and J.A. Ferreira, "Varying magnetization orientation for permanent magnet volume reduction in machines," *IEEE Trans. Magnetics*, vol. 36, pp. 1793-1799, May 2003.

[Dur 1953] E. Durand, *Electrostatique et magnétostatique*, Paris: Masson et cie, 1953, p. 579. [In French]

[Dur 1955] E. Durand, "Théorie générale des masses magnétiques au repos et en mouvement", *Revue Générale de l'Électricité*, tome 64, no. 7, 1955, pp. 350-356. [In French]

[Dur 1968] E. Durand, *Magnétostatique*, Paris: Masson et cie, 1968. [In French]

[Edw 1984] A. L. Edwards, *An Introduction to Linear Regression and Correlation*, New York: W.H. Freeman and Co., 2nd Ed., 1984.

[EWE 1999] "Wind energy - The Facts.", European Wind Energy Association, Brussels, Belgium, 1999.

[Fan 1960] R.M. Fano, L. J. Chu, and R. B. Adler, *Electromagnetic Fields, Energy, and Forces*, New-York: John Wiley & Sons, 1960, pp. 520.

[Fic 2001] R.L. Ficheux, F. Caricchi, F. Crescimbini, and O. Honorati, "Axial-Flux Permanent-Magnet Motor for Direct-Drive Elevator Systems Without Machine Room," *IEEE Trans. Ind. Applicat.*, vol. 37, no. 6, pp. 1693-1701, Nov./Dec. 2001.

[Fre 2002] C.D. French, C. Hodge and M. Husband, "Optimised torque control of marine transverse-flux propulsion machines," in *Proc. 2002 Power Electronics, Machines & Drives Conf.*, pp. 1-6.

[Gel 1997] C. Gélinas, L.-P. Lefebvre, S. Pelletier and P. Viarouge, "Effect of Temperature on Properties of Iron-Resin Composites for Automotive Applications," in *Proc. Int. Conf. SAE Eng. Soc. for Advancing Mobility Land, Sea, Air and Space*, SAE Technical paper 970421, 1997.

[Gra 1996a] A. Grauers, "Efficiency of three wind energy generator systems," *IEEE Trans. Energy Conversion*, vol. 11, pp. 650-657, Sept. 1996.

[Gra 1996b] A. Grauers, "Design of Direct-driven Permanent-magnet Generators for Wind Turbines," Ph. D. dissertation, School Elect. and Computer Eng., Chalmers Univ. Tech., Göteborg, Sweden, 1996.

[Gra 1997] A. Grauers, O. Carlson, A. Hogberg, P. Lundmark, M. Johnsson and S. Svenning, "Test and Design Evaluation of a 20 kW Direct Driven PM Generator with a Frequency Converter", in *Proc. 1997 European Wind Energy Conference*, pp. 686-689.

[Had 1999] J.R. Hadji-Minaglou, and G. Henneberger, "Comparison of different motor types for electric vehicle application," *EPE Journal*, vol. 8, pp. 46-55, Sept. 1999.

[Hal 1980] K. Halbach, "Design of permanent multipole magnets with oriented rare earth Cobalt material," *Nuclear Instruments and Methods,* vol. 169, pp. 1-10, 1980.

[Hao 1997] I. Haouara, A. Tounzi and F. Piriou, "Study of a Variable Reluctance Generator for Wind Power Conversion," in *Proc. 1997 Europ. Pow. Elec. Conf.*, vol. 2, pp. 631-636.

[Har 1989] M.R. Harris and T.J.E. Miller, "Comparison of Design and Performance Parameters in Switched Reluctance and Induction Motors," in *Proc. 1989 IEE Conf. Elec. Mach. and Drives*, pp. 303-307.

[Har 1993] M.R. Harris and B.C. Mecrow, "Variable reluctance permanent magnet motors for high specific output," in *Proc. 1993 IEE Conf. Elec. Mach. and Drives*, pp. 437-442.

[Har 1996] M.R. Harris, G.H. Pajooman, and S.M. Abu Sharkh, "Performance and design optimization of electric motors with heteropolar surface magnets and homopolar windings," *IEE Proc. - Electr. Power Appl.*, vol. 143, no. 6, pp. 429-436, Nov. 1996.

[Har 1997] T. Hartkopf, M. Hofmann and S. Jöckel, "Direct-drive Generators for Megawatt Wind Turbines," in *Proc. 1997 Europ. Wind Energy Conf.*, pp. 668-671.

[Har 1998] M. R. Harris, G.H. Pajooman, S.M. Abu Sharkh, B.C. Mecrow, "Comparison of Flux-Concentrated and Surface-Magnet Configurations of the VRPM (Transverse-Flux) machine", in *Proc. 1998 Int. Conf. on Elec. Mach.*, pp. 1119-1122.

[Hau 1989] H. A. Haus, and J. R. Melcher, *Electromagnetic fields and energy*, Englewood Cliffs, New Jersey*:* Prentice Hall, 1989.

[Hei 1989] S. Heier, *Grid Integration of Wind Energy Conversion Systems*, New York*:* John Wiley & Sons, 1998.

[Hen 1997] G. Henneberger and Bork M., "Development of a new Transverse flux motor," in *Proc. 1997 IEE Colloquium on New Topologies for PM Machines*, pp. 1/1-1/6.

[Hol 2002] S.R. Holm, H. Polinder, J.A. Ferreira, P. van Gelder and R. Dill, "Analytical calculation of the Magnetic Field in Electrical Machines due to the Current Density in an Airgap Winding," in *Proc. 2002 Int. Conf. on Elec. Mach.*, paper 486.

[Hon 1991] O. Honorati, F. Caricchi, F. Crescimbini and G. Noia, "Gear-Less Wind Energy Conversion System Using an Axial Flux PM Synchronous Machine," in *1991 Proc. European Wind Energy Conference*, pp. 814-818.

[Hou 1996] C.-K. Hou , "The Effects of Grain Size on the Magnetic Properties of Fully Processed, Continuous-Annealed Low-Carbon Electrical Steels," *IEEE Trans. Mag.*, vol. 32, no. 2, March 1996, pp. 471-477.

[Hua 1999] S. Huang, J. Luo, F. Leonardi, and T.A. Lipo, "A Comparison of Power Density for Axial Flux Machines Based on General Purpose Sizing Equations," *IEEE Trans. Energy Conversion*, vol. 14, no.2, June 1999, pp. 185-192.

[Jöc 1996] S. Jöckel, "Gearless wind energy converters with permanent magnet generators- an option for the future?," in *Proc. 1996 Europ. Union Wind Energy Conf.*, pp. 414-417.

[Lai 1971] E.R. Laithwaite, J.F. Eastham, H.R. Bolton, and T.G. Fellows, "Linear motors with transverse flux," *IEE Proc.*, vol. 118, no. 12, pp. 1761-1767, Dec. 1971.

[Lam 1996] P. Lampola, J. Perho and J. Vaananen, "Analysis of a low speed PM Wind Generator connected to a frequency converter," in *Proc. 1996 International Conference on Electrical Machines*, pp. 393-398.

[Lam 1997] P. Lampola, J. Saari, and J. Perho, "Electromagnetic Design of a Low-Speed Surface-Mounted Permanent-Magnet Wind Generator," *Electromotion*, vol. 4, no. 4, pp. 147-154, 1997.

[Lam 2000] P. Lampola, "Directly Driven, Low-Speed Permanent-Magnet Generators for Wind Power Applications," Ph. D. dissertation, Lab. Electromechanics, Helsinki Univ. Tech., Finland, 2000.

[Lan 2000a] A. Lange, W.-R. Canders, F. Laube and H. Mosebach, "Comparison of different drive systems for a 75 kW electrical vehicle drive," in *Proc. 2000 Int. Conf. on Elec. Mach.*, pp. 1308-1312.

[Lan 2000b] A. Lange, W.-R. Canders and H. Mosebach, "Investigation of iron losses of soft magnetic powder components for electrical machines," in *Proc. 2000 Int. Conf. on Elec. Mach.*, pp. 1521-1525.

[Lan 2001] A. Lange, “Analytische Methoden zur Berechnung elektromagnetischer und thermischer Probleme in elektrischen Maschinen,” Ph. D. dissertation, Carolo-Wilhelmina Univ. Tech., Braunschweig, Germany, 2001 [In German].

[Law 1980] P.J. Lawrenson, J.M. Stephenson, P.T. Blenkinsop, J. Corda, and N.N. Fulton, “Variable-speed switched reluctance motors,” *IEE Proc.- B*, vol. 127, no. 4, pp. 253-265, July 1980.

[Lef 2002] L.-P. Lefebvre, and C. Gélinas, “Effect of Material Insulation and Part Geometry on AC Magnetic Performance of P/M Soft Magnetic Composites,” in *Proc. 2001 Conf. and Advanced Powder Metallurgy & Particle Materials,* pp. 7.36-7.50.

[Let 1997] P. Letellier, “High power permanent magnet machines for electric propulsion drives,” in *Proc. 2000 All Elec. Ship Conf.*, pp. 126-133.

[Liu 1998] K. Liu, M. Stiebler and S. Güngör, “Design of a Switched Reluctance Generator for Direct-Driven Wind Energy System,” in *Proc. 1998 Universities Pow. Eng. Conf.*, pp. 411-414.

[LoB 1997] G. Lo Bianco, F. Caricchi, F. Crescimbini and O. Honorati, “Design of Gearless Wind Generator for Off-Shore Applications,” in *1997 Proc. OWEMES*, pp. 365-374.

[Mad 1998] C.P. Maddison, B.C. Mecrow and A.G. Jack, “Claw Pole Geometries For High Performance Transverse Flux Machines,” in *Proc. 1998 Int. Conf. on Elec. Mach.*, pp. 340-345.

[Map 2001] Mapes & Sprowl, Magnetic material specification data sheets, 2001.

[Mar 1979] M. Marinescu, “Analytische Berechnungen und Modellvorstellungen für Systeme mit Dauermagneten und Eisen”, Ph. D. dissertation, Braunschweig, 1979. [In German]

[Mar 1980] J.-M. Martel, and R. Nadeau, *Statistique en gestion et en économie,* Chicoutimi:Morin, 1980. [In French]

[Mat 1994] Matlab for Windows, Release 4.2c.1 (Oct 3 1994), Copyright The Mathworks Inc. 1984-1994.

[Mat 1998] P.C. Matthews, *Vector Calculus*, London: Springer-Varlag, 1998.

[Maw 1957] O. K. Mawardi, ‘‘On the concept of coenergy,‘‘ *Journ. of Franklin Institute*, vol. 264, no. 1, pp. 313-332, 1957.

[Max 2002] Maxwell 3-D field simulator, Version 9.0 (June 2002), Copyright Ansoft Corporation 1984-2002.

[Mec 1996] B.C. Mecrow, A.G. Jack and C.P. Maddison, "Permanent Magnet Machines for High Torque, Low Speed Applications," in *Proc. 1996 Int. Conf. on Elec. Mach.*, pp. 461-466.

[Med 1998] L.H.A. De Medeiros, "Méthodes de calcul de forces électromagnétiques - Application au calcul des distributions de forces sur les aimants permanents," Ph. D. dissertation, Inst. Nat. Polytechnique de Grenoble, France, 1998 [In French].

[Mil 1985] T.J.E. Miller, ''Converter volt-ampere requirements of the switched reluctance motor drive,'' *IEEE Trans. Ind. Applicat.*, vol. 21, no. 5, pp. 1136-1144, 1985.

[Mil 1989] T.J.E. Miller, *Brushless permanent-magnet and reluctance motor drives,* Oxford:Clarendon, 1989.

[Mil 1993] T.J.E. Miller, *Switched Reluctance Motors and their Controls,* Oxford:Clarendon, 1993.

[Mil 2001] D. Millborow, "Looking More Competitive than Ever," *WindPower Monthly*, pp. 32-33, Jan. 2001.

[Mit 1995] A. J. Mitcham and J.J.A. Cullen, "Motors and drives for surface ship propulsion: comparison of technologies," in *Proc. 1995 Electric Propulsion Conf.*, paper 4.

[Mit 1997] A. J. Mitcham, "Transverse Flux Motors for Electric Propulsion of Ships,"in *Proc. 1997 IEE Colloquium on New Topologies for PM Machines*, pp. 3/1-3/6.

[Mit 2002] A. J. Mitcham and J.J.A. Cullen, "Permanent Magnet Generator Options for the More Electric Aircraft," in *Proc. 2002 Power Electronics Machines & Drives Conf.*, pp. 241-245.

[Mue 1999] M.A. Mueller, "Design of Low Speed Switched Reluctance Machines for Wind Energy Converters," in *Proc. 1999 IEE Elec. Mach. and Drives Conf.*, pp. 60-64.

[Net 1985] J. Neter, W. Wasserman, and M. H. Kutner, *Applied Linear Statistical Models*, 2nd ed., Illinois: Irwin, 1985.

[Paj 1997] G. H. Pajooman, "Performance Assessment and Design Optimisation of VRPM (Transverse Flux) Machines by Finite Element Computation," Ph. D. dissertation, Southampton Univ., UK, 1997.

[Pen 1996] R. Pena, J. C. Clare, and G. M. Asher, "A doubly fed induction generator using back-to-back PWM converters supplying an isolated load from a variable speed wind turbine," *IEE Proc.- Electr. Power Appl.*, vol. 143, no. 5, pp. 380-387, Sept. 1996.

[Per 1995] M. Persson, P. Jansson, A.G. Jack, and B.C. Mecrow, "Soft Magnetic Composite Materials - Use for Electrical Machines," *Proc. 1995 IEE Elec. Mach. and Drives Conf.*

[Per 1996] M. Persson, P. Jansson, A.G. Jack, and B.C. Mecrow, "Soft magnetic composites offer new PM opportunities," *Metal Powder Report*, pp. 24-28, Jan. 1996.

[Pol 1998] H. Polinder, "On the losses in a high-speed permanent-magnet generator with rectifier," Ph. D. dissertation, Delft Univ. Tech., Delft, The Netherlands, 1998.

[Pol 2000] H. Polinder, F. Gardner and B. Vriesema, "Linear PM generator for wave energy conversion in the AWS," in *Proc. 2000 Int. Conf. on Elec. Mach.*, pp. 309-313.

[Pol 2001] H. Polinder and J.G. Slootweg, "Design optimization of a synchronous generator for a direct-drive wind turbine," in *Proc. 2001 Europ. Wind Energy Conf.*, pp. 1067-1070.

[Pol 2003] H. Polinder, M.R. Dubois, and J.G. Slootweg, "Generator systems for wind turbines," in *Proc. 2003 Int. Conf. Pow. Conv., Intelligent Motion and Pow. Quality*, Nuremberg.

[Pro 2000] F. Profumo, A. Tenconi, Z. Zhang, and A. Cavagnino, "Design and Realization of a Novel Axial Flux Interior PM Synchronous Motor for Wheel-Motors Applications," *Elec. Mach. and Power Syst.*, vol. 28, pp. 637-649, 2000.

[Que 2001] Quebec Metal Powders, ATOMET/FLOMET EM-1 specification data sheets, 2001.

[Rei 1976] K. Reichert, H. Freundl and W. Vogt, "The calculation of forces and torques within numerical magnetic field calculation methods," in *Proc. 1976 IEEE Compumag Conf.*, pp. 64-73.

[Ric 1967] R. Richter, *Elektrische Maschinen, erster Band.* (3rd ed,) Basel: Birkhäuser, 1967. [In German]

[Sad 1992] N. Sadowski, Y. Lefèvre, M. Lajoie-Mazenc, and J.P.A. Bastos., "Sur le calcul des forces magnétiques," *Journal de Physique III*, vol. 2, no. 5, pp. 859-870, May 1992. [In French]

[Saf 1990] M. Safiuddin, "Evaluation of losses in DC machines-a statistical approach," *IEEE Trans. Ind. Appl.*, vol. 26, no. 2, March/April 1990, pp. 252-258.

[Sah 2001] F. Sahin, "Design and development of a high-speed axial-flux permanent-magnet machine," Ph. D. dissertation, Eindhoven Univ. Tech., Eindhoven, The Netherlands, 2001.

[Seb 1987] T. Sebastian, and G. Slemon, "Transient Torque and Short Circuit Capabilities of Variable Speed Permanent Magnet Motors," *IEEE Trans. Mag.,* vol. MAG-23, no. 5, Sept. 1987, pp. 3619-3621.

[Sen 1997] P.C. Sen, *Principles of Electric Machines and Power Electronics*. (2nd ed.) New York: Wiley, 1997, p. 355.

[Sit 2000] K. Sitapati and R. Krishnan, "Performance Comparisons of Radial and Axial Field, Permanent Magnet, Brushless Machines," in *Proc. 2000 IEEE Conf. Ind. Appl. Soc.,* pp. 228-234.

[Sle 1992] G.R. Slemon, and X. Liu, "Modeling and design optimization of permanent magnet motors," *Elec. Mach. and Power Syst.*, vol. 20, pp. 71-92, 1992.

[Slo 2003] J.G. Slootweg, "Wind Power Modelling and Impact on Power System Dynamics," Ph. D. dissertation, Delft Univ. Tech., Delft, The Netherlands, 2003.

[Smi 1981] G.A. Smith, and K.A. Nigim, "Wind-energy recovery by a static Scherbius induction generator," *IEE Proc.- C*, vol. 128, no. 6, pp. 317-324, Nov. 1981.

[Söd 1997] L. Söderlund, A. Koski, H. Vihriala, J.-T. Eriksson and R. Perala, "Design of an Axial-Flux Permanent Magnet Wind Power Generator," in *Proc. 1997 IEE Conf. Elec. Mach. and Drives*, pp. 224-228.

[Spo 1992a] E. Spooner and A.C. Williamson, "Permanent-Magnet Generators for Wind Power Applications," in *Proc. 1992 Int. Conf. on Elec. Mach.*, pp. 1048-1052.

[Spo 1992b] E. Spooner, and B.J. Chalmers, "'TORUS': A slotless, toroidal-stator, permanent-magnet generator," *IEE Proc.- B*, vol. 139, no. 6, pp. 497-506, Nov. 1992.

[Spo 1996] E. Spooner, and A.C. Williamson, "Direct coupled, Permanent Magnet Generators for Wind Turbines," *IEE Proc.- Electr. Power Appl.*, vol. 143, no. 1, pp. 1- 8, Jan. 1996.

[SPS 1996] SPSS for Windows, Release 7.5 (Nov 14 1996), Standard Version, Copyright SPSS Inc. 1989-1996.

[Sti 1992] M. Stiebler and O. Okla, "A Permanent-Magnet Toroid Wind-Generator," in *Proc. 1992 Int. Conf. on Elec. Mach.*, pp. 1043-1047.

[Sto 1974] R.L. Stoll, *The analysis of eddy currents*, Oxford: Clarendon Press, 1974.

[Str 1941] J.A. Stratton, *Electromagnetic Theory*, New-York: McGraw-Hill, 1941.

[Str 1998] R.J. Strahan, "Energy conversion by nonlinear permanent magnet machines," *IEE Proc.- Electr. Power Appl.*, vol. 145, no. 3, pp. 193- 198, May 1998.

[Tor 1993] D.A. Torrey, "Variable-Reluctance Generators in Wind-Energy Systems," in *Proc. 1993 Pow. Electr. Specialists Conf.*, pp. 561-567.

[Voy 2000] J.E. Voyce, S.M. Husband and D.J. Mattick, "The PM propulsion motor: from infancy to adolescence," in *Proc. All Elec. Ship Conf.*, pp. 134-139.

[Weh 1986] H. Weh and H. May, "Achievable Force Densities for Permanent Magnet Excited Machines in New Configurations," in *Proc. 1986 Int. Conf. on Elec. Mach.*, pp. 1107-1111.

[Weh 1988a] H. Weh, H. Hoffmann, J. Landrath, H. Mosebach and J. Poschadel, "Directly-Driven Permanent-Magnet Excited Synchronous Generator for Variable Speed Operation," in *Proc. 1988 Europ. Wind Energy Conf.*, pp. 566-572.

[Weh 1988b] H. Weh, "Permanentmagneterregte Synchronmaschinen hoher Kraftdichte nach dem Transversalflusskonzept," *etzArchiv,* vol.10, no.5, pp. 143 - 149, 1988. [In German].

[Weh 1991] H. Weh, "Synchronous Machines with New Topologies," in *Proc. 1991 Int. Conf. on the Evolution and Modern Aspects of Sync. Mach.*, pp. C1-C9.

[Weh 1994] M.R. Dubois, "Multiple track transversal flux machine with ring coils", German patent DE 4 300 440, German patent Office, 1994. [In German].

[Weh 1995] H. Weh, "Transverse Flux Machines in Drive and Generator Application," in *Proc. 1995 Stockholm Power Tech. Conf.*, pp. 75-80.

[Won 1969] T. H. Wonnacott, and R.J. Wonnacott, *Introductory Statictics*, New York: Whiley & Sons, 1969.

[Zha 1996] Z. Zhang, F. Profumo, and A. Tenconi, "Axial-Flux versus Radial-Flux permanent-magnet motors," *Electromotion*, vol. 3, p. 134, 1996.

[Zin 1997] D.S. Zinger, and E. Muljadi, "Annualized Wind Energy Improvement Using Variable Speeds," *IEEE Trans. Industry Application*, vol. 33, pp. 1444-1447, No. 1997.

Appendices

Appendix I

Dimensions of rotor coils and PM in Conventional synchronous machines

The relationship between the thickness h_{PM} of the PM and the no-load flux density B_g in the air gap is herein derived. It is assumed that the PM constitutive relation is given by:

$$\vec{B}_{PM} = \mu_0 \vec{H}_{PM} + \vec{B}_r \qquad \text{(I-2)}$$

Assuming the iron as infinitely permeable, the PM and the air gap can be modeled by the equivalent magnetic circuit shown in figure I-1.

Solving the magnetic circuit of figure I-1, we obtain the flux density in the air gap:

$$B_g = B_r \frac{h_{PM}}{h_{PM} + g} \qquad \text{(I-3)}$$

We can also express the magnet thickness as a function of the flux density in the air gap:

$$h_{PM} = g \frac{B_g}{B_r - B_g} \qquad \text{(I-4)}$$

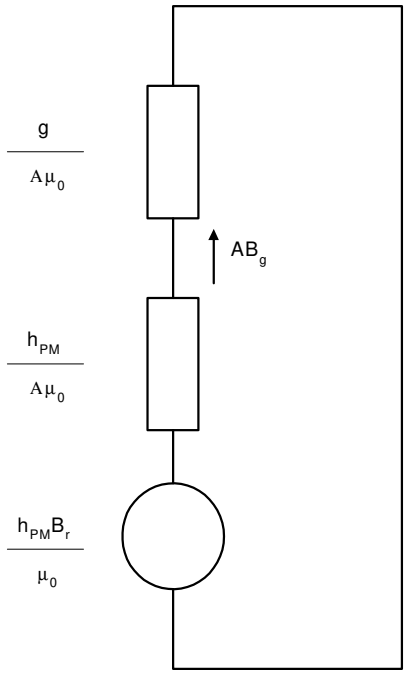

Figure I-1: Equivalent magnetic circuit of one PM and one airgap.

The rotor excitation can be replaced by a coil wound around an iron core. This coil is fed with a magnetomotive force $n_r I_r$, which creates a flux density B_g in the air gap. Again assuming infinitely permeable iron, we draw the magnetic circuit of figure I-2.

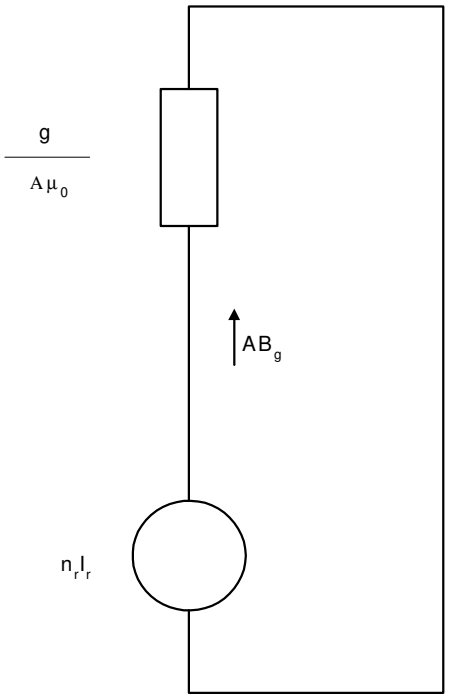

Figure I-2: Equivalent magnetic circuit of one rotor coil and one airgap in a wound-rotor synchronous machine.

Solving the magnetic circuit of figure I-2, we obtain the flux density in the air gap:

$$B_g = n_r I_r \frac{\mu_0}{g} \tag{I-5}$$

The magnetomotive force $n_r I_r$ can also be expressed as a function of the dimensions of the rotor winding window area:

$$n_r I_r = J_r A_{Cur} = J_r (h_{Cur} w_{Cur} k_{rfill}) \tag{I-6}$$

The coil width w_{Cur} is dependent on the saturation flux density B_{Fesat} of the rotor core, and the flux density B_g in the air gap. In figure 2-2, the flux density is higher in the central part of the rotor pole, than inside the pole shoe. The width of that central part must be sufficiently large, so that iron does not saturate in that region. By assuming the width of the copper winding and the width of the iron core to occupy the total pole pitch, we can express the coil width as a function of the flux density in the air gap, and as a function of the saturation flux density of the steel laminations:

$$w_{Cur} = \frac{\tau_p}{2}\left(\frac{B_{Fesat} - B_g}{B_{Fesat}}\right) \tag{I-7}$$

By inserting equation (I-5) and equation (I-6) into equation (I-7), we can write:

$$B_g = \frac{\mu_0 J_r k_{rfill} \tau_p h_{Cur}}{2g}\left(\frac{B_{Fesat} - B_g}{B_{Fesat}}\right) \tag{I-8}$$

which is rearranged as:

$$h_{Cur} = \frac{2 g B_g B_{Fesat}}{\mu_0 J_r k_{rfill} \tau_p (B_{Fesat} - B_g)} \tag{I-9}$$

Equation (I-9) provides the thickness of the copper winding in the rotor coil, in order to give a flux density B_g in the air gap. At this point, we can write the ratio of the thickness between the copper winding and the permanent magnet which creates an equivalent flux density in the air gap. This ratio is obtained by dividing equation (I-9) by equation (I-4):

$$\frac{h_{Cur}}{h_{PM}} = \frac{2 B_{Fesat} (B_r - B_g)}{\mu_0 J_r k_{rfill} \tau_p (B_{Fesat} - B_g)} \tag{I-10}$$

Appendix II

Expressions for energy and coenergy

The volume *V* includes and extends beyond the whole machine. The machine volume *V* and surface *S* are illustrated in figure II-1. This volume *V* is bounded by a closed surface *S* divided into an infinite number of surface elements *dn*. Each surface element *dn* is defined by a vector $d\vec{n}$ and is crossed by a certain value of the Poynting vector $\vec{S}$, defined by:

$$\vec{S} = \vec{E} \times \vec{H} \qquad \text{(II-1)}$$

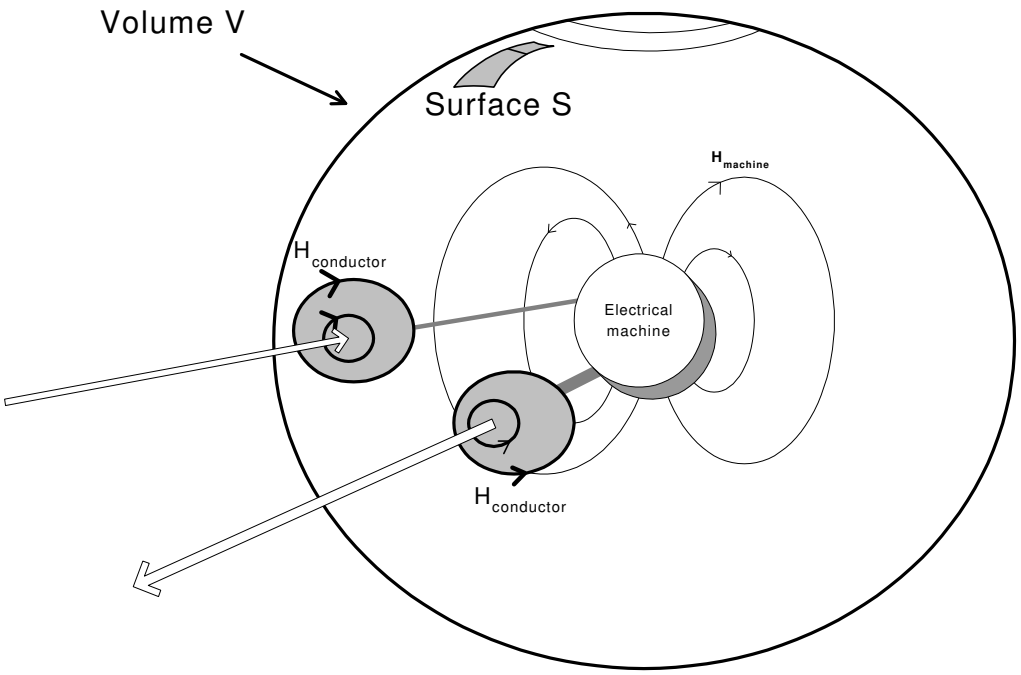

Figure II-1: Chosen volume and surface around the machine.

The following assumptions are made on surface *S* and volume *V*:

- 1) the machine is totally enclosed inside volume *V*;
- 2) two infinitely thin terminals enter surface *S*. These two terminals are the machine terminals;

- 3) volume V is chosen large enough so that the magnetic field $\vec{H}$ created by the machine is negligible on its surface S;
- 4) volume V is chosen so that the magnetic field $\vec{H}$ created by the machine terminals is parallel to its surface S;

Suppose a change in the stored magnetic energy inside volume V. The increase in magnetic energy can be expressed as:

$$dW_{mag} = \int_V (\vec{H} \cdot d\vec{B}) dV \tag{II-2}$$

where W_{mag} includes both the stored magnetic energy W_m and the energy W_{mloss} associated to the magnetic losses (like hysteresis losses). This expression is derived from Maxwell's equations and is valid in static (or quasi-static) conditions.

In a dual manner, magnetic coenergy W'_{mag} may be expressed as:

$$dW'_{mag} = \int_V (\vec{B} \cdot d\vec{H}) dV \tag{II-3}$$

where W'_{mag} is the sum of two terms W'_m and W'_{mloss}, respectively the stored magnetic coenergy and the magnetic losses (hysteresis losses). In this appendix, we show how equation (II-2) and equation (II-3) can be expressed with equivalent expressions, written in terms of the magnetic vector potential $\vec{A}$ and current density $\vec{j}$, but also in terms of the flux linkage λ and current i.

Expression of W_{mag} and W'_{mag} in terms of A and j

We rewrite equation (II-2) and equation (II-3) in the following way:

$$dW_{mag} = \int_V (\vec{H} \cdot d\vec{B}) dV + \oint_S (\vec{H} \times d\vec{A}) \cdot d\vec{n} \tag{II-4}$$

$$dW'_{mag} = \int_V (\vec{B} \cdot d\vec{H}) dV + \oint_S (\vec{A} \times d\vec{H}) \cdot d\vec{n} \tag{II-5}$$

In equation (II-4) and equation (II-5), the second term can be added because it is equal to zero. It is equal to zero because the boundaries of V are chosen according to assumptions 3) and 4). Writing the first term as a function of the magnetic vector potential $\vec{A}$ and applying the divergence theorem to the second term, equation (II-4) and equation (II-5) are rewritten:

$$dW_{mag} = \int_V [\vec{H} \cdot (\nabla \times d\vec{A}) dV + \nabla \cdot \vec{H} \times d\vec{A}] dV \quad \text{(II-6)}$$

$$dW'_{mag} = \int_V [(\nabla \times \vec{A}) \cdot d\vec{H} dV + \nabla \cdot \vec{A} \times d\vec{H}] dV \quad \text{(II-7)}$$

Using a classical mathematical identity [Mat 1998]:

$$(\nabla \times \vec{A}) \cdot \vec{B} - (\nabla \times \vec{B}) \cdot \vec{A} = \nabla \cdot (\vec{A} \times \vec{B}) \quad \text{(II-8)}$$

we rewrite equation (II-6) and equation (II-7):

$$dW_{mag} = \int_V (\nabla \times \vec{H}) \cdot d\vec{A} dV \quad \text{(II-9)}$$

$$dW'_{mag} = \int_V (\nabla \times d\vec{H}) \cdot \vec{A} dV \quad \text{(II-10)}$$

and from Ampère's law, equation (II-9) and equation (II-10) become:

$$dW_{mag} = \int_V \vec{j} \cdot d\vec{A} dV \quad \text{(II-11)}$$

$$dW'_{mag} = \int_V \vec{A} \cdot d\vec{j} dV \quad \text{(II-12)}$$

Expression of W_{mag} and W'_{mag} in terms of λ and i

For the calculation of W_{mag}, every volume element dV is subjected to a given current density $\vec{j}$. In the case of the calculation of W'_{mag}, every volume element dV is subjected to an increase in $d\vec{j}$ in current density. In insulating material and air, $\vec{j}$ and $d\vec{j}$ will be equal to zero. However, there will be areas where $\vec{j}$ and $d\vec{j}$ will not be equal to zero, like in the machine coils and also in the core laminations where eddy currents are created. Using the approach proposed by Stratton [Str 1941], we can divide the total volume V into an infinite set of current tubes. Each current tube carries a given current value di throughout the total tube length.

Firstly, we set the current tube cross-section and total length respectively equal to $d\sigma$ and u. It must be noted that the tube cross-section $d\sigma$ is allowed to vary along the tube length, in order to keep the current di constant. It will be the case if the coil conductors are bent. In

the latter condition, the current will be concentrated in the bent parts of the coil and the tube cross-section $d\sigma$ will become smaller in those areas. Secondly, we divide each current tube further, by splitting the total tube length u into an infinite number of small elements du. The total volume V can now be split into an infinite number of small volume elements dV, which are equal to the product of $d\sigma$ and du. Thirdly, the current tubes are selected so that in every point of the tube, the cross-section $d\sigma$ is perpendicular to the vector density $\vec{j}$ and perpendicular to the increase $d\vec{j}$ in current density.

Now, let us write equation (II-11) and equation (II-12) in terms of the current tube geometry:

$$dW_{mag} = \int_{\sigma}\int_{u} \vec{j} \cdot d\vec{A}\, du\, d\sigma \tag{II-13}$$

$$dW'_{mag} = \int_{\sigma}\int_{u} \vec{A} \cdot d\vec{j}\, du\, d\sigma \tag{II-14}$$

To simplify the mathematical writing, we adopt Stratton's notation [Str 1941], where the geometrical infinitesimal elements are written with a roman ''d'' and the infinitesimal variations of the field, vector potential and current density and the resulting variations in energy are written with greek delta ''δ''. Equation (II-13) and equation (II-14) are rewritten:

$$\delta W_{mag} = \int_{\sigma}\int_{u} \vec{j} \cdot \delta\vec{A}\, du\, d\sigma \tag{II-15}$$

$$\delta W'_{mag} = \int_{\sigma}\int_{u} \vec{A} \cdot \delta\vec{j}\, du\, d\sigma \tag{II-16}$$

which are equivalent to

$$\delta W_{mag} = \int_{\sigma}\int_{u} (\vec{j}\, d\sigma) \cdot \delta\vec{A}\, du \tag{II-17}$$

$$\delta W'_{mag} = \int_{\sigma}\int_{u} (\delta\vec{j}\, d\sigma) \cdot \vec{A}\, du \tag{II-18}$$

If $d\vec{\sigma}$ and $d\vec{u}$ are infinitesimal vectors, which are parallel together and are also both parallel to $\vec{j}$ and $\delta\vec{j}$, we may rewrite equation (II-17) and equation (II-18):

$$\delta W_{mag} = \int_{\sigma}\int_{u} (j d\sigma)\delta\vec{A} \cdot d\vec{u} \tag{II-19}$$

$$\delta W'_{mag} = \int_{\sigma}\int_{u} (\delta j d\sigma)\vec{A} \cdot d\vec{u} \tag{II-20}$$

since $jd\sigma$ is equal to di, which is constant throughout the tube length, it is not dependent upon the element du chosen. Consequently, it can be taken out of the second integral. The same also applies to $\delta jd\sigma$. Consequently, we rewrite equation (II-19) and equation (II-20) as:

$$\delta W_{mag} = \int_{\sigma} (j d\sigma)\int_{u} \delta\vec{A} \cdot d\vec{u} \tag{II-21}$$

$$\delta W'_{mag} = \int_{\sigma} (\delta j d\sigma)\int_{u} \vec{A} \cdot d\vec{u} \tag{II-22}$$

Assuming the current tube to close on itself, equation (II-21) and equation (II-22) can be written as closed line integrals:

$$\delta W_{mag} = \int_{\sigma} (j d\sigma)\oint_{u} \delta\vec{A} \cdot d\vec{u} \tag{II-23}$$

$$\delta W'_{mag} = \int_{\sigma} (\delta j d\sigma)\oint_{u} \vec{A} \cdot d\vec{u} \tag{II-24}$$

and we can apply Stoke's theorem to obtain:

$$\delta W_{mag} = \int_{\sigma} (j d\sigma) \int_{S_{coil}} \nabla\times\delta\vec{A} \cdot d\vec{s} \tag{II-25}$$

$$\delta W'_{mag} = \int_{\sigma} (\delta j d\sigma) \int_{S_{coil}} \nabla\times\vec{A} \cdot d\vec{s} \tag{II-26}$$

where the coil boundary is the current tube defining a surface S_{coil}. S_{coil} is divided into an infinite number of surface elements ds. The direction of the vector $d\vec{s}$ is perpendicular to the surface element ds.

We can rewrite equation (II-25) as:

$$\delta W_{mag} = \int_{\sigma} (j d\sigma) \int_{S_{coil}} \delta(\nabla \times \vec{A}) \cdot d\vec{s} \tag{II-27}$$

and from the definition of the magnetic vector potential:

$$\delta W_{mag} = \int_{\sigma} (j d\sigma) \int_{S_{coil}} \delta \vec{B} \cdot d\vec{s} \tag{II-28}$$

$$\delta W'_{mag} = \int_{\sigma} (\delta j d\sigma) \int_{S_{coil}} \vec{B} \cdot d\vec{s} \tag{II-29}$$

If flux linkage is defined as:

$$\lambda = \int_{S_{coil}} \vec{B} \cdot d\vec{s} \tag{II-30}$$

we may rewrite equation (II-28) and equation (II-29) as:

$$\delta W_{mag} = \int_{\sigma} (j d\sigma) \delta\lambda \tag{II-31}$$

$$\delta W'_{mag} = \int_{\sigma} (\delta j d\sigma) \lambda \tag{II-32}$$

If the flux linkage is the same throughout all the current tubes, then equation (II-31) and equation (II-32) may be written as:

$$\delta W_{mag} = \delta\lambda \int_{\sigma} di = i\delta\lambda \tag{II-33}$$

$$\delta W'_{mag} = \lambda \int_{\sigma} d(\delta i) = \lambda \delta i \tag{II-34}$$

or,

$$W_{mag} = \int_0^{\lambda} i \delta\lambda \tag{II-35}$$

$$W'_{mag} = \int_0^i \lambda \delta i \qquad \text{(II-36)}$$

Equation (II-35) and equation (II-36) are well-known expressions. However, they are only valid if the flux linking every single current tube has the same value. This condition is in theory only possible if the coils are filamentary, as it is the case in the derivations in [Str 1941][Dur 1953][Fan 1960]. In practice, equation (II-35) and equation (II-36) may also be used in the case of thick conductors, if the magnetic flux linking the coil is concentrated inside the coil boundary. Mostly, a coil surrounding an iron core will meet this condition. If thick coils are used with an air core, then equation (II-31) and equation (II-32) must be used to calculate the magnetic energy and coenergy.

Sum of W_{mag} and W'_{mag}

From equation (II-2) and equation (II-3), the sum of magnetic energy and coenergy is expressed as:

$$dW_{mag} + dW'_{mag} = d\left[\int_V (\vec{B} \cdot \vec{H}) dV\right] \qquad \text{(II-37)}$$

From equation (II-11) and equation (II-12), the sum of magnetic energy and coenergy is expressed as:

$$dW_{mag} + dW'_{mag} = d\left[\int_V (\vec{J} \cdot \vec{A}) dV\right] \qquad \text{(II-38)}$$

From equation (II-35) and equation (II-36), the sum of magnetic energy and coenergy is expressed as:

$$dW_{mag} + dW'_{mag} = d[i\lambda] \qquad \text{(II-39)}$$

Appendix III

PM Machine designs reported in literature

Table III-1. Characteristics of conventional PM synchronous machine designs reported in literature.

Source data	Outer Diameter (m)	Torque (kNm)	Speed (rpm)	Total active mass (kg)	Mass PM (kg)	Eff. (%)	Cost of active material (Euro)	Cost/ Torque (Euro/ kNm)	Torque /mass (Nm/ kg)
[Zha 1996]	0.16	0.03	750	17.2	0.73	86	128	4022	1.9
[Mit 2002]	0.21	0.23	10500	52	N/A	97	N/A	N/A	4.4
[Lan 2000]	0.41	1.16	616	79	4.04	94	634	545	14.7
[Mit 2002]	0.46	2.27	1050	128	N/A	95	N/A	N/A	17.8
[Mit 2002]	0.54	2.27	1050	201	N/A	97	N/A	N/A	11.3
[Gra 1997]	1.00	2.55	75	610	N/A	89	N/A	N/A	4.2
[Gra 1996b]	1.60	20.6	46	750	40	93	5860	285	27.5
[Spo 1992a]	1.65	43	46	1600	N/A	94	N/A	N/A	26.9
[Gra 1996b]	2.00	48	40	1200	55	93	9070	189	40.0
[Gra 1996b]	2.40	113	34	2100	110	94	16340	145	53.8
[Spo 1992a]	2.64	180	28	4100	N/A	94	N/A	N/A	43.8
[Lam 1996]	2.67	119	40	3300	150	95	24900	209	36.2
[Spo 1992a]	3.30	347	23	6400	N/A	94	N/A	N/A	54.2
[Gra 1996b]	3.30	244	29	4000	190	95	30460	125	61.0
[Gra 1996b]	3.60	348	27	5100	270	95	39780	114	68.2

Table III-2. Characteristics of conventional PM synchronous machine designs with flux concentration reported in literature.

Source data	Outer Diame-ter (m)	Torque (kNm)	Speed (rpm)	Total active mass (kg)	Mass PM (kg)	Eff. (%)	Cost of active mate-rial (Euro)	Cost/ Torque (Euro/ kNm)	Torque /mass (Nm/ kg)
[Spo 1992a]	1.65	43	46	2300	N/A	95	13800	321	18.7
[Spo 1996]	2.16	106.1	36	5600	650	91	55700	525	19.0
[Spo 1992a]	2.64	179.5	28	6000	N/A	95	36000	201	29.9
[Spo 1992a]	3.30	346.5	23	9000	N/A	95	54000	156	38.5

Table III-3. Characteristics of transverse-flux PM machine designs reported in literature.

Source data	Outer Diame-ter (m)	Torque (kNm)	Speed (rpm)	Total active mass (kg)	Mass PM (kg)	Eff. (%)	Cost of active mate-rial (Euro)	Cost/ Torque (Euro/ kNm)	Torque /mass (Nm/ kg)
[Har 1998]	0.17	0.07	N/A	9.3	1.2	N/A	97	1361	7.6
[Hen 1997]	0.28	0.30	1200	25	1.8	90	211	704	12
[Mad 1998]	0.34	0.54	N/A	20.8	2.1	N/A	195	361	25.9
[Har 1998]	0.36	0.26	N/A	22.7	1.2	N/A	178	695	11.3
[Har 1998]	0.36	0.32	N/A	22.7	1.2	N/A	178	549	14.3
[Mec 1996]	0.36	0.31	N/A	22.7	1.2	N/A	178	567	13.8
[Lan 2000]	0.37	1.26	570	73	11.5	98	829	660	17.2
[Bli 2000]	0.39	2.50	600	110	N/A	N/A	N/A	N/A	22.7
[Weh 1988a]	0.50	0.28	195	27.2	2.0	91	231	814	10.4
[Weh 1988a]	1.00	6.73	78	176	14.0	94	1532	228	38.3

Table III-4. Characteristics of TORUS designs reported in literature.

Source data	Outer Diame-ter (m)	Torque (kNm)	Speed (rpm)	Total active mass (kg)	Mass PM (kg)	Eff. (%)	Cost of active mate-rial (Euro)	Cost/ Torque (Euro/ kNm)	Torque /mass (Nm/ kg)
[Car 1994]	0.15	0.030	500	14	2.0	90	152	5069	2.1
[Spo 1992b]	0.16	0.008	3000	6.4	0.8	75	66	8330	1.2
[Spo 1992b]	0.17	0.008	3000	7.7	0.9	69	76	9523	1.0
[Cha 1997]	0.21	0.023	3300	7.1	2.0	84	111	4777	3.3
[Cha 1997]	0.22	0.029	750	6.8	1.0	84	75	2611	4.2
[Car 1997]	0.22	0.023	750	8.4	1.0	N/A	84	3683	2.7
[DiN 1991]	0.24	0.033	375	8.6	0.95	82	84	2536	3.8
[Bro 2002]	0.29	0.054	3000	29	1.8	90	235	4347	1.9
[Cha 1997]	0.32	0.22	1100	26.8	8.5	93	450	2089	8.0
[Cha 1997]	0.40	0.23	750	42	6.5	90	473	2064	5.5
[Car 1999a]	0.46	0.19	256	60	11.9	90	765	4100	3.1
[Cha 1999]	0.47	0.24	200	98.5	15.8	81	1128	4726	2.4
[Sti 1992]	0.50	0.09	300	35	N/A	86	N/A	N/A	2.5
[Car 1999b]	3.10	372.2	195	7320	1080	98	80640	217	50.8
[LoB 1997]	3.20	260.4	22	5325	1116	94	69894	268	48.9
[Hon 1991]	3.46	95.5	100	3000	N/A	97	N/A	N/A	31.8
[LoB 1997]	3.60	260.4	22	4900	1002	95	63468	244	53.2
[Car 1999b]	3.80	685.6	195	13640	1920	98	147120	215	50.2
[LoB 1997]	4.50	260.4	22	4198	817	96	52966	203	62.0

Appendix IV

Derivation of geometrical expressions for longitudinal machines

Slot depth h_s in radial-flux machine

$$h_s = \left[\frac{h_s}{b_t}\right] b_t \tag{IV-1}$$

The sum of slot width and tooth width are related to the pole pitch as:

$$b_t + b_s = \frac{\tau_p}{mq} \tag{IV-2}$$

or

$$b_t + \left\{\left[\frac{b_s}{b_t}\right] b_t\right\} = \frac{\tau_p}{mq} \tag{IV-3}$$

or

$$b_t = \frac{\tau_p}{mq} \frac{1}{\left\{1 + \left[\frac{b_s}{b_t}\right]\right\}} = \frac{\tau_p}{mq} \frac{\left[\frac{b_t}{b_s}\right]}{\left\{\left[\frac{b_t}{b_s}\right] + 1\right\}} \tag{IV-4}$$

Inserting equation (IV-4) into equation (IV-1), we obtain:

$$h_s = \frac{\left[\frac{h_s}{b_t}\right]\left[\frac{b_t}{b_s}\right]\frac{\tau_p}{mq}}{\left[\frac{b_t}{b_s}\right] + 1} \tag{IV-5}$$

Slot width b_s in slotted axial-flux machine

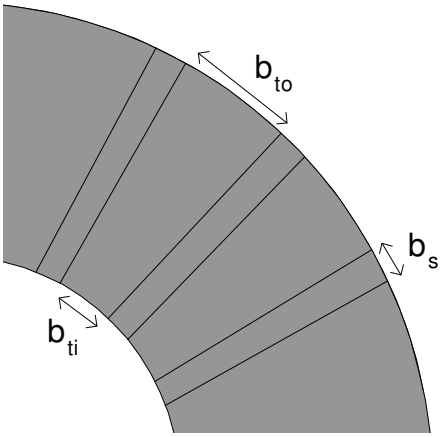

Figure IV-1: Geometrical parameters of the slotted axial-flux PM synchronous machine.

The sum of slot width b_s and tooth width at the outer radius b_{to} are related to the pole pitch τ_{po} at the outer radius as:

$$b_{to} + b_s = \frac{\tau_{po}}{mq} \tag{IV-6}$$

or

$$b_s = \frac{\tau_{po}}{mq} - b_{to} \tag{IV-7}$$

or

$$1 = \frac{\tau_{po}}{b_s mq} - \left[\frac{b_{to}}{b_s}\right] \tag{IV-8}$$

giving

$$b_s = \frac{\tau_{po}}{mq\left(1 + \left[\frac{b_{to}}{b_s}\right]\right)} \tag{IV-9}$$

Slot depth h_s in slotted axial-flux machine

$$h_s = \left[\frac{h_s}{b_{ti}}\right] b_{ti} \tag{IV-10}$$

where b_{ti} is the tooth width at the inner radius. The sum of slot width b_s and tooth width at the inner radius b_{ti} are related to the pole pitch at the inner radius as:

$$b_{ti} + b_s = \frac{\tau_{pi}}{mq} \tag{IV-11}$$

Inserting equation (IV-9) into equation (IV-11), we obtain:

$$b_{ti} + \frac{\tau_{po}}{mq\left(1 + \left[\frac{b_{to}}{b_s}\right]\right)} = \frac{\tau_{pi}}{mq} \tag{IV-12}$$

or

$$b_{ti} = \frac{1}{mq}\left(\tau_{pi} - \frac{\tau_{po}}{\left[1 + \frac{b_{to}}{b_s}\right]}\right) \tag{IV-13}$$

The ratio of pole pitch at the inner radius over the pole pitch at the outer radius is given by:

$$\frac{\tau_{pi}}{\tau_{po}} = K_{ax} \tag{IV-14}$$

Inserting equation (IV-14) into equation (IV-13), we obtain:

$$b_{ti} = \frac{\tau_{po}}{mq}\left(K_{ax} - \frac{1}{\left[1 + \frac{b_{to}}{b_s}\right]}\right) \tag{IV-15}$$

Inserting equation (IV-15) into equation (IV-10), we obtain:

$$h_s = \left[\frac{h_s}{b_{ti}}\right]\frac{\tau_{po}}{mq}\left(K_{ax} - \frac{1}{\left[\frac{b_{to}}{b_s}\right]}\right) \tag{IV-16}$$

Volume of stator teeth in radial-flux machine

The total pole area is A_p. The part of the pole area covered occupied by the slots is mql_sb_s. Therefore, the part of the pole area covered by the stator teeth is $A_p - mql_sb_s$. To obtain the total volume V_{st} of stator teeth in the machine, we must multiply this by the number of pole pairs $2p$ and the tooth height h_s:

$$V_{st} = [2p][h_s][A_p - mql_sb_s] \quad \text{(IV-17)}$$

Volume of stator teeth in axial-flux machine

The total pole area is A_p. The part of the pole area covered occupied by the slots is $mqb_s(r_{lo} - r_{li})$. Therefore, the part of the pole area covered by the stator teeth is $A_p - mqb_s(r_{lo} - r_{li})$. To obtain the total volume V_{st} of stator teeth in the machine, we must multiply this by the number of pole pairs $2p$ and the tooth height h_s:

$$V_{st} = [2p][h_s][A_p - mqb_s(r_{lo} - r_{li})] \quad \text{(IV-18)}$$

Appendix V

Optimized longitudinal PM machines

Table V-1. Slotted axial-flux PM machine: results of cost/torque optimization.

d_{out} (m)	η (%)	τ_p (cm)	J (A/mm^2)	B_g (T)	b_{to}/b_s	K_{ax}	m_{act} (kg)	c_{act} (Euro)	T (kNm)	Satu-rates ?
1.0	90	7.0	2.12	0.94	2.01	0.68	183	1495	0.89	yes
2.0	90	3.8	4.82	0.78	1.64	0.80	328	2946	11.31	no
3.0	90	5.9	6.24	0.81	1.30	0.79	1106	10502	83.58	no
4.0	90	4.2	6.48	0.74	1.24	0.85	1123	11813	116.02	no
1.0	95	Could	not be	achieve	d	------	Could	not	be ach	ieved
2.0	95	12.0	1.48	0.97	2.22	0.64	1499	13425	14.1	yes
3.0	95	9.6	2.35	0.89	1.75	0.73	2337	21176	63.0	no
4.0	95	9.6	2.73	0.87	1.51	0.77	3771	35874	170.5	no

Table V-2. Slotted axial-flux PM machine: results of torque/mass optimization.

d_{out} (m)	η (%)	τ_{po} (cm)	J (A/mm^2)	B_g (T)	b_{to}/b_s	K_{ax}	m_{act} (kg)	c_{act} (Euro)	T (kNm)	Satu-rates ?
1.0	90	6.8	2.35	0.97	2.14	0.65	188	1679	0.96	yes
2.0	90	4.1	6.00	0.94	1.71	0.78	442	5194	18.7	no
3.0	90	4.6	7.33	0.91	1.51	0.81	1020	12341	85.5	no
4.0	90	5.3	8.0	0.90	1.49	0.81	2082	26319	257.1	no
1.0	95	Could	not be	achiev	ed		Could	not	be	achieve
2.0	95	13.0	1.65	0.98	2.39	0.58	1670	15697	16.1	yes
3.0	95	9.7	2.55	0.96	2.00	0.72	2716	28174	75.2	no
4.0	95	8.4	2.97	0.93	1.67	0.77	3694	41303	174.7	no

Table V-3. Conventional PM synchronous machine: results of cost/torque optimization.

d_{out}	η (%)	τ_p (cm)	J (A/mm^2)	B_g (T)	b_t/b_s	K_{rad}	m_{act} (kg)	c_{act} (Euro)	T (kNm)
1.0	90	3.3	3.4	0.76	0.77	0.097	69	547	0.90
2.0	90	3.6	5.6	0.72	0.68	0.06	198	1755	11.34
3.0	90	4.6	7.2	0.69	0.70	0.079	737	6655	83.58
4.0	90	4.1	7.3	0.70	0.76	0.049	794	8149	117.29
2.0	95	5.9	2.2	0.72	0.68	0.107	567	4391	14.1
3.0	95	5.9	3.1	0.72	0.70	0.097	1181	10159	63.0
4.0	95	6.9	3.4	0.72	0.70	0.085	2191	19446	171.3

Table V-4. Conventional PM synchronous machine: results of torque/mass optimization.

d_{out}	η (%)	τ_p (cm)	J (A/mm^2)	B_g (T)	b_t/b_s	K_{rad}	m_{act} (kg)	c_{act} (Euro)	T (kNm)
1.0	90	3.4	3.5	0.82	0.88	0.087	72	586	0.96
2.0	90	2.7	7.6	0.86	0.92	0.081	255	2973	18.7
3.0	90	3.3	9.2	0.86	0.93	0.071	638	8037	86.5
4.0	90	4.4	8.7	0.75	0.73	0.079	1385	14914	258.2
2.0	95	4.9	2.4	0.86	0.95	0.106	587	5359	16.3
3.0	95	5.0	3.7	0.84	0.89	0.096	1208	12404	75.2
4.0	95	5.3	3.8	0.79	0.79	0.090	2018	21031	174.7

Table V-5. Conventional PM synchronous machine with flux concentration: results of cost/ torque optimization.

d_{out}	η (%)	τ_p (cm)	J (A/mm^2)	B_g (T)	b_t/b_s	K_{rad}	m_{act} (kg)	c_{act} (Euro)	T (kNm)
1.0	90	3.1	3.6	0.81	0.82	0.098	80	550	0.95
2.0	90	2.4	6.9	0.84	0.89	0.066	180	1568	11.3
3.0	90	3.5	8.7	0.85	0.91	0.069	577	4504	84.2
4.0	90	2.6	9.1	0.78	0.78	0.064	684	7676	117.4
2.0	95	5.2	2.4	0.81	0.83	0.111	658	4824	16.1
3.0	95	5.4	3.2	0.78	0.76	0.097	1247	9510	65.8
4.0	95	5.4	3.7	0.77	0.76	0.093	2081	16799	172.1

Table V-6. Conventional PM synchronous machine with flux concentration: results of torq ue/mass optimization.

d_{out}	η (%)	τ_p (cm)	J (A/mm^2)	B_g (T)	b_t/b_s	K_{rad}	m_{act} (kg)	c_{act} (Euro)	T (kNm)
1.0	90	3.2	3.5	0.75	0.78	0.105	81	560	0.96
2.0	90	2.4	7.5	0.82	0.85	0.089	243	1870	18.7
3.0	90	3.1	9.2	0.83	0.86	0.080	573	4669	86.6
4.0	90	3.0	10.3	0.82	0.85	0.100	1185	10884	265.8
2.0	95	5.6	2.3	0.74	0.71	0.120	673	4709	16.1
3.0	95	5.5	3.4	0.82	0.85	0.098	1350	10264	75.2
4.0	95	4.6	4.0	0.85	0.90	0.098	2086	18483	174.9

Appendix VI

Derivation of torque expression in a multi-pole single-phase machine with saliency

The stator inductance L_s was defined by equation . The electrical angle α may be related to the electrical frequency (in rad/s) ω and time t as follows:

$$\alpha = \omega t \tag{VI-1}$$

We can rewrite L_s:

$$L_s(t) = \left[\frac{L_a + L_u}{2}\right] + \left[\frac{L_u - L_a}{2}\right]\cos(2\omega t) \tag{VI-2}$$

where

$$\omega = 2\pi f \tag{VI-3}$$

The no-load voltage *e(t)* and current *i(t)* were assumed sinusoidal and are defined as follows:

$$e(t) = \hat{e}\cos(\omega t) \tag{VI-4}$$

$$i(t) = \hat{i}_s\cos(\omega t + \psi) \tag{VI-5}$$

where ψ is the phase angle between the current phasor and the no-load voltage phasor. The flux linkage λ_s created around the coil by the current *i(t)* is expressed as:

$$\lambda_s(t) = L_s(t)i(t) \tag{VI-6}$$

Inserting equation (VI-5) and equation (VI-2) into equation (VI-6), we obtain:

$$\lambda_s(t) = \hat{i}_s\left(\left[\frac{L_a + L_u}{2}\right] + \left[\frac{L_u - L_a}{2}\right]\cos(2\omega t)\right)\cos(\omega t + \psi) \tag{VI-7}$$

or:

$$\lambda_s(t) = \frac{\hat{i}_s}{2}([L_a + L_u]\cos(\omega t + \psi) + [L_u - L_a]\cos(2\omega t)\cos(\omega t + \psi)) \quad \text{(VI-8)}$$

Or, by applying well-known geometrical identities:

$$\lambda_s(t) = \frac{\hat{i}_s}{2}\left([L_a + L_u]\{\cos\psi\cos\omega t - \sin\psi\sin\omega t\} + \frac{[L_u - L_a]}{2}\{\cos(\omega t - \psi) + \cos(3\omega t + \psi)\}\right) \quad \text{(VI-9)}$$

or,

(VI-10)

$$\lambda_s(t) = \frac{\hat{i}_s}{2}\left([L_a + L_u]\{\cos\psi\cos\omega t - \sin\psi\sin\omega t\} + \frac{[L_u - L_a]}{2}\{[\cos\psi\cos\omega t + \sin\psi\sin\omega t] + [\cos\psi\cos 3\omega t - \sin\psi\sin 3\omega t]\}\right)$$

or,

(VI-11)

$$\lambda_s(t) = \frac{\hat{i}_s}{4}(\sin\psi[-(L_u + 3L_a)\sin\omega t + (L_a - L_u)\sin(3\omega t)] + \cos\psi[(L_a + 3L_u)\cos\omega t + (L_u - L_a)\cos(3\omega t)])$$

The terminal voltage $v_s(t)$ can be deduced from equation (VI-4) and equation (VI-11). Here we neglect the voltage drop in the machine conductors.

$$v_s(t) = e(t) - \frac{d\lambda_s(t)}{dt} \quad \text{(VI-12)}$$

(VI-13)

$$v_s(t) = \hat{e}\cos(\omega t) - \frac{\pi \hat{i}_s f}{2}(\sin\psi[3(L_a - L_u)\cos(3\omega t) - (L_u + 3L_a)\cos(\omega t)] - \cos\psi[3(L_u - L_a)\sin(3\omega t) + (L_a + 3L_u)\sin(\omega t)])$$

or,

(VI-14)

$$v_s(t) = \hat{e}\cos(\omega t) + \frac{\pi \hat{i}_s f}{2}\{(L_a + 3L_u)\cos\psi\sin(\omega t) + (L_u + 3L_a)\sin\psi\cos(\omega t) + 3(L_u - L_a)\sin(3\omega t + \psi)\}$$

The instantaneous electrical power $p_{elec}(t)$ is written:

$$p_{elec}(t) = v_s(t)i(t) \quad \text{(VI-15)}$$

From equation (VI-13) and equation (VI-5), we rewrite $p_{elec}(t)$:

$$p_{elec}(t) = a_1(t) - \frac{\pi \hat{i}_s^2 f}{2}\{a_2(t) - a_3(t)\} \tag{VI-16}$$

where

$$a_1(t) = \hat{e}\hat{i}_s \cos(\omega t)\cos(\omega t + \psi)$$

$$a_2(t) = \sin\psi[3(L_a - L_u)\cos(\omega t + \psi)\cos(3\omega t) - (L_u + 3L_a)\cos(\omega t)\cos(\omega t + \psi)]$$

$$a_3(t) = \cos\psi[3(L_u - L_a)\sin(3\omega t)\cos(\omega t + \psi) + (L_a + 3L_u)\sin(\omega t)\cos(\omega t + \psi)]$$

Transforming $a_1(t)$, $a_2(t)$ and $a_3(t)$ with well-known geometrical identities, we obtain:

$$a_1(t) = \frac{\hat{e}\hat{i}_s}{2}[\cos\psi + \cos(2\omega t + \psi)]$$

$$a_2(t) = \frac{\sin\psi}{2}\{3(L_a - L_u)[\cos(-2\omega t + \psi) + \cos(4\omega t + \psi)] - (L_u + 3L_a)[\cos\psi + \cos(2\omega t + \psi)]\}$$

$$a_3(t) = \frac{\cos\psi}{2}\{3(L_u - L_a)[\sin(2\omega t - \psi) + \sin(4\omega t + \psi)] + (L_a + 3L_u)[\sin(2\omega t + \psi) - \sin\psi]\}$$

To obtain the average power extracted from the machine terminal, $p_{elec}(t)$ is integrated over one electrical period, that is:

$$P_{elec} = \frac{1}{T}\int_0^T p_{elec}(t)dt \tag{VI-17}$$

or,

$$P_{elec} = f\int_0^T a_1(t)dt - \frac{\pi \hat{i}_s^2 f^2}{2}\int_0^T \{a_2(t) - a_3(t)\}dt \tag{VI-18}$$

All terms inside $a_1(t)$, $a_2(t)$ and $a_3(t)$ which are sines or cosines of $2\omega t$ and $4\omega t$ are zero when integrated over a complete period T. Equation (VI-18) is simplified to:

(VI-19)

$$P_{elec} = f\int_0^T \frac{\hat{e}\hat{i}_s}{2}\cos\psi\, dt - \frac{\pi \hat{i}_s^2 f^2}{2}\int_0^T \left\{-(L_u + 3L_a)\frac{\sin\psi}{2}\cos\psi + (3L_u + L_a)\frac{\cos\psi}{2}\sin\psi\right\}dt$$

or,

$$P_{elec} = \frac{\hat{e}\hat{i}_s}{2}\cos\psi - \frac{\pi\hat{i}_s^{\,2} f}{2}\frac{\sin\psi\cos\psi}{2}(2L_u - 2L_a) \qquad \text{(VI-20)}$$

or,

$$P_{elec} = \frac{\hat{e}\hat{i}_s}{2}\cos\psi + \frac{\pi\hat{i}_s^{\,2} f}{4}(L_a - L_u)\sin 2\psi \qquad \text{(VI-21)}$$

or in terms of rms value of the current and no-load voltage:

$$P_{elec} = EI\cos\psi + \frac{\pi I^2 f}{2}(L_a - L_u)\sin 2\psi \qquad \text{(VI-22)}$$

Equation (VI-22) assumes the voltage drop in the stator windings to be zero. If we take into account the copper losses, equation (VI-22) must be rewritten:

$$P_{elec} = EI\cos\psi + \frac{\pi I^2 f}{2}(L_a - L_u)\sin 2\psi - P_{Cu} \qquad \text{(VI-23)}$$

or

$$P_{elec} = EI\cos\psi + \frac{\pi I^2 f}{2}(L_a - L_u)\sin 2\psi - R_s I^2 \qquad \text{(VI-24)}$$

Appendix VII

Lists of the geometrical values and β factors computed with FEA for 3-D lumped reluctances

- Reluctance U_g

g	lf	wsc	wrc2	RgN	Rg FEA	Beta g	wsc/wrc2	lf/g	wrc2/g
(mm)	(mm)	(mm)	(mm)	(MA/Wb)	(MA/Wb)				
0,5	10	4	6	6,64	6,33	0,95	0,67	20,00	12,00
1	10	4	6	13,28	10,4	0,78	0,67	10,00	6,00
1,5	10	4	6	19,92	13,88	0,70	0,67	6,67	4,00
2	10	4	6	26,56	16,43	0,62	0,67	5,00	3,00
0,5	45	4	6	1,48	1,58	1,07	0,67	90,00	12,00
1	45	4	6	2,95	2,77	0,94	0,67	45,00	6,00
1,5	45	4	6	4,43	4,01	0,91	0,67	30,00	4,00
2	45	4	6	5,90	4,93	0,84	0,67	22,50	3,00
0,5	10	8	6	6,64	5,22	0,79	1,33	20,00	12,00
1	10	8	6	13,28	9,07	0,68	1,33	10,00	6,00
1,5	10	8	6	19,92	11,85	0,59	1,33	6,67	4,00
2	10	8	6	26,56	14,8	0,56	1,33	5,00	3,00
0,5	45	8	6	1,48	1,34	0,91	1,33	90,00	12,00
1	45	8	6	2,95	2,54	0,86	1,33	45,00	6,00
1,5	45	8	6	4,43	3,56	0,80	1,33	30,00	4,00
2	45	8	6	5,90	4,18	0,71	1,33	22,50	3,00
0,5	10	12	6	6,64	5,09	0,77	2,00	20,00	12,00
1	10	12	6	13,28	8,76	0,66	2,00	10,00	6,00
1,5	10	12	6	19,92	11,82	0,59	2,00	6,67	4,00
2	10	12	6	26,56	14,3	0,54	2,00	5,00	3,00
0,5	45	12	6	1,48	1,34	0,91	2,00	90,00	12,00
1	45	12	6	2,95	2,45	0,83	2,00	45,00	6,00
1,5	45	12	6	4,43	3,47	0,78	2,00	30,00	4,00
2	45	12	6	5,90	4,23	0,72	2,00	22,50	3,00
0,5	10	16	6	6,64	5,09	0,77	2,67	20,00	12,00
1	10	16	6	13,28	8,45	0,64	2,67	10,00	6,00
1,5	10	16	6	19,92	11,3	0,57	2,67	6,67	4,00
2	10	16	6	26,56	14,5	0,55	2,67	5,00	3,00
0,5	45	16	6	1,48	1,34	0,91	2,67	90,00	12,00
1	45	16	6	2,95	2,46	0,83	2,67	45,00	6,00
1,5	45	16	6	4,43	3,41	0,77	2,67	30,00	4,00
2	45	16	6	5,90	4,26	0,72	2,67	22,50	3,00
0,5	10	4	9	4,43	5,7	1,29	0,44	20,00	18,00
1	10	4	9	8,85	8,9	1,01	0,44	10,00	9,00
1,5	10	4	9	13,28	11,38	0,86	0,44	6,67	6,00

g	lf	wsc	wrc2	RgN	Rg FEA	Beta g	wsc/wrc2	lf/g	wrc2/g
(mm)	(mm)	(mm)	(mm)	(MA/Wb)	(MA/Wb)				
0,5	10	16	12	3,32	2,68	0,81	1,33	20,00	24,00
1	10	16	12	6,64	4,64	0,70	1,33	10,00	12,00
1,5	10	16	12	9,96	6,34	0,64	1,33	6,67	8,00
2	10	16	12	13,28	7,7	0,58	1,33	5,00	6,00
0,5	45	16	12	0,74	0,67	0,91	1,33	90,00	24,00
1	45	16	12	1,48	1,28	0,87	1,33	45,00	12,00
1,5	45	16	12	2,21	1,85	0,84	1,33	30,00	8,00
2	45	16	12	2,95	2,38	0,81	1,33	22,50	6,00
1	45	8	8	2,21	1,96	0,89	1,00	45,00	8,00

- Reluctance $\boldsymbol{R}_{hi}$

hm	hri	wrc2		RhiN	Rhi FEA	Beta hi	hm/wrc2	d/hri
(mm)	(mm)	(mm)		(MA/Wb)	(MA/Wb)			
1	5	6		7,3675926	3,108139	0,421866	0,166667	1,6
2	5	6		7,3675926	3,461914	0,469884	0,333333	2
3	5	6		7,3675926	3,896179	0,528827	0,5	2,4
1	8	6		11,788148	2,999849	0,25448	0,166667	1
2	8	6		11,788148	3,65444	0,31001	0,333333	1,25
3	8	6		11,788148	4,323737	0,366787	0,5	1,5
1	12	6		17,682222	2,875591	0,162626	0,166667	0,666667
2	12	6		17,682222	3,647142	0,20626	0,333333	0,833333
3	12	6		17,682222	4,476491	0,253163	0,5	1
1	5	8		5,5256944	2,455505	0,444379	0,125	2
2	5	8		5,5256944	3,113247	0,563413	0,25	2,4
3	5	8		5,5256944	3,507469	0,634756	0,375	2,8
1	8	8		8,8411111	2,661344	0,301019	0,125	1,25
2	8	8		8,8411111	3,383061	0,382651	0,25	1,5
3	8	8		8,8411111	3,827444	0,432914	0,375	1,75
1	12	8		13,261667	2,647541	0,199639	0,125	0,833333
2	12	8		13,261667	3,342403	0,252035	0,25	1
3	12	8		13,261667	4,136873	0,311942	0,375	1,166667
1	5	10		4,4205556	2,296838	0,519581	0,1	2,4
2	5	10		4,4205556	2,773216	0,627346	0,2	2,8
3	5	10		4,4205556	3,012585	0,681495	0,3	3,2
1	8	10		7,0728889	2,37731	0,336116	0,1	1,5
2	8	10		7,0728889	3,039769	0,429778	0,2	1,75
3	8	10		7,0728889	3,501401	0,495045	0,3	2
1	12	10		10,609333	2,494761	0,235148	0,1	1

hm	hri	wrc2		RhiN	Rhi FEA	Beta hi	hm/wrc2	d/hri
(mm)	(mm)	(mm)		(MA/Wb)	(MA/Wb)			
2	12	10		10,609333	3,091902	0,291432	0,2	1,166667
3	12	10		10,609333	3,68958	0,347767	0,3	1,333333
1	5	12		3,6837963	2,081591	0,565067	0,083333	2,8
2	5	12		3,6837963	2,37142	0,643744	0,166667	3,2
3	5	12		3,6837963	2,674087	0,725905	0,25	3,6
1	8	12		5,8940741	2,262452	0,383852	0,083333	1,75
2	8	12		5,8940741	2,728243	0,462879	0,166667	2
3	8	12		5,8940741	3,260888	0,553249	0,25	2,25
1	12	12		8,8411111	2,412216	0,272841	0,083333	1,166667
2	12	12		8,8411111	2,905097	0,32859	0,166667	1,333333
3	12	12		8,8411111	3,458273	0,391158	0,25	1,5

- Reluctance $\boldsymbol{R}_{ctc}$

(hm + wrc1)	g	lf	lrt1	wsc	wrc2	RctcN	Rctc FEA	Beta ctc	wsc/wrc2	lf/g	d/lrt1	lf/lrt1
(mm)	(mm)	(mm)	(mm)	(mm)	(mm)	(MA/Wb)	(MA/Wb)					
10	2	45	60	6	10	66,30833	147,8561	2,229826	0,6	22,5	0,167	0,75
10	2	45	60	6	6	66,30833	131,1151	1,977355	1	22,5	0,167	0,75
10	2	45	60	10	6	66,30833	186,7276	2,816051	1,66667	22,5	0,167	0,75
10	2	45	60	10	10	66,30833	102,3772	1,543956	1	22,5	0,167	0,75
10	2	15	30	6	10	132,6167	134,3575	1,013127	0,6	7,5	0,333	0,5
10	2	15	30	6	6	132,6167	174,7579	1,317768	1	7,5	0,333	0,5
10	2	15	30	10	6	132,6167	239,7867	1,808119	1,66667	7,5	0,333	0,5
10	2	15	30	10	10	132,6167	186,0246	1,402724	1	7,5	0,333	0,5
6	2	45	60	6	10	39,785	80,57952	2,025374	0,6	22,5	0,1	0,75
6	2	45	60	6	6	39,785	123,7324	3,110026	1	22,5	0,1	0,75
6	2	45	60	10	6	39,785	113,4002	2,850326	1,66667	22,5	0,1	0,75
6	2	45	60	10	10	39,785	90,73835	2,280718	1	22,5	0,1	0,75
6	2	15	30	6	10	79,57	115,683	1,453851	0,6	7,5	0,2	0,5
6	2	15	30	6	6	79,57	127,0626	1,596865	1	7,5	0,2	0,5
6	2	15	30	10	6	79,57	141,1892	1,774402	1,66667	7,5	0,2	0,5
6	2	15	30	10	10	79,57	116,0411	1,458353	1	7,5	0,2	0,5
10	1	45	60	6	10	132,6167	95,01889	0,716493	0,6	45	0,167	0,75
10	1	45	60	6	6	132,6167	713,3898	5,379338	1	45	0,167	0,75
10	1	45	60	10	6	132,6167	254,6384	1,920109	1,66667	45	0,167	0,75
10	1	45	60	10	10	132,6167	216,4683	1,632286	1	45	0,167	0,75
10	1	15	30	6	10	265,2333	207,2633	0,781438	0,6	15	0,333	0,5
10	1	15	30	6	6	265,2333	185,9888	0,701227	1	15	0,333	0,5
10	1	15	30	10	6	265,2333	233,4389	0,880126	1,66667	15	0,333	0,5
10	1	15	30	10	10	265,2333	216,362	0,815742	1	15	0,333	0,5
6	1	45	60	6	10	79,57	169,5283	2,130555	0,6	45	0,1	0,75

(hm + wrc1)	g	lf	lrt1	wsc	wrc2	RctcN	Rctc FEA	Beta ctc	wsc/wrc2	lf/g	d/lrt1	lf/lrt1
(mm)	(mm)	(mm)	(mm)	(mm)	(mm)	(MA/Wb)	(MA/Wb)					
6	1	45	60	6	6	79,57	188,0437	2,363249	1	45	0,1	0,75
6	1	45	60	10	6	79,57	134,2891	1,687686	1,66667	45	0,1	0,75
6	1	45	60	10	10	79,57	95,38656	1,198775	1	45	0,1	0,75
6	1	15	30	6	10	159,14	156,3765	0,982635	0,6	15	0,2	0,5
6	1	15	30	6	6	159,14	162,3703	1,020299	1	15	0,2	0,5
6	1	15	30	10	6	159,14	148,1793	0,931126	1,66667	15	0,2	0,5
6	1	15	30	10	10	159,14	146,0165	0,917535	1	15	0,2	0,5
5	1	22,5	30	5	5	132,6167	243,0056	1,832391	1	22,5	0,167	0,75
5	1	15	30	5	5	132,6167	137,7425	1,038651	1	15	0,167	0,5
10	1	30	60	6	6	132,62	188,5658	1,42	1,00	30,00	0,17	0,50
10	1	40	60	6	6	132,62	243,7354	1,84	1,00	40,00	0,17	0,67
10	1	50	60	6	6	132,62	134,9619	1,02	1,00	50,00	0,17	0,83
8	1	45	75	8	8	84,87	120,0664	1,41	1,00	45,00	0,11	0,60
8	2	45	75	8	8	42,44	80,65284	1,95	1,00	22,50	0,11	0,60

- Reluctance $\boldsymbol{R}_{LEC}$

d	wm	wrc2	RlecN	Rlec FEA	Beta LEC	wrc2/d	wm/d
(mm)	(mm)	(mm)	MA/Wb	MA/Wb			
1	12	4	66,40	108,57	1,64	4,00	12,00
1	10	6	79,68	115,78	1,45	6,00	10,00
2	10	6	159,36	148,88	0,93	3,00	5,00
4	10	6	318,72	172,81	0,54	1,50	2,50
8	10	6	637,44	253,42	0,40	0,75	1,25
12	10	6	956,16	342,33	0,36	0,50	0,83
16	10	6	1274,88	308,16	0,24	0,38	0,63
20	10	6	1593,60	318,85	0,20	0,30	0,50
4	20	6	159,36	87,60	0,55	1,50	5,00
8	20	6	318,72	120,93	0,38	0,75	2,50
12	20	6	478,08	141,50	0,30	0,50	1,67
16	20	6	637,44	186,04	0,29	0,38	1,25
20	20	6	796,80	179,94	0,23	0,30	1,00
4	30	6	106,24	53,00	0,50	1,50	7,50
8	30	6	212,48	83,83	0,39	0,75	3,75
12	30	6	318,72	122,41	0,38	0,50	2,50
16	30	6	424,96	145,27	0,34	0,38	1,88
20	30	6	531,20	166,78	0,31	0,30	1,50
4	10	9	318,72	135,03	0,42	2,25	2,50
8	10	9	637,44	156,87	0,25	1,13	1,25
12	10	9	956,16	312,64	0,33	0,75	0,83
16	10	9	1274,88	331,10	0,26	0,56	0,63
20	10	9	1593,60	406,38	0,26	0,45	0,50
1	20	9	39,84	50,53	1,27	9,00	20,00
2	20	9	79,68	64,11	0,80	4,50	10,00
4	20	9	159,36	80,56	0,51	2,25	5,00
8	20	9	318,72	83,10	0,26	1,13	2,50
12	20	9	478,08	116,01	0,24	0,75	1,67
16	20	9	637,44	152,08	0,24	0,56	1,25

d	wm	wrc2	RlecN	Rlec FEA	Beta LEC	wrc2/d	wm/d
(mm)	(mm)	(mm)	MA/Wb	MA/Wb			
20	20	9	796,80	169,76	0,21	0,45	1,00
4	30	9	106,24	53,90	0,51	2,25	7,50
8	30	9	212,48	75,35	0,35	1,13	3,75
12	30	9	318,72	88,10	0,28	0,75	2,50
16	30	9	424,96	111,85	0,26	0,56	1,88
20	30	9	531,20	110,04	0,21	0,45	1,50
4	10	12	318,72	109,81	0,34	3,00	2,50
8	10	12	637,44	201,58	0,32	1,50	1,25
12	10	12	956,16	196,52	0,21	1,00	0,83
16	10	12	1274,88	209,14	0,16	0,75	0,63
20	10	12	1593,60	241,70	0,15	0,60	0,50
4	20	12	159,36	67,69	0,42	3,00	5,00
8	20	12	318,72	92,23	0,29	1,50	2,50
12	20	12	478,08	76,39	0,16	1,00	1,67
16	20	12	637,44	126,96	0,20	0,75	1,25
20	20	12	796,80	166,09	0,21	0,60	1,00
4	30	12	106,24	42,02	0,40	3,00	7,50
8	30	12	212,48	70,38	0,33	1,50	3,75
12	30	12	318,72	77,20	0,24	1,00	2,50
16	30	12	424,96	80,27	0,19	0,75	1,88
20	30	12	531,20	98,72	0,19	0,60	1,50
8	12	8	531,20	172,24	0,32	1,00	1,50

- Reluctance $\boldsymbol{R}_{icore}$

dicore	lf	lrt1	Ricore FEA	RicoreN	Betaicore	dicore/lf	kf
(mm)	(mm)	(mm)	(MA/Wb)	(MA/Wb)			
4	10	10	18,11	31,832	0,57	0,40	1,00
4	10	15	24,7	31,832	0,78	0,40	0,67
4	10	20	32,3	31,832	1,01	0,40	0,50
8	10	10	25,3	63,664	0,40	0,80	1,00
8	10	15	31,6	63,664	0,50	0,80	0,67
8	10	20	38,1	63,664	0,60	0,80	0,50
12	10	10	39	95,496	0,41	1,20	1,00
12	10	15	45,6	95,496	0,48	1,20	0,67
12	10	20	51,2	95,496	0,54	1,20	0,50
16	10	10	47,6	127,328	0,37	1,60	1,00
16	10	15	54,2	127,328	0,43	1,60	0,67
16	10	20	59,3	127,328	0,47	1,60	0,50
4	30	30	5,1	3,536889	1,44	0,13	1,00
4	30	40	7,5	3,536889	2,12	0,13	0,75
4	30	60	16,3	3,536889	4,61	0,13	0,50
8	20	20	10,9	15,916	0,68	0,40	1,00
8	30	30	6,6	7,073778	0,93	0,27	1,00
8	30	40	9,9	7,073778	1,40	0,27	0,75
8	30	60	17,8	7,073778	2,52	0,27	0,50

dicore	lf	lrt1	Ricore FEA	RicoreN	Betaicore	dicore/lf	kf
(mm)	(mm)	(mm)	(MA/Wb)	(MA/Wb)			
12	30	30	9	10,61067	0,85	0,40	1,00
12	30	40	11,8	10,61067	1,11	0,40	0,75
12	30	60	18,6	10,61067	1,75	0,40	0,50
16	30	30	10,5	14,14756	0,74	0,53	1,00
16	30	40	13,3	14,14756	0,94	0,53	0,75
16	30	60	19,7	14,14756	1,39	0,53	0,50
4	60	60	1,9	0,884222	2,15	0,07	1,00
4	60	85	3,9	0,884222	4,41	0,07	0,71
4	60	100	5,53	0,884222	6,25	0,07	0,60
8	60	60	3	1,768444	1,70	0,13	1,00
8	60	85	5,7	1,768444	3,22	0,13	0,71
8	60	100	4,9	1,768444	2,77	0,13	0,60
12	60	60	3,8	2,652667	1,43	0,20	1,00
12	60	85	6	2,652667	2,26	0,20	0,71
12	60	100	8,6	2,652667	3,24	0,20	0,60
16	60	60	4,3	3,536889	1,22	0,27	1,00
16	60	85	6,9	3,536889	1,95	0,27	0,71
16	60	100	10,3	3,536889	2,91	0,27	0,60
4	90	90	1	0,392988	2,54	0,04	1,00
4	90	120	1,76	0,392988	4,48	0,04	0,75
8	90	90	1,38	0,785975	1,76	0,09	1,00
8	90	120	2,73	0,785975	3,47	0,09	0,75
12	90	90	1,83	1,178963	1,55	0,13	1,00
12	90	120	2,9	1,178963	2,46	0,13	0,75
16	90	90	2,07	1,571951	1,32	0,18	1,00
16	90	120	5,1	1,571951	3,24	0,18	0,75

- Reluctance $\boldsymbol{R}_{side}$

g	lf	wsc	wrc2	wrc1	dside	RsideN	Rside FEA	Beta side	ds/g	ds/wrc2	wsc/wrc2	wsc/g
(mm)	(mm)	(mm)	(mm)	(mm)	(mm)	(MA/Wb)	(MA/Wb)					
1	45	4	4	2	0	4,43	4,83	1,09	0,00	0,00	1,00	4,00
1,5	45	4	4	2	0	6,64	5,48	0,83	0,00	0,00	1,00	2,67
2	45	4	4	2	0	8,85	6,15	0,69	0,00	0,00	1,00	2,00
1	45	4	4	2	2	4,43	6,95	1,57	2,00	0,50	1,00	4,00
1,5	45	4	4	2	2	6,64	7,34	1,11	1,33	0,50	1,00	2,67
2	45	4	4	2	2	8,85	7,65	0,86	1,00	0,50	1,00	2,00
1	45	4	4	2	4	4,43	8,62	1,95	4,00	1,00	1,00	4,00
1,5	45	4	4	2	4	6,64	8,72	1,31	2,67	1,00	1,00	2,67
2	45	4	4	2	4	8,85	8,9	1,01	2,00	1,00	1,00	2,00
1	45	6	4	3	0	4,43	4,83	1,09	0,00	0,00	1,50	6,00
1,5	45	6	4	3	0	6,64	5,45	0,82	0,00	0,00	1,50	4,00
2	45	6	4	3	0	8,85	6,05	0,68	0,00	0,00	1,50	3,00
1	45	6	4	3	2	4,43	6,73	1,52	2,00	0,50	1,50	6,00
1,5	45	6	4	3	2	6,64	7,02	1,06	1,33	0,50	1,50	4,00
2	45	6	4	3	2	8,85	7,56	0,85	1,00	0,50	1,50	3,00
1	45	6	4	3	4	4,43	8,42	1,90	4,00	1,00	1,50	6,00
1,5	45	6	4	3	4	6,64	8,96	1,35	2,67	1,00	1,50	4,00
2	45	6	4	3	4	8,85	9,05	1,02	2,00	1,00	1,50	3,00
1	45	6	8	4	0	2,21	4,31	1,95	0,00	0,00	0,75	6,00
1,5	45	6	8	4	0	3,32	4,87	1,47	0,00	0,00	0,75	4,00

Appendix VIII

Optimized TFPM machines with toothed rotor and conventional PM synchronous machine

Table VIII-1. TFPM machine with toothed rotor: results of cost/torque optimization.

d_{out} (m)	0.5	1.0	2.0	3.0	0.5	1.0	2.0	3.0
Target η (%)	90	90	90	90	95	95	95	95
g (mm)	0.5	1.0	2.0	3.0	0.5	1.0	2.0	3.0
τ_p (mm)	10	14.4	32.2	39.7	24.8	36.0	56.6	89
J (A/mm^2)	9.7	7.0	5.2	3.6	2.6	2.1	1.4	1.1
h_m (mm)	1.5	2.7	7.0	9.0	3.9	7.5	6.3	8.0
l_{rt1} (mm)	30	36	56	77	45	60	68	111
l_f (mm)	18	23	34	51	36	49	41	62
w_m (mm)	10	14	18	18.7	16	17	35	53
w_{rc1} (mm)	2	2	4.2	5.0	3	5	25	47
w_{rc2} (mm)	5	7	14	16.7	14	16	19	26
w_{sc} (mm)	7.3	10	18	20	16	20	28	41
ψ (degrees)	-32	- 31	- 32	-34	-38	- 31	- 30	- 33
Φ_{pnl} (μWb) (model)	136	235	709	1056	788	1147	1461	3061
$\mathcal{U}_{ap}$ (A/μWb) (model)	11.2	10.1	8.1	5.8	5.0	4.5	6.1	4.1
$\mathcal{U}_{up}$ (A/μWb) (model)	8.8	7.7	6.6	4.6	3.6	3.7	5.2	3.1
$\hat{\Im}_s$ (A-turns) (model)	2586	3817	8840	10451	4755	7525	12161	17661
$\Im_s$ (A-turns) (FEA)	2586	4550	9643	10451	4755	8465	12161	19623
m_{act} (kg) (per phase)	21	76	352	922	74	274	979	3025
c_{act} (Euro) (per phase)	192	733	3504	8631	604	2280	7510	23051
T (kNm) (model) (per phase)	0.88	4.9	26.9	72.4	1.3	6.6	22.9	65.5
h_{ri} (mm)	3	6	14	25	8	16	15	21
F_p *(FEA)*	35	76	199	277	130	262	240	426
T (kNm) (FEA) (per phase)	0.56	3.7	17.9	46.9	0.76	4.8	11.7	32.1
Cost / Torque	343	198	196	184	795	475	642	718
Torque/mass	27	48	51	51	10	18	12	11
Corrected Efficiency (%)	84	87	85	85	93	93	90	90

Table VIII-2. TFPM machine with toothed rotor: results of torque/mass optimization.

d_{out} (m)	0.5	1.0	2.0	3.0	0.5	1.0	2.0	3.0
Target η (%)	90	90	90	90	95	95	95	95
g (mm)	0.5	1.0	2.0	3.0	0.5	1.0	2.0	3.0
τ_p (mm)	8.8	13.7	21.3	42.0	20.4	36.0	56.6	89
J (A/mm^2)	9.7	7.0	5.0	4.0	2.5	2.1	1.4	1.1
h_m (mm)	1.4	2.7	5.0	11.0	3.7	7.5	6.3	8.0
l_{rt1} (mm)	30	37	60	77	45	60	68	111
l_f (mm)	15	21	35	54	36	49	41	62
w_m (mm)	13.2	16	21	22	13.2	17	35	53
w_{rc1} (mm)	2	2	2	2	2	5	25	47
w_{rc2} (mm)	4	6.3	9.3	18	11	16	19	26
w_{sc} (mm)	6.3	9	9.7	18	9	20	28	41
ψ (degrees)	-34	- 33	-35	-34	-38	- 31	- 30	- 33
Φ_{pnl} (μWb) (model)	118	229	495	1312	564	1147	1461	3061
U_{ap} (A/μWb) (model)	13.9	11.9	8.5	5.4	6.0	4.5	6.1	4.1
U_{up} (A/μWb) (model)	11.5	9.4	7.5	4.6	5.0	3.7	5.2	3.1
$\hat{\Im}_s$ (A-turns) (model)	2521	3885	5884	9926	3645	7525	12161	17661
$\hat{\Im}_s$ (A-turns) (FEA)	3041	4316	6877	9926	3645	8465	12161	19623
m_{act} (kg) (per phase)	20	73.2	310	853	54	274	979	3025
c_{act} (Euro) (per phase)	212	803	3718	9256	476	2280	7510	23051
$\overline{T}$ (kNm) (model) (per phase)	0.9	5.1	27.1	72.4	0.99	6.6	22.9	65.5
h_{ri} (mm)	3	5	9	26	10	16	15	21
$\overline{F}_p$ *(FEA)*	30	66	113	271	81	262	240	426
$\overline{T}$ (kNm) (FEA) (per phase)	0.54	3.3	15.4	42.2	0.58	4.8	11.7	32.1
Cost / Torque	393	243	241	219	821	475	642	718
Torque/mass	27	45	50	50	11	18	12	11
Corrected Efficiency (%)	83	85	82	83	91	93	90	90

Table VIII-3. Conventional PM synchronous machine: results of cost/torque optimization.

d_{out}	η (%)	τ_p (cm)	J (A/mm^2)	B_g (T)	b_t/b_s	K_{rad}	m_{act} (kg)	c_{act} (Euro)	T (kNm)
0.5	84	2.8	7.6	0.80	0.80	0.29	40	300	0.56
1.0	87	3.5	7.2	0.76	0.73	0.186	131	1043	3.71
2.0	85	3.9	8.4	0.66	0.61	0.066	214	1786	17.9
3.0	85	3.9	9.4	0.61	0.59	0.050	353	3157	46.9
0.5	93	5.3	2.3	0.89	1.00	0.61	171	1221	0.76
1.0	93	5.3	3.3	0.79	0.79	0.31	342	2540	4.82
2.0	90	4.6	5.3	0.68	0.64	0.077	280	2311	17.6
3.0	90	3.8	6.4	0.69	0.65	0.043	337	3228	32.2

Table VIII-4. Conventional PM synchronous machine: results of torque/mass optimization.

d_{out}	η (%)	τ_p (cm)	J (A/mm^2)	B_g (T)	b_t/b_s	K_{rad}	m_{act} (kg)	c_{act} (Euro)	T (kNm)
0.5	83	2.3	8.8	0.84	0.88	0.280	36	215	0.54
1.0	85	3.4	7.8	0.70	0.64	0.180	113	677	3.3
2.0	82	2.8	9.9	0.65	0.69	0.072	170	1016	15.4
3.0	83	2.5	11	0.5	0.56	0.088	331	1988	42.3
0.5	91	3.5	3.5	0.85	0.90	0.475	88	648	0.6
1.0	93	5.1	3.4	0.81	0.82	0.310	343	2590	4.89
2.0	90	3.0	6.0	0.68	0.60	0.085	206	1911	12.0
3.0	90	3.1	6.8	0.68	0.66	0.055	336	3481	32.3

Summary

Wind energy makes the generation of clean electricity possible. In the last years, an annual growth rate of 30% has been observed in the installed wind power capacity. Among other reasons, the developments of advanced electromechanical conversion technologies have significantly contributed the field. Three configurations are used in commercial wind turbines: constant-speed, doubly-fed and direct-drive configurations. The first two configurations use a gearbox with an induction generator of rotational speed around 1500 rpm, where the stator winding is directly connected to the grid. The direct-drive configuration uses a synchronous generator mechanically attached to the low-speed shaft of the wind turbine. In this configuration, the stator winding is connected to a power electronic converter, which output is connected to the grid. The power electronic converter decouples the generator frequency from the grid frequency, thus providing a wide-range variable-speed operation. Today, the combination gearbox-induction generator dominates the market of MW-scale wind turbines, due to their lower costs compared to the costs of gearless systems. Nevertheless, there is an acute interest among researchers and wind turbine suppliers in the possibility of removing gears and slip rings, eventually leading to lower maintenance (no oil required and slip rings avoided) and higher reliability due to the absence of wear between gears.

The thesis deals with the issue of cost reduction of direct-drive generators for wind turbines. The focus is set to permanent magnet (PM) synchronous generators, for they provide lower costs and weight. Therefore, the direction followed by the thesis is the investigation and comparison of permanent magnet (PM) machine topologies. The comparison is based on the cost and weight of active material, namely stator copper, rotor PM, magnetically-active steel and powdered iron. The main topologies investigated are separated in two families: longitudinal-flux machines and transverse-flux machines.

The longitudinal-flux machines analyzed are:conventional PM synchronous machine, conventional PM synchronous machine with flux concentration, slotted axial-flux PM machine, TORUS machine. The transverse-flux machines analyzed are: flux-concentrating transverse-flux PM machine sand surface-mounted transverse-flux PM machine.

Longitudinal-flux PM machines

The TORUS is discarded because it is a slotless machine type, which requires thick magnets and generally has a lower air-gap flux density. A wide literature survey of PM machine designs built confirmed the higher costs and weight of the TORUS machines.

The conventional PM synchronous machines using rare earth magnets with or without flux concentration also give lower costs and weight compared to the slotted axial-flux PM machine. The same conclusion has been consistently obtained for diameters of 1, 2, 3 and 4 meters and for efficiencies of 90% and 95%. The analysis was based on design optimization, which uses analytical models assuming straight flux in the air gap.

Transverse-flux PM machines

The surface-mounted TFPM machine is not selected for cost and weight reduction because compared to the flux-concentrating TFPM machine, it needs a larger PM volume for a given torque rating. This is based on a new expression for the machine flux linkage, written as a volume integral applied to the volume of PM material. Compared to the flux-concentrating TFPM machine, the surface-mounted TFPM machine suffers from a lower volumetric contribution of its PM material to the no-load flux linkage.

The thesis gives a review of flux-concentrating transverse-flux PM machines. Five flux-concentrating TFPM machines are discussed and none appear as satisfactory in terms of construction. Good TFPM machines should have a single-sided stator. The construction of the rotor must be independent of the mechanical tolerances of the PM and flux concentrators. The insertion of the rotor parts should be automatable and laminated steel should be used in the stator core for higher efficiency. A new TFPM geometry, called TFPM machine with toothed rotor, is derived in the thesis to fulfill these construction requirements.

An approximate three-dimensional analytical model is developed for the TFPM machine with toothed rotor. The model allows analytical prediction of the nominal average torque, losses and efficiency. This model is based on equivalent linear magnetic circuits, consisting of a number of lumped reluctances determined from finite element analysis. Similarly to longitudinal PM machines, efficiency plays a dominant role in the performance of the TFPM machine with toothed rotor.

A prototype of the TFPM machine with toothed rotor is presented. The measurements show good agreement between the values of no-load flux and inductances measured experimentally and those predicted with the linear model. However, the average nominal torque measured experimentally is 35% lower than the value predicted with the analytical model. For improved accuracy, the model should include local saturation in the stator core.

Comparison between TFPM and conventional PM synchronous machines

Finally, the TFPM machine with toothed rotor and conventional PM synchronous machine are compared with respect to their cost and weight. To allow a valuable comparison, the two machine topologies were optimized with the same constraints, that is efficiency, average nominal torque, outside diameter, rotational speed, air gap thickness and material properties. Comparison of the cost and weight of the two machine topologies for diameters ranging between 0.5 m and 3.0 m showed favorable expected performance of the TFPM machine with toothed rotor for diameters of 0.5 m and 1.0 m. However, for diameters larger than 1.0 m, the conventional PM synchronous machines with/without flux-concentration are better. The degradation of performances of TFPM machines at diameters above 1.0 m is due to the

larger air gaps used and especially the resulting larger pole pitches. The TFPM machine with toothed rotor is a valuable option as long as its optimized pole pitch can be kept significantly lower than the pole pitch of the conventional PM synchronous machines. This can only be obtained for an air gap thickness lower than 1.5 mm.

Using the results of the optimization process, the cost of active material is computed for a 1.5 MW wind turbine. It is found that active material represents about 5% of the total turbine cost, while previous estimates indicated that the generator prices are rather up to 40% of a complete direct-drive wind turbine. Therefore, further optimization of direct-drive machines should also include the costs of manufacturing and the costs of the mechanical structure.

Samenvatting

Wind energie maakt het mogelijk om schone elektriciteit op te wekken. De laatste jaren groeit het geïnstalleerd vermogen van windenergie jaarlijks met 30%. Naast andere redenen heeft de ontwikkeling van geavanceerde elektromechanische conversie technologieën hieraan in belangrijke mate bijgedragen. In commerciële windturbines worden drie configuraties gebruikt: constant toerental, dubbel gevoede en direct-drive systemen. De eerste twee gebruiken een tandwielkast en een inductiegenerator met een toerental van ongeveer 1500 rpm waarvan de statorwikkeling direct aan het net gekoppeld is. De direct-drive configuratie gebruikt een synchrone generator die mechanisch direct aan de langzaam draaiende as van de windturbine gekoppeld is. In dit systeem is de statorwikkeling via een frequentieomzetter gekoppeld aan het net. Deze omzetter ontkoppelt de generatorfrequentie en de netfrequentie, waardoor variabel toerental over een groot toerenbereik mogelijk is. De combinatie van tandwielkast met inductiegenerator domineert de markt van de MW windturbines vanwege de lagere kosten vergeleken met het direct-drive systeem. Echter, onderzoekers en wind turbine leveranciers zijn zeer geïnteresseerd in de mogelijkheid om tandwielkasten en sleepringen te verwijderen, wat uiteindelijk leidt tot minder onderhoud (geen olie en sleepringen) en hogere betrouwbaarheid door de afwezigheid van slijtage in de tandwielkast.

Dit proefschrift gaat over kostenbesparing in direct-drive generatoren voor windturbines. Het concentreert zich op synchrone generatoren met permanente magneten (PM) omdat die minder kosten en wegen. Daarom onderzoekt en vergelijkt dit proefschrift PM generatortypologieën. De vergelijking is gebaseerd op de kosten en het gewicht van actief materiaal, namelijk statorkoper, permanente magneten op de rotor, en magnetisch actief ijzer. De belangrijkste onderzochte typologieën worden onderscheiden in twee families: machines met longitudinale flux en machines met transversale flux.

De machines met longitudinale flux zijn de conventionele PM synchrone machine, de conventionele PM synchrone machine met flux concentratie, de machine met axiale flux en vertande stator, en de TORUS machine. De machines met transversale flux zijn machines met flux concentratie en machines met magneten op het rotoroppervlak.

PM machines met longitudinale flux

De TORUS machine valt af omdat dit een machine met luchtspleetwikkeling is die dikke magneten nodig heeft en meestal een lagere luchtspleetfluxdichtheid heeft. Literatuuronder-

zoek van PM machineontwerpen bevestigde de hogere kosten en het hogere gewicht van TORUS machines.

Ook PM machines met axiale flux en vertande stator vallen af omdat ze zwaarder en duurder zijn dan conventionele PM machines met zeldzame aarden magneten. Dezelfde conclusie is steeds getrokken voor diameters van 1 tot 4 meter en voor rendementen van 90% en 95%. Deze analyse is gebaseerd op een ontwerpoptimalisatie met analytische modellen, waarbij aangenomen is dat de flux de luchtspleet loodrecht oversteekt.

PM machines met transversale flux

Ook TFPM machines met magneten op het rotoroppervlak worden niet gekozen voor reductie van kosten en gewicht. Dit is gebaseerd op een nieuwe uitdrukking voor de gekoppelde flux, geschreven als een volume integraal over het volume van het PM materiaal. Vergeleken met de TFPM machine met flux concentratie heeft de TFPM machine met magneten op het rotoroppervlak een lagere bijdrage van het PM materiaal aan de gekoppelde flux in nullast.

Het proefschrift geeft een overzicht van TFPM machines met flux concentratie. Vijf typologieën worden beschreven, maar geen daarvan blijkt een bevredigende constructie te hebben. Goede TFPM machines moeten de volgende karakteristieken hebben: een enkelzijdige stator, de opbouw van de rotor onafhankelijk van de mechanische toleranties van de PM en de flux concentratoren, automatiseerbare rotorassemblage, en gebruik van gelamineerd blik in de stator voor een hoger rendement. Het proefschrift introduceert een nieuwe TFPM topologie die aan deze constructie-eisen voldoet en de TFPM machine met vertande rotor genoemd wordt.

Er is een benaderend drie-dimensionaal analytisch model van de TFPM machine met vertande rotor ontwikkeld. Dit model voorspelt nominale gemiddelde koppels, verliezen en rendementen. Het model is gebaseerd op lineaire magnetische circuits die bestaan uit samengestelde reluctanties bepaald met behulp van eindige elementen berekeningen. Evenals bij PM machines met longitudinale flux speelt het rendement een dominante rol in de prestaties van de TFPM machine met vertande rotor.

Een prototype van de TFPM machine met vertande rotor wordt gepresenteerd. De metingen van de flux in nullast en van de inductiviteit komen goed overeen met de berekeningen op grond van het lineaire model. Echter, het gemeten gemiddelde nominale koppel is 35% lager dan de waarde berekend met het lineaire model. Om dit te verbeteren, moet verzadiging in het statorijzer opgenomen worden in het model.

Vergelijking tussen TFPM en conventionele PM synchrone machines.

Uiteindelijk worden de TFPM machine met vertande rotor en conventionele PM synchrone machine vergeleken op kosten en gewicht. Voor een zinvolle vergelijking, zijn de twee machine typologieën geoptimaliseerd met dezelfde randvoorwaarden voor rendement, gemiddeld nominaal koppel, buitendiameter, toerental, luchtspleet en materiaaleigenschappen. Vergelijking van de twee typologieën laat zien dat voor diameters beneden 1 m de TFPM met vertande rotor beter presteert, en dat voor diameters van 1 m tot 3 m de conventionele PM synchrone machine beter is. Dat de TFPM voor grotere diameters minder goed

is, komt door de grotere luchtspleet en de grotere poolsteek. De TFPM machine met vertande rotor is een waardevolle optie zolang de geoptimaliseerde poolsteek veel kleiner kan zijn dan de poolsteek van de conventionele PM synchrone machine. Dit is alleen het geval voor luchtspleten kleiner dan 1.5 mm.

Met de resultaten van de optimalisatie zijn de kosten van het actieve materiaal van een generator voor een 1.5 MW windturbine berekend. Het blijkt dat de kosten het actieve materiaal ongeveer 5% van de totale kosten van de turbine zijn, terwijl eerdere schattingen aangaven dat de kosten van een direct-drive generator tot zo'n 40% van de totale kosten opliepen. Daarom moeten de kosten van het produceren en de kosten van de mechanische constructie ook meegenomen worden in de optimalisatie van direct-drive generatoren.